Doctoral Dissertation

Study on Material Properties of Si Thin Films Crystallized on Yttria-Stabilized Zirconia in Solid Phase by Pulsed Laser Annealing

(パルスレーザアニールによりイットリア安定化ジルコニア上に固相結晶化したSi薄膜の膜質に関する研究)

Mai Thi Kieu Lien

Supervisor: Assoc. Prof. Susumu Horita

School of Materials Science

Japan Advanced Institute of Science and Technology

September 2015

Study on Material Properties of Si Thin Films Crystallized on Yttria-Stabilized Zirconia in Solid Phase by Pulsed Laser Annealing

Horita Laboratory

Student number: 1240206

Student name: Mai Lien Thi Kieu

1. Introduction:

In thin-film transistor (TFT) fabrication, although oxide and organic materials have been studied extensively for active channel material, the most prolonged and widely used materials are hydrogenated-amorphous silicon (a-Si:H) and polycrystalline silicon (poly-Si). The a-Si:H TFT can be fabricated at a lower cost than poly-Si TFT. However, low carrier mobility (~ 1 $cm^2V^{-1}s^{-1}$), instability, and low reliability are its drawbacks, which can be addressed by poly-Si TFT. As a fabrication method, generally, crystallization of deposited a-Si films has been widely used to obtain high quality films. It can be carried out by several techniques, such as solid phase crystallization (SPC), metal-induced crystallization (MIC), metal-induced lateral crystallization (MILC), and pulsed laser annealing (PLA). Among them, although PLA has become a leading technique to fabricate poly-Si films at low temperature, high surface roughness and non-uniform-sized grain in the melted poly-Si films limit the extent of applications. To overcome these limitations, we proposed using a crystallization-induction (CI) layer of yttria-stabilized zirconia [$(ZrO_2)_{1-x}(Y_2O_3)_x$:YSZ] combined with PLA for micro-crystallization with non-intentional melting. In this method, an amorphous Si (a-Si) film is deposited on a YSZ layer that covers the surface of a glass substrate. Then, the a-Si film is crystallized in solid phase by the PLA method at room temperature. Since YSZ has a small lattice mismatch of ~5% and the same cubic crystal structure as Si, it can be expected that the obtained poly-Si film will have uniform grain size and crystallographic information, owing to the crystallographic information of the YSZ layer. The combination of the CI layer and SPC-PLA methods is thought to have high potential not only for eliminating the drawback of the melting-PLA method, but also for satisfying the demands for the application of poly-Si TFTs.

The main research purpose is to improve crystallization technique of Si thin film by using YSZ-CI layer combined with SPC-PLA methods. In order to achieve the purpose, firstly, we investigate the crystallinity of pulsed-laser crystallized Si films on YSZ layers, comparing with those on glass substrates. From the obtained results, for further improving the crystallinity of Si films, we propose a new two-step irradiation method using a pulsed laser, which will be mentioned later in more details. We then investigate crystalline quality and electrical properties of crystallized Si films with/without the YSZ layers obtained by the new method, in comparison with the conventional method.

2. Experimental:

A 60 nm YSZ (111)-CI layer is deposited on a cleaned quartz substrate at a substrate temperature of 50 °C by reactive magnetron sputtering. Then, a 60 nm a-Si film is deposited on a YSZ/quartz substrate by e-beam evaporation at 300 °C. For comparison, an a-Si film is also deposited directly on a quartz substrate without a YSZ layer. For investigating electrical properties, undoped and P-doped samples are prepared. P ion implantation is performed at an acceleration voltage of 40~50 kV and the average estimated doping concentration in the Si film is about 3.7×10^{17}~4.9×10^{19} cm^{-3}. Then, crystallization of the a-Si films in solid phase is carried out by PLA together with activation of the implanted P ions in N_2 ambient. For this annealing, we use the new two-step method, which is illustrated in Fig. 1(b), in comparison with the conventional or one-step method in Fig. 1(a). The pulsed laser is Nd:YAG laser (λ = 532 nm) with a repetition frequency of 10 Hz and a pulsed duration of 6~7 ns. In the two-step method, firstly, a-Si films are irradiated at a low initial energy density E_i to generate nuclei, following by irradiation at a high growth energy density E_g to accelerate the nuclei growth and film crystallization without random nucleation in the bulk. For comparison, some samples without doping are also prepared by a conventional method at a fixed high energy density E.

The crystallization degree of Si films without doping is estimated by two kinds of Raman spectroscopies. For evaluation of average crystalline quality of a whole Si film, we used He-Ne laser with the excitation wavelength of 633 nm as a probe beam. The

absorption depth D for a-Si is more than 200 nm. For local evaluation of the surface or interface with YSZ of the Si film, we used He-Cd laser with the wavelength of 442 nm. The Ds for a-Si and poly-Si are 20–30 nm and more than 200 nm, respectively. The crystalline fraction X_c is determined by $X_c = (I_c + I_m) = (I_c + I_m + I_a)$, where I_c, I_m, and I_a are integrated intensities of crystalline silicon (c-Si), intermediate-crystalline silicon (m-Si), and a-Si peaks, respectively. The grain size of poly-Si films after Secco etching is observed by scanning electron microscopy (SEM). The cross-section of the Si films on the YSZ/glass substrate without doping was observed by transmission electron microscopy (TEM). The surface crystallinity of Si films with/without the YSZ layer is observed by reflection high-energy electron diffraction (RHEED) after crystallization. The average carrier concentration n, Hall mobility μ_H, and conductivity σ over in-grains and grain boundaries of the crystallized Si films are measured by AC Hall effect and conductivity measurements, using the Van der Pauw method at a magnetic field of 0.4 T. The measurement temperature is varied from room temperature (RT) to 300 °C, and activation energies of n, μ_H, and σ are estimated.

3. Results and discussion:

Figure 2(a) shows the dependence of crystalline fraction X_c on pulse number N using a He-Ne laser beam for Raman spectroscopy, where the irradiation energy density is a parameter. The Si films in this figure were crystallized by the conventional method. It can be seen that increasing N (or annealing time) makes X_c of Si films increase. At the lower energy density E, X_c is smaller. At the higher E, X_c increases rapidly. The both X_c's become saturated even a the small N. X_c's of Si films on glass substrates are found to be higher, or faster crystallization, than those on YSZ layers at the same E and N. This is because optical absorption in Si film for Si/glass is larger than that for Si/YSZ/glass. The difference in optical absorption between them is calculated to about 10 %, taking multi-reflection into account. Figure 2(b) shows the He-Cd Raman spectra from front and back side measurements of the Si/YSZ/glass, where annealing conditions of E and N are 78 – 80 mJ/cm^2 and 10, respectively, near the onset of X_c saturation as enclosed by a solid circle in Fig. 2(a). Although, from the front side measurement, a very small c-Si peak might be observed, from the back side measurement, a relative high and sharp c-Si peak is clearly seen as shown by dashed circles in Fig. 2(b). This indicates enhanced crystallization growth from the interface between Si and YSZ layers and few nucleation near the surface of Si film. From this result, it can be inferred that annealing at lower E can promote the interface crystallization to keep relatively good quality. However, with only lower E, complete crystallization is impossible.

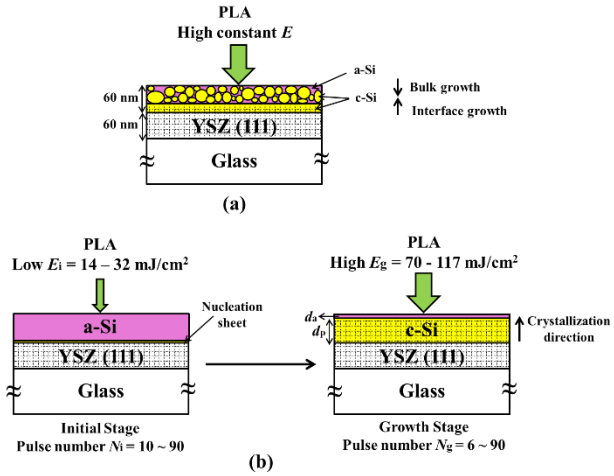

Fig. 1 Schematic illustrations of crystallization in Si/YSZ/glass for the (a) conventional or one-step and (b) new two-step methods together with the irradiation conditions.

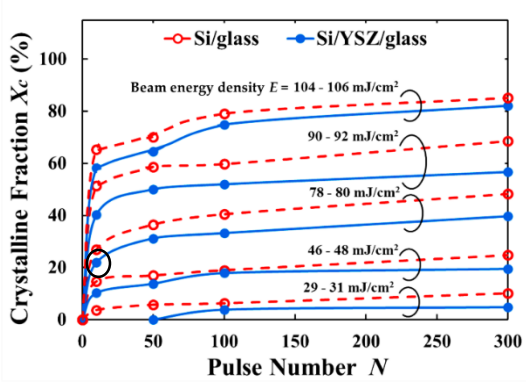

(a) Dependence of crystalline fraction X_c on pulse number N by He-Ne system with absorption depth D (a-Si) > 200 nm.

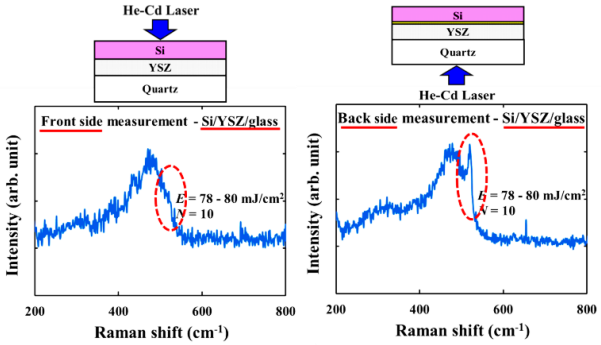

(b) Raman spectra of the Si/YSZ/glass by He-Cd system with D (a-Si) = 20 ~ 30 nm and D (c-Si) > 200 nm.

Fig. 2 Raman analysis results.

From the above results and discussion, in order to obtain a fully crystallized Si film with high quality, we tried to crystallize them with the two-step method as shown in Fig. 1(b). The initial irradiation at a low energy E_i and small N_i makes nuclei at the

interface without in-bulk, and the growth irradiation at high energy E_g and larger N_g enhances crystallization growth from the interface nuclei to the surface with high rate, which should be faster than bulk crystallization. Table I shows the comparison of the typical X_c and FWHM values of the c-Si peak of Si/glass and Si/YSZ/glass for the conventional method with N = 100 and the two-step method with N_i = 10 and N_g = 90, which are obtained by He–Ne Raman spectral analysis. For the conventional method, the samples were irradiated at a high constant E. In the two-step method, two irradiation conditions (A) and (B) were used, shown in Table I. Both the optimized E_i and E_g for Si/YSZ/glass are slightly higher than those for Si/glass due to a small optical absorption difference between them as mentioned before. Firstly, it can be clearly seen that the crystalline quality of the crystallized Si films is more improved by the two-step method (labelled ③ and ④) for both the Si/glass and Si/YSZ/glass structures than by the conventional method (labelled ① and ②). That is, a higher X_c and a smaller FWHM are obtained by the two-step method despite using the same total pulse number and a lower total irradiation energy density E_t, where $E_t = E \cdot N$ for the conventional method and $E_t = E_i \cdot N_i + E_g \cdot N_g$ for the two-step method. Next, we compare the Si/YSZ/glass case ④ with the Si/glass case ③ in the two-step method. Although X_c = 82% for Si/YSZ/glass is apparently smaller than 87% for Si/glass, the FWHM for both is approximately 6.0. This indicates that it is still possible to increase X_c and improve crystalline quality for Si/YSZ/glass by optimizing E. Actually, using the optimized irradiation condition for Si/YSZ/glass in the two-step method, we obtain a higher X_c and a smaller FWHM in ⑤ than in ③ and ④. From these results, it can be concluded that a Si film with a higher crystalline quality can be obtained on YSZ/glass than on the glass substrate for both the conventional and two-step methods, which may be due to the CI effect of the YSZ layer.

Table I. X_c and FWHM of c-Si peaks of Si/glass and Si/YSZ/glass for the conventional and two-step methods.

Method		Irradiation conditions	Si/glass	Si/YSZ/glass
Conventional		E = 104 – 106 mJ/cm², N = 100	X_c = 79% ① FWHM = 8.1	X_c = 75% ② FWHM = 7.6
Two-step	(A)	E_i = 18 – 22 mJ/cm², N_i = 10 E_g = 106 – 109 mJ/cm², N_g = 90 (optimized for Si/glass)	X_c = 87% ③ FWHM = 6.0	X_c = 82% ④ FWHM = 6.1
	(B)	E_i = 20 – 24 mJ/cm², N_i = 10 E_g = 111 – 114 mJ/cm², N_g = 90 (optimized for Si/YSZ/glass)	/	X_c = 91% ⑤ FWHM = 5.2

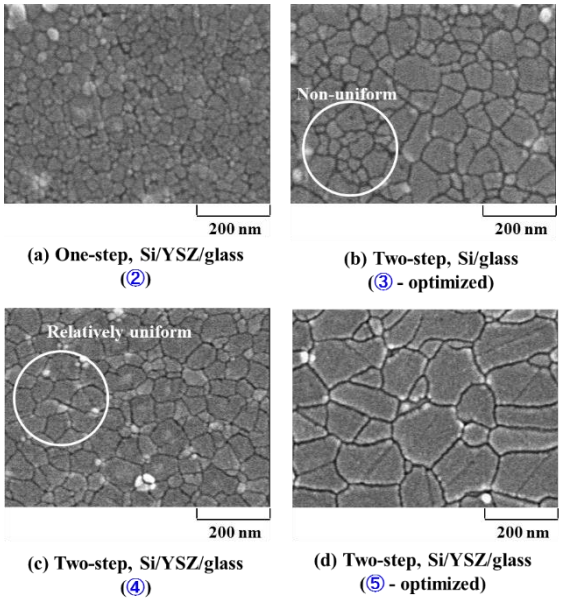

(a) One-step, Si/YSZ/glass (②)
(b) Two-step, Si/glass (③ - optimized)
(c) Two-step, Si/YSZ/glass (④)
(d) Two-step, Si/YSZ/glass (⑤ - optimized)

Fig. 3 SEM images of the Secco-etched Si films crystallized by the conventional and two-step methods. (a)–(d) irradiation conditions are the same as those indicated by ②-⑤ in Table I, respectively.

To determine the effect of the two-step method clearly, by SEM, we observed Secco-etched Si films crystallized by both the conventional and two-step methods. The irradiation conditions are the same as those in Table I. Figure 3(a) shows the SEM image of the Si film irradiated by the conventional method while Figs. 3(b)–3(d) show those by the two-step method, where the sample structures are Si/YSZ/glass except for (b), i.e., Si/glass. The labels ②-⑤ in Fig. 3 correspond to the numbers or the same irradiation conditions in Table I. Firstly, from the comparison between Fig. 3(a) and Fig. 3(c), it can be seen that large grains are obtained in Si/YSZ/glass by the two-step method. This clearly indicates the effectiveness of the two-step method in promoting the crystallization of the a-Si film. Next, we compare the Si film on glass with that on YSZ in the two-step method under the same irradiation conditions, as shown in Figs. 3(b) and 3(c), respectively. It can be found easily that the difference in grain size or grain size non-uniformity is larger in the Si/glass than in the Si/YSZ/glass, for instance, as shown by circles in Figs. 3(b) and 3(c). For Si/YSZ/glass irradiated under its optimized conditions as shown in Fig. 3(d), the grain size apparently becomes larger than that for Si/glass under its optimized irradiation conditions [Fig. 3(b)]. This result indicates better quality of the Si film on the YSZ layer than on the glass substrate, even by using the two-step method.

Figures 4 and 5 show the Arrhenius plots of conductivity σ with respect to the reciprocal of the measurement temperature T for the crystallized undoped and P-doped Si/YSZ/glass and Si/glass structures, respectively, with different doping concentrations. The Si films in these structures were crystallized by the two-step method. The activation energies $E_{\sigma i}$ for σ are also shown in these figures, where i = 1 to 5. It was found that all of Si films are n-type. On the whole, excepting at high doping concentration of 4.9×10^{19} cm^{-3}, the conductivity exhibits the behavior of an activation process for both the undoped and P-doped films on both Si/YSZ/glass and Si/glass structures. For the films at the highest doping concentration of 4.9×10^{19} cm^{-3}, the saturation tendency of conductivity can be

attributed mainly to the saturation of carrier concentration. In Fig. 4, the activation energy of the undoped Si/YSZ/glass film is changed from 0.25 to 0.55 eV around 100 °C. Since $E_{\sigma 2}$ is near half of energy gap $E_g/2$ or intrinsic energy level E_i, the carrier may be generated from carrier traps at grain boundaries due to thermal excitation. On the other hand, in the low temperature region (T ≤ 100 °C), carriers are excited from the some donors with an impurity level around 0.46 eV (data are not shown). Also, at the low temperature, free carriers are hardly excited from the trap levels at the grain boundaries. For the doped Si/YSZ/glass cases, the activation energies are lower than $E_{\sigma 2}$ = 0.55 eV of the undoped film and decrease with increasing doping concentration. This is probably because doped P ions segregate mainly into grain boundaries and passivate electrical defects. The amount of passivated defects increases with doping concentration, as a result, the conductivity increases. However, at higher doping concentration, the amount of dopant for passivation is enough and some doped P atoms are thermally activated from the normal donor level of 0.044 eV. For example, for the doping concentration of 4.9×10^{19} cm^{-3}, almost dopant P atoms give free electron carriers at RT. Therefore, E_σ is lower value of 0.01 eV (Si/YSZ/glass) or 0.03 eV (Si/glass).

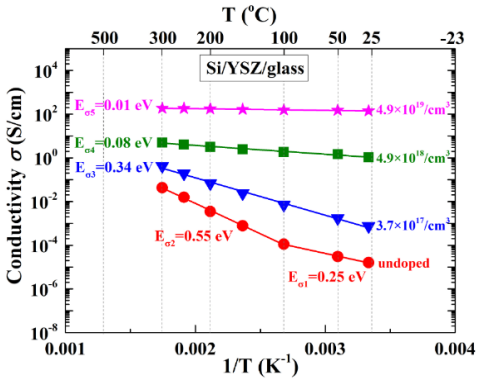

Fig. 4 Measurement temperature dependences of conductivity σ for the undoped and doped Si/YSZ/glass structures crystallized by the two-step method.

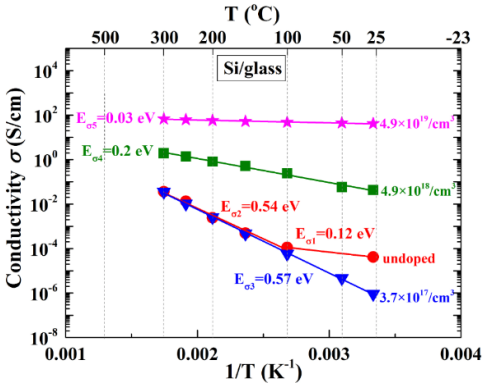

Fig. 5 Measurement temperature dependences of conductivity σ for the undoped and doped Si/glass structures crystallized by the two-step method.

In Fig. 5 of the Si/glass films, the conductivities are almost the same for both the undoped and low P-doped (3.7×10^{17} cm^{-3}), which means that the P-doping is not effective. Although the obtained Hall mobility for the low P-doped film is a little higher than that of the undoped one, the carrier concentrations (e.g., ~1.5×10^{14} cm^{-3} at 100 °C) are nearly the same for both cases (the data are not shown). This is probably because the amount of the P dopant atoms are not so much to passivate most of the defects in the Si/glass film, compared with the Si/YSZ/glass one. The higher defect density in the Si/glass than in the Si/YSZ/glass also leads to the lower conductivity and higher activation energy in the former than in the latter at the same doping concentration. From the above results, it can be concluded that electrical property of the Si films on YSZ layers are much better than those on the glass substrates.

Figures 6(a) and (b) show typical transfer characteristics of the fabricated TFTs for the **Si/YSZ/glass** and **Si/glass** structures with $W = L$ = 40 μm. It can be seen that the TFTs can operate with relatively small off leakage current of ~10^{-12} A. The field-effect mobility for TFTs fabricated on the **Si/YSZ/glass** is about twice higher than that on the **Si/glass**. We estimated and summarized several important parameters of the device characteristics for the two structures of the Si/glass and Si/YSZ/glass. The field-effect mobility (μ_{eff}) and subthreshold swing (S.S) are evaluated from the linear and subthreshold regions, respectively, at V_D = 0.1 V. The ON/OFF current ratio is defined as the ratio of maximum drain current I_{Dmax} over minimum drain current I_{Dmin} within the measured range of I_D-V_G curve at V_D = 0.1 V. The threshold voltage (V_{th}) is determined by an interception of linear extrapolation of the I_D-V_G curve at V_D = 0.1 V. Table I summarizes the average values of device parameters together with their standard deviations of the TFTs with $W = L$ = 40 μm for the two structures. For each structure, 15 TFTs were measured. It can be seen that the TFTs fabricated on the **Si/YSZ/glass** structure exhibit a relatively higher μ_{eff} with smaller deviation than those on the Si/glass. The average V_{th} and average S.S of TFTs fabricated on the **Si/YSZ/glass** are both smaller with smaller deviations than those on the **Si/glass**. On the other hand, the average ON/OFF current ratio of TFTs fabricated on the Si/YSZ/glass is a little lower than those on the Si/glass. The field-effect mobility, threshold voltage, and subthreshold swing are strongly affected by the presence of grain boundaries and defects inside the channel. Therefore, comparing to the TFTs fabricated on the Si/glass, the relatively better performance of the TFTs fabricated on the Si/YSZ/glass are considered owing to the better crystalline quality of the Si film on the YSZ/glass. This is thank to the CI effect of the YSZ layer as discussed in the previously. The superior device-to-device uniformity in performance (expressed

by smaller standard deviations) of the TFTs fabricated on the **Si/YSZ/glass** than on the **Si/glass** is considered to be due to the more uniform grain size and crystalline defects distributions in the Si films for the former than for the latter.

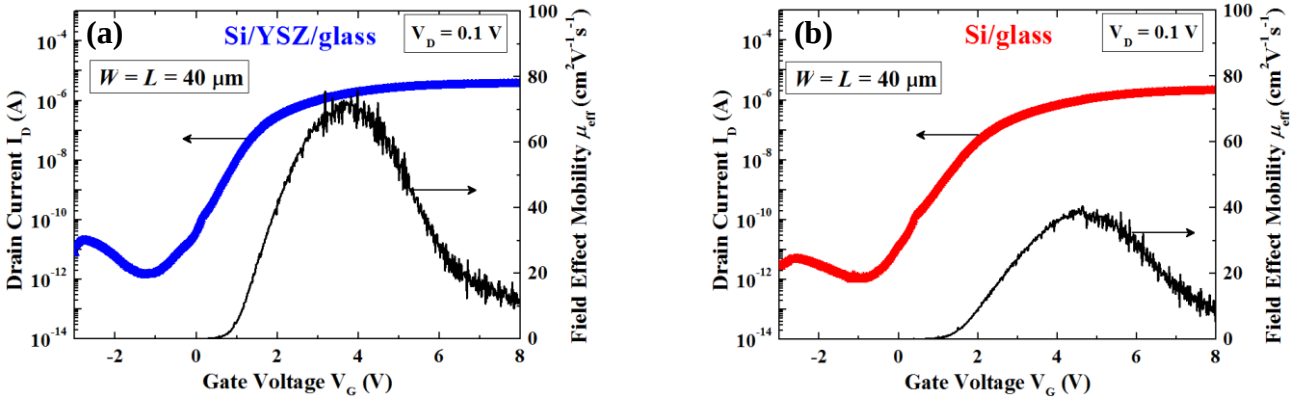

Fig. 6 Transfer characteristics of fabricated poly-Si TFTs for (a) the Si/YSZ/glass and (b) Si/glass structures with *W*=*L*=40 μm.

Table I Average values of μ_{eff}, V_{th}, and S.S together with their standard deviations, and average ON/OFF ratio of the TFTs with *W* = *L* = 40 μm for the two structures of the Si/glass and Si/YSZ/glass.

	Field-effect mobility μ_{eff} ($cm^2V^{-1}s^{-1}$)		Threshold voltage V_{th} (V)		Subthreshold swing S.S (mV/dec.)		ON/OFF ratio
	Average value	Standard deviation	Average value	Standard deviation	Average value	Standard deviation	Average value
Si/glass	40.3	28	2.83	0.78	426	99	1.74×10^6
Si/YSZ/glass	78.1	18	2	0.22	306	31	9.14×10^5

4. Conclusion:

We crystallized Si films on glass substrates with/without a YSZ-CI layer in the solid phase by PLA, and investigated not only their crystalline but also electrical properties. It was found that, for Si/YSZ/glass, nucleation occurs faster at the YSZ interface than in the bulk of the a-Si film at a low energy density *E*. For further improving the crystallinity of the Si films, we proposed the two-step method. The Raman analysis and SEM observation show that higher crystallization degree with better quality, and large-sized grains were obtained by the two-step method compared with the conventional method at the same total pulse number *N* and high total irradiation energy density E_t. Comparing the Si/YSZ/glass and Si/glass at their own optimized irradiation conditions, we obtained a higher crystallization degree with better quality in the former. The electrical property measurement results for both the undoped and doped Si films revealed that higher carrier concentration, Hall mobility, and conductivity are obtained for the Si/YSZ/glass structure compared with those of the Si/glass. Further, we fabricated poly-Si TFTs on both the structures. The device parameters of μ_{eff}, V_{th}, S.S, and ON/OFF current ratio of the fabricated TFTs were estimated as well as their uniformity. It was found that the TFTs fabricated on the Si/YSZ/glass exhibit a relatively better performance and superior device-to-device uniformity than those on the Si/glass. This result is considered owing to the better crystalline quality of the Si film on the YSZ/glass and uniform distribution of grains as well as crystalline defects, which indicating effectiveness of the crystallization-induction effect of the YSZ layer.

References: 1) M. T. K. Lien and S. Horita, Jpn. J. Appl. Phys. **53**, 03CB01 (2014) and refs. in there.

2) M. T. K. Lien and S. Horita, Jpn. J. Appl. Phys. **54**, 03CA01 (2015) and refs. in there.

Keywords: poly-Si, pulsed laser, YSZ, crystallization-induction layer, low temperature, solid phase crystallization, TFT.

Table of contents

ACKNOWLEDGEMENTS

First of all, I would like to express my deepest gratitude to my respected supervisor, Associate Professor Susumu Horita for his encouragement, guidance and support during my study and completion of this thesis. Without his support and guidance, my study and this thesis may not be completed on time. He taught me a lot, not only in technical knowledge, but also in life. From the bottom of my heart, I express my gratefulness to him about this.

I am heartily thankful to Professor Masahiko Tomitori for his valuable help and encouragement during the time I am here. He always accepted me readily and friendly whenever I need his help.

I would like to thank Professor Eisuke Tokumistu for his supervision and guidance sincerely. Without his help, my minor thesis may not be possible.

I would like to express my great respect and thankfulness to Associate Professor Shin-Ichiro Kuroki, Professor Seiichirou Higashi, and their lab. members for welcoming and supporting me during my study and completion of my minor thesis. Without their support and guidance, my minor research may not be completed.

I sincerely thank to my internal committee members, Professor Tatsuya Shimoda, Professor Eisuke Tokumistu, and Associate Professor Keisuke Ohdaira from School of Materials Science – JAIST. I specially thank to Professor Seiichiro Higashi from Hiroshima University, the external committee member. I thank all of them for their time and consideration in serving on my thesis committee.

I would like to acknowledge Japan Advanced Institute of Science and Technology (JAIST), Heiwa Nakajima Foundation, Marubun Research Promotion Foundation, and NEC C&C Foundation for their financial support during my Ph. D

study in Japan.

Personally and finally, I would like to express my respect and thankfulness to my family and my friends, especially my parents and my husband, for their encouragement and love that gave me more energetic to overcome many difficulties in living and studying in Japan.

Mai Thi Kieu Lien

Ishikawa – Japan

September, 2015

Chapter 1:

Introduction

1.1 Overview of thin-film transistors (TFTs)

In the more than eight decades since their conception in Lilienfeld's patent[1)] (1933), thin-film transistors (TFTs) have been experienced extensive evolution, development, and refinement. Up to now, many new materials, structures, and fabrication techniques have been introduced in order to apply TFTs to switching systems, low-cost computer logic, flat panel display addressing, and so on.

A TFT is a special kind of field-effect transistor made by depositing thin films of a semiconductor active layer as well as a dielectric layer and metallic contacts over a substrate. Its structure and operation principles are similar to those of the metal oxide field effect transistor (MOSFET), which is the most critical device component in modern integrated circuits (ICs). The early popular TFT versions were made of compound semiconductors, such as CdS and CdSe.[2,3)] This kind of TFT has a high field effect mobility (> 40 $cm^2V^{-1}s^{-1}$). However, mass production of liquid crystal displays (LCDs) on large-area substrates of these TFTs has never been realized due to complications in controlling the properties of the thin film compound semiconductor material and device reliability over large areas.[4)] The innovation came from a report in 1979 of the first functional TFT made from hydrogenated amorphous silicon (a-Si:H) with a silicon nitride gate dielectric layer.[5)] The fabrication process is simple and the device is stable at room temperature under atmospheric conditions. The a-Si:H TFT was recognized as the most suitable device for large-area active matrix (AM) LCDs immediately after its invention. Almost major electronics companies in the world had activities on this device with the common goal of realizing mass production of high performance flat panel displays. However, few large-scale production facilities were built. This is because there are some drawbacks remaining in the a-Si:H TFTs device although their characteristics are good enough for pixel switching in LCD. First, the mobility is too low (≤ 1 $cm^2V^{-1}s^{-1}$) for high-speed or large-current applications, such as the driving circuit of the display and the pixel driving in the organic light emitting diode (OLED) display. Second, since a-Si:H is a photoconductor, the TFT has a large leakage current under light exposure conditions.

Third, stability of the TFT, e.g., threshold voltage shift under extensive stress condition, has been a concern.[6-8)]

In order to improve properties of TFTs such as higher mobility and higher reliability, and to lower production costs to meet application needs, a large number of studies of TFTs channel materials using oxides,[9-11)] organic materials,[12,13)] and crystalline silicon (c-Si)[14,15)] have been carried out extensively. Oxide TFTs are transparent and can be fabricated on flexible substrates at a low temperature. Oxide TFTs such as indium gallium zinc oxide (IGZO) and zinc oxide (ZnO) have low production cost and relatively high reliability. They are much attractive to many researchers. In spite of their attraction, they still have some issues of instability under bias stress and illumination.[16-18)] Organic TFTs have the advantages of flexibility, low manufacturing costs, but the serious problem is unreliability.[19-20)] On the other hand, although having higher fabrication cost than that of a-Si:H, polycrystalline silicon (poly-Si) TFTs have great advantages of stability, higher reliability, and higher mobility, compared with the above TFTs.

Poly-Si is a material consisting of multiple small Si crystals, which are oriented randomly with respect to one another. Various techniques have been developed to improve quality of the poly-Si films so that single-crystal like behavior is realized. Roughly, there are two kinds of methods. One is direct deposition of a polycrystalline film, and the other is crystallization of an a-Si film deposited on an insulator. These methods will be discussed in detail in the next section. Crystalline grain size of poly-Si is from tens nanometers up to three micrometers, which depends on the fabrication process. In order to satisfy the demands for low cost and high performance, it is necessary to develop a low-temperature fabrication process of poly-Si TFTs with uniform grain size, uniform orientation of grain, and smooth surface. The uniform grain size and orientation of poly-Si films are desired to obtain high carrier mobility uniformly over a system. The smooth surface of poly-Si films is also necessary to obtain uniform threshold voltage (V_{th}) and subthreshold swing (S), which determine a system performance, consisting of many devices.

1.2 Conventional fabrication methods of poly-Si thin films

1.2.1 Direct deposition method of poly-Si thin films

There are various methods reported by several groups such as chemical vapor deposition (CVD) and magnetron sputtering to deposit a poly-Si film on a substrate

directly. In CVD methods, a poly-Si film is deposited by catalytic CVD at a substrate temperature lower than 450 ^{o}C,[21-22] or plasma enhanced CVD (PECVD) [23] using a gas mixture of silane (SiH_4) and hydrogen (H_2). For magnetron sputtering methods, a poly-Si thin-film is successfully deposited on a glass substrate at temperatures lower than 250 °C with a mixture of H_2 and argon (Ar).[24] P. Reinig et al. reported that poly-Si films were grown successfully by pulsed-dc magnetron sputtering in pure Ar atmosphere.[25]

It is found that the directly deposited poly-Si thin films have grain sizes less than 50 nm with a considerable surface roughness (up to 0.1 μm). Due to the presence of small grains as well as defects, TFTs made in this poly-Si material exhibit a very low mobility less than 1 $cm^2V^{-1}s^{-1}$.[26] Moreover, an a-Si phase incubation (or transition) layer is formed between the glass substrate and the polycrystalline region during film growth. This is because there is a transition time for the formation of Si nuclei during the deposition. In other words, nucleation does not occur on the substrate surface. By decreasing the deposition pressure, the grain size can be increased up to 100 nm and defect density can be reduced, resulting in an increased mobility to ~10 $cm^2V^{-1}s^{-1}$. However, lowering the pressure even further is not effective any more since the TFT mobility is degraded by increase in surface roughness with decreasing the deposition pressure.[27]

1.2.2 Crystallization methods of deposited amorphous Si (a-Si) films

A solution to the problems of grain size and surface roughness encountered in the direct deposition technique is obtained when processes of Si film deposition and grain growth are separated. Firstly, a film is fabricated mainly in amorphous phase. When this material is annealed, the amorphous material will crystallize, and a poly-Si film is obtained. This approach results in a higher mobility due to a larger grain size and a lower crystalline defect density. The crystallization of deposited a-Si films can be carried out by several methods, such as solid phase crystallization (SPC), nucleation enhancement, and pulsed laser annealing.

a) Solid phase crystallization (SPC) method

A clear difference between amorphous and crystalline phases of Si is free energy. Although crystalline state has lower free energy than amorphous state, it is needed to supply some energy for the crystallization of a-Si in order to overcome activation energy barrier. The simplest method for supplying energy is raising temperature, which is so-called solid phase crystallization (SPC) method. The SPC of a-Si film consists of two main

steps, which are nucleation and growth of crystalline clusters.[28] The more detailed mechanism will be mentioned in chapter 2. R. B. Iverson and R. Reif[29] reported that large grain size of crystalline film could be obtained when the crystal growth rate was high and the nucleation rate was low. This can be easily achieved at low temperature crystallization (< 700 ^{o}C) because nucleation needs higher activation energy compared to that of crystal growth.

There are two general ways to obtain a starting a-Si material. The first way is to subject a directly deposited poly-Si film to a high dose Si ion implantation.[30,31] The second way is to use systems of direct deposition of poly-Si, but reduce the deposition temperature such that an a-Si layer instead of poly-Si is deposited. For the first way, the ion implantation will amorphize most of the poly-Si film, except for certain crystals. Under optimum condition of ion dose and crystallization time, films with a grain size up to 3 μm have been reported.[32,33] Due to this large grain-size, a significant higher mobility has been obtained, compared with the direct deposition case. However, in practice, self-implantation of poly-Si is not an economical way of obtaining a-Si films. On the other hand, the second way is more preferable in practice due to its lower cost. There are several methods to deposit a precursor a-Si film, namely vacuum evaporation, sputtering, CVD, hot-wire CVD, PECVD, etc.

The precursor film is crystallized by various techniques. The simplest and most common technique is to anneal the film in a furnace filled with inert gases (like N_2) or in vacuum at temperatures ranging from 500 to 600 ^{o}C. However, a disadvantage of this technique is long annealing time. In order to solve this problem, there are some groups reported a faster annealing technique or rapid thermal annealing (RTA), which heats a-Si films at higher temperature (> 700 ^{o}C) with a broad-spectrum tungsten-halogen lamp. [34,35] Even if annealing temperature is higher than glass soften temperature (660 ^{o}C),[36] some short annealing time is expected to induce small thermal stress on a glass substrate. However, grain size of the poly-Si film obtained by short annealing time is smaller than that of normal furnace annealing due to increasing number of nucleation sites during RTA.

A poly-Si film fabricated by SPC method has smooth surface and uniform in grain size. Furthermore, SPC by furnace annealing can be applied for large area fabrication. However, not only high annealing temperature by either furnace annealing or RTA, but also long annealing time by furnace annealing are disadvantages of the SPC method. Recently, a new SPC technique using microwave heating[37] has been applied in order to decrease

annealing temperature and time. a-Si thin films were annealed by microwave heating at 550 °C in N_2 after the deposition at temperature range of 100 – 400 °C by PECVD. Microwave heating can lower annealing temperature and reduce annealing time for complete crystallization thanks to interaction between microwave and silicon atoms. However, this method is difficult to anneal a large area. Further, up to now, the mechanism of microwave heating effect is not well-known. It is also necessary for further work to understand the microwave heating effect in order to apply this technique more effectively.

(b) Nucleation enhancement method

In order to reduce the drawbacks of SPC method, various methods and techniques have been proposed. In this section, we briefly introduce the nucleation enhancement methods, which include metal-induced crystallization, ion beam-induced crystallization, and plasma-induced crystallization.

- *Metal-induced crystallization (MIC) method*

In 1969, Oki et al.[38] observed that amorphous Ge crystallizes at surprisingly low temperatures when it is in contact with a metal such as Al, Ag, Au, Cu, or Sn. Shortly thereafter, Bosnell and Voisey[39] reported that such decreased crystallization temperatures also occur for a-Si in contact with a metal. In both studies, the amorphous semiconductors and the metals were prepared by vacuum evaporation and an electron diffraction technique was used to detect the occurrence of crystallization. The more detailed investigations were carried out by Herd et al.,[40] and this phenomenon was named metal-contact-induced crystallization, nowadays usually referred to as metal-induced crystallization (MIC). In MIC method, there are some ways to introduce a metal in a semiconductor, such as covering a capping metal layer onto a semiconductor,[38-40] ion implantation,[41] spin coating,[42] co-deposition of semiconductor-metal alloys,[43] and so on. After that, the film is annealed to transform from amorphous into crystalline phase. It was found that the MIC process does not involve the formation of any liquid phase: it is a fully solid-state process. Furthermore, no formation of any (metastable) metal semiconductor compound was detected during MIC in such systems.

The crystallization temperature is reduced thanks to dissolution of metal atoms in semiconductor films. In the case of Si, the metallic impurities lower activation energy for nucleation and growth of c-Si by weakening Si-Si bonds. As a variant of this method, metal-induced lateral crystallization (MILC) was identified in the late 1990s, [44-46] in which

some metal is deposited only on some area of the a-Si. Upon annealing, crystallization starts from a portion of a-Si, which is covered by metal, and proceeds laterally. Unlike MIC process, where metal contamination in obtained poly-Si films is relatively high, laterally crystallized Si films in MILC process contain a very small amount of metal. Its crystallization speed is low, but is sufficient for applications such as fabrication of TFTs. In this case, metal is deposited on the source/drain area of the transistor and the channel is laterally crystallized. Although MIC and MILC can hasten the crystallization process or reduce the crystallization temperature, high leakage current due to remaining metal contaminant in the Si films is a main drawback of these methods.

- *Ion-beam-induced crystallization method*

As mentioned earlier, free energy of a-Si is higher than that of c-Si. This implies the presence of a driving force for transition from amorphous to crystalline phase. At room temperature, a-Si is metastable and it transforms into c-Si upon heating. In the case of an a-Si layer formed on the top of a single-crystal substrate, this transition occurs by a planar motion of the crystalline-amorphous interface from the interface towards the surface of a-Si. This process is referred to as epitaxial crystallization.[47)] The growth rate of epitaxial crystallization is strongly dependent on temperature. At lower temperature, this rate is very small and amorphous to crystal transition becomes kinetically inhibited.

Epitaxial crystallization of a-Si layers can be promoted by ion-beam-induced epitaxial crystallization (IBIEC) at low temperature (150−300 ^{o}C). For typical ion fluxes, irradiation has been shown to produce crystallization of Si through displacement of a planar interface, and induce a planar crystal growth. However, in amorphous matrix, small crystalline grains are embedded and they collide one another accompanying with grain boundaries. More interestingly, ion bombardment has been shown to dramatically enhance SPC with respect to pure thermal process. For instance, when a-Si is bombarded by xenon ions at 1.5 MeV, nucleation and growth rates can be enhanced by eight and four orders of magnitude, respectively, compared to pure thermal processes.[48)] Some reports showed that ion-bombardment-induced crystallization is controlled by beam parameters such as dose rate and average energy deposited by elastic collisions in the solid, and finally it may allow independent control of nucleation and growth rates.[49,50)] This method is still being studied to optimize the conditions in order to achieve large grain Si. However, IBIEC method is high cost, low productivity, and unsuitable for large area crystallization. They are serious drawbacks for TFT fabrication.

- *Plasma-induced crystallization method*

In addition to the above-mentioned techniques to enhance the nucleation rate and thereby the crystallization kinetics of a-Si films, it has been reported that plasma treatment of a-Si:H deposited by PECVD resulted in enhancement of the crystallization rate of the film during subsequent annealing. The plasma treatment using either oxygen,[51,52] helium,[53] or hydrogen[54] was conducted in an electron cyclotron resonance (ECR) plasma system at a substrate temperature of 400 °C for 1 h. During the successive annealing of the films in a furnace, it was found that the films exposed to the plasma prior to annealing were crystallized faster than the untreated films. In addition, it was also found that the plasma effect could be masked using a hard mask like SiO_2, and hence be used to create both polycrystalline and amorphous regions in the same single silicon layer.

In comparison with MIC method, plasma-enhanced crystallization of a-Si:H might be a method that introduces less contaminations in the films. The radiation damage by this method is also lower than ion beam-induced crystallization. However, comparing with the conventional furnace annealing, a main disadvantage of this method is to use toxic, explosive, and expensive gases, such as silane (SiH_4), monomethylsilane (MMS), methane (CH_4), and hydrogen (H_2), etc. The other drawback is that it requires the use of a vacuum system to generate plasma, and a more complex reactor to contain the plasma. Therefore, it is an expensive method.

(c) Pulsed laser annealing (PLA) method

The field of laser crystallization and laser annealing has its origin in the late 1970s. The utilization of a laser beam as a direct energy source was considered advantageous since the time of the heat flow, and the location of the specimen can be controlled in a unique way. One of the first utilization of laser annealing was the removal of implantation damage and the subsequent electrical activation of dopants.[55] Crystallization of a-Si films using pulsed laser beams has quickly become one of the leading techniques to fabricate poly-Si films at low temperature. The success of PLA method results from the fact that it is appropriate for inexpensive low temperature glass and plastic substrates. The crystallization process using a short and high-intensity pulsed laser is carried out through fast selective melting and subsequent solidification of a-Si layers without significant thermal loading of substrates. Moreover, the pulsed laser can produces poly-Si films with relatively large grains (up to hundreds of micron depending on the laser energy density used for the crystallization) and

with electrical properties suitable for fabrication of thin film electronic devices. In comparison with SPC and MIC methods, PLA method can limit rapid heating and cooling to thin surface layers. This is mainly controlled by pulse duration time and absorption depth of the laser beam irradiating the material. A variety of lasers has been used for the processing of materials, such as gas laser (Ar ion),[56] excimer laser (ArF, XeCl, KrF),[57,58] solid-state laser (Nd:YAG, Nd:YLF),[59] and so on. However, melting-crystallized films by PLA method have the drawbacks of high film surface roughness and nonuniformity of grain size, which lead to nonuniform device performance as mentioned before.

Table 1.1 shows the summary of process temperature, carrier mobility, grain size/uniformity, and drawbacks in conventional fabrication methods and the deposited Si film characteristics.[60]

Table 1.1 Summary of process temperature, carrier mobility, grain size/uniformity, and drawbacks in conventional fabrication methods and characteristics of the deposited Si films.

Film		**Process temp.**	**Carrier mobility**	**Grain size /uniformity**	**Drawbacks**
a-Si		~ 300 °C	~1 $cm^2V^{-1}s^{-1}$	uniform over large area	- Low carrier mobility - Low device reliability
Direct deposited poly-Si (CVD, sputtering)		250 ~ 600 °C	5~ 10 $cm^2V^{-1}s^{-1}$	~ 50 nm	- High rough surface - A lot of crystalline defects - Formation of amorphous transition layer
Poly-Si	SPC	500 °C ~	~ 50 cm^2/V.s	- Small and uniform grain size - Smooth surface	- High process temperature - Long annealing time
	MIC MILC	150 ~ 500 °C	~ 120 cm^2/V.s	Larger grain size than SPC	- Remnant of metal impurities in poly-Si film
	PLA	Room temp. ~	~ 500 cm^2/V.s	- Tens to hundreds nm - Nonuniform of grain size	- High surface roughness

1.3 Crystallization method using a crystallization-induction (CI) layer

1.3.1 Overview of CI layer method

The directly deposited poly-Si film on glass substrate has relatively uniform grain size, but formation of incubation layer and low field-effect mobility are drawbacks for application. The nucleation enhancement and PLA methods can produce poly-Si films with high carrier mobility at low temperature. However, high leakage current due to remaining contaminant is a main drawback of the former. The disadvantages of the latter is non-uniformity in grain size and crystallographic orientation, which reduces device quality. Therefore, in order to obtain a low temperature poly-Si film without any incubation layer, uniformity in grain size and crystallographic orientation, low impurities and smooth surface, we propose a crystallization induction (CI) layer method. In this method, an Si film is deposited on a CI layer that covers surface of a substrate as shown in Fig. 1.1, comparing with no CI layer or conventional method. The CI layer, which is a polycrystalline dielectric, should have similar lattice constant and crystal structure to Si. The small lattice mismatch and same crystal structure give some advantages for low-temperature crystallization, although the heteroepitaxial growth of the Si film may not occur on the CI layer because of its too low process temperature. It is expected that the CI layer provides nucleation sites for arriving a-Si atoms during the deposition, and hence leading crystallization of the Si film at low temperature. Also, it is believed that the nucleation starts at the interface between the Si film and the CI layer, and crystalline information of the CI layer can be transmitted to the deposited Si film. Consequently, crystal growth of the Si film can take place smoothy and uniformly from nuclei at the CI layer surface. By this way, the obtained poly-Si film has a uniform grain size and crystallographic orientation. Moreover, it can be expected that there is no incubation layer at the CI layer interface.

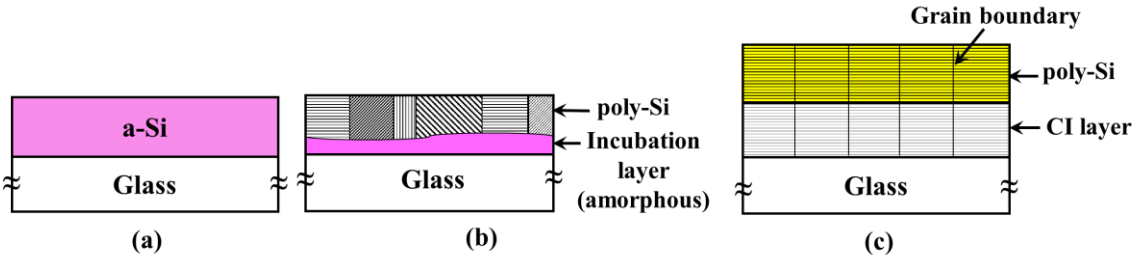

Fig. 1.1 Schematic illustrations of deposited Si films on glass substrates.

1.3.2 Materials for CI layer

As a CI material, there are several candidates have been proposed and investigated, such as ZrO_2[61] and CaF_2.[62,63] However, on the ZrO_2 layer, an amorphous incubation layer is formed, which means that ZrO_2 does not act as an actual CI material. CaF_2 is not an appropriate candidate material for electron devices owing to its low breakdown voltage and fluoride trap charges. On the other hand, we use a polycrystalline yttria-stabilized zirconia [$(ZrO_2)_{1-x}(Y_2O_3)_x$: YSZ] layer, whose structure is shown in Fig. 1.2. It is a zirconium oxide (ZrO_2) based ceramic, in which its particular crystal structure is made stable at room temperature by an addition of yttrium oxide (Y_2O_3). The addition of Y_2O_3 to pure ZrO_2 replaces some of the Zr^{4+} ions in the ZrO_2 lattice with Y^{3+} ions. This produces oxygen vacancies because three O^{2-} ions replace four O^{2-} ions. YSZ is a thermally and chemically stable material. It has been reported that YSZ films can be grown heteroepitaxially at temperatures higher than 800 ^oC on Si and vice versa[66,67] thanks to YSZ properties, which are small lattice mismatch ~ 5% (the lattice constants of YSZ and Si are 0.515 nm and 0.543 nm,[64] respectively) and the same cubic crystal structure with Si. These are important and favorable factors for the CI effect of YSZ on crystallization of an a-Si film. Table 1.2 shows the properties of YSZ.

Based on the YSZ properties which are the small lattice mismatch and same cubic crystal structure with Si, we choose it as a CI material to enhance crystallization of a deposited a-Si film at low temperature. We expect that an obtained poly-Si film has

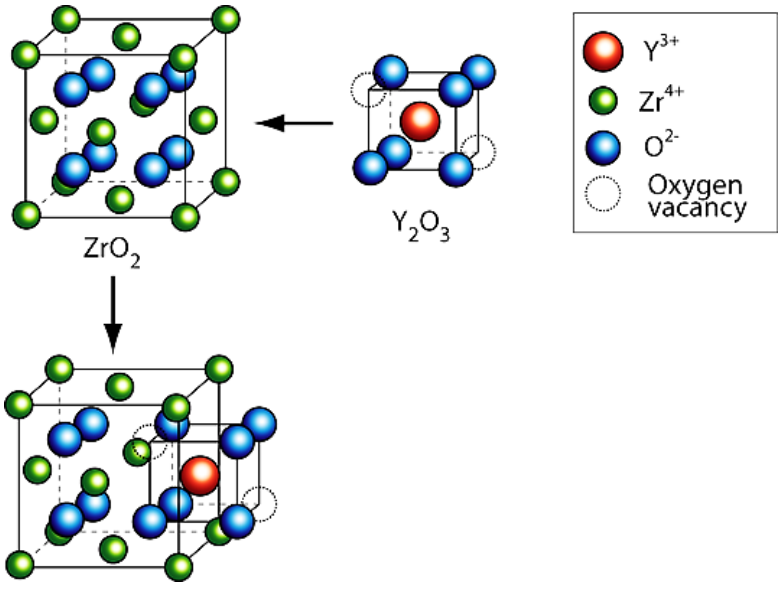

Fig. 1.2 Crystal structure of YSZ.[65]

uniform grain size and crystallographic information, which is achieved thanks to the crystallographic information of the YSZ layer.

Table 1.2 Properties of yttria-stabilized zirconia (YSZ).[64,68,69)]

Melting point	~ 2700 ^{o}C
Thermal expansion coefficient	$11x10^{-6}$ / ^{o}C
Thermal conductivity	3.8 $Wm^{-1}K^{-1}$
Dielectric constant	25 ~ 29.7
Band gap	4.96 eV
Resistivity	10^{13} ~ 10^{16} Ω .cm

1.3.3 Previous works in YSZ-CI layer method

Previously in our laboratory, it was reported that Si films directly deposited on YSZ layers were crystallized, while Si films on glass substrates were still amorphous at the deposition temperature of 430 ^{o}C.[70)] It was also found that the chemical cleaning of the surface of a YSZ layer just prior to Si film deposition is a critical key process, as follows: After dipping YSZ layers into HF solution for removing contaminated and damaged surface layers, they were rinsed with ethanol solution or deionized water (DIW). The Si films deposited on the ethanol-rinsed YSZ layers were crystallized, but not those on the DIW-rinsed YSZ layers. The following reason was proposed. During the HF etching process, F atoms adsorb on the YSZ layer surface. Even after the ethanol rinsing process, some of the F atoms remain on the layer surface, and the residual F atoms may protect the bare etched YSZ surface from exposure to contaminants in the preparation atmosphere. Just before Si film deposition in a vacuum chamber, most of the F atoms desorb at substrate heating. Therefore, the residual F atoms can contribute to the smooth transmission of crystallographic information from the YSZ surface to the deposited Si. Because the residual amount of F atoms after the DIW rinsing process was much smaller than that after the ethanol rinsing process, Si crystallization on the DIW-rinsed YSZ layers hardly occurred.

Another report had found that crystalline fractions of Si films were strongly dependent of the yttrium content ratios R_{YA} = Y/(Zr + Y) of as-deposited YSZ layers. When R_{YA} was 0.21, even on DIW-rinsed YSZ layers, the crystallization of Si films occurred at 430 °C.[71] By further improving rinse process, the crystallization of a Si film directly deposited on a YSZ layer occurs at a lower substrate temperature of 320°C, which is lower than that on a glass substrate without a YSZ layer by more than 100°C.[72] However, the deposition temperature >300°C is not low enough for non-heat-resistant device applications such as flexible displays with a plastic substrate, and the surface of the directly deposited poly-Si film is generally much rougher than that of SPC poly-Si films. Therefore, for reduction in fabrication temperature and surface roughness of crystallized Si films, we tried to crystallize an a-Si film in the solid phase by the PLA method at room temperature as shown in Fig. 1.3. The combination of the CI layer and SPC-PLA methods is thought to have high potential not only for eliminating the drawback of the melting-PLA method, but also for satisfying the demands of uniform performance in both short time and low temperature for the application of poly-Si TFTs.

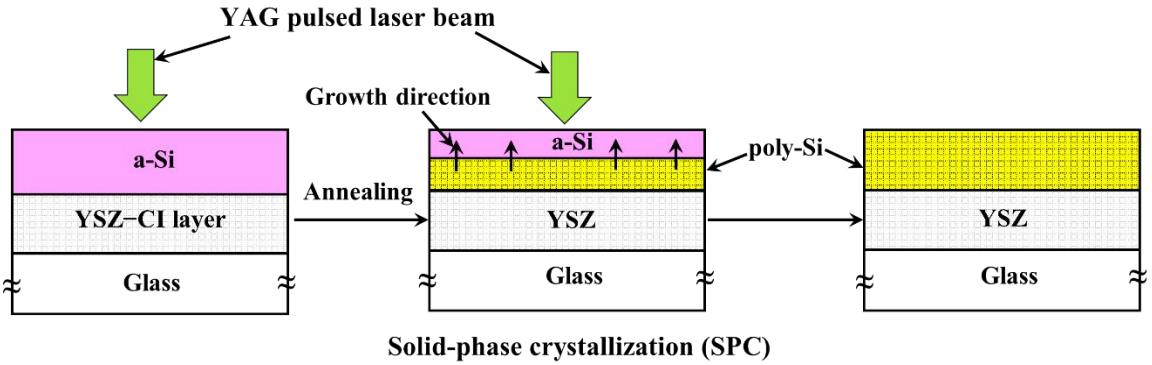

Fig. 1.3 Schematic illustrations of PLA method for crystallization of an a-Si film deposited on a glass substrate with a CI layer of YSZ.

1.4 Purpose of this study

The main research purpose is to improve crystallization technique of Si thin film on non-heat resistant and cheap insulating substrates of glass or plastic for state-of-the-art electronic device applications by using YSZ CI layer combined with SPC-PLA methods.

In order to achieve the purpose, firstly, we investigate the crystallinity of pulsed-laser crystallized Si films on YSZ layers, comparing with those on glass substrates. The

crystallized Si films are measured mainly by Raman spectroscopies, from which the crystallization degree, and the FWHM and position of the c-Si peak are evaluated. We can roughly estimate crystalline quality from the FWHM of the c-Si peak and film stress from the peak position. Also, Secco-etched Si films are observed by scanning electron microscopy (SEM) for comparison with the films observed by Raman spectral analysis. From these measurements, the results are discussed including the CI effect of YSZ layer and a crystallization model of an a-Si film on a YSZ layer is speculated, comparing with that of an a-Si film on a glass substrate.

From the obtained results, for further improving the crystallinity of Si films, we propose a new irradiation method using a pulsed laser, which will be mentioned in the next chapters in more detail. We then investigate the crystalline quality of crystallized Si films with or without the YSZ layers obtained by the new method, in comparison with the conventional method. The crystalline quality are estimated mainly by Raman spectroscopy as above-mentioned and by SEM observation of Secco-etched Si films. Further, reflection high energy electron diffraction (RHEED) is used to observe and compare the surface crystalline quality of YSZ, as-deposited a-Si, and crystallized Si films. Transmission electron microscopy (TEM) is used to observe micro- or atomic structure of the fabricated sample. Resistivity and Hall effect measurements are used to characterize transport properties (resistivity, carrier concentration, and mobility) of the Si films. After improving and optimizing crystallization conditions of Si films on YSZ/glass substrates by the new method, poly-Si TFTs are fabricated and their properties are evaluated. The final structure of fabricated poly-Si TFTs is shown in Fig. 1.4. The factors influencing electrical properties of poly-Si TFTs should be found out. Thence, solutions are proposed and studied for improvement of their performance.

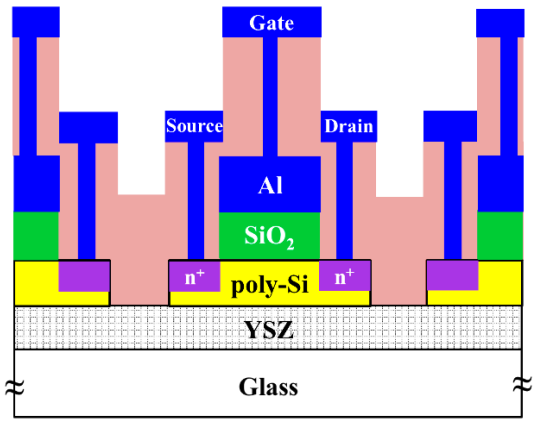

Fig. 1.4 Cross-section of a final fabricated poly-Si TFT structure.

1.5 Structure of dissertation

The structure of this thesis is as follows:

Chapter 1, this chapter, has already briefly introduced about poly-Si TFTs as well as fabrication methods of poly-Si thin films. Also, crystallization-induction (CI) layer method used in this study has been introduced in combination with pulsed-laser annealing (PLA) method.

Chapter 2 shows principle of the solid-phase crystallization (SPC) of an amorphous film to understand experimental results or crystallization mechanism of crystallized Si film by the CI layer in combination with PLA method.

Chapter 3 outlines fabrication procedures of film structure for crystallization and for material properties investigation by resistivity and Hall effect measurements, TFTs fabrication procedure, and evaluation methods for fabricated films.

Chapter 4 shows effect of YSZ–CI layer on quality of crystallized Si films by investigation the dependences of crystallinity on laser energy density and pulse number. Then, we speculate a model for crystallization mechanism of Si films with and without YSZ–CI layers.

In order to further improve the crystalline quality of Si films, we propose a new irradiation method and investigate the film quality. The investigated results are shown in chapter 5. After optimizing the irradiation conditions of this new method, we try to expand the crystallization area. Chapter 5 also shows some results on the expanded area.

When Si films crystallized on the YSZ–CI layer are used for TFT fabrication, it is better to use the YSZ layer as a gate insulator. To do this, a gate electrode layer must be deposited on a glass substrate, followed by a YSZ–CI layer. Therefore, after obtaining the optimal crystallization condition for a-Si thin films on YSZ/glass substrates by the new method using PLA, we deposit a-Si thin films on **YSZ/metal/glass** substrates and crystallize them. Then, we estimate crystalline quality of **Si/YSZ/metal/glass** structure as well as the role of metal film in enhancing crystallization rate of the Si film. The estimation results are shown in chapter 6.

For more investigation of electrical properties of Si films by the new irradiation method, we perform the resistivity and Hall effect measurements, whose results are mentioned and discussed in chapter 7. We compare the resistivity and Hall effect

measurements results for both structures of Si/glass and Si/YSZ/glass in two cases of undoped and P-doped films. Further, we show the investigation results of the fabricated poly-Si TFTs. The device-to-device uniformity in TFT performance is shown and compared between two structures of Si/glass and Si/YSZ/glass.

Finally, we summarize our results and give some suggestions for future work in chapter 8.

Chapter 2:

Theory of Solid-Phase Crystallization (SPC) of an Amorphous Film

In chapter 1, we have introduced that the poly-Si formed by the solid phase crystallization (SPC) of a-Si has better qualities than the directly deposited poly-Si due to the larger grains and smooth surface. Many extensive research efforts have been carried out to develop a comprehensive understanding of the kinetics and mechanisms of SPC in a-Si thin films. This is not only because Si has an important technological role in electronic applications, but also because of the many interesting scientific questions that underlie a detailed description of phase transformations in this material.[73)] The SPC of a-Si consists of two distinct processes, namely the nucleation of seeds (formation of clusters of c-Si) and their growth to polycrystalline films.[74)] The rate-limiting step of the crystallization process is the rate of nucleation of seeds, which has an activation energy of about 5 eV.[75)] The rate of crystal growth has an activation energy of about 2.7 eV. [73,75,76)] In this chapter, we will introduce the theory of SPC method in order to understand more about SPC mechanism of amorphous alloyed thin films and semiconducting films, especially a-Si films.

The composition of the film in crystalline phase can be either different from or the same with that in amorphous phase. The former case is due to the phase separation into a crystalline and an amorphous phase, or into two crystalline phases, and including a certain amount of long-range diffusion. Otherwise, the latter case is simpler, which is often preferable to crystallize an amorphous compound film which is deposited. This is because no long-range diffusion is needed, and thus it takes less time than producing the same compound film by interdiffusion of a multilayer film with the same overall composition. Here, we only consider the process of nucleation and growth of crystalline grains, which have the same composition as the amorphous film.[77)] K.-N. Tu, J. W. Mayer, and L.C. Feidman investigated thin film and surface phenomena more than twenty years ago. They described the nucleation and growth of thin films from amorphous to crystalline phase as follows.

In the initial stage, the number of nucleated grains is small and increases with time as well as their size. When the grain size is large enough, their collision occurs and a grain

boundary is formed between grains. The process continues and leads to the formation of a polycrystalline microstructure. If the nucleation and growth processes can be controlled to produce microstructure of a thin film, the extrinsic film properties can be controlled. By understanding well the nucleation and growth, the development of microstructure can be modified.

The kinetics of crystallization is described by KJMA theory, which was derived independently by Kolmogorov, Johnson and Mehl, and Avrami. This theory has been used intensively by materials scientists to study various mechanisms of phase transformations in metals, polymers, and glasses. In order to understand KJMA theory, we start with the consideration a volume V participated in the transformation, which is described by:

$$V = V_U + V_T, \tag{2.1}$$

where V_U and V_T are untransformed and transformed volumes, respectively, which are shown in Fig. 2.1. If we set $X_U = V_U/V$ and $X_T = V_T/V$, which are called the fractions of untransformed and transformed volumes, respectively, eq. (2.1) is rewritten:

$$1 = X_U + X_T\,. \tag{2.2}$$

Avrami showed that X_T is given by:

$$X_T = 1 - \exp\,(-X_{ext}\,), \tag{2.3}$$

where $X_{ext} = V_{ext}/V$ is the fraction of extended volume V_{ext}, which is described more later. To obtain the eq. (2.3), we assume that the transformation occurs by nucleation and growth, and that the nucleation is random in time and in space. We also set R_N as a nucleation rate, which is the number of nuclei per unit time and unit volume. Then, the

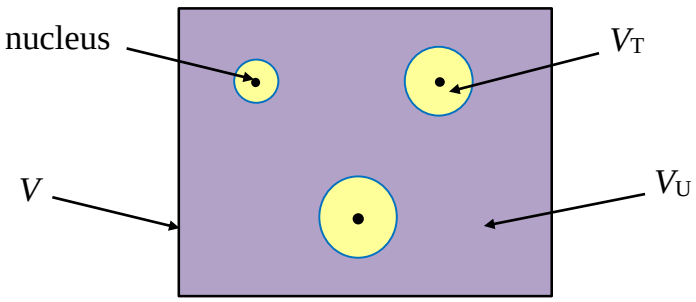

Fig. 2.1 Illustration of a considered volume V, which is participated in the transformation.

number dN of new transformed regions nucleated in V_U in the interval between t and $t + d\tau$ is:

$$dN = R_N V_U \, d\tau. \tag{2.4}$$

We also assume that each of the transformed regions has the same isotropic growth rate of R_G. This means that the transformed regions shape is nearly sphere, whose radius is $R_G(t-\tau)$. The volume V_τ of a transformed region, which started from τ, is given by:

$$\begin{cases} V_\tau = \dfrac{4\pi}{3} R_G^3 (t-\tau)^3 & \text{for } t > \tau \\ V_\tau = 0 & \text{for } t \le \tau \end{cases} \tag{2.5}$$

From eq. (2.4), the differential change of the untransformed volume in the period dτ is described by:

$$-dV_U = dNV_\tau = V_\tau R_N V_U \, d\tau \,, \tag{2.6}$$

in which the negative sign means the reduction of the untransformed volume. We have $-dV_U = dV_T$ from eq. (2.1) and rewrite eq. (2.6) as:

$$dV_T = V_\tau R_N V_U \, d\tau \,. \tag{2.7}$$

By substitution eq. (2.5) into (2.7) and then integration, we have:

$$\begin{aligned} V_T &= \int_{\tau=0}^{\tau=t} dV_T = \frac{4\pi}{3} \int_{\tau=0}^{\tau=t} V_U R_N R_G^3 (t-\tau)^3 \, d\tau \\ &= \frac{\pi}{3} V_U R_N R_G^3 t^4 . \end{aligned} \tag{2.8}$$

With the assumption that the nucleation rate is constant in time and in the initial stage of the transformation $V_T << V_U$ (or $V_U \approx V$), we obtain the next equation:

$$X_T = \frac{V_T}{V} \approx \frac{\pi}{3} R_N R_G^3 t^4 \,. \tag{2.9}$$

Equation (2.9) describes the fraction of transformed volume and it is correct if there is no interference between transformed regions (i.e., no overlapping and no collision) as shown in Fig. 2.2(a). This means that it is only correct in the initial stage, however, that it is incorrect for later stages of the transformation when interference or collision occurs between individual growth grains [Fig. 2.2(b) and (c)].

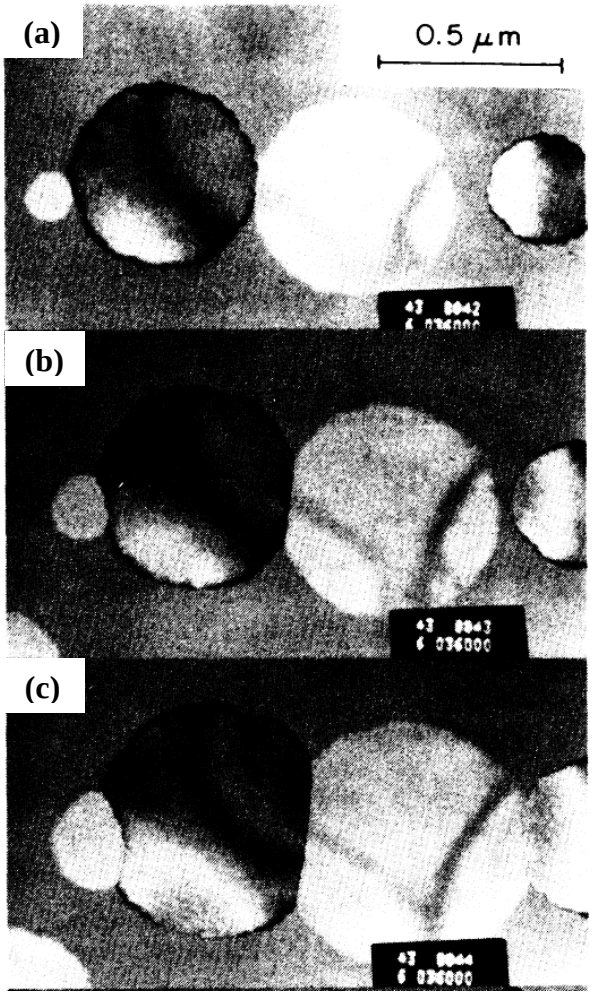

Fig. 2.2 Sequential growth of the two circular grains and the formation of a grain boundary between them.[78)]

To solve this problem, it is needed to introduce the concept of "extended volume" V_{ext}, whose value in the interval between t and $t + d\tau$ is defined as:

$$dV_{ext} = V_{\tau} R_N (V_U + V_T) d\tau , \qquad (2.10)$$

where dV_{ext} is called as the differential change in volume in both transformed and untransformed regions during $d\tau$.

An illustration of V_{ext} is given in Fig. 2.3. If we only consider three grains whose volumes are V_1, V_2, and V_3; V_{ext} and V_T are calculated as shown in Fig. 2.3, in which V_{12} and V_{23} are the overlapping volumes between grains. A different point between eq. (2.10) and eq. (2.7) is that eq. (2.10) consists of the random nucleation and isotropic growth in both transformed and untransformed regions, i.e, total volume of $V = V_U + V_T$ regardless of whether transformed or not. Avrami called nuclei in the transformed region as "phantom nuclei" because their growth does not affect the untransformed region and does not provide

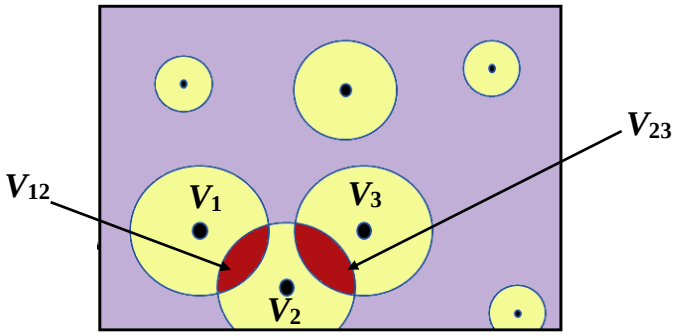

$$V_{ext} = V_1 + V_2 + V_3$$

$$V_T = V_1 + V_2 + V_3 - V_{12} - V_{23}$$

Fig. 2.3 Illustration of the difference between V_T and V_{ext}.

any more transformation information. Noting that only the transformation in the untransformed region is important and meaningful.

In order to understand more about "phantom nuclei", we consider interference of raindrops on surface of a lake, which is illustrated in Fig 2.4. Circular ripples are formed and expand when raindrops fall and touch the surface of the lake. If there are few raindrops and they separate from each other, no interference phenomenon is observed. When number of raindrops increases, the interference occurs. Note that we can see some of raindrops fall inside of the existing ones and form smaller ripples in the existing larger ripples. They can be considered as "phantom nuclei". Although they produce changes, these changes are in the transformed region and do not influence the transformation of the unstranformed region. However, it is needed to take account of phantom nuclei when we consider the random nucleation in space and in time. From eq. (2.1), we have:

$$V_U = V - V_T = \frac{(V - V_T)V}{V} = \frac{(V - V_T)(V_U + V_T)}{V} = \left(1 - \frac{V_T}{V}\right)(V_U + V_T). \tag{2.11}$$

Substituting eqs. (2.10) and (2.11) into eq. (2.7), we have:

$$dV_T = \left(1 - \frac{V_T}{V}\right) V_\tau R_N (V_U + V_T)\, d\tau = \left(1 - \frac{V_T}{V}\right) dV_{ext}. \tag{2.12}$$

It is clearly seen that $dV_T < dV_{ext}$ because of $0 < V_T < V$. The quantity of $(1 - V_T/V)$ in eq. (2.12) is the fraction of the untransformed region to total volume V. Rewriting eq. (2.12):

$$dV_{ext} = \frac{dV_T}{\left(1 - \frac{V_T}{V}\right)} = \frac{-V d\left(1 - \frac{V_T}{V}\right)}{\left(1 - \frac{V_T}{V}\right)}. \tag{2.13}$$

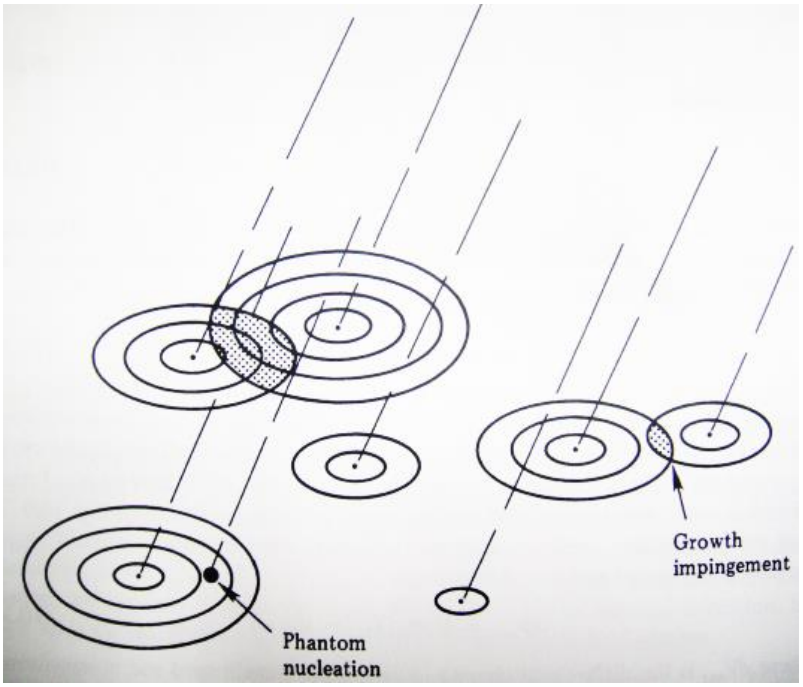

Fig. 2.4 Illustrated image of raindrops on the surface of a lake.[77)]

Integrating this equation, we obtain:

$$V_{\mathrm{ext}} = -V\ln\left(1-\frac{V_{\mathrm{T}}}{V}\right) + \text{constant}\,. \tag{2.14}$$

Because of $V_{\mathrm{ext}} = 0$ when $V_{\mathrm{T}} = 0$, the constant in eq. (2.14) is zero. Eq. (2.14) becomes:

$$-\frac{V_{\mathrm{ext}}}{V} = \ln\left(1-\frac{V_{\mathrm{T}}}{V}\right). \tag{2.15}$$

We obtain Avrami's equation as eq. (2.3) by taking the exponential function of eq. (2.15). To derive the formula for X_{ext}, we integrate eq. (2.10):

$$V_{\mathrm{ext}} = \int_{\tau=0}^{\tau=t} V_{\tau} R_{\mathrm{N}} \left(V_{\mathrm{U}} + V_{\mathrm{T}}\right) \mathrm{d}\tau\,, \tag{2.16}$$

where t is the transformation time. Substituting eq. (2.5) into (2.16), we obtain:

$$V_{\mathrm{ext}} = \frac{4\pi}{3} V \int_{\tau=0}^{\tau=t} R_{\mathrm{N}} R_{\mathrm{G}}^{3} \left(t-\tau\right)^{3} \mathrm{d}\tau\,. \tag{2.17}$$

or $$X_{\text{ext}} = \frac{4\pi}{3} \int_{\tau=0}^{\tau=t} R_{\text{N}} R_{\text{G}}^3 \left(t-\tau\right)^3 \,\text{d}\tau \,. \tag{2.18}$$

Eq. (2.17) is more general than eq. (2.8) because it can be applied for any stage of the transformation. If the nucleation is random and continuous at a constant rate, and the growth is isotropic and linear with time, eq. (2.18) becomes:

$$X_{\text{ext}} = \frac{\pi}{3} R_{\text{N}} R_{\text{G}}^3 t^4 \,. \tag{2.19}$$

Setting $K = \frac{\pi}{3} R_{\text{N}} R_{\text{G}}^3$, X_{T} is described as:

$$X_{\text{T}} = 1 - \exp\left(-X_{\text{ext}}\right) = 1 - \exp(-K\,t^4). \tag{2.20}$$

If we assume that R_{N} and R_{G} follow Boltzmann's distribution, they are given by:

$$R_{\text{N}} = R_{\text{N}_0} \exp\left(-\frac{\Delta H_{\text{N}}}{kT}\right), \tag{2.21}$$

$$R_{\text{G}} = R_{\text{G}_0} \exp\left(-\frac{\Delta H_{\text{G}}}{kT}\right), \tag{2.22}$$

in which ΔH_{N} and ΔH_{G} are the activation enthalpies of nucleation and of growth, respectively. Then quantity K is rewritten as:

$$K = \frac{\pi}{3} R_{\text{N}_0} R_{\text{G}_0}^3 \exp\left(-\frac{\Delta H_{\text{N}} + 3\Delta H_{\text{G}}}{kT}\right). \tag{2.23}$$

Experimentally, X_{T} is measured as a function of time and temperature. Keeping X_{T} constant, we can have:

$$Kt^4 = \text{constant}. \tag{2.24}$$

Then, substituting eq. (2.23) into (2.24) and taking logarithm it:

$$-\frac{\Delta H_{\text{N}} + 3\Delta H_{\text{G}}}{kT} + 4 \ln t = \text{constant}\,. \tag{2.25}$$

The activation enthalpy of transformation, ΔH_{T}, can be estimated from the slope of the graph of ln t versus 1 / kT (as shown in Fig. 2.5):

$$\Delta H_{\text{T}} = \frac{\Delta H_{\text{N}} + 3\Delta H_{\text{G}}}{4} = \tan\alpha \,. \tag{2.26}$$

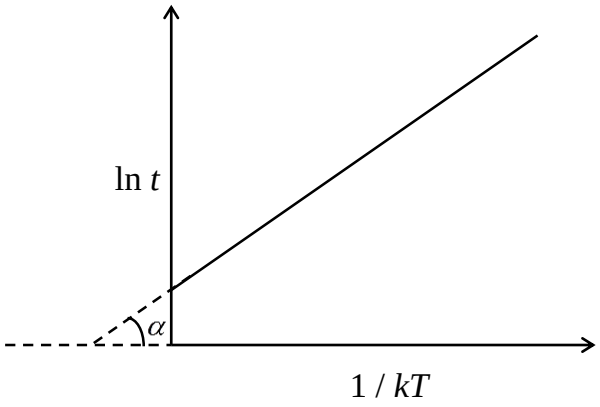

Fig. 2.5 Relation between ln *t* and 1 / *kT*, keeping X_T constant.

From eq. (2.26), if we know the activation enthalpy of nucleation or of growth, we can infer the other. As mentioned above, we assume many conditions. In order to get the general description, eq. (2.20) is rewritten as:

$$X_T = 1 - \exp(-K t^n), \tag{2.27}$$

where n is the mode parameter of transformation. Setting $K = (\tau_0)^{-n}$, we obtain:

$$X_T = 1 - \exp\left[-\left(\frac{t}{\tau_0}\right)^n\right]. \tag{2.28}$$

When $t = \tau_0$, $X_T = 1 - 1/e = 0.63$. By taking twice taking the logarithm of eq. (2.27), we obtain:

$$\ln[-\ln(1 - X_T)] = n \ln t + \text{constant}. \tag{2.29}$$

From eq. (2.29), n is the the slope of a graph of $\ln[-\ln(1 - X_T)]$ versus $\ln t$ and can be calculated from experimental data. n is termed the Avrami exponent, whose value depends on the dimensionality of growth process and on the kinetic order of nucleation. The growth process is either 1, 2, or 3 dimensional, corresponding to rod-like, disc-like, or spherulitic growth. The time dependence of nucleation is either zero order or first order, which means that all nuclei form instantaneously or number of formed nuclei increases linearly with time, respectively. Exponents n of the Avrami equation for different nucleation and growth mechanisms are listed in Table 2.1. In most general case, where 3 dimensional growth is combined with the first order nucleation, the value of n is 4. If the film thickness is very thin, the growth in thickness direction can be neglected. In this case, we can assume that the growth of thin film is in 2 dimensional (2-D). Then, n = 3 or 2. For 1 dimensional (1-D) growth, n = 2 or 1.

Table 2.1 Exponents *n* of the Avrami equation for different nucleation and growth mechanisms.

n	Growth and nucleation mechanisms
3 + 1 = 4	Spherulitic growth + random nucleation
3 + 0 = 3	Spherulitic growth + instantaneous nucleation
2 + 1 = 3	Disc-like growth + random nucleation
2 + 0 = 2	Disc-like growth + instantaneous nucleation
1 + 1 = 2	Rod-like growth + random nucleation
1 + 0 = 1	Rod-like growth + instantaneous nucleation

For the case of a-Si, since the free energy of the crystalline state is lower than for the amorphous state, a-Si tends to crystallize. Si forms strongly covalent and directional bonds, and the condition of minimum free energy in solid state is achieved by arranging these bonds in a tetrahedral configuration.[73] On the contrary, the amorphous state of Si maintains tetrahedral coordination locally but does not possess the long-range order seen in the crystal. The most important feature distinguishing a-Si from the crystalline phase is a relatively well defined free energy difference of higher about 0.1 eV per atom at 300 K. This energy is taken up mostly in the form of bond angle distortions, which is required to accommodate the disordered atom arrangement in the amorphous solid. Since the crystalline state has a lower free energy, there is always a driving force toward rearranging the atom positions of a-Si into those of the crystal.

The thermodynamic considerations of the transformations between amorphous, crystalline, and liquid states of Si have been reported by Turnbull[79] and by Spaepen and Turnbull.[80] Fig. 2.6 shows the calculation by Donovan et al. of the Gibbs free energy difference ΔG for a-Si and liquid Si (ℓ-Si), referring the crystalline phase one.[81,82] The ℓ-Si curve was calculated using existing thermodynamic data, and the free energy of the amorphous phase was calculated using the measured heat of crystallization and an estimate of the difference in specific heat. It can be seen that a-Si is thermodynamically less stable than c-Si at temperatures up to and beyond the c-Si melting temperature ($T_{c\ell}$). Another interesting feature of this calculation is that a-Si and ℓ-Si have equal free energies at a temperature $T_{a\ell}$ which is lower than $T_{c\ell}$. This indicates that above $T_{a\ell}$ the free energy of a-Si can be lowered by a transition to the liquid state. Thus, a-Si can have a lower melting point than that of c-Si. Because of the free energy difference between a-Si and c-Si, an

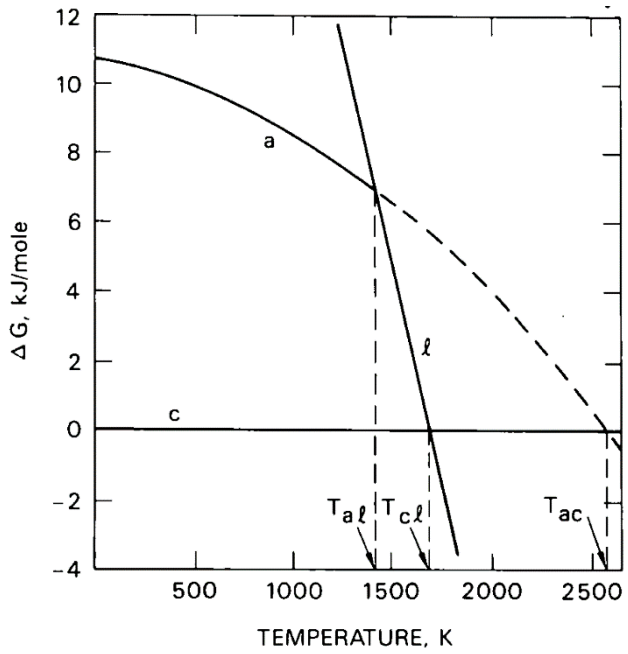

Fig. 2.6 Gibbs free energy differences for Si crystal (c), metallic liquid (*ℓ*), and amorphous (a).[81)]

isolated piece of a-Si would eventually become crystalline even at room temperature. Raising the temperature will speed up the transformation but the basic homogeneous crystallization process is the same at all temperatures.

Figure 2.7 shows the illustrations of cross-section and top-view for the growth of c-Si grains in a-Si matrix on a glass substrate and a YSZ layer for this work. First, we consider models for c-Si growth on glass substrate. It can be seen that the nucleation is random and c-Si grains grow laterally (or disc-like as shown in the top-view) in 2-D on the glass substrate [Fig. 2.7 (a)]. Therefore, $n = 1 + 2 = 3$. In the case of 1-D growth, $n = 2$ [Fig. 2.7 (b)] corresponds to a slab-like growth from a random nucleation sheet in the film. Next, the CI-YSZ case is considered. If nucleation occurs simultaneously at the interface between the YSZ layer and a-Si film due to the CI effect of YSZ, crystallization growth of a-Si proceeds toward the surface uniformly as shown in Fig. 2.7(c). This condition is suitable for $n = 1$.

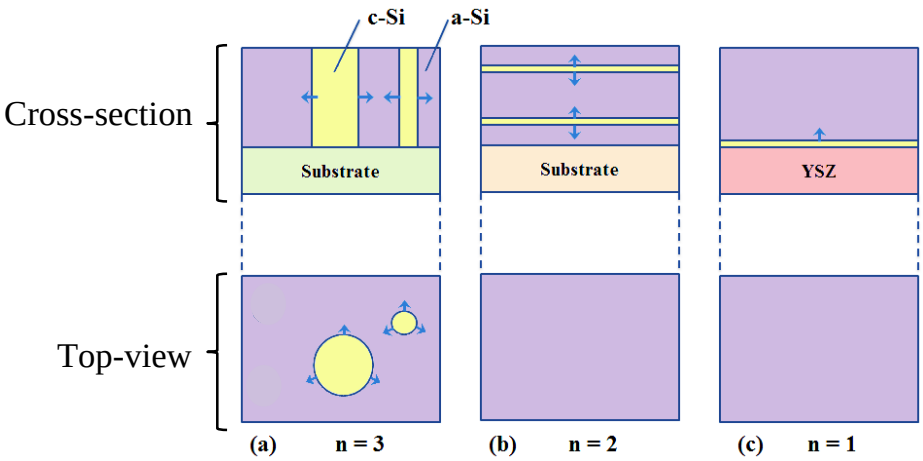

Fig. 2.7 Illustrations for the crystallization growth in (a) 2-D, (b) 1-D randomly, and (c) 1-D uniformly.

Chapter 3:

Fabrication Procedures and Evaluation Methods

3.1 Sample preparation for Si film crystallization

The fabricated sample structure for Si film crystallization is cross-sectional illustrated in Fig. 3.1. The outline of full sequence of the sample fabrication is shown in Fig. 3.2. First, a quartz substrate is cleaned by chemical solution before the deposition of a crystallization induction (CI) layer of YSZ by sputtering method. Then, the YSZ/quartz film is treated by a series of chemical solutions, followed by an a-Si film deposition by electron-beam evaporation method. Thickness of the a-Si film is 60 nm and equals to that of the YSZ layer. Next, the a-Si/YSZ/quartz film is cleaned by a succession of chemical solutions before the micro-crystallization of the a-Si film in solid phase by PLA method to form poly-Si film. For comparison, the a-Si film is also deposited and crystallized on a glass substrate directly. In the following, we will introduce the detailed method and apparatus to fabricate poly-Si/YSZ/quartz sample.

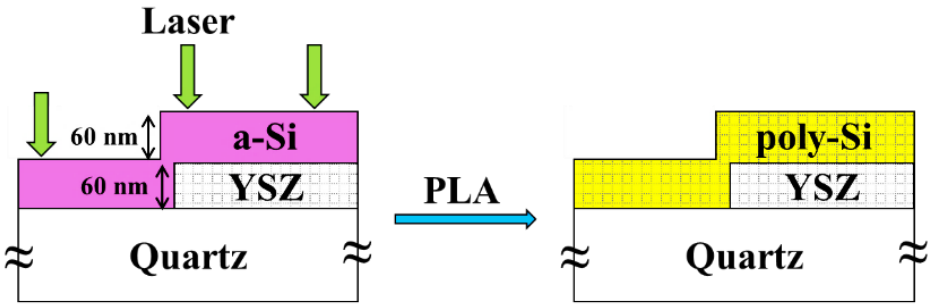

Fig. 3.1 Cross-sectional illustration of the fabricated sample structure for Si film crystallization.

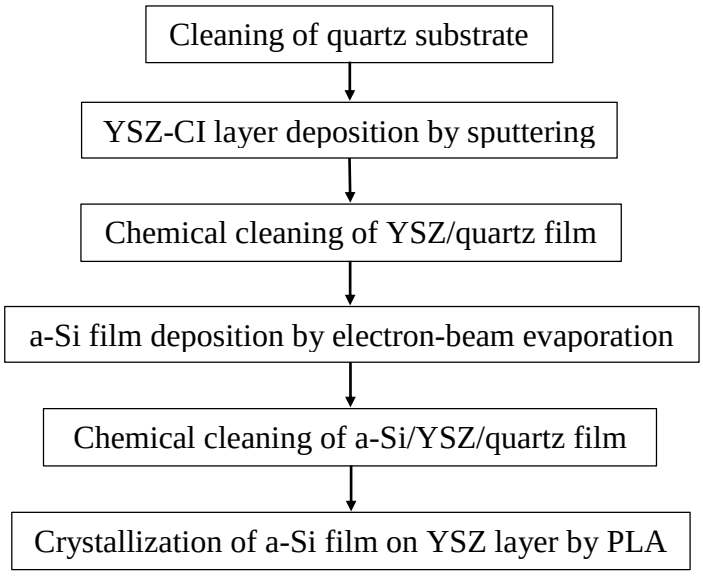

Fig. 3.2 Poly-Si/YSZ/quartz sample fabrication process sequence.

3.1.1 Deposition of yttria-stabilized zirconia (YSZ) crystallization-induction (CI) layer

a) Reactive magnetron sputtering system

Figure 3.3 shows a schematic illustration of the direct current (DC) magnetron sputtering system used to deposit YSZ-CI layers in this work. The system consists of a custom-made deposition chamber connected to a sample exchange chamber. Both the deposition and sample exchange chambers are exhausted by ULVAC turbo molecular pumps UTM-500M and UTM-150M, respectively. The background and sputtering pressures are measured by the Bayard-Alpert (B-A) gauge (operating pressure range from 10^{-10} to 10^{-3} Torr) and capacitance manometer (operating pressure range from 10^{-5} to 10^{2} Torr), respectively. The deposition chamber is usually exhausted until a background pressure less than 1×10^{-7} Torr before the deposition. The sputtering target is a 99.9% zirconium (Zr) metallic target with 98-nm-diameter, on which 8 pieces of 10×10 mm^2 99.9% yttrium (Y) metallic chips are arranged circularly as shown in Fig. 3.3. The Y content in the YSZ layer is controlled by varying the diameter of the Y chips circle, and balancing two magnetic fields applied to the system. One magnetic field is produced by a permanent rod beneath the target, and the other one is produced by the solenoid coil placed surrounding the target. An anode plate with a 30×40 mm^2 window in the center is placed between the target and the shutter, over which a substrate is located. The sputtering and

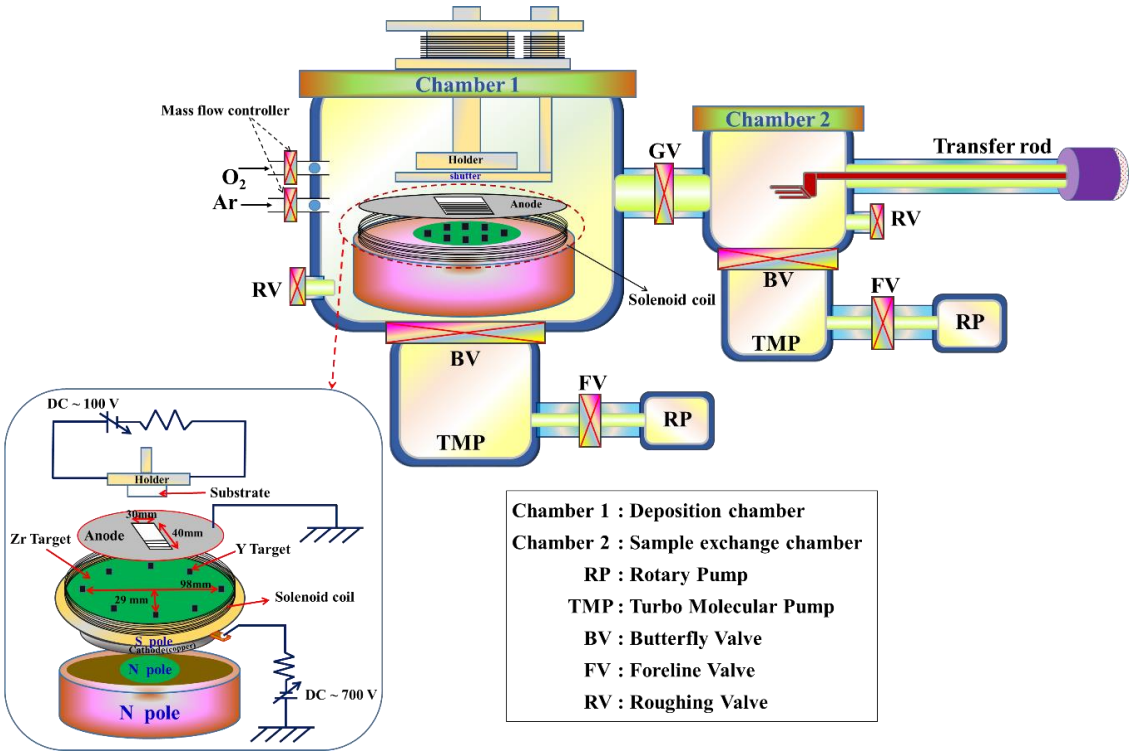

Fig. 3.3 Schematic illustration of the DC magnetron sputtering system used to deposit YSZ-CI layers in this work.

reactive gases are argon (Ar) (99.999%) and oxygen (O_2) (99.999%), respectively. In general, when a metallic target is used in DC reactive sputtering method to deposit insulator films, the target surface will be oxidized during the sputtering process. So, the target surface is charged-up and anomalous discharge sometimes occurs. In our system, the DC source is coupled with an anomalous discharge prevention unit (ULVAC: A2KH) that applies a pulse voltage up to 20 kHz.

b) Deposition procedure

Figure 3.4 shows the full process series of the YSZ layer deposition. A 20×10 mm^2 quartz substrate is chemically cleaned before a YSZ-CI layer deposition. The detailed cleaning process is mentioned in the Appendix A.1. After cleaning, the substrate is immediately loaded into a sample exchange chamber of a DC magnetron sputtering system, which is evacuated to less than $5x10^{-6}$ Torr. Next, the pre-sputtering process is done in pure Ar gas for 10 min before loading the

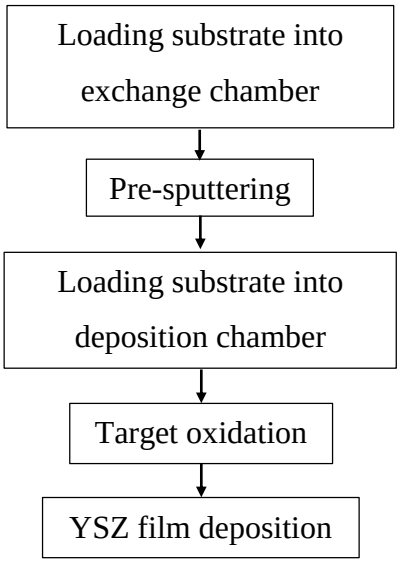

Fig. 3.4 YSZ film deposition process sequence.

substrate into the deposition chamber. This step is necessary to remove an unfavorable oxide layer, which covered the metallic sputtering target due to the previous sputtering process, or natural oxide, and contaminants. When the sample is in the deposition chamber, target oxidation process is carried out to oxidize the clean metallic target surface in pure O_2 gas for 10 min. This is because the YSZ films in this study are deposited in the oxide mode. The detail of deposition modes for the YSZ layer is mentioned in the Appendix B. After that, the deposition of YSZ layer is performed under the conditions listed in Table 3.1 at the substrate temperature of 50 ^oC by a ceramic heater. However, during the YSZ deposition, the substrate might be heated up to more than 200 ^oC by plasma radiation to the substrate.

Table 3.1 YSZ layer deposition conditions.

DC power	100 W
Sputtering pressure	6.5 mTorr
Sputtering time	10 min
Ar flow	5.8 sccm
O_2 flow	0.75 sccm
Substrate setting temperature	~ 50 ^oC
Target oxidation pressure	40 mTorr
Target oxidation time	10 min
YSZ layer thickness	~ 60 nm

3.1.2 Fabrication of a-Si film

a) Electron-beam evaporation system

Figure 3.5 shows the schematic illustration of the electron-beam evaporation system used in this work for a-Si film deposition. An ultra-high vacuum evaporation chamber is connected to a sample exchange chamber by a load lock system. It is vacuumed to a background pressure of ~3×10^{-9} Torr by an ion pump (Variant). The sample exchange chamber is pumped down to less than 1×10^{-6} Torr by a turbo molecular pump (ULVAC GLD-135) before transferring the sample into the deposition chamber by a transfer rod. The deposition chamber is also equipped with a titanium sublimation pump (Cannon

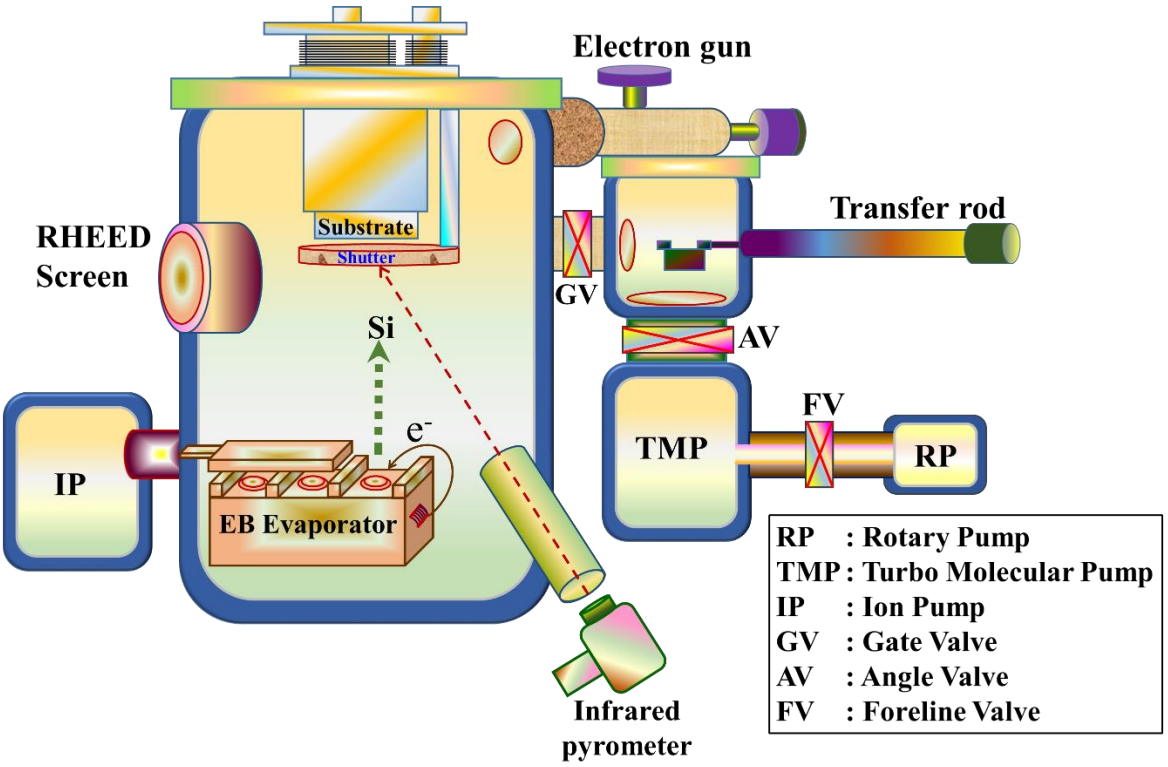

Fig. 3.5 Schematic illustration of the electron-beam evaporation system used to deposit a-Si films in this work.

ANELVA 922-9119), which is used at appropriate time. There is a shroud attached inside the deposition chamber, in which liquid nitrogen is inserted before and during the Si film deposition to maintain a high vacuum.

The pressures of the deposition and sample exchange chambers are measured by the cold-cathode gauge (BALSERS PKR250) and nude-ion gauge (Canon ANELVA 954-7912), respectively. A quadrupole mass analyzer (SPECTRA/SKK) is used to monitor the residual gas in the deposition chamber. The deposition rate and Si film thickness are measured by a crystal oscillator (LEYBOLD INFICON XTC/2) during the film deposition. The substrate temperature was measured by the infrared pyrometer.

b) Deposition procedure

Figure 3.6 shows the full process series of the a-Si film deposition. A YSZ/glass film is chemically cleaned before an a-Si film deposition. Then, the sample is set on the sample holder carefully. The detailed cleaning and setting processes are mentioned in the Appendix A.2. After fixing on the sample holder, the sample is immediately loaded into the sample exchange chamber, which is evacuated less than 1×10^{-6} Torr. The sample is next loaded into the deposition chamber of electron-beam evaporation system. When the

pressure of deposition chamber is less than 3×10^{-9} Torr, the deposition of a-Si film is done under the condition listed in Table 3.2. It is noted that, during the temperature increasing up to the deposition temperature, F atoms which are adsorbed on the YSZ layer surface due to dipping the sample in HF solution are also removed. For comparison, a-Si films are also deposited directly on quartz substrates without YSZ layers.

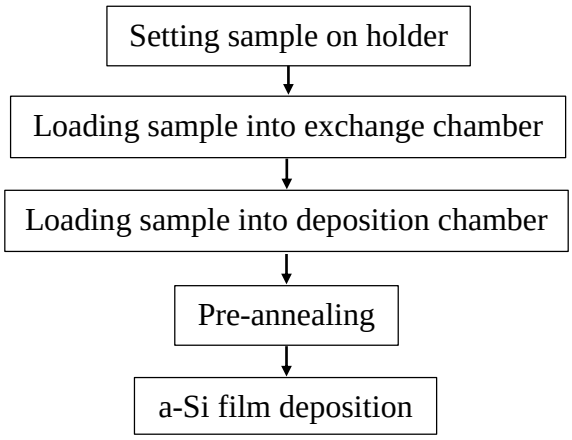

Fig. 3.6 a-Si film deposition process sequence.

Table 3.2 a-Si film deposition conditions.

Deposition pressure	~ $1x10^{-8}$ Torr
Deposition temperature	~ 300 ^{o}C
Deposition rate	~ 1 nm/min
a-Si film thickness	~ 60 nm

3.1.3 Crystallization of a-Si film in solid phase by pulsed-laser annealing (PLA) method

The as-deposited a-Si/YSZ/quartz sample is chemically cleaned with the detailed process shown in the Appendix A.3 before the crystallization. It is then micro-crystallized by PLA in N_2 ambient. A Q-switched Nd:YAG laser (λ = 532 nm) is used for annealing with a repetition frequency of 10 Hz, a pulse duration of 6–7 ns, and a beam diameter of ~4 mm. The laser system setup for annealing is shown in Fig. 3.7. The irradiation energy density *E* and the pulse number *N* are 14–160 mJ/cm^2 and 10–300, respectively. The detailed irradiation techniques and conditions will be introduced in the next chapters. An a-Si film is irradiated normal to its surface by an incident beam with a beam energy adjusted by an attenuator. Laser beam patterns are taken for each beam power by a CCD camera and analyzed by using a software, namely *Image J*, for the estimation of the energy density

distribution. Figure 3.8 shows an example of an actual beam pattern of 1 irradiation shot captured by the CCD camera and its time-average energy density distribution profile at a laser power of 150 mW. In Fig. 3.8(b), the x-axis is the horizontal distance through the scanning length and the y-axis is the averaged laser energy density through the beam width along the vertical distance at each scanning point. Figure 3.9 shows the line profiles, which are indicated by yellow lines in the insets, of energy density distribution along the scanning length at 4 different positions of beam width. From these line profiles, we can determine the irradiation energy density at a position being investigated.

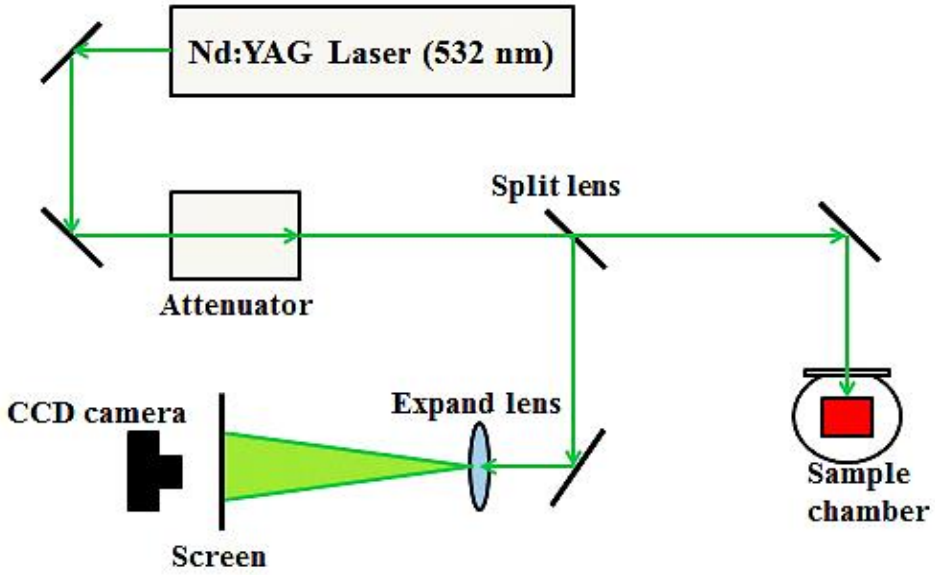

Fig. 3.7 Schematic illustration of laser annealing system.

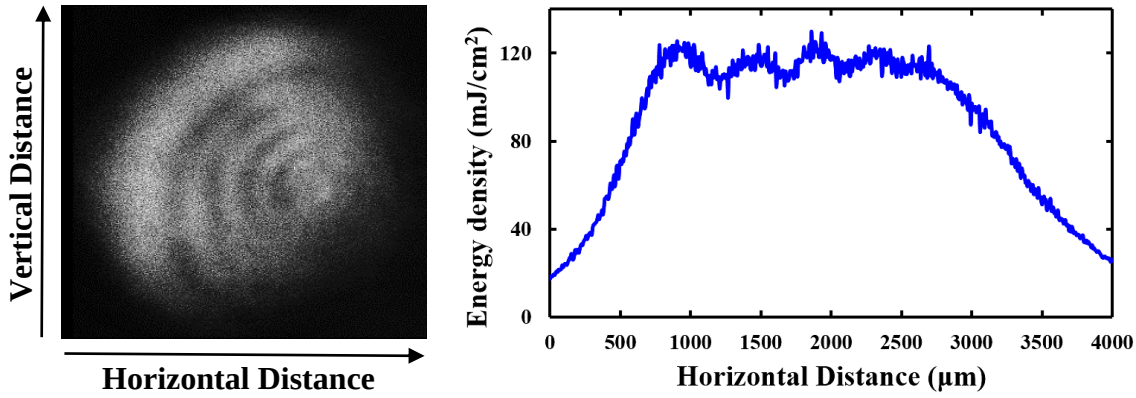

(a) **(b)**

Fig. 3.8 (a) Actual beam pattern of 1 irradiation shot and (b) its average energy density distribution profile at laser power of 150 mW.

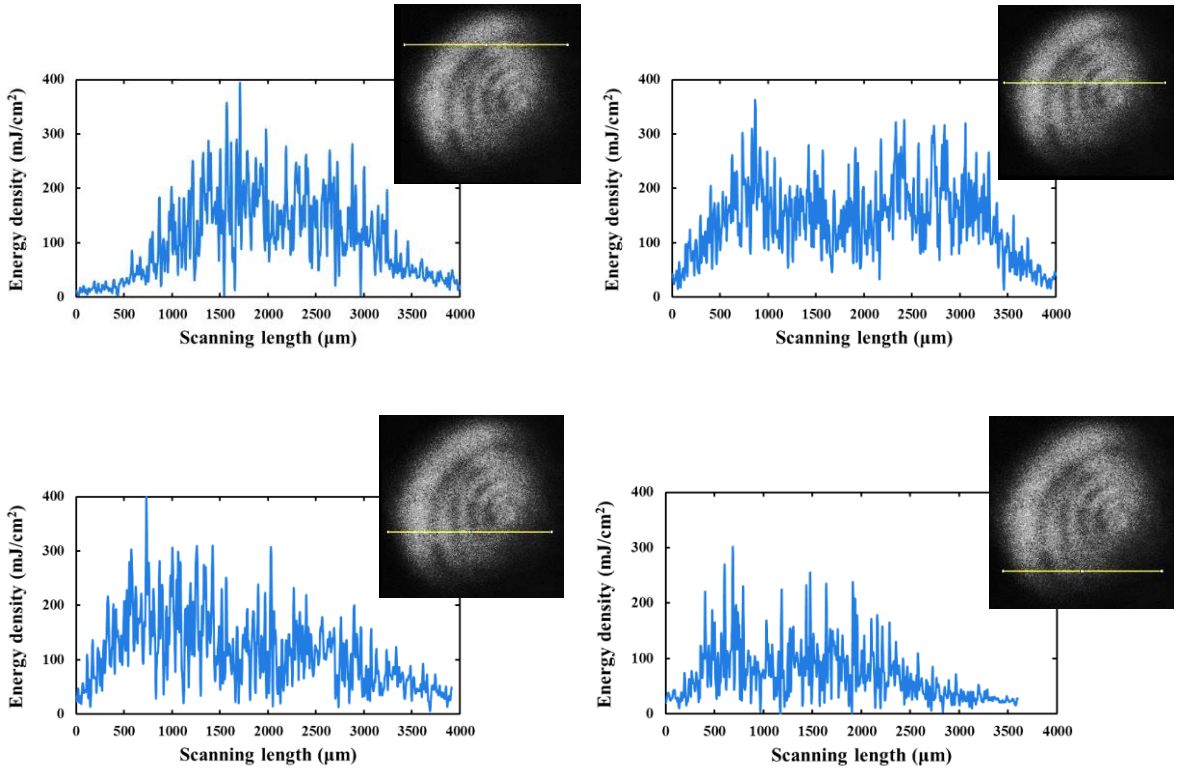

Fig. 3.9 Line profiles of energy density distribution along the scanning length for 1 irradiation shot in Fig. 3.8 at various positions of beam width, which are indicated by yellow lines in the insets.

3.2 Fabrication of patterns for resistivity and Hall effect measurements

The fabrication sequence of patterns for resistivity and Hall effect measurements is illustrated in Fig. 3.10, which shows the sample cross sections schematically. For investigating electrical properties, undoped and doped samples are prepared. In the doping case, a SiO_2 capping layer with thickness of 50~60 nm is deposited by atmospheric pressure chemical vapor deposition (APCVD) at 200 ^oC after cleaning the as-deposited a-Si film. Then, it is annealed in N_2 ambient at 350 ^oC for 30 min. Next, P ion implantation is performed on the whole Si film at an acceleration voltage and ion dose of 40~50 kV and 4.44×10^{12} ~ 5.56×10^{14} cm^{-2}, respectively. The average estimated doping concentration in the Si film is about 3.7×10^{17} ~ 4.9×10^{19} cm^{-3}. Subsequently, the capping layer is removed, following by the crystallization of the a-Si film in solid phase by PLA together with activation of the implanted P ions in N_2 ambient. For this annealing, we use the two-step method, where the detailed experimental condition will be mentioned later in chapter 5.

For comparison, some samples without doping are also prepared by a one-step (or conventional) method at a fixed high laser energy. After crystallization, the deposition of 135-nm-thick SiO_2 passivation layer is done by APCVD. Patterns for resistivity and Hall effect measurements are then formed, and Al metal electrodes are deposited by vacuum evaporation. Finally, sintering process is carried out at 350 ^oC in N_2 for 30 min. The patterns for the undoping case are formed after the same processes as those of the doping case except deposition of a SiO_2 capping layer and P ion implantation. The Appendix C shows the detailed processes of SiO_2 capping and passivation layers deposition by APCVD, and the ion implantation. The final pattern for Van der Pauw method is formed as shown in Fig. 3.11 from the top view. The regions 1, 2, 3, and 4 are for contacting, and the area 5 is the main region for measurement. Depositions of the YSZ layer and the a-Si film as well as crystallization of the a-Si film are the same with those in section 3.1.

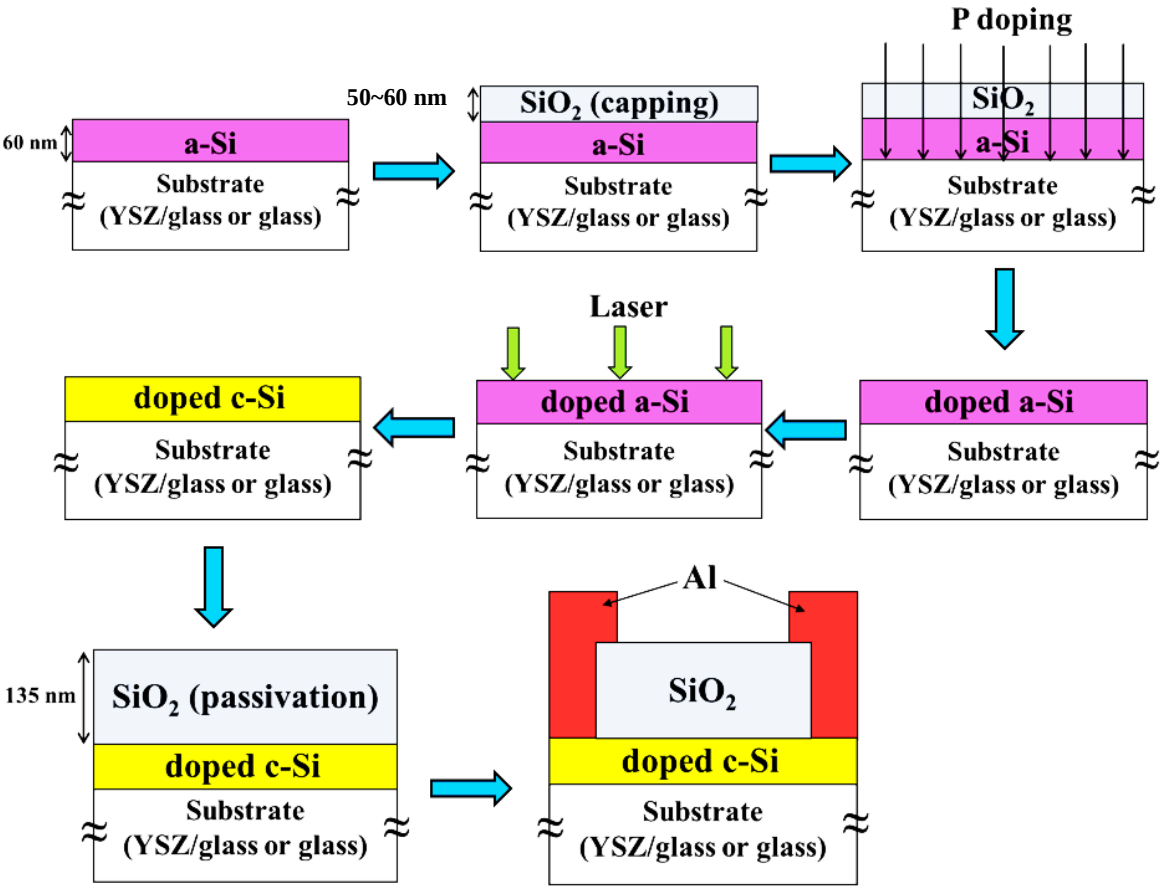

Fig. 3.10 Cross-sectional illustrations of the fabricated patterns for Hall effect measurement.

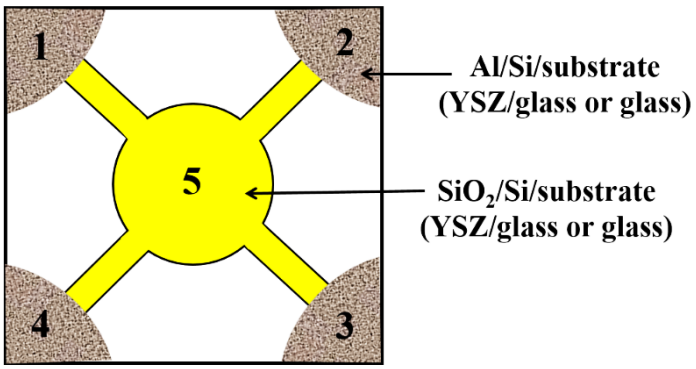

Fig. 3.11 Top-view illustration of the final Hall effect measurement pattern, which is a form of Van der Pauw pattern.

3.3 TFT fabrication

Figure 3.12 shows the process flow of top-gate poly-Si TFTs. The reason for fabrication of not bottom-gate but top-gate TFTs will be discussed later. First, an undoped 60-nm-thick a-Si film is deposited on a substrate (YSZ/glass or glass) by electron-beam evaporation. Then, a 45~50-nm-thick SiO_2 capping layer is deposited on the as-deposited a-Si film by APCVD. After that, the sample is annealed in N_2 ambient at 350 ^oC for 30 min. After lithography patterning and removing SiO_2 capping layer by HF on source and drain (S&D) regions, P ion implantation is performed with an acceleration voltage and an ion dose of 40~50 kV and 4.29×10^{14} ~ 4.53×10^{14} cm^{-2}, respectively. The average estimated doping concentration in the S&D regions is about 5×10^{19} cm^{-3}. Subsequently, the capping layer is removed before the crystallization of the a-Si film in solid phase by the two-step method with pulsed laser together with activation of the implanted P ions in N_2 ambient. After crystallization, Si islands are patterned by lithography and a chemical solution of 1HF: 20HNO_3: 20CH_3COOH is used for etching the film outside of the Si islands. Then, the deposition of ~110-nm-thick SiO_2 passivation layer is carried out on the whole film by APCVD. Lithography patterning of contact holes is performed and the SiO_2 passivation layer on these contact holes is removed before the deposition of Al metal electrodes by vacuum evaporation. Finally, sintering process is carried out at 350 ^oC in N_2 for 30 min. In this work, three types of TFTs having the different designed channel lengths *L* of 10, 20, and 40 μm are fabricated, in which the designed channel width *W* is fixed at 40 μm.

Totally, 4 masks are used for fabrication of TFTs. Figures 3.13 shows a schematic illustration of the fabricated TFT.

- Deposition of 60-nm a-Si on substrate (YSZ/glass or glass).
- Deposition of 45~50-nm SiO_2 capping layer.
- Patterning of source and drain regions.
- Ion doping (P^+, 40~50 kV, 4.29~4.53×10^{14}/cm^2).
- Crystallization together with activation annealing by two-step method in PLA.
- Patterning and etching to form Si islands.
- Deposition of ~110 nm SiO_2 gate insulator.
- Contact holes formation.
- Deposition of Al gate electrode.
- Sintering (N_2, 350 °C, 30 min).

Fig. 3.12 Process flow of TFTs fabrication.

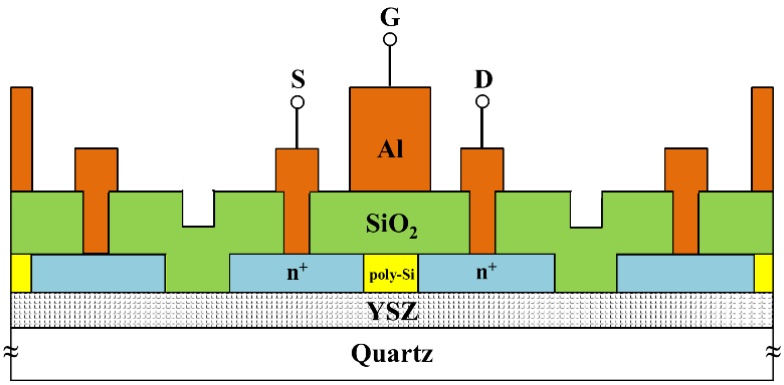

Fig. 3.13 Cross-sectional schematic illustration of the fabricated poly-Si TFTs.

3.4 Evaluation methods

3.4.1 Crystallinity of Si films

a) X-ray diffraction (XRD)

A non-destructive X-ray diffraction (XRD) technique is used to determine crystallinity of YSZ layer. The used XRD system is produced by Philips (MRD). The voltage and current used in this study are 40 kV and 20 mA, respectively, with a Cu Kα radiation at wavelength of 0.15406 nm in steps of 0.06° of θ-2θ scan mode. The measurement mode is parallel diffracted beam optics. In Appendix D, the measurement principle is described in detail.

b) Raman spectroscopies

The crystallization degree of Si films is estimated by two kinds of Raman spectroscopies. The first one is He-Ne system with the excitation wavelength of 632.8 nm. The absorption depth *D* for a-Si is more than 200 nm. So, the He-Ne system is used to evaluate average crystalline quality of a whole Si film. The second one is He-Cd system with the wavelength of 441.6 nm. The *D*s for a-Si and poly-Si are 20–30 nm and more than 200 nm, respectively. Therefore, the He-Cd system can be used to not only estimate crystalline quality of local region, i.e., surface or interface between Si/substrate, but also identify the location of a-Si region. Figure 3.14 shows the schematic illustrations of the measurement methods and the obtained spectra by two kinds of Raman spectroscopies. The crystalline fraction of the Si film is calculated based on decomposition result of He-Ne Raman spectrum as shown in Fig. 3. 15.

The spectrum is decomposed into:

- amorphous silicon (a-Si)/TO phonon: 470–490 cm^{-1}
- intermediate silicon (m-Si)/TO phonon: 503–510 cm^{-1}
- crystalline silicon (c-Si)/TO phonon: 514–520 cm^{-1}
- LO phonon: 380 ± 20 cm^{-1}
- LA phonon: 300 ± 10 cm^{-1}

The crystalline fraction X_c and intermediate-crystalline fraction X_m are determined by:

$$X_c = \frac{I_m + I_c}{I_m + I_c + \alpha I_a}, \tag{3.1}$$

and

$$X_m = \frac{I_m}{I_m + I_c + \alpha I_a}, \tag{3.2}$$

where I_c, I_m, I_a and are integrated intensities of c-Si, m-Si, and a-Si peaks, respectively.[83] For estimation of the crystalline fraction, many researchers considered the differences between a-Si and c-Si with respect to the scattering cross section. The ratio of the cross section is denoted as α in eqs. (3.1) and (3.2), whose value is usually 0.8~0.9.[84,85] In our work, for simplicity, we used $\alpha = 1$. The principle of Raman spectroscopy is mentioned in Appendix E. The detailed calculations of power reflectivity, power transmissivity, and total absorptivity in the Si films for three kinds of incident laser wavelengths (441.6 nm–He-Cd

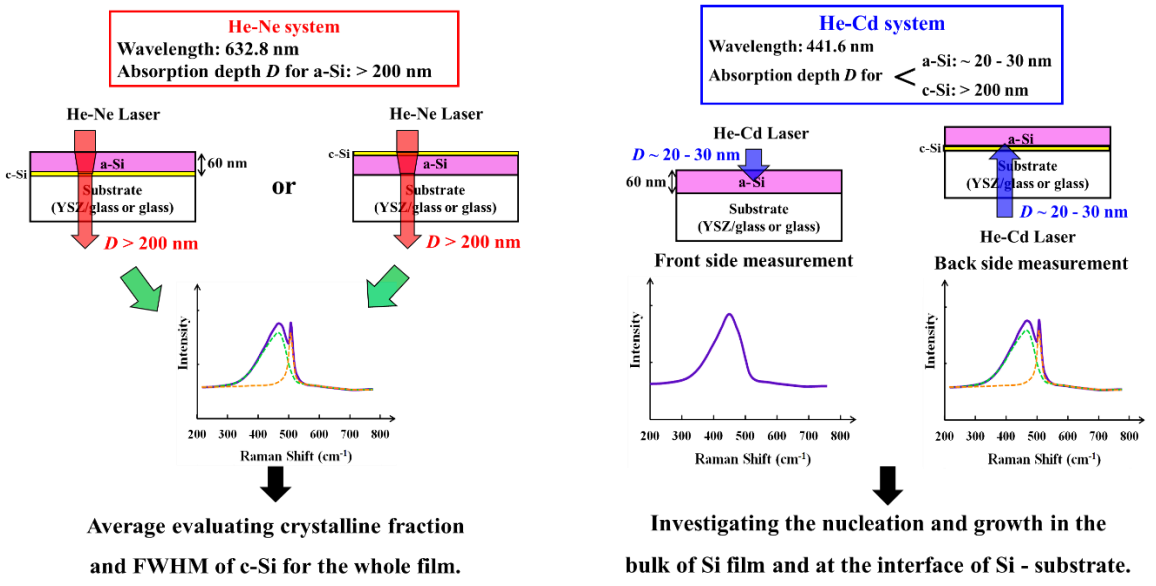

(a) **(b)**

Fig. 3.14 Schematic illustrations of the measurement methods and the obtained spectra by (a) He-Ne and (b) He-Cd Raman spectroscopies.

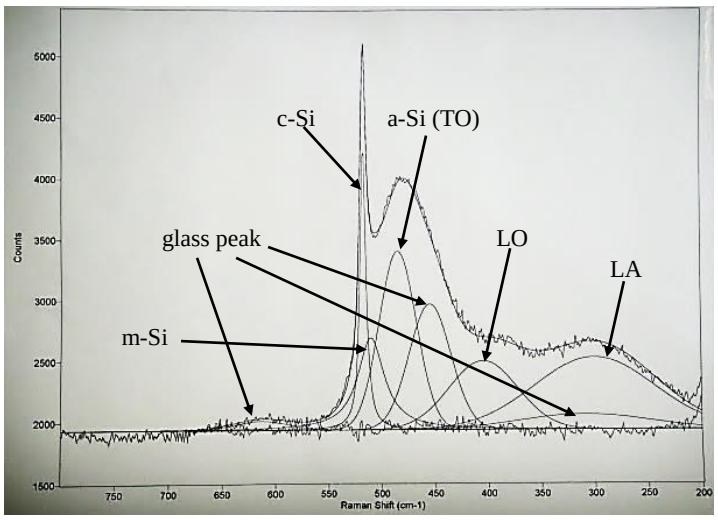

Fig. 3.15 Decomposition example in a Raman spectrum of a crystallized Si film.

Raman system, 532 nm–Nd:YAG pulsed laser annealing system, and 632.8 nm–He-Ne Raman system) are shown in Appendix F.

c) Reflection high-energy electron diffraction (RHEED)

Reflection high energy electron diffraction (RHEED) is a representative electron diffraction technique used to estimate surface structure. In this study, RHEED (Vacuum Products) is used to observe the surface crystalline quality of the YSZ layer prior to the Si film deposition, the as-deposited a-Si, and crystallized Si films. The acceleration voltage,

filament current, and emission current of the electron gun are 20 kV, 2 A, and 50 μA, respectively. In Appendix G, the measurement principle of RHEED is shown.

d) Scanning electron microscopy (SEM)

Scanning electron microscopy (SEM) is used to observe surface morphology of the crystallized Si film. In this work, we use the SEM apparatus by HITACHI (S-4100) with the accelerating voltage of 20 kV. Before SEM observation, Si films are Secco-etched in order to observe the grains easier. Then, the deposition of ~10-nm-thick Pt-Pd thin layer on the surface of Si film is carried out by ion-sputtering to reduce a charge-up phenomenon due to insulating substrate (YSZ layer or glass). Appendix H shows the measurement principle of SEM.

e) Transmission electron microscopy (TEM)

Microstructure of the fabricated Si/YSZ/glass sample is observed by the transmission electron microscopy (TEM) with the acceleration voltage of 300 kV. The principle of TEM is described in Appendix I.

3.4.2 Chemical composition of YSZ layer by X-ray photoelectron spectroscopy (XPS)

Chemical composition of the YSZ layer surface are estimated by X-ray photoelectron spectroscopy (XPS). The used XPS apparatus is Surface Science Instruments (S-PROBE) with the X-ray source of AlKα (1486.6 eV). During the measurement by XPS, an insulating sample of YSZ is easily charged up, which balances with electron loss from the surface. To minimize this, an adjacent neutralizer or electron flood gun is recommended to use. They add low energy electrons to the sample surface. Also, any shift in electron binding energies is calibrated using adventitious carbon (C) 1s whose binding energy is 284.6 eV. The Y component of YSZ layer, R_Y, is determined by dividing the integrated intensity of Y3d peak to the total integrated intensities of Y3d and Zr3d:

$$R_Y = \frac{A_Y / C_Y}{A_{Zr} / C_{Zr} + A_Y / C_Y} = \frac{I_Y}{I_{Zr} + I_Y}, \tag{3.3}$$

where $I_Y = A_Y / C_Y$ and $I_{Zr} = A_{Zr} / C_{Zr}$ are integrated intensities while A_Y and A_{Zr} are spectra areas of Y3d and Zr3d, respectively. C_Y = 6.61 and C_{Zr} = 7.65 are sensitivity factors of Y3d and Zr3d, respectively. In Appendix J, principle of XPS measurement is described.

3.4.3 Impurities diffusion into an Si film by secondary ion mass spectroscopy (SIMS)

Secondary ion mass spectroscopy (SIMS), namely CAMECA IMS-6f, is used to measure impurities diffusion into the crystallized Si film from the YSZ layer. The primary ion species is O_2^+ with the primary acceleration voltage of 3.0 kV. The quantitative concentrations were estimated by using a standard sample of an ion-implanted Si. Appendix K will show the measurement principle of SIMS.

3.4.4 Electrical properties by resistivity and Hall effect measurements

In order to estimate electrical properties of the crystallized Si film, resistivity and AC Hall effect measurements are performed by Model 8403, ToYo Corporation, using the Van der Pauw method. The measurement temperature is varied from room temperature (RT) to 300 ^{o}C, and activation energies of carrier concentration n, Hall mobility μ_H, and conductivity σ are estimated. Detailed explanations on the resistivity and Hall effect measurements are mentioned in Appendix L.

Chapter 4*:

Effect of Crystallization-Induction Layers of YSZ on Quality of Crystallized Si Films

4.1 Property of the YSZ crystallization-induction (CI) layer

Since a YSZ layer acts as a CI layer, its crystalline quality is expected to influence crystallization of an a-Si film strongly. It is supposed that the higher quality of the YSZ is, the higher quality of the crystallized Si film can be obtained. Influence factors of crystalline quality of the deposited YSZ film by sputtering are target oxidation, yttrium content, substrate temperature, O_2 flow rate, sputtering pressure, etc.. In previous studies, Hana et al. reported that a YSZ layer deposited from oxidized surface of a metallic sputtering target had better crystalline quality than that from metallic surface under the same sputtering deposition conditions.[86)] They also suggested the optimum conditions of all influence factors for improving the YSZ crystalline quality. On the basis of these conditions, the actual conditions used in this study are summarized in Table 3.1 of chapter 3. They are a little different from the previous study because the optimum conditions are very critical due to unknown and uncontrolled factors.

Figure 4.1 shows the XRD and RHEED patterns of the 60-nm-thick YSZ layer

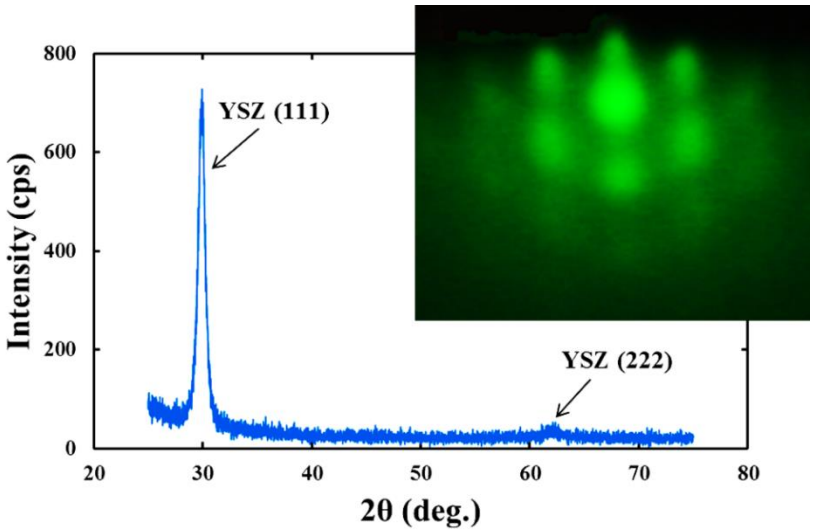

Fig. 4.1 XRD and RHEED patterns of the 60-nm-thick YSZ layer deposited on the quartz substrate.

* This chapter is referred from Jpn. J. Appl. Phys. **53**, 03CB01 (2014), in which I am the first author.

deposited on a fused quartz glass substrate. It can be seen from the XRD pattern that the deposited YSZ layer has a preferential orientation of (111). Moreover, a spotty pattern can be observed from the RHEED measurement, which indicates a highly oriented film surface. The YSZ layer is found to be uniaxially (111)-oriented because the observed RHEED pattern does not change with rotation along the normal axis of the sample surface, which is in good agreement with the XRD pattern.[87,88)]

4.2 Irradiation energy density dependences of nucleation and crystallization growth of Si films on YSZ layers

Figure 4.2(a) and 4.2(b) shows the He-Ne Raman spectra of the Si films deposited on the YSZ/glass and glass substrates at the irradiation energy densities E of 29–31 and 104–106 mJ/cm^2, respectively, with the pulse number N = 300. The irradiation He-Ne laser beams for the measurement are illustrated schematically as the insets. At a low E of 29–31 mJ/cm^2 [Fig. 4.2(a)], we observe broad and large peaks at ~480 cm^{-1} corresponding to an a-Si phase accompanied by very small c-Si peaks at ~517 cm^{-1} for both the Si/glass and Si/YSZ/glass. This suggests that the crystallization of Si films starts at approximately this irradiation energy density. At a high E of 104–106 mJ/cm^2, the Raman spectra in Fig. 4.2(b) show high and sharp c-Si peaks at ~515 cm^{-1} with small a-Si peaks, which indicate that a small fraction of a-Si phase still remains. Around this irradiation energy density, it seems that the crystallization process is almost completed. It can also be seen that the c-Si

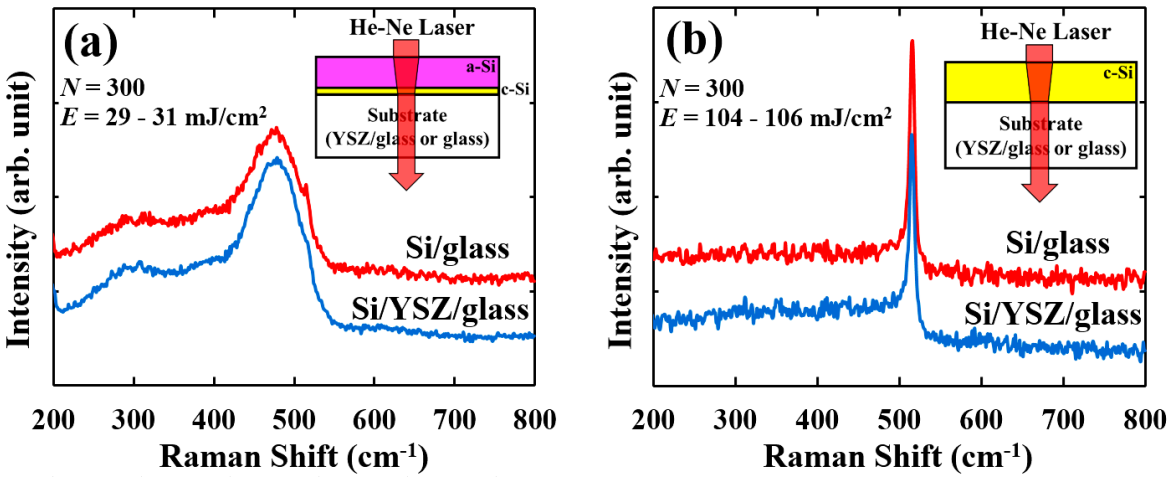

Fig. 4.2 He-Ne Raman spectra of the Si films deposited on the YSZ/glass and glass substrates at irradiation energy densities E of (a) 29–31 and (b) 104–106 mJ/cm^2 with pulse number N = 300. The irradiation He-Ne laser beams in the measurement are illustrated schematically as the insets.

peaks of Si/glass are slightly higher than those of Si/YSZ/glass at both energy densities. The reason will be explained in the next section.

From the He-Ne Raman spectra, we have observed an average evaluation of crystalline quality for a whole Si film. Next, we show the He-Cd Raman spectra at a middle irradiation energy density for local estimation of the Si surface and the interface between Si film and substrate (YSZ/glass or glass). Figures 4.3(a) and (b) show the He–Cd Raman spectra of the Si/glass and Si/YSZ/glass, respectively, obtained from the front and back surface measurements at the pulse number N = 10. It can be seen that, from the front side measurement for both the structures, a very small c-Si peak might be formed. From the back surface measurement, a relatively high and sharp c-Si peak clearly appears. This indicates that, at this irradiation energy density, the crystallization growth is enhanced from the interface between the Si film and the underlayer (YSZ/glass or glass), but little nucleation occurs near the surface of the Si film. This enhancement of crystallization from the interface is considered to be due to the heterostructure.[89,90] If E is much higher than those in Fig. 4.3, the crystallization would be nearly completed, which would show no

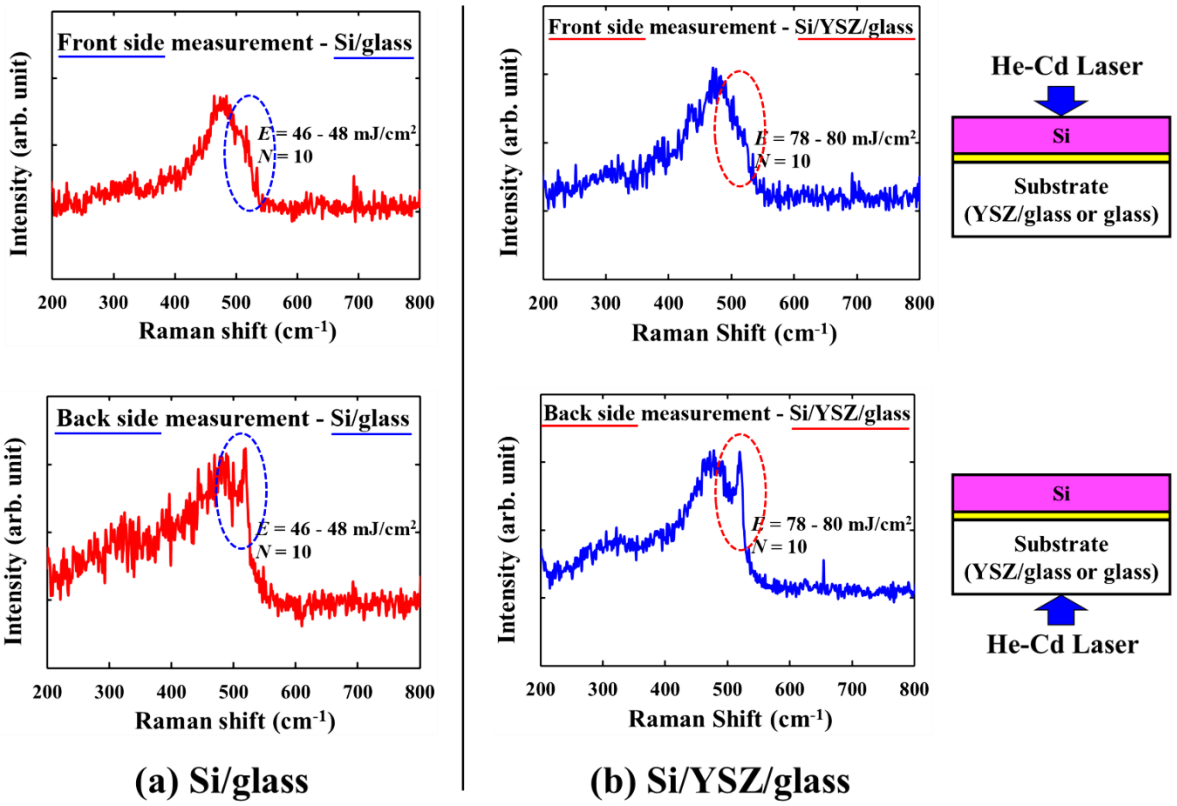

Fig. 4.3 He–Cd Raman spectra of (a) Si/glass and (b) Si/YSZ/glass from the front side and back side measurements. The dotted circles indicate crystalline Si peak regions.

significant difference in crystallization behavior at the surface and interface of the Si films. On the other hand, if E is much lower, the nucleation would be less and the crystallization growth would be local, which would hardly be observed by He–Cd Raman spectroscopy.

4.3 Irradiation energy density dependences of crystalline fraction and film quality

In this section, we show the results of crystalline quality of the Si film, which are obtained from He-Ne Raman spectroscopy measurement. Figures 4.4(a) and (b) show the dependence of crystalline fraction X_c on irradiation energy density E with the pulse numbers N of 300 and 50, respectively. The analyzed data of X_c (vertical axis) are shown as averages, where the error bars indicate the upper and lower values among three measurements at the same point. The estimation error of E (horizontal axis) is ± 2%. It can be seen from these figures that X_c increases monotonously with E for both the Si/glass and Si/YSZ/glass. With pulse number N = 300 in Fig. 4.4(a), at $E \geq 105$ and 110 mJ/cm^2 for Si/glass and Si/YSZ/glass, respectively, Si films begin to melt, and X_c nearly saturates at a high value. The critical melting energy densities for Si/glass and Si/YSZ/glass with N = 50 in Fig. 4.4(b) are in turn 110 and 115 mJ/cm^2, which are a little higher than those with N = 300 due to the shorter annealing time. It is considered that, in the low-E region, Si films do not receive sufficient thermal energy for completion of crystalline phase transformation from amorphous. Therefore, most of films are in amorphous phase. Then, with increasing

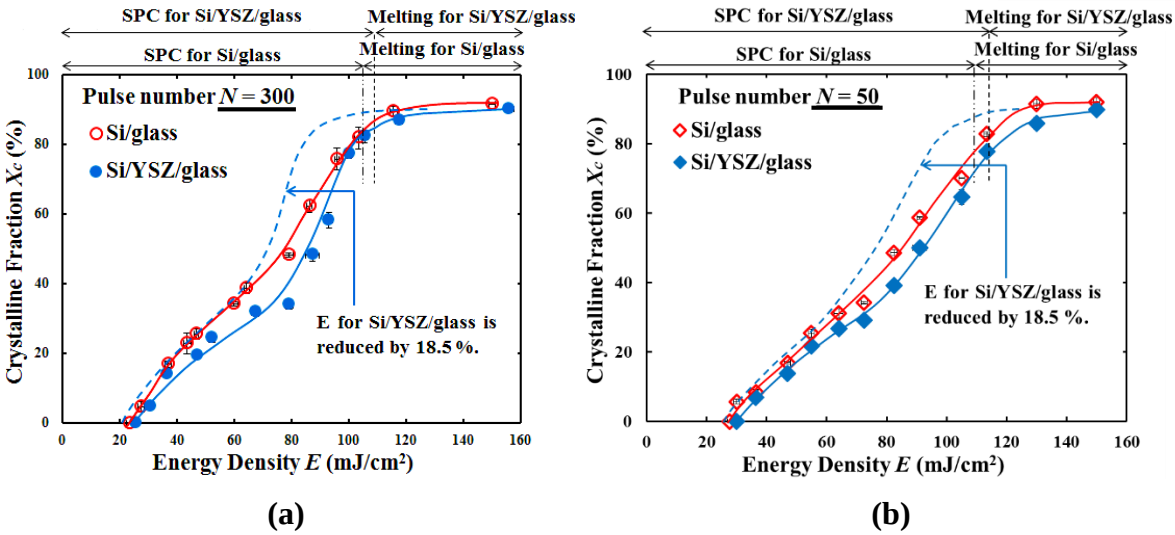

Fig. 4.4 Dependence of crystalline fraction X_c on the laser energy density E with (a) N = 300 and (b) N = 50. The broken lines are curves redrawn for the data of the Si/YSZ/glass, considering the difference in optical absorption.

E, more new nuclei are more formed and crystallization area extends, causing X_c to increase. The X_cs of the Si films on the glass substrates are higher, indicating faster crystallization of the films than those on the YSZ layers at the same energy density for both cases of pulse numbers. This is due to the difference in the optical absorption of the a-Si film between the Si/glass and Si/YSZ cases. This difference also leads to a difference in the critical *E* for melting between Si/glass and Si/YSZ/glass, as shown in Figs. 4.4(a) and (b). The blue broken lines in both figures are the curves redrawn for the data of the Si/YSZ/glass, considering the difference in optical absorption. The horizontal energy density *E* is reduced by 18.5% or the whole curve is shifted along the negative *E* direction by $\Delta E = 0.185E$. The derivation of these lines will be discussed later.

Figure 4.5 shows the YSZ film thickness (d) dependences of the optical absorptivities *A* of a-Si and poly-Si films, which are calculated using a fundamental optics theory. The calculation model of the sample structure is drawn schematically in the inset of Fig. 4.5, in accordance with the actual experimental conditions. In this model, we consider multireflection in a Si film and a YSZ layer in a normal incidence case. The refractive indices of a-Si, poly-Si, YSZ, and the glass substrate are $n_{\text{a-Si}} \approx 4.53-i0.897$, $n_{\text{poly-Si}} \approx 4.15-i0.0428$, $n_{\text{YSZ}} \approx 2.18$, and $n_{\text{SiO2}} \approx 1.46$, respectively, at a wavelength of 532 nm.[91,92] The derivation of *A* is described in detail in Appendix F. It can be seen that the absorptivity

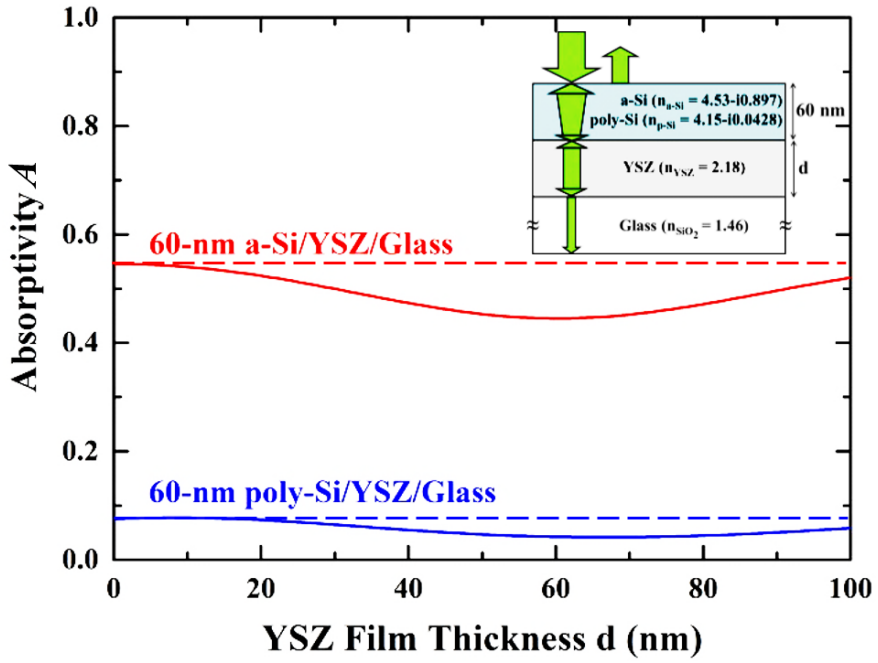

Fig. 4.5 Dependences of absorptivity in Si on the YSZ film thickness d for 60-nm-a-Si/YSZ/glass and 60-nm-poly-Si/YSZ/glass structures.

of the a-Si film in a 60-nm-a-Si/glass structure (d = 0), $A \approx 0.546$, is higher than that in a 60-nm-a-Si/YSZ/glass structure with d = 60 nm, $A \approx 0.445$. For a poly-Si film, a similar result is obtained, but with much smaller values, i.e., $A \approx 0.075$ and 0.042 for d = 0 and 60 nm, respectively. This indicates that the Si film in Si/glass is heated more than that in Si/YSZ/glass at a same irradiation energy density E because the amount of heat H generated by optical absorption can be proportional to the product (A•E). This essentially results from the smaller difference in refractive index between Si (n_{Si}) and YSZ (n_{YSZ}) than between Si (n_{Si}) and glass (n_{SiO_2}), which leads to the smaller absorptivity in the former compared with the latter.

Considering the above differences, the data for the Si/YSZ/glass in Figs. 4.4(a) and (b) are redrawn by the broken blue lines, as mentioned earlier. The value of 18.5% is calculated using $A \approx 0.546$ for a-Si/glass and $A \approx 0.445$ for a-Si/YSZ/glass by taking $(0.546-0.445)/0.546 \approx 18.5\%$. We can see that the corrected line for Si/YSZ/glass becomes more fitted to the red line curve for Si/glass in the low-E region. In the high-E or high-X_c region, since the Si film contains both amorphous and polycrystalline phases, the refractive index should be considered not only of the poly-Si but also of the a-Si. Therefore, it can be concluded that the difference in X_c at the same E between Si/YSZ/glass and Si/glass is mainly attributed to the difference in optical absorption between them. Actually, in order to explain the behavior shown in Fig. 4.4 in more detail, we should take the temperature dependence of the refractive index into account. Owing to this, the absorptivity of poly-Si increases with temperature monotonically, and thus the Si film should be exposed to more heating than that predicted from the calculated absorptivity in Fig. 4.4.[93)]

Figures 4.6(a) and (b) show the energy density E dependences of the intermediate-crystalline fraction X_m and the FWHM of the c-Si peak with the pulse number N = 300, respectively. X_m, which is associated with small size nano- or micro-crystals, is determined by [$X_m = I_m/(I_m + I_c + I_a)$], where I_c, I_m, and I_a are integrated intensities of c-Si, m-Si, and a-Si peaks, respectively. The analyzed data of X_m in Fig. 4.6(a) are also shown as averages, where the error bars indicate the same as in Fig. 4.4. The estimation errors of FWHM in Fig. 4.6(b) is about ± 1 and the estimation error of E in both figures is ± 2%. It can be seen from Fig. 4.6(a) that the X_m initially increases with E and decreases gradually after $E \approx 45$–55 mJ/cm^2. In the low-E region, since most of the Si films are in the amorphous phase, X_m increases with E. However, after passing a maximum value, the X_m decreases with increasing E probably because the crystal Si–Si bond network extends with higher E or

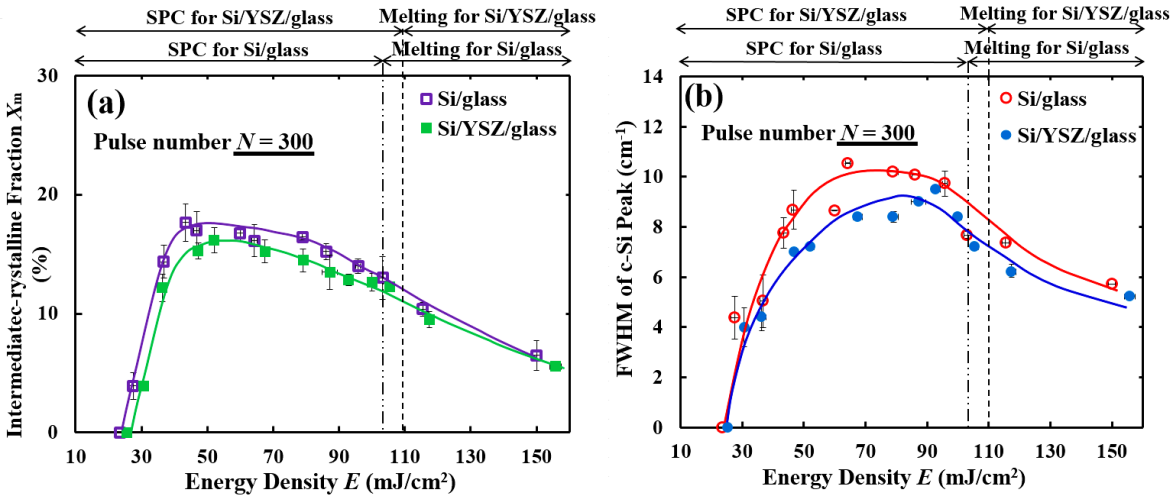

Fig. 4.6 Dependences of (a) intermediate-crystalline fraction X_m and (b) FWHM of c-Si peak on the laser energy density E with pulse number N = 300.

higher heating so that grain size becomes larger. It should be noted that the X_m of Si/YSZ/glass is slightly lower than that of Si/glass. This may indicate that the volume of small grains or micro-grains is smaller in the former than in the latter.

In Fig. 4.6(b), the FWHM of the c-Si peak varies from 4 to 10.5, with increasing E in both Si/glass and Si/YSZ/glass in the SPC regime (i.e., E < 105 and 110 mJ/cm^2 for Si/glass and Si/YSZ/glass, respectively). However, near/in the melting regime (i.e., $E \geq$ 105 and 110 mJ/cm^2 for Si/glass and Si/YSZ/glass, respectively), the opposite tendency occurs. The increase in FWHM with E in the SPC regime can be explained by the increase in the defect density inside and outside of the grains owing to the rapid crystallization and impingement of grains grown in an inhomogeneous direction.[94,95] In contrast, near/in the melting regime of E, defects inside and outside of the grains are removed and reduced in number by a higher temperature or a melting process. Moreover, the good lattice realignment of Si atoms in the melting regime makes films more homogeneous. Also, as a whole, it can be seen that the FWHMs of the c-Si peaks for Si/YSZ/glass are smaller than those for Si/glass, which is similar to the result of X_m in Fig. 4.6(a). Since FWHM is taken as one of indicators of crystalline quality of c-Si grains, the crystalline quality of the Si films on the YSZ layers can be better than that on the glass substrates.

The same results as Fig. 4.6 are obtained with smaller pulse number N of 50. Figures 4.7(a) and (b) show the energy density E dependences of the intermediate-crystalline fraction X_m and the FWHM of the c-Si peak with the pulse number N = 50, respectively. However, both the X_m and FWHM of the c-Si peak in Fig. 4.7 reach the maximum values

at energy densities higher than those in Fig. 4.6. This is because the film in the former case is irradiated with the smaller pulse number or shorter annealing time than the latter one as the same with the difference in critical melting energy densities, which was mentioned before.

Figures 4.8(a) and (b) show the SEM images of the Secco-etched SPC Si films on the glass and YSZ/glass, respectively, where the annealing conditions are E = 60–80 mJ/cm^2 and N = 300. The grain size is roughly about 20 nm for the Si films on both the YSZ layer and glass substrate. Carefully observing some areas in the Si/glass sample of Fig. 4.8(a), we can find a large difference in grain size or nonuniform grains. For example, in the left-hand and right-hand circles, smaller and larger grains exist, respectively. This is probably due to the random nucleation of Si on the glass substrate. In contrast, on the YSZ layer, the grain sizes become relatively uniform, as shown in Fig. 4.8(b). This is probably because, owing to the CI effect of the YSZ layer, the random nucleation and crystallization of the Si film are suppressed more on the YSZ layer than on the glass substrate. Therefore, it can be considered that crystallization with uniform grain size due to the presence of the YSZ layer may contribute to a smaller FWHM or better crystalline quality of crystallized Si films than of Si films on glass.

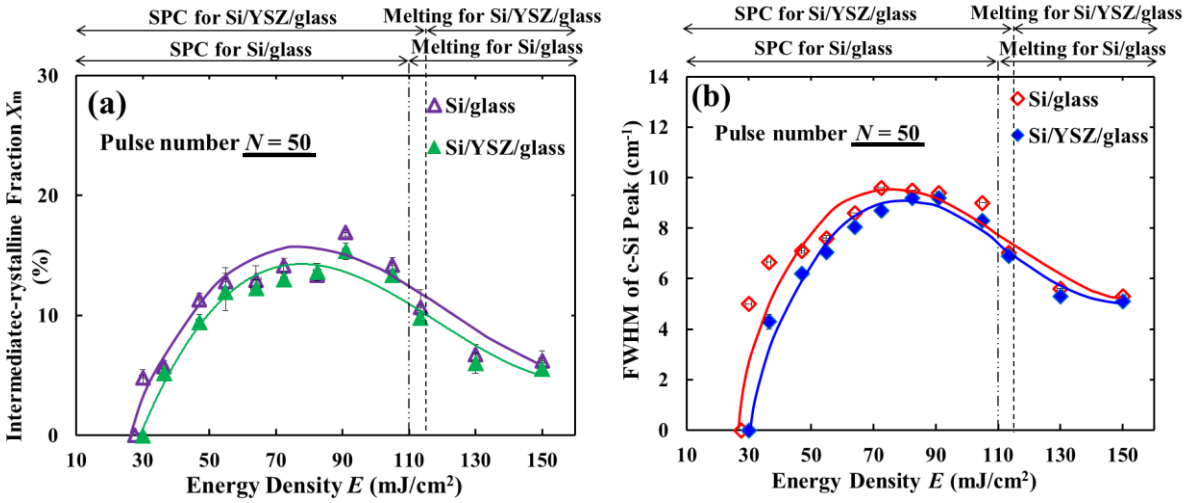

Fig. 4.7 Dependences of (a) intermediate-crystalline fraction X_m and (b) FWHM of c-Si peak on the laser energy density E with pulse number N = 50.

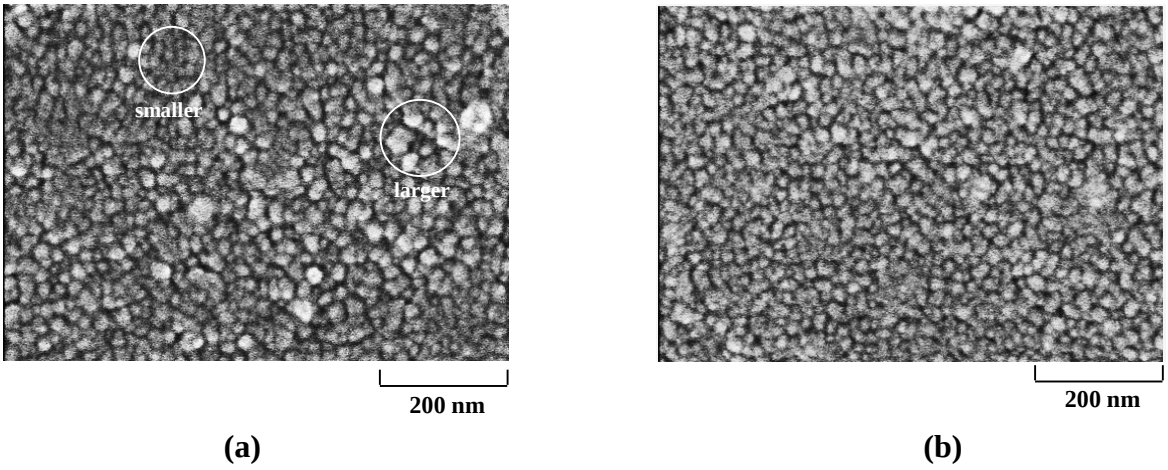

Fig. 4.8 SEM images of the crystallized Si films on the (a) glass and (b) YSZ/glass at E = 60–80 mJ/cm^2 with N = 300.

4.4 Pulse number N dependences of crystalline fraction and film quality

Figures 4.9(a) and (b) show the dependences of the crystalline fraction X_c and the FWHM of the c-Si peak, respectively, on the pulse number N, where the energy density is a parameter. These results are obtained from He-Ne Raman spectroscopy measurement. It can be seen from Fig. 4.9(a) that the X_c of Si films increases with N because increasing N increases annealing time substantially, which enhances the crystallization of Si films. It is well known that, for bulk nucleation, the initial crystalline fraction depends on annealing time with the power of 4, under the assumptions that nucleation occurs randomly at a constant rate and that crystallization proceeds isotropically in direction and linearly in time as mentioned in the chapter 2. Therefore, we can say that the rapid increase and saturation

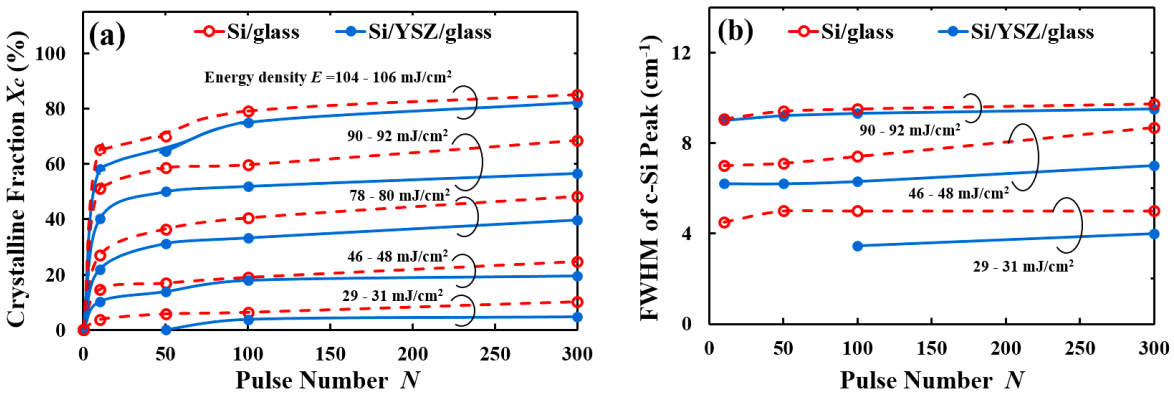

Fig. 4.9 Dependences of (a) crystalline fraction X_c and (b) c-Si peak FWHM on the pulse number N. The energy density E is the parameter.

tendency of X_c with a small N at a high E indicates bulk nucleation and growth. It can also be seen that the X_cs of the Si films on the YSZ/glass are lower than those on the glass substrates at the same E and N, in general. This is due to the difference in optical absorption of the a-Si film between the two structures of Si/glass and Si/YSZ/glass as discussed earlier. The saturation behavior X_c of will be discussed later in more details.

In Fig. 4.9(b), at a low E = 29–31 mJ/cm^2, the FWHMs are small and almost the same for all the pulse numbers. This indicates that annealing with a small E enables crystallization that retains relatively good quality with low defect density. However, by increasing E within the SPC regime, the FWHM becomes larger and increases slightly with N. The increase in FWHM with E is due to increase in defect density or degraded crystalline quality, as mentioned earlier in Fig. 4.6(b). Since the crystallization rate is very high owing to the high E, sudden impingement of grains may promote defect generation not only in grain boundary regions, but also inside grains. Furthermore, it is notable that, at the same N, the FWHMs for Si/YSZ/glass are smaller than those for Si/glass. This suggests the better crystalline quality of the former than of the latter, as in Fig. 4.6.

4.5 Crystalline fraction dependences of FWHM and position of crystalline Si peak by He-Ne Raman spectroscopy

In the above results (sections 4. 3 and 4.4), we compare the FWHMs of the c-Si peak of the Si/YSZ/glass and Si/glass samples at the same energy density and pulse number. Carefully seeing the data, it seems that FWHM or crystalline quality in the SPC region is determined by X_c. In other words, when X_c increases, FWHM increases or crystalline quality becomes poor. When X_c is smaller, FWHM is smaller or crystalline quality is better. Although FWHM actually depends on E and N, it can be considered that a unique determination factor for FWHM is X_c. Therefore, as a function of X_c, we check the behaviors of the FWHM and position of the c-Si peak, which are measures of crystalline quality and film stress, respectively. Figure 4.10 shows the dependences of the FWHM and position of the c-Si peak on X_c with N = 300 for the Si/YSZ/glass and Si/glass. FWHM and position of c-Si peak are estimated within the error of ± 0.5. Also, the estimation error of E is ± 2%. In this figure, every set of two data points with the same E is enclosed together by one solid circle. The critical X_cs for melting are almost the same for both the Si/YSZ/glass and Si/glass. From this figure, it can be seen that the FWHMs for both Si films increase

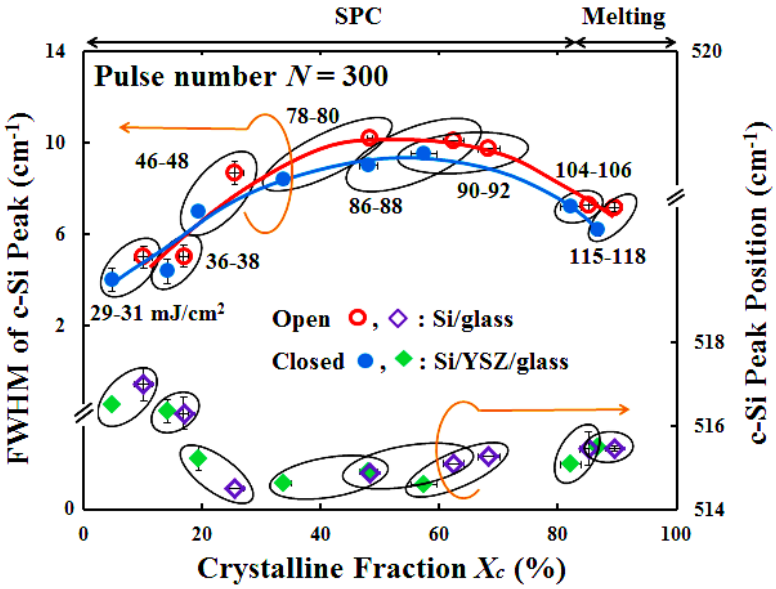

Fig. 4.10 Dependences of the FWHM and position of c-Si peak on the crystalline fraction X_c for the pulse number N = 300.

with X_c up to ~60%, then decrease beyond it. Also, at $X_c \geq 30\%$, it can be seen that the FWHMs for the Si/YSZ/glass are smaller than those for the Si/glass. The differences between them are clearly larger than the measurement error bars. Therefore, it can be concluded that the crystalline quality of the SPC Si film on the YSZ layer is essentially better than that on the glass substrate.

Also, it can be seen from Fig. 4.10 that the c-Si peak positions in both the cases are nearly the same at the identified X_c and in the range from 514.5 to 517.4 cm^{-1}, which is lower than the peak position of single-crystalline Si (520 cm^{-1}). This indicates that the Si films exhibit tensile stress on both the YSZ layer and glass substrate, and that the YSZ layer does not serve as a strain buffer layer. Therefore, it can be considered that the small FWHM of the Si/YSZ/glass is not related to film stress. Generally, tensile stress in a crystallized Si film on a glass substrate can be explained by the difference in thermal expansion coefficients (TECs) between Si and glass (quartz), which are 2.8×10^{-6}/°C and 0.5×10^{-6}/°C,[96] respectively. Since the TEC of Si is much larger than that of glass and the crystallization or atomic arrangement temperature, e.g., the melting temperature is higher, crystallized Si films at room temperature suffer from tensile stress.[94,95,97,98] However, in our case, since the TEC of YSZ is 11×10^{-6}/°C,[99] it is expected that the Si film will be compressed by the YSZ layer. However, this is opposite to the result in Fig. 4.10, which shows almost the same stress in Si/YSZ/glass and Si/glass. Therefore, we infer that the tensile stress in Fig. 4.10 may be caused by the densification during the phase transition

from amorphous to crystalline. This is because the mass density of a-Si containing voids and defects is generally lower than that of crystalline Si.[100,101] Since Si atoms at the interface are tightly bonded to the underlayer atoms, the Si position there may be almost fixed or negligibly changed even after subsequent pulse irradiation. On the other hand, Si atoms in the bulk of the film over the interface move from their original position in the as-deposition state during crystallization, which may lead to the densification or shrinkage of the Si film. Therefore, this densification causes tensile stress in the crystallized Si film.

On the basis of this hypothesis, we can explain the behavior of the stress in Fig. 4.10 as follows. The c-Si peak position gradually shifts to lower values with X_c up to ~40% or $E \leq$ 70m J/cm^2. This may be in a transition state of densification, in which small crystallized Si regions that have been isolated from one another with amorphous regions make contact with and bind tightly to one another. With further increase in X_c to 80% or in E to ~100 mJ/cm^2, the peak position remains almost constant or unchanged, which means that the strength of the stress or the bonding of Si atoms in the crystallized region is in a steady state. However, with increasing X_c beyond 80% or E beyond 100 mJ/cm^2, the annealed Si films become nearly melted in solid or melted. Then, the lattice alignment of Si atoms occurs and the stress is partially relaxed or released.

Comparison of the FWHM curve with the peak position curve reveals that they seem to be related to each other. When X_c is smaller than 40%, the crystalline quality shown by FWHM is relatively good but is gradually degraded with increasing X_c, and the film stress is not so large but gradually increases with X_c. This is probably because, in the smaller range of X_c, the amount of amorphous phase remains large such that it could relax stress, acting like a sponge. Furthermore, the defective crystallization region is small owing to the small E. However, X_c or E increases, since the amorphous region reduces in size and the defective crystallization region extends with X_c. In the midrange of X_c, the FWHM and stress are almost constant. This is considered to be a critical for the complete change from an amorphous network region into a crystalline network, including defects and isolated or non-network atomic regions. Atoms constituting the defects and non-network atomic regions rarely move into the lattice sites at an E lower than the critical E for melting. However, at X_c of more than 80%, i.e., near or higher than the critical E, some Si atoms in the defect and non-network regions can bond well to other atoms so that FWHM and film stress can be reduced.

4.6 Discussion on the saturation behavior of crystalline fraction X_c

Figure 4.11 explains the saturation behavior of X_c, which was mentioned in Fig. 4.9. The dotted line in Fig. 4.11(a) shows the theoretical calculation for the relationship between the total film absorptivity A and the poly-Si film thickness d_p from the interface. Figure 4.11(b) shows a sample structure model for the calculation, where d_a is an a-Si film thickness and the total thickness of the Si film (d_p + d_a) is constant of 60 nm. The absorptivity A is defined as the ratio of ($E - E_R - E_T$)/E, where E_R is the reflected beam energy density at the Si film surface and E_T is the transmitted one at the YSZ layer interface. Additionally, in Fig. 4.11(a), the experimental data for the relationship between the saturation X_c and the irradiation energy density E are shown by closed circles and the solid line is shown as a visual guide. The two relationships (i.e., d_p–A and X_c–E) are shown together because they are interdependent on each other; this aspect is discussed later. The assumptions for the calculation of the total film absorptivity A is the same as in section 4.3. It can be seen from Fig. 4.11(a) that A decreases with increasing d_p. Because the absorptivity of a-Si (~0.445) is much higher than that of poly-Si (~0.042) for the incident beam, increasing d_p leads to a decrease in d_a such that A should decrease in the case of a constant total Si film thickness of 60 nm. Moreover, in Fig. 4.11(a), increasing the irradiation energy density E leads to an increase in the experimental saturation X_c, which is

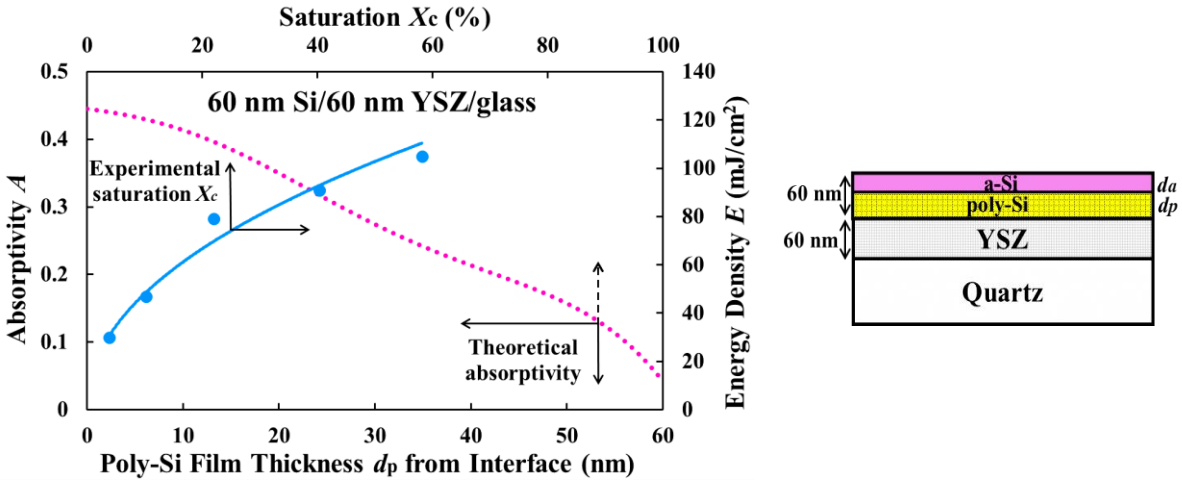

(a) **(b)**

Fig. 4.11 (a) Theoretical calculation curve of the Si film absorptivity as a function of the poly-Si thickness d_p (dotted line) from the YSZ interface and experimental data relationship between saturation crystalline fraction X_c and laser energy density E (closed circles and solid line), and (b) sample structure for the calculation in (a).

exactly opposite to the relationship between A and d_p. From the above results, we can explain the saturation X_c behavior related to E as follows: First, it can be postulated that the ratio between the poly-Si film thickness and the total thickness, $[d_p/(d_p + d_a)] = d_p$ (nm)/60, corresponds or roughly equals the saturation X_c. That is, X_c (%) = 100 × d_p (nm)/60 = 5d_p (nm)/3. This is possible because X_c reveals the ratio between the crystallized volume and the total volume of the Si film, which are proportional to the thickness ratio between d_p and (d_p+d_a). The amount of heat H generated by optical absorption in the irradiated Si film can be proportional to the product $A \bullet E$ of the total absorptivity A and irradiation energy density E ($H \propto A \bullet E$), and the heat increases the film temperature T_f ($T_f \propto H$). Therefore, T_f strongly depends on $A \bullet E$ ($T_f \propto A \bullet E$). Strictly speaking, the temperature distribution in the film thickness direction is not uniform and depends on the depth position in the film because the beam energy decreases with the traveling or penetration depth in the film owing to optical absorption. However, the thermal diffusion lengths of a-Si and c-Si are calculated to be ~75 and ~738 nm at 300 K, respectively, for the pulse duration time of 6 ns, which are larger than the total film thickness of 60 nm. The film temperature T_f may become almost uniform in the film thickness direction at least after the pulse duration time. That is, $A \bullet E$ (mJ/cm^2) is the dissipation energy in the film per unit area and the heat H generated due to $A \bullet E$ is diffused instantaneously and uniformly in the Si film. Therefore, we can hypothesize that T_f is uniform in the film. At a very low E, the crystallization cannot start because T_f is smaller than the critical crystallization temperature T_c. To induce crystallization growth, T_f should be more than or equal to T_c. To keep T_f constant above T_c, the sample should be irradiated at a higher E. At $T_f \geq T_c$ and E = constant, the crystallization progresses continuously with increasing pulse number N. Thus, the thickness d_p of the poly-Si film also increases, accompanied by the decrease in A, as shown in Fig. 4.10(a). Then, H and T_f decrease because $H \propto A \bullet E$ and $T_f \propto H$. Therefore, the crystallization is suspended or stopped and the crystalline fraction X_c saturates since T_f decreases below T_c. Owing to this negative feedback phenomenon, X_c finally saturates at a fixed E. If you want to increase X_c further by raising T_f above T_c again, a higher E should be needed because A is a lower and $T_f \propto A \bullet E$. Thanks to the self-limiting process of the saturation behavior, the crystallization of Si films can be performed in a relatively stable manner even if E fluctuates within a certain range during irradiation.

4.7 Models of crystallization mechanism of Si films with and without YSZ CI layers

From the aforementioned experimental results and discussion, we speculate a mechanism of Si film crystallization with/without the YSZ CI layer at low and high energy densities E. The schematic models are shown in Fig. 4.12. At a low energy density in Fig. 4.12(a) (e.g., $E \approx 29$–31 mJ/cm^2 in Fig. 4.9) and in the initial state (e.g., $N \leq 50$ in Fig. 4.9), nucleation sites may be formed mainly at the interface between Si and the underlayer in both Si/glass and Si/YSZ/glass. According to the previous reports from other researchers,[89,90] nucleation in a-Si films occurs faster at the interface than in the bulk. In Si/glass, due to the lack of crystallographic information on glass, crystallization growth proceeds randomly as does random nucleation. In the Si/YSZ/glass case, in contrast, owing to YSZ being highly oriented or fiber-textured (Fig. 4.1), nucleation might be induced more uniformly like a sheet at the interface of the YSZ layer. For example, at $X_c \approx 0$ for $N = 50$ and $E \approx 29$–31 mJ/cm^2 in Fig. 4.9, there is no observable crystallized region grown from the nucleation. This is probably because the optical absorptivity is smaller than that of Si/glass, as shown in Fig.4.5. With increasing annealing time or pulse number (e.g., $N >$ 50), crystallization occurs from the interface and proceeds at a low rate, as shown in Fig. 4.12(a). The orientation of the crystallized regions might be similar to that of the grains of

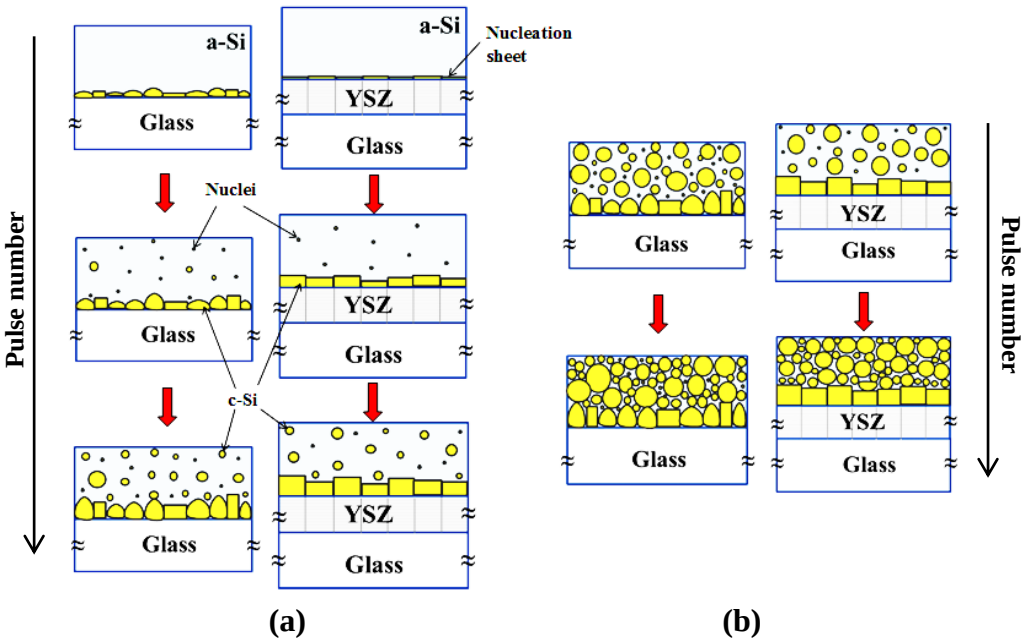

Fig. 4.12 Schematic models of crystallization mechanism of Si films with/without YSZ CI layers at (a) low and (b) high energy densities.

the YSZ layer, as shown in the right-hand side in Fig. 4.12(a), in contrast to the random nucleation and crystallization growth of the Si/glass. With increasing *N*, film bulk nucleation may occur in not only Si/glass but also Si/YSZ/glass, although the crystallized region extends more from the interface, where the nucleation density in the bulk for Si/YSZ/glass is lower than that for Si/glass because of the lower optical absorptivity. On the other hand, at high *E* in Fig. 4.12(b) (e.g., $E > 90$ mJ/cm^2), since the crystallization rate is very high, nucleation and growth occur quickly even with a short annealing time or a small pulse number (e.g., $N \approx 10$). Due to the higher nucleus density and the lack of crystallographic information in the bulk, crystallization growth from the interface is impeded by bulk random growth and terminates midway in not only Si/glass but also Si/YSZ/glass. From the above discussion, we expect that annealing with low *E* will produce Si films with better crystallinity. However, the crystallization rate is so low that it should take a long time for complete crystallization. Annealing with high *E* can reduce the annealing time, but the crystallized Si film quality becomes poorer or more defective due to faster random nucleation and crystallization growth.

4.8 Summary

We crystallized Si films on glass substrates with and without a YSZ CI layer in the solid phase by PLA, and investigated their properties mainly by Raman spectroscopy. We obtained the following results. For the Si/YSZ/glass, nucleation occurs faster at the YSZ interface than in the bulk of the a-Si film at a low irradiation energy density *E*. This enhancement is considered to be due to not only the heterostructure (e.g., Si/SiO_2) but also the crystallization-induction (CI) effect of the YSZ layer. Therefore, in the CI layer method using a small *E*, it is possible to control nucleation sites on the YSZ interface to make crystallization growth proceed to the film surface smoothly without random nucleation. From the results of irradiation energy density *E* dependences, it was revealed that the crystalline fraction X_c increased with the *E* monotonically in both the Si/YSZ/glass and Si/glass. The crystallization rate to *E* was lower for the Si/YSZ/glass than for the Si/glass. This is because the optical absorption in the Si film for the Si/YSZ/glass is lower than that for the Si/glass owing to the difference in refractive index between n_{YSZ} and n_{SiO_2}. At the same X_c, the FWHM of the c-Si peak for the Si/YSZ/glass was smaller than that for Si/glass, which indicates better crystalline quality of the Si film on the YSZ layer than that

on the glass substrate. It can be considered from this result that Si atoms in the Si/YSZ/glass are arranged more orderly during the phase transition from amorphous to crystalline and that the defect density is lower in the Si/YSZ/glass than in the Si/glass. This may be due to the CI effect of the YSZ layer. The film stress was tensile and increased with X_c, and almost saturated at approximately X_c = 40%, regardless of using a YSZ layer or not. This can be explained by the mass density change from the amorphous phase to the crystalline phase. From the pulse number N dependences of X_c, it was found that X_c increases with the pulse number N and tends to saturate around a certain number, e.g., 10, at a fixed E and the saturation value increases with increasing E. This saturation behavior was found to be a self-limiting process, by which the crystallization of Si films can be performed in a relatively stable manner even if E fluctuates within a certain range during irradiation. It is expected that annealing with low E will produce Si films with better crystallinity. However, since the crystallization rate is so low and the crystalline fraction is saturated at a short annealing time with self-limiting behavior, it should take a very long time or might be impossible to complete the crystallization. Annealing with high E can reduce the annealing time, but the crystallized Si film quality becomes poorer or more defective due to faster random nucleation and crystallization growth. For these reasons, we should consider a better method of producing good-quality Si films within a shorter time.

Chapter 5*:

Improving Crystalline Quality by a Two-Step Irradiation Method

5.1 Proposal model of a two-step method

It was found from chapter 4 that, for the Si/YSZ/glass, interface nucleation is stimulated at the YSZ interface due to YSZ properties. On the other hand, for the Si/glass, random Si nucleation occurs at the glass interface owing to the lack of crystallographic information on glass. Probably because of this, the grain size of the poly-Si film on the YSZ layer is more uniform than that on glass. However, before the crystallization growth front from the interface reaches the a-Si film surface, film bulk random nucleation and growth occur even using the YSZ layer as shown in Fig. 5.1(a). Thus, the crystalline quality of the entire Si film decreases. To further improve the crystalline quality of Si

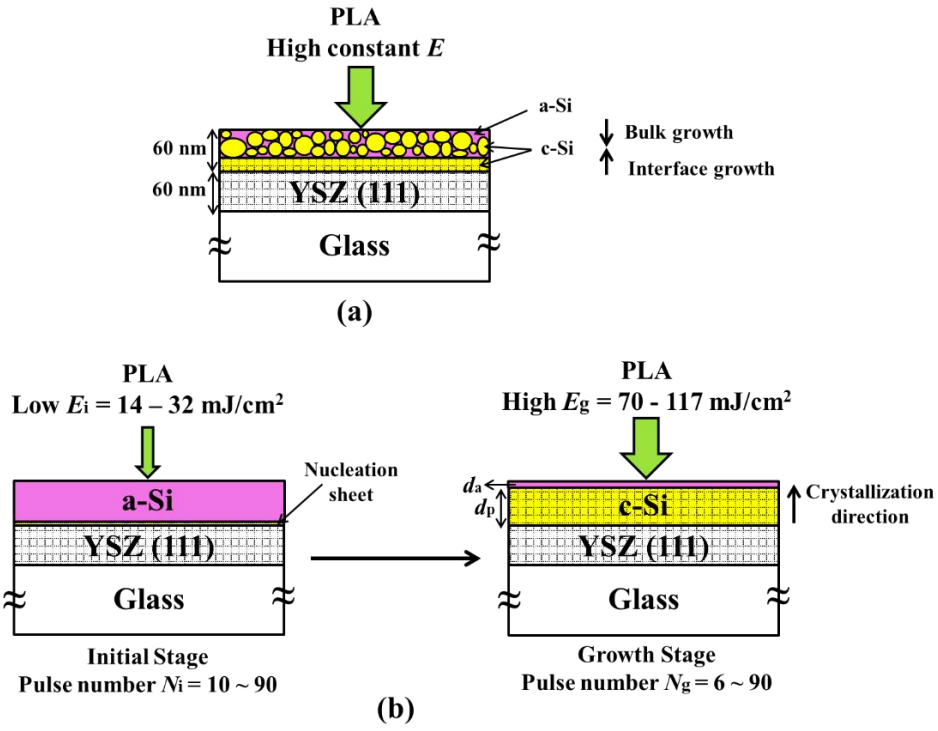

Fig. 5.1 Schematic illustrations of crystallization in Si/YSZ/glass for the (a) one-step (conventional) and (b) two-step methods together with the irradiation conditions. d_p is the thickness of the crystallized Si film from the YSZ interface and d_a is the thickness of the remaining a-Si film.

* This chapter is referred from Jpn. J. Appl. Phys. **54**, 03CA01(2015), in which I am the first author.

films, we have proposed a new two-step irradiation method (hereafter referred to as the two-step method), in which an a-Si film is irradiated using two irradiation energy densities E_i and E_g, as shown in Fig. 5.1(b). First, in the initial stage, the film is irradiated at a low irradiation energy density E_i for a short time to promote Si nucleation at the YSZ interface with the complete suppression of bulk nucleation. Next, in the second step of the growth stage, the Si film is irradiated at a higher irradiation energy density E_g to accelerate the growth from the nuclei and complete the crystallization. The procedure will be discussed in detail later. In fact, the concept of the two-step method is based on the following two important findings obtained by the one-step (or conventional) method with a fixed E: interface nucleation enhancement with the suppression of bulk nucleation at a lower E and the energy-self-limiting crystallization. It is noted that, without the energy-self-limiting crystallization, a stable process in the two-step method could never be expected.

5.2 Effect of the two-step method on enhancing the interface nucleation and growth

Figure 5.2 shows the **He–Cd** Raman spectra of the front side and back side measurements of Si/YSZ/glass crystallized by the two-step method. First, this sample was irradiated at a low initial energy density E_i of 18–22 mJ/cm^2 with the initial pulse number

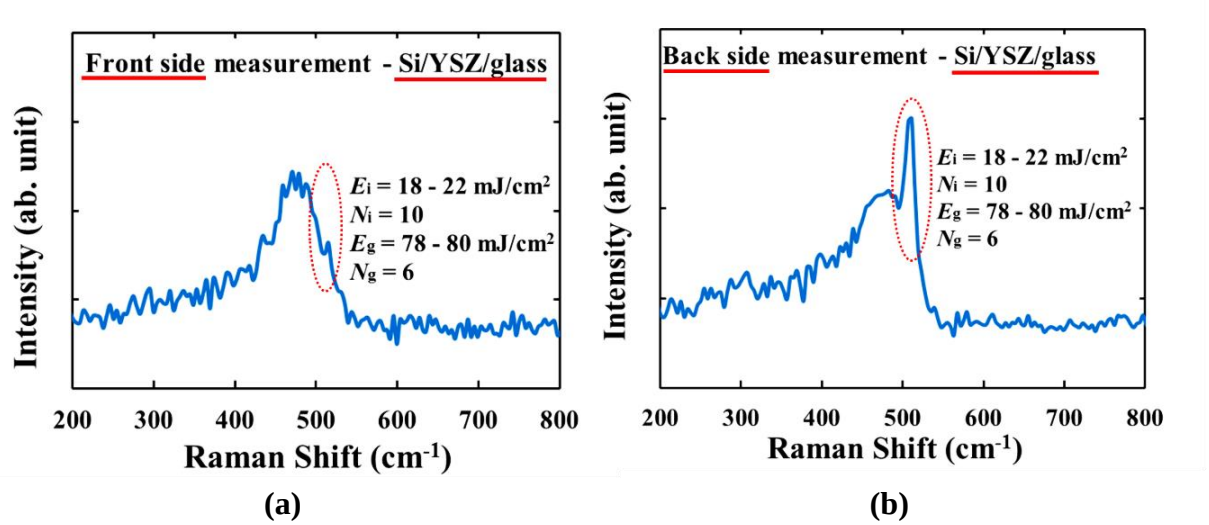

Fig. 5.2 He–Cd Raman spectra of Si/YSZ/glass crystallized by the two-step method from the (a) front side and (b) back side measurements. The dotted circles indicate crystalline Si peak regions.

N_i of 10 and then at a high growth energy density E_g of 78–80mJ/cm^2 with the growth pulse number N_g of 6. E_g is chosen for comparison with the result of the one-step method in Fig. 4.3(b) of chapter 4. From the front side measurement in Fig. 5.2(a), an unclear small c-Si peak might be observed similarly to that in the case of the one-step method in Fig. 4.3(b), which indicates that the near-surface crystallization hardly occurs. However, from the back side measurement, a high and sharp c-Si peak is clearly observed, compared with that in the case of the one-step method. This means that the interface growth is more enhanced by the two-step method even with the smaller pulse number at the high energy density E_g and lower total irradiation energy density E_t, where $E_t = E_i \bullet N_i + E_g \bullet N_g$ for the two-step method. For the one-step method case, $E_t = E \bullet N$. From this result, it can be considered as follows: In the two-step method, the initial irradiation with a low E_i induces formation of nuclei at the YSZ interface with suppression of bulk nucleation, and the next irradiation with a high E_g accelerates crystallization growth from the interface nuclei at a higher rate than in the one-step method.

5.3 Optimization of irradiation conditions

In this section, irradiation conditions of the initial stage, i.e., N_i and E_i, are investigated and optimized because they are very important in the two-step method. If there is little nucleation in the initial stage at a very low E_i, the crystallinity of the Si film is almost as same as the case of the one-step method probably because of the nearly same irradiation condition. On the other hand, if, at a very high E_i, the nucleation occurs not only at the YSZ interface but also in the bulk or near the surface of the Si film, crystallization growths from the bulk nuclei prevents growth from the interface nuclei. As a result, crystallinity of the Si film becomes not good. Figure 5.3(a) shows the dependences of the FWHM of the c-Si peak and the crystalline fraction X_c on the pulse number $N_i = N - N_g$ (N = 100) in the Si/YSZ/glass case in the two-step method ($N_i \neq 0$), compared with those in the one-step method (N_i = 0). The closed squares and open circles indicate the data of X_c and the FWHM of the c-Si peak, respectively. Also, the energy densities for the initial and growth stages are 26–29 and 92–96 mJ/cm^2, respectively. It can be seen that, at N_i = 10, FWHM decreases abruptly and X_c increases from N_i = 0. Then, both FWHM and X_c decrease slightly with further increase in N_i. The decrease in X_c is due to the reduction in the irradiation number N_g or annealing time at a high energy density E_g with increasing N_i. The slight decrease in FHWM with increasing N_i indicates that a longer annealing time at a low

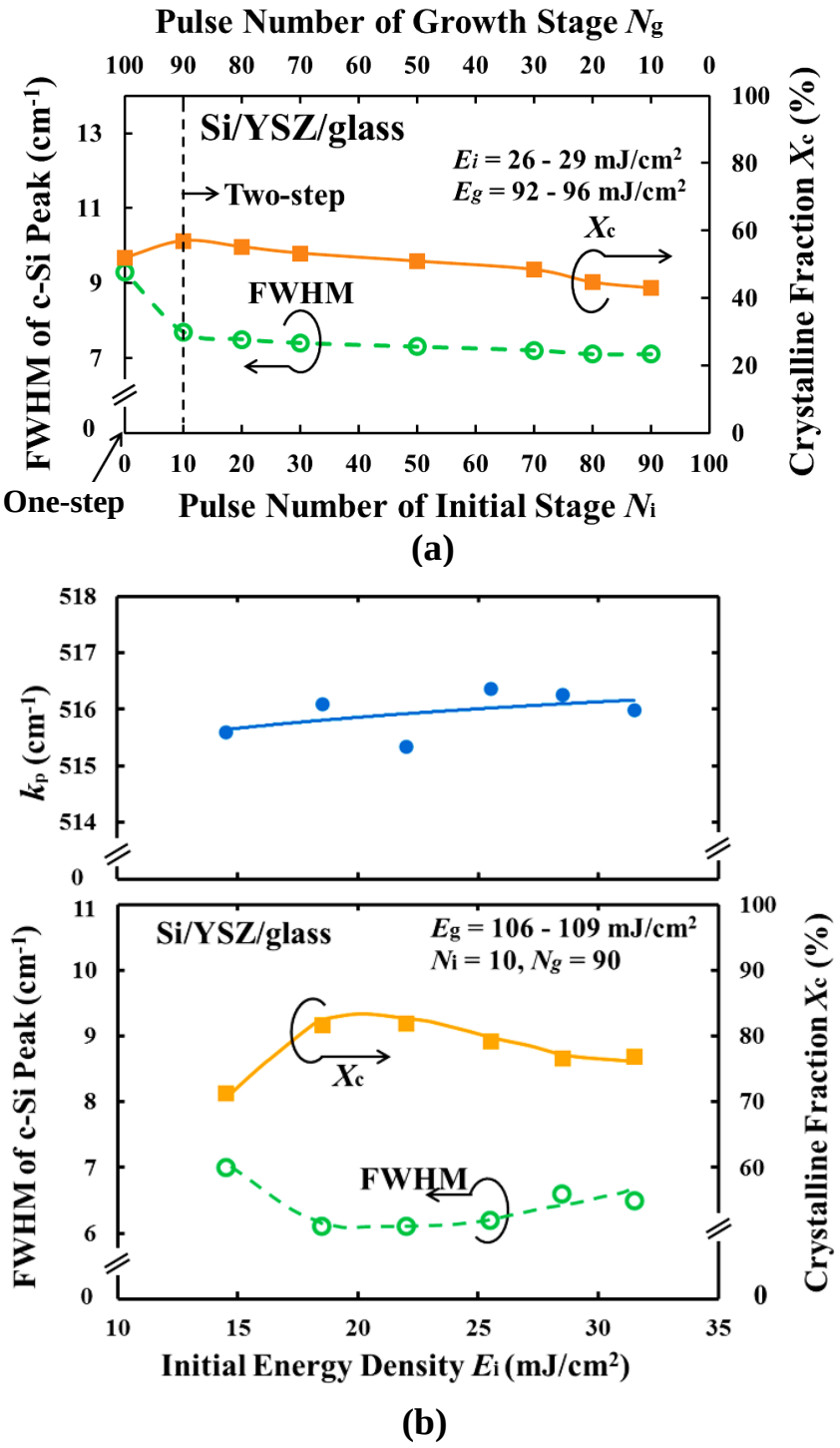

Fig. 5.3 **Dependences of c-Si peak FWHM and crystalline fraction X_c on (a) the initial pulse number N_i for the two-step ($N_i \neq 0$) and one-step ($N_i = 0$) methods, and (b) dependences of FWHM and position k_p of c-Si peak, and X_c on the initial energy density E_i for the two-step method. The upper horizontal axis in (a) indicates the pulse number of the growth stage, $N_g = N - N_i$, with $N = 100$.**

energy density might promote interface nucleation, which is effective for the direction alignment of the crystallization growth caused by irradiation with a high energy density E_g. From this figure, it can be concluded that the two-step method can improve the crystalline quality of the Si film significantly. At a constant N = 100, we choose N_i = 10 and N_g = 90 for the next investigation because X_c is apparently maximum and FWHM is relatively low.

We also investigated the dependence of the degree of crystallization in the crystallized Si films on the initial energy density E_i. This is because E_i is a very important factor that controls the location of nucleus generation, i.e., only at the YSZ interface. Figure 5.3(b) shows the dependences of the FWHM and position k_p of the c-Si peak, and the crystalline fraction X_c on the initial E_i for the Si/YSZ/glass structure in the two-step method, where E_g, N_i, and N_g are fixed at 106–109 mJ/cm^2, 10, and 90, respectively. The growth energy density E_g is close to but less than the critical melting energy density of the Si film such that the Si film would not be intentionally melt-crystallized. Generally, because of using E_g higher than that in Fig. 5.3(a), the crystallized Si films show a higher crystalline fraction or a higher X_c and a higher crystalline quality or a lower FWHM. It can be seen from Fig. 5.3(b) that X_c increases with E_i to ~22 mJ/cm^2, then decreases with E_i in the higher range. An opposite tendency is observed for the FWHM. At E_i = 18.5–22 mJ/cm^2, X_c is maximum, while FWHM is minimum. Now, the case of E_i < 18.5 mJ/cm^2 is considered. Very few nuclei might be generated at the interface between the Si film and the YSZ layer at the initial irradiation. Next, under the high-E_g irradiation, the crystallization growth from these interface nuclei proceeds rapidly. Also, in the other interface region, new nuclei are formed and then crystallization proceeds rapidly from there. However, the crystallization front may not be uniformly flat or may not be parallel to the interface. That is, it may be rugged and irregular. This irregular crystallization front might enhance random nucleation near the front and induce a change in growth direction. As a result, many small grains are formed after the crystallization at the high E_g. X_c, therefore, is not very high and FWHM is large at E_g < 18.5 mJ/cm^2. At the higher E_i of approximately 20 mJ/cm^2, a larger number of interface nuclei might be formed without bulk nucleation. Under the high-E_g irradiation, the crystallization growth from these nuclei proceeds smoothly and the front is relatively flat and parallel to the interface, compared with that of the low-E_i case. Therefore, the crystalline fraction X_c increases significantly and the defect density decreases, which leads to the decrease in FWHM. When E_i > 22 mJ/cm^2, the nucleation might occur not only at the interface but also slightly in the bulk Si film. The crystallization growth from bulk nuclei under the high-E_g irradiation partially prevents the growth from the interface nuclei.

As a result, the X_c of the Si film and FWHM decreases and increases, respectively, slightly. Also, it can be seen in Fig. 5.3(b) that the peak positions are nearly the same for all initial energy density E_i values and are in the range from 515 to 517cm^{-1}, which is lower than the peak position of single-crystalline Si (520 cm^{-1}). This indicates that the Si films exhibit tensile stress on the YSZ layer at all E_i values. On the other hand, the variations in X_c and FWHM with E_i for Si/YSZ/glass are not clearly related to k_p or the film stress. This might be due to a reason that the film stress is mainly caused by densification during the phase transition from amorphous to crystalline as mentioned in chapter 4. From the Fig. 5.3(b), it can be concluded that the value E_i = 18.5–22 mJ/cm^2 is nearly optimum from the viewpoints of Si film crystalline fraction and crystallinity.

5.4 Comparison between the one-step and two-step methods

Table 5.1 shows the comparison of the typical X_c and FWHM values of the c-Si peak of the Si/glass and Si/YSZ/glass for the one-step method with N = 100 and the two-step method with N_i = 10 and N_g = 90, which are obtained by **He–Ne** Raman spectral analysis. For the one-step method, the samples were irradiated at a constant E = 104–106 mJ/cm^2. The obtained crystallinities (crystalline fraction X_c and FWHM) of the Si/glass and Si/YSZ/glass by the one-step method are labelled ① and ②, respectively, in Table 5.1. In the two-step method, two irradiation conditions were used, (A) and (B). For the condition (A), E_i = 18–22 mJ/cm^2 and E_g = 106–109 mJ/cm^2, which is the optimized condition for the Si/glass. The condition (B) is the optimized condition for the Si/YSZ/glass, which is E_i

Table 5.1 Crystalline fraction X_c and FWHM of c-Si peak of Si/glass and Si/YSZ/glass for the one-step and two-step methods. The two-step method has the two kinds of irradiation conditions (A) and (B).

Method		Irradiation conditions	Si/glass	Si/YSZ/glass
Conventional		E = 104 – 106 mJ/cm^2, N = 100	X_c = 79% ① FWHM = 8.1	X_c = 75% ② FWHM = 7.6
Two-step	(A)	E_i = 18 – 22 mJ/cm^2, N_i = 10 E_g = 106 – 109 mJ/cm^2, N_g = 90 (optimized for Si/glass)	X_c = 87% ③ FWHM = 6.0	X_c = 82% ④ FWHM = 6.1
	(B)	E_i = 20 – 24 mJ/cm^2, N_i = 10 E_g = 111 – 114 mJ/cm^2, N_g = 90 (optimized for Si/YSZ/glass)	—	X_c = 91% ⑤ FWHM = 5.2

= 20–24 mJ/cm^2 and E_g = 111–114 mJ/cm^2. The X_c and FWHM values of Si/glass and Si/YSZ/glass obtained under the condition (A) are labelled ③ and ④, respectively, in Table 5.1. The crystallinity of the Si/YSZ/glass obtained under the condition (B) is labelled ⑤ in Table 5.1. Both the optimized E_i and E_g for Si/YSZ/glass are slightly higher than those for Si/glass. This is because the calculated absorptivity of the a-Si film in the a-Si/glass structure (~0.546) is higher than that in the a-Si/YSZ/glass structure (~0.445). A similar calculation result is obtained in the case of a poly-Si film, but the absorptivities of poly-Si films are much lower, i.e., ~0.075 and ~0.042 for the poly-Si/glass and poly-Si/YSZ/glass structures, respectively. (These calculations have been mentioned in chapter 4 and the detail is shown in Appendix L.) This means that, under the same irradiation condition, the Si film in Si/glass is heated more than that in Si/YSZ/glass. This suggests that, in order to compare these two structures fairly, we should examine Si films crystallized at their own optimized conditions. This will be carried out and discussed in detail later.

From the Table 5.1, first, it can be clearly seen that the crystalline quality of the crystallized Si films is more improved by the two-step method (③ and ④) for both the Si/glass and Si/YSZ/glass structures than by the one-step method (① and ②). That is, a higher X_c and a smaller FWHM are obtained by the two-step method despite using the same total pulse number and a lower total irradiation energy density E_t. The reason for the improvement in the crystallinity of the Si film on, for example, YSZ/glass, by the two-step method is discussed later using a growth model. Next, we compare the Si/YSZ/glass case ④ with the Si/glass case ③ in the two-step method. Although X_c = 82% for the Si/YSZ/glass is apparently smaller than 87% for the Si/glass, and the difference is more than the estimation error of ±2%, the FWHM for both is approximately 6.0 and is within the estimation error of ±0.5. This indicates that it is still possible to increase X_c and improve crystalline quality for Si/YSZ/glass by optimizing E. Actually, using the optimized irradiation condition for the Si/YSZ/glass in the two-step method, we obtain a higher X_c and a smaller FWHM in ⑤ than in ③ and ④. From these results, it can be concluded that a Si film with a higher crystalline quality can be obtained on YSZ/glass than on glass substrate for both the one-step and two-step methods, which may be due to the CI effect of the YSZ layer.

The actual Raman spectra of the samples in Table 5.1 are shown. Figures 5.4(a) show the He–Ne Raman spectra of the Si/glass and Si/YSZ/glass irradiated under the condition (A) of Table 5.1 by the two-step method. Figure 5.4(b) shows the spectrum of only the Si/YSZ/glass under its optimized condition of (B) in Table 5.1. It can be seen from Fig. 5.4(a) that the shoulder of the amorphous phase (denoted by the dotted circle) in the spectrum from the Si/glass is smaller than that in the spectrum from the Si/YSZ/glass, indicating the higher X_c. Moreover, the height and width of crystalline Si peaks are the same for both the structures, indicating the same FWHM. On the other hand, under the condition (B) for Si/YSZ/glass shown in Fig. 5.4(b), an obviously higher crystalline peak intensity with a much smaller a-Si phase shoulder can be observed, compared with those in Fig. 5.4(a).

To determine the effect of the two-step method clearly, by using SEM, we observed Secco-etched Si films crystallized by both the one-step and two-step methods. The images are shown in Fig. 5.5 and the used irradiation conditions are the same as those in Table 5.1. Figure 5.5(a) shows the SEM image of the Si film irradiated by the one-step method while Figs. 5.5(b)– 5.5(d) show those by the two-step method, where the sample structures are Si/YSZ/glass except for (b), i.e., Si/glass. The labels ②-⑤ in Fig. 5.5 correspond to the numbers or the same irradiation conditions in Table 5.1.

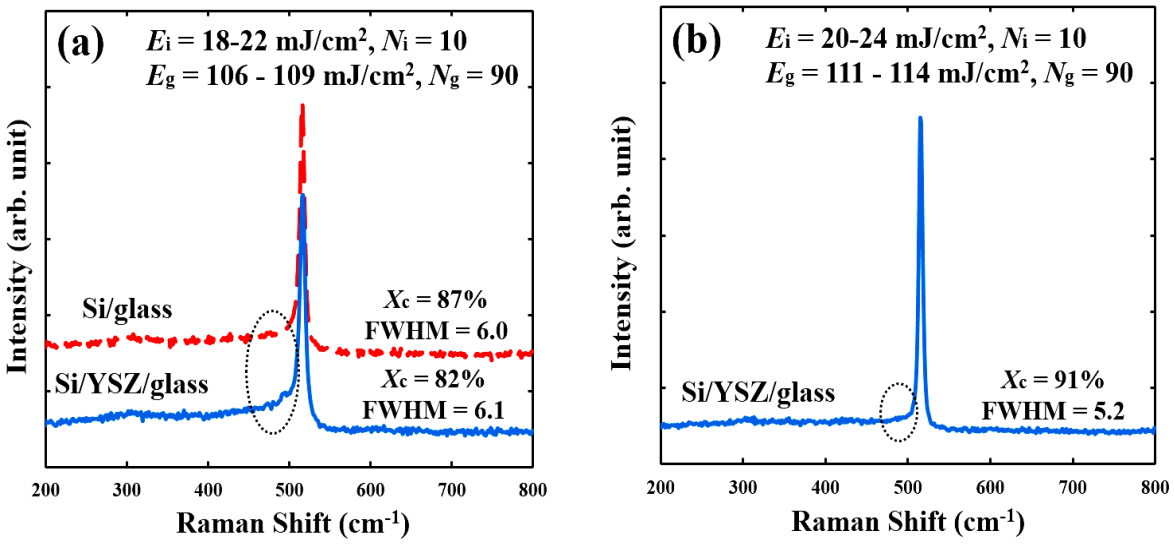

Fig. 5.4 He–Ne Raman spectra of (a) Si/glass and Si/YSZ/glass under the condition (A) of E_i = 18–22 mJ/cm^2 and E_g = 106–109 mJ/cm^2 and (b) Si/YSZ/glass under the condition (B) of E_i = 20–24 mJ/cm^2 and E_g = 111–114 mJ/cm^2. The shoulders of the a-Si phase are encircled.

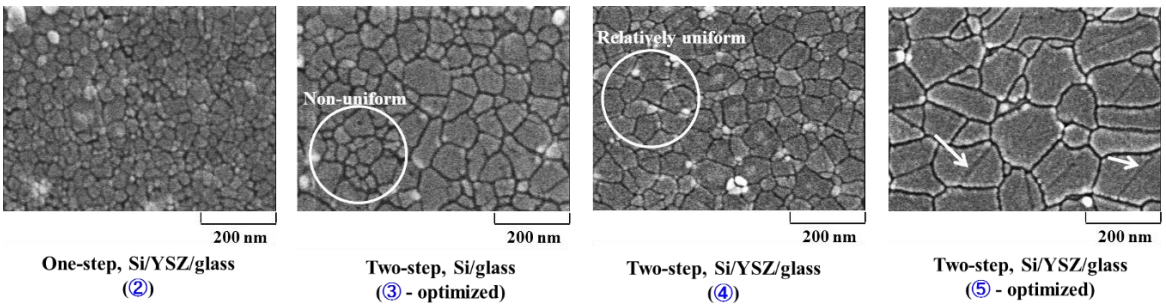

Fig. 5.5 SEM images of the Secco-etched Si films crystallized by the one-step and two-step methods. (a)–(d) irradiation conditions are the same as those indicated by ②-⑤ in Table 5.1, respectively. Note that the difference in grain size uniformity between (b) and (c) is encircled. Arrows in (d) indicate examples of twins on the film surface.

Firstly, from the comparison between Fig. 5.5(a) for the one-step method and Fig. 5.5(c) for the two-step method, it can be seen that large grains are obtained in the Si/YSZ/glass by the two-step method. This clearly indicates the effectiveness of the two-step method in promoting the crystallization of the a-Si film. Next, we compare the Si film on glass with that on YSZ in the two-step method under the same irradiation conditions, as shown in Figs. 5.5(b) and 5.5(c), respectively. It can be found easily that the difference in grain size or grain size nonuniformity is larger in the Si/glass than in the Si/YSZ/glass, for instance, as shown by circles in Figs. 5.5(b) and 5.5(c). For the Si/YSZ/glass irradiated under its optimized conditions as shown in Fig. (d), the grain size apparently becomes larger than that for the Si/glass under its optimized irradiation conditions [Fig. 5.5(b)]. This can be explained as follows:

In the initial stage at the low energy density E_i and small pulse number N_i for each structure, the Si nucleation only occurs at the interface between the Si film and the underlayer (SiO_2 or YSZ) for both the structures. However, in the Si/glass, random Si nucleation occurs at the interface owing to the lack of crystallographic information on the glass substrate. On the other hand, in the Si/YSZ/glass, owing to the CI effect of the YSZ layer, uniform nucleation may occur at the YSZ interface. With the higher energy density E_g and larger pulse number N_g in the growth stage, for the Si/glass, the direction and rate of crystallization growth from the individual nucleus are not uniform due to the random nucleation. Also, since the nonuniform crystallization growth prevents a smooth crystallization process, bulk nucleation might occur before the completion of

crystallization. On the other hand, for the Si/YSZ/glass, crystallization proceeds from the interface more smoothly owing to the formation of interface nuclei induced promptly by the YSZ. Therefore, the grains in the Si/YSZ/glass have larger and more uniform sizes than those in Si/glass.

By carefully analyzing Fig. 5.5(d), some twins can be observed as straight lines along the Si film surface, some of which are indicated by arrows inside. It is reported that the typical deformation twinning mode in diamond-type crystals is {111}/⟨112⟩, which is the major defect mode observed in a stressed crystal.[102)] If it is assumed that the twins observed in Fig. 5.4(d) are due to the {111}/⟨112⟩ mode, the surface orientation of the Si film might be (110).

5.5 Crystallization growth models of Si films on YSZ CI layers

On the basis of the aforementioned experimental results and discussion, we discuss a growth model for the Si film crystallization on the YSZ layer for the one-step and two-step methods, as shown in Fig. 5.6. In the one-step method at a high energy density E [Fig. 5.6(a)], although crystallization from the interface nuclei is more preferable than that from the bulk of the Si film owing to the YSZ layer, crystallization growth from the interface is impeded by the bulk random nucleation and growth. This might be due to the high nucleus density at a high E and the lack of ordered crystallographic information in the bulk of the a-Si film. On the other hand, in the two-step method in Fig. 5.6(b), nucleation preferably occurs in the a-Si film only on the YSZ layer surface with the suppression of bulk nucleation in the initial stage with a low E_i. Then, in the growth stage with a high E_g, crystallization from the interface nuclei proceeds in a cone shape at a high rate toward the surface. Therefore, the Si film crystallized by the two-step method has a higher X_c and a much smaller FWHM as well as a larger grain size than that by the one-step method, as shown in Table 5.1 and Fig. 5.5.

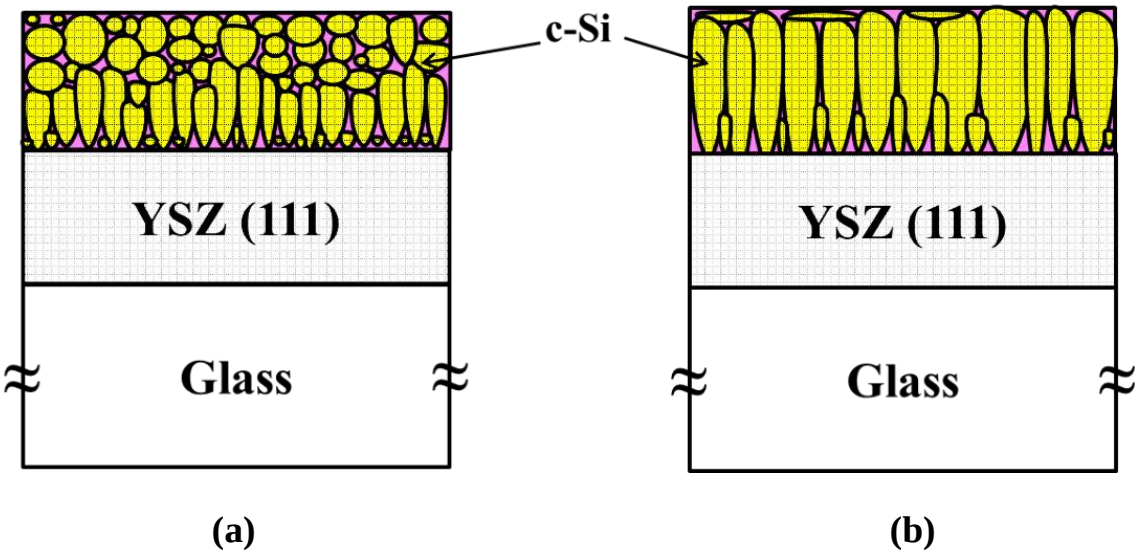

Fig. 5.6 Si film crystallization growth models of Si/YSZ/glass for the (a) one-step and (b) two-step methods.

5.6 Three-step irradiation method for further improvement of crystalline quality

5.6.1 Irradiation condition of a three-step method

In the previous sections, the two-step method can produce the better crystalline quality of the Si film than that by one-step method. Since the difference in energy density between the initial and growth stages of the two-step method seems quite large, we proposed a three-step method for further improving crystalline quality of the Si film, in which a middle energy density is used in addition to the initial and growth energy densities in the two-step method. The irradiation process is shown in Fig. 5.7. Firstly, an a-Si film is irradiated at a low energy density E_i to generate nuclei only at the interface between Si and underlayer. Next, in the second step, the Si film continues to be irradiated at a middle energy density E_m to slightly accelerate the growth of nuclei at the interface. Finally, it is irradiated at a high energy density E_g to speed up the nuclei growth and film crystallization. The initial and growth irradiation energy densities are taken as the optimum values for the Si/glass, i.e., E_i = 18–22 mJ/cm^2 and E_g = 106–109 mJ/cm^2. There are two possible values of middle energy density E_m, which are 46–48 and 78–80 mJ/cm^2, considering the results of Fig. 4.8 in chapter 4. If E_m is a smaller value than 46 mJ/cm^2, the

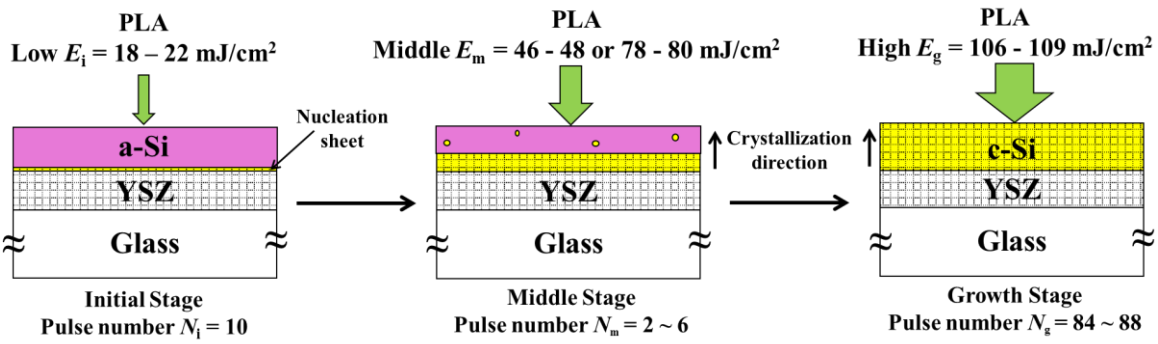

Fig. 5.7 Schematic illustrations of crystallization in Si/YSZ/glass for the three-step method together with the irradiation condition.

crystallization growth of nuclei from the interface is not accelerated much for a small middle pulse number (N_m) and the crystalline quality seems to be the same with the two-step method. On the other hand, if E_m is larger than 80 mJ/cm^2, bulk crystallization will impede crystallization growth from the interface crystallization. The initial pulse number N_i is kept constant at 10 while the middle N_m and growth N_g pulse numbers are changed so as to $N = N_i + N_m + N_g = 100$ (fixed). From Fig. 4.8 in chapter 4, it was found that X_c in both the E_m cases (46–48 and 78–80 mJ/cm^2) become saturate even with small pulse number (N = 10). In order to perform the annealing effectively by means of avoiding too much irradiation in the saturation region of X_c, N_m should be smaller than 10. Under this condition, E_m and N_m are optimized for the three-step method in the next section.

5.6.2 Middle pulse number N_m and middle energy density E_m dependences of film quality

Figures 5.8(a) and (b) show the middle pulse number N_m dependences of crystalline fraction X_c and intermediate-crystalline fraction X_m for the two samples irradiated with the middle energy density E_m of 46–48 and 78–80 mJ/cm^2, respectively. X_c and X_m are in turn determined by $X_c = (I_m+I_c)/(I_m + I_c + I_a)$ and $X_m = I_m/(I_m + I_c + I_a)$, where I_c, I_m, and I_a are integrated intensities of c-Si, m-Si, and a-Si peaks, respectively. Figures 5.9(a) and (b) show the middle pulse number N_m dependences of FWHM and position of c-Si peak for the two samples irradiated with the middle energy density E_m of 46–48 and 78–80 mJ/cm^2, respectively. These results are obtained from He-Ne Raman spectroscopy measurement. Other parameters of E_i, E_g, and N_i are the same for both the samples and shown in the inset of each figure. The middle pulse number N_m and growth pulse number N_g are changed

from 2 to 6 and 88 to 84, respectively. For comparison, data of the two-step method are shown at N_i = 10 and N_g = 90 (i.e., N_m = 0).

Firstly, the results for the two conditions of E_m are discussed. In general, it can be seen from Figs. 5.8(a) and (b) that the crystalline fractions X_cs are a little improved with N_m whereas the crystalline fractions X_ms are almost unchanged for two structures of Si/glass and Si/YSZ/glass in both the cases of E_m. The FWHM and position of c-Si peak in Fig. 5.9(a) and (b) are almost the same within the error bars of ± 0.5 and ± 1, respectively, for both the structures of Si/glass and Si/YSZ/glass in both the cases of E_m. Among three

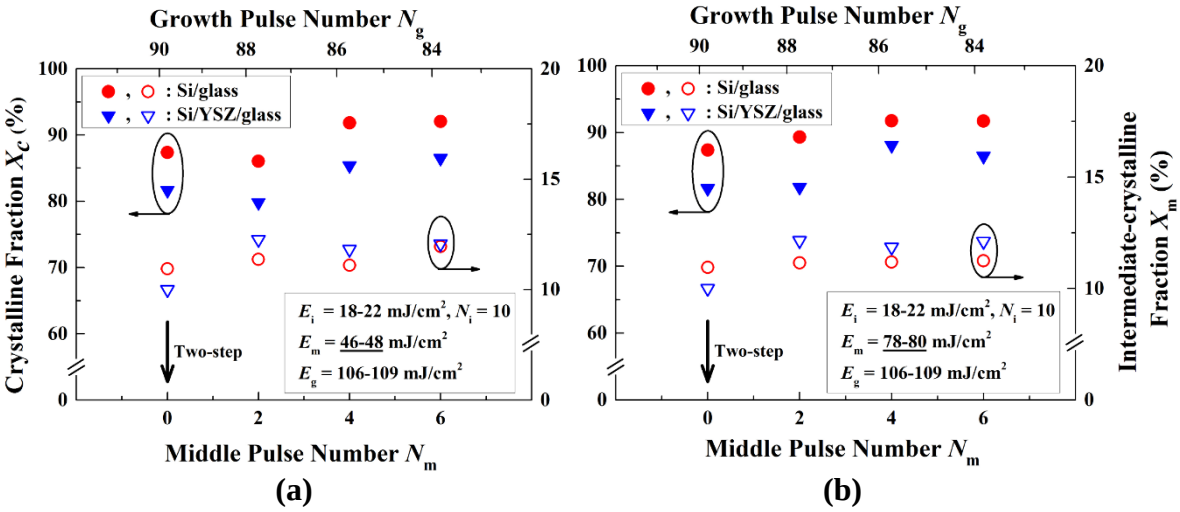

Fig. 5.8 Middle pulse number N_m dependences of crystalline fraction X_c and intermediate-crystalline fraction X_m for two samples irradiated with middle energy density E_m of (a) 46–48 and (b) 78–80 mJ/cm^2.

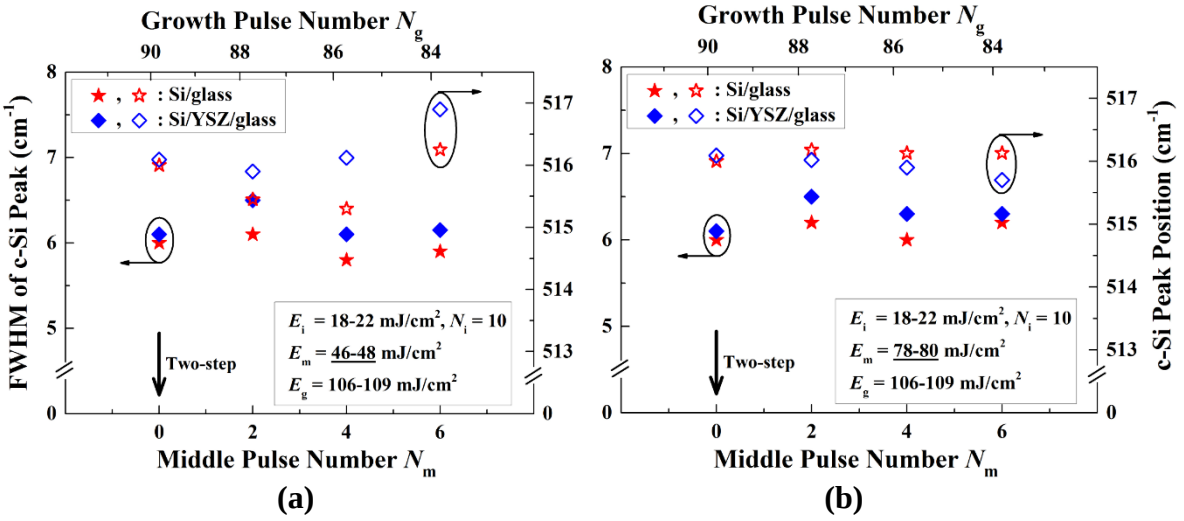

Fig. 5.9 Middle pulse number N_m dependences of FWHM and position of c-Si peak for two samples irradiated with middle energy density E_m of (a) 46–48 and (b) 78–80 mJ/cm^2.

investigated values of N_m in the three-step method (i.e., 2, 4, and 6), $N_m = 6$ is considered to be the optimized value due to its highest crystalline fraction X_c and relatively good quality. However, from these results, it is seen that there is no difference between the two conditions of E_m.

Next, we compare results of the three-step method at $N_m = 6$ for the both cases of E_m (46–48 and 78–80 mJ/cm^2) and those of the two-step method ($N_m = 0$). Although X_cs of the three-step method are higher than those of the two-step method, the film quality (indicated by X_ms, FWHM, and c-Si peak position) of the former seems to be not improved, compared with the latter. Considering the mass production, the two-step method is more suitable than the three-step method. Therefore, in the next investigations, we use the two-step method for annealing a-Si films.

5.7 Expansion of crystallization area by the two-step method

5.7.1 Setup of annealing system

After obtaining the optimum irradiation condition for the two-step method as mentioned in the previous sections, we apply it to expand the crystallization area. The schematic illustration for the expansion experiment is shown in Fig. 5.10, in which the total crystallized area is 10×20 mm^2. The optical line of a 4-mm-diameter laser beam is fixed while the sample is moved during the irradiation by a stage controller with a stepping motor, where the moving speed v is 1 mm/s and the moving step distance per one shot is 100 μm. In this experiment, the initial energy P_i and growth energy P_g are set 6.3 and 15 mJ/pulse, respectively, which correspond to the optimized energy densities in the static case without sample moving for the Si/YSZ/glass structure. However, for expansion of crystallization area to keep crystallized film quality uniformly, a sample should be annealed with the initial energy P_i three times, then it is annealed with growth energy P_g three times for each scanning line as shown in Fig. 5. 10. The detailed investigation for optimizing irradiation condition will be mentioned in the next sub-section. For comparison, samples are also irradiated by the one-step method with a fixed high energy of P_g.

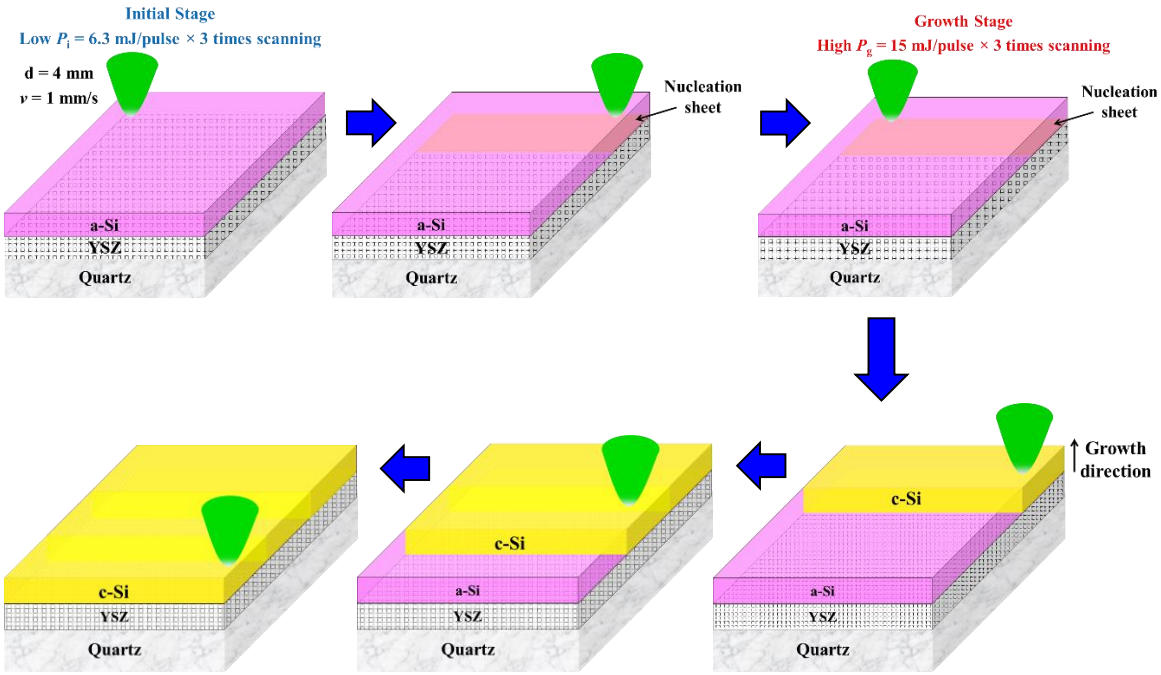

Fig. 5.10 Schematic illustration for expansion of crystallization area by moving the sample stage during irradiation with the moving speed *v* of 1 mm/s.

5.7.2 Optimization of scanning conditions

When, for area expansion, we used the optimized irradiation condition of the static case without sample moving, we had a trouble of non-uniformity in crystallization degree of the scanned area. This is because the beam pattern is not uniform as shown in Fig. 3.8 of chapter 3. Since uniformity of crystallization degree is one of the most important requirements for device application, it should be as high as possible. Figure 5.11 shows the schematic illustration of scanning condition together with an actual laser beam profile, in which a sample is scanned at P_i = 6.3 mJ/pulse only **one time**, followed by the **one-time** scanning at P_g = 15 mJ/pulse. The actual beam profile in Fig. 5.11(b) seems to be non-uniform, in which a whiter region is irradiated at a higher laser energy density. However, it is difficult to determine the non-uniformity degree from the color framework of the actual beam profile. In order to identify the uniformity degree more clearly, this beam profile is changed into another color framework using the *Image J* software. The analyzed results are shown in Fig. 5.12. It can be seen from Fig. 5.12 that the analyzed laser beam intensity distribution is non-uniform on the whole of the scanned area. In order to homogenize the laser beam intensity on the scanned area, we tried to double and triple scannings for both

initial and growth stages. The schematic illustration of scanning condition and analyzed laser beam profiles of double and triple scannings are shown in Figs. 5.13 and 5.14, respectively.

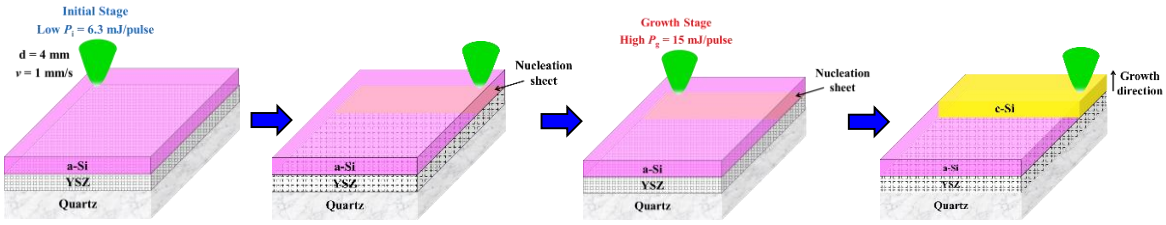

(a)

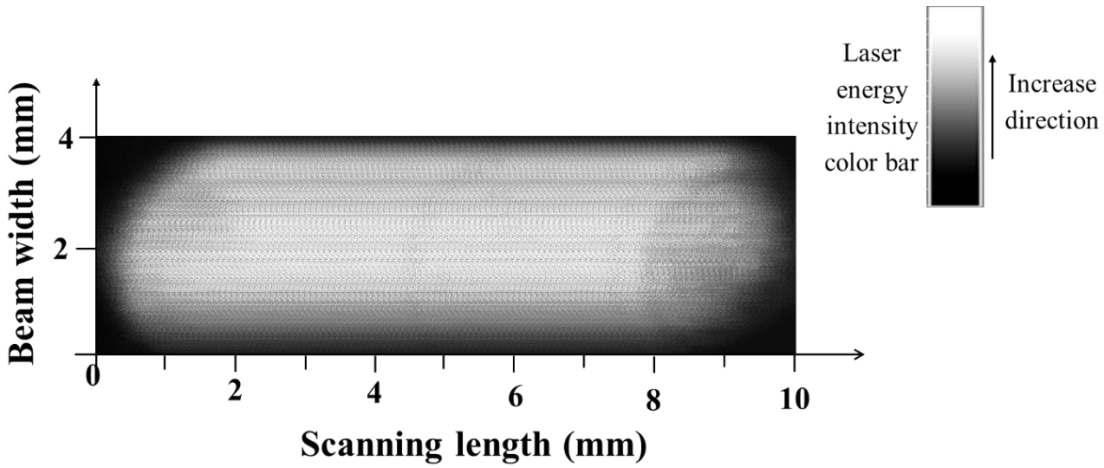

(b)

Fig. 5.11 (a) Schematic illustration of scanning condition of P_i = 6.3 mJ/pulse only one time, followed by the one-time scanning at P_g = 15 mJ/pulse, and (b) an actual laser beam profile.

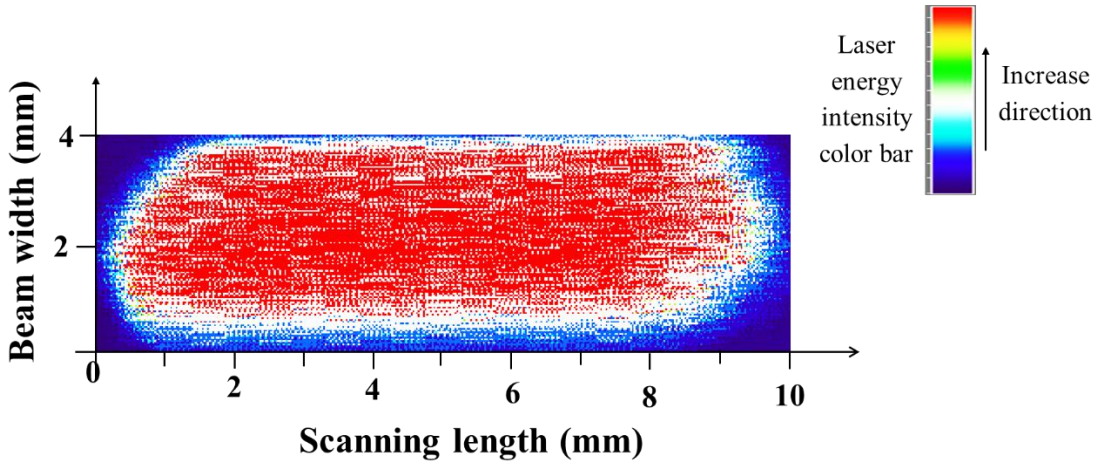

Fig. 5.12 Analyzed profile of the actual laser beam in Fig. 5.11(b).

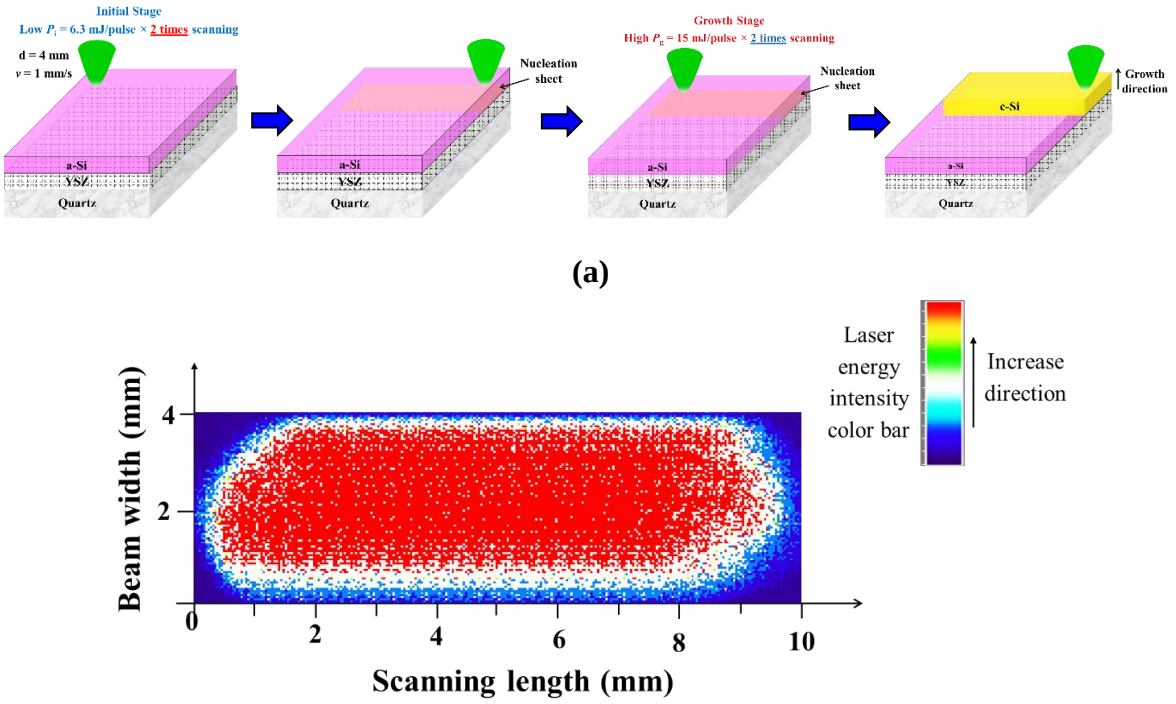

Fig. 5.13 **(a) Schematic illustration of scanning condition of P_i = 6.3 mJ/pulse × 2 times scanning, followed by P_g = 15 mJ/pulse × 2 times scanning, and (b) an analyzed laser beam profile.**

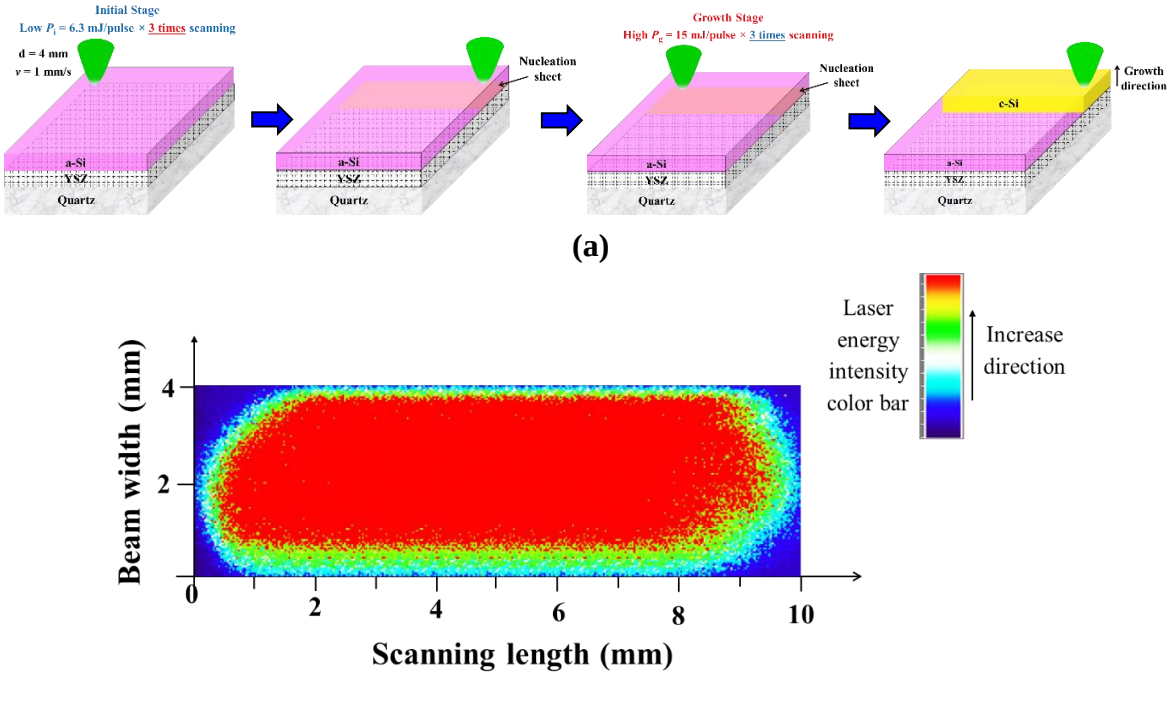

Fig. 5.14 **(a) Schematic illustration of scanning condition of P_i = 6.3 mJ/pulse × 3 times scanning, followed by P_g = 15 mJ/pulse × 3 times scanning, and (b) an analyzed laser beam profile.**

Comparing Figs. 5.14(b) with 5.13(b), it is found that the distribution of laser beam intensity on the scanned area for the former is more uniform than for the latter, except border region. Therefore, the scanning condition of P_i = 6.3 mJ/pulse × 3 times scanning, followed by P_g = 15 mJ/pulse × 3 times scanning seems to be more suitable for expansion of crystallization area. In order to apply this condition for the next experiments, we crystallized a test sample of a-Si/YSZ/glass and observed the sample morphology after crystallization by optical microscopy. Its optical microscope image is shown in Fig. 5.15. It can be seen that the morphology is quite uniform and smooth, which suggests that the sample is crystallized in solid phase without melting.

Fig. 5.15 Optical microscope image of the test Si/YSZ/glass sample irradiated by the two-step method under condition of P_i = 6.3 mJ/pulse × 3 times scanning, followed by P_g = 15 mJ/pulse × 3 times scanning.

5.8 Crystalline quality of the crystallized Si film on expanded area

Figure 5.16 shows the comparison of the He-Cd Raman spectra of localized regions of the crystallized Si films on the expanded area between the one-step (with a fixed beam energy) and two-step methods. It can be seen that Raman intensities from the front side and back side measurements are the same for the one-step method, indicating the surface and interface crystallizations occur simultaneously as well as in film bulk without preference. On the other hand, in the two-step method, higher Raman intensities with smaller shoulders of a-Si phase (denoted by the dash circles) can be seen from the both front and back side measurements, compared with those of the one-step method. This result indicates

that crystallinity of the Si films is improved by the two-step method in the case of moving during irradiation as well as non-sample moving or static irradiation. Moreover, in the two-step method, the Raman intensity obtained from the back side measurement is about twice higher with a smaller shoulder of a-Si phase, indicating the smaller FWHM of c-Si peak and higher crystalline fraction than those from the front side. It is considered that the interface crystallization in the two-step method proceeds better than the surface crystallization.

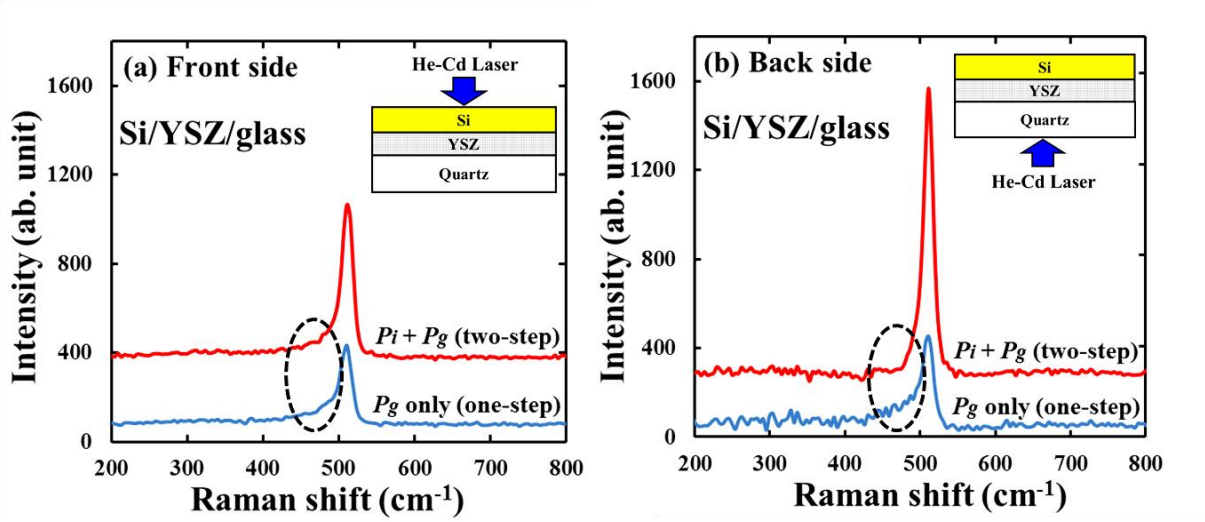

Fig. 5.16 He-Cd Raman spectra of the Si/YSZ/glass for the one-step and two-step methods from (a) the front side and (b) the back side measurements under the sample-moving condition of Fig. 5.10.

Since the thickness of the Si film is thin (~ 60 nm) and the grain size is small and roughly less than 200 nm, it was found that estimation of its crystallinity by X-ray diffraction technique was difficult. Therefore, we used RHEED technique to observe the surface crystalline structure of the Si films. Figures 5.17(a), (b), (c), and (d) show the RHEED patterns of the bare YSZ layer on the glass substrate, a-Si film on the YSZ/glass, crystallized Si film on the YSZ/glass, and crystallized Si film on the glass, respectively. The Si films were crystallized by the two-step method under sample-moving condition of Fig. 5.10. All of these patterns were observed at room temperature. Figure 5.17(a) is the same with RHEED pattern in Fig. 4.1 of chapter 4, which shows the uniaxially (111)-oriented YSZ layer. The spotty patterns disappear after deposition of the a-Si film as shown in Fig. 5.17(b), which suggests that the deposited Si film is in amorphous phase completely. On the other hand, in Figs. 5.17(c) and 5.17(d), after crystallization of the a-Si

films, the spotty patterns reappear, which confirms the crystallization of a-Si films. Moreover, the spotty patterns in Fig. 5.17(c) are more clear than in Fig. 5.17(d) and similar to those of the bare YSZ layer in Fig. 5.17(a). From this result, it can be inferred that the (111)-preferential orientation of the YSZ is transferred into the crystallized Si film, thanks to the crystallization-induction effect of the YSZ.

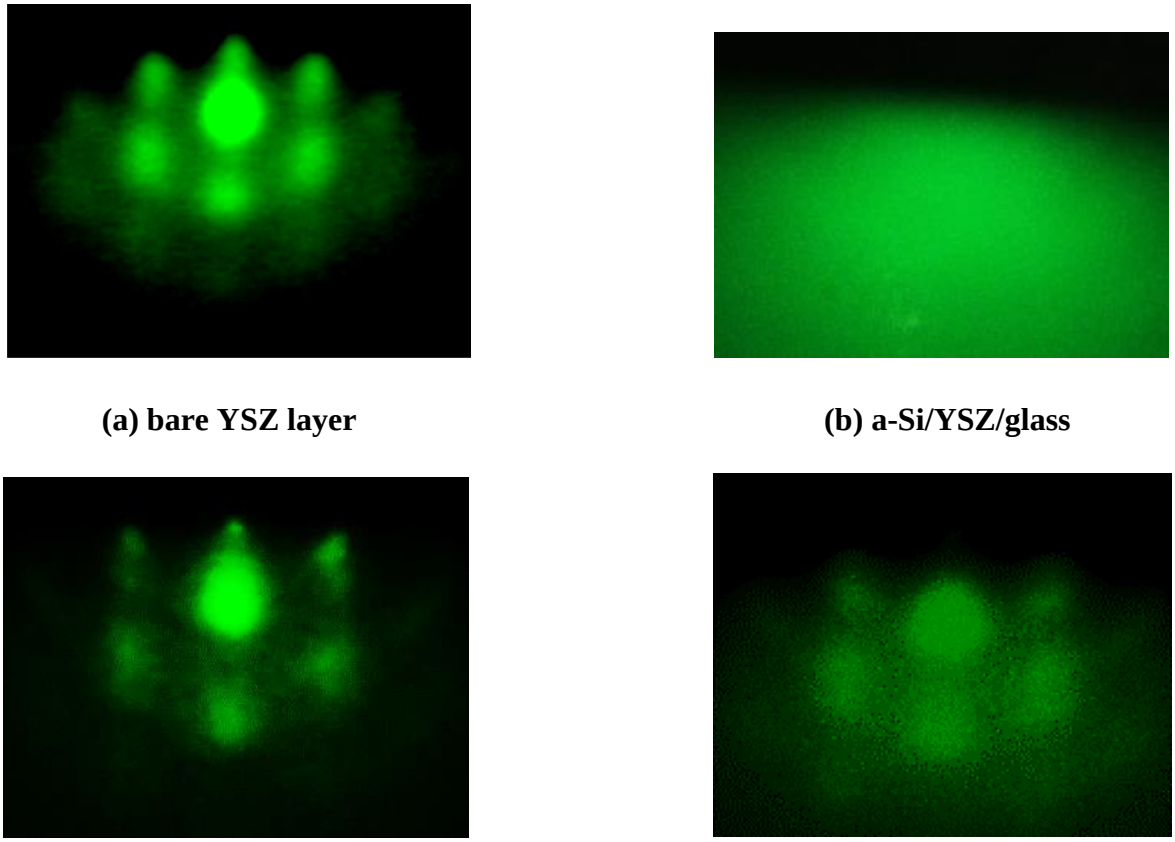

(a) bare YSZ layer **(b) a-Si/YSZ/glass**

(c) crystallized Si/YSZ/glass **(d) crystallized Si/glass**

Fig. 5.17 RHEED patterns of the bare (a) YSZ layer on the glass substrate, (b) 60-nm-thick a-Si film on the YSZ/glass, (c) 60-nm-thick crystallized Si film on the YSZ/glass, and (d) 60-nm-thick crystallized Si film on the glass at room temperature.

Figures 5.18(a) and (b) show the cross-sectional low-resolution and high-resolution (HR-) TEM images, respectively, of the Si film on the YSZ/glass crystallized by the two-step method under the sample-moving condition of Fig. 5.10. The HR-TEM image in Fig. 5.18(b) shows a close-up image of one area around the interface. This also shows the electron-diffraction (ED) patterns simulated by using the fast Fourier transform (FFT) based on the local lattice images enclosed by white (labeled as points 1 and 3) and black

(labeled as points 2 and 4) square frames in the YSZ layer and the crystallized Si film, respectively. It can be seen from Fig. 5.18(a) that the crystallized Si film has a smooth surface, which is probably due to non-intentionally melting crystallization of the Si film,

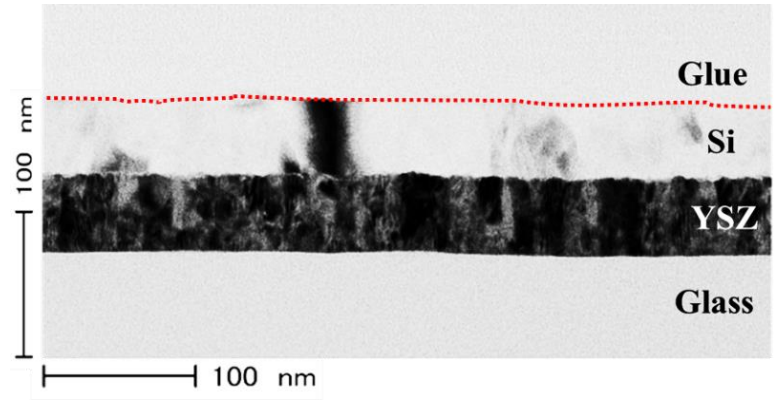

(a)

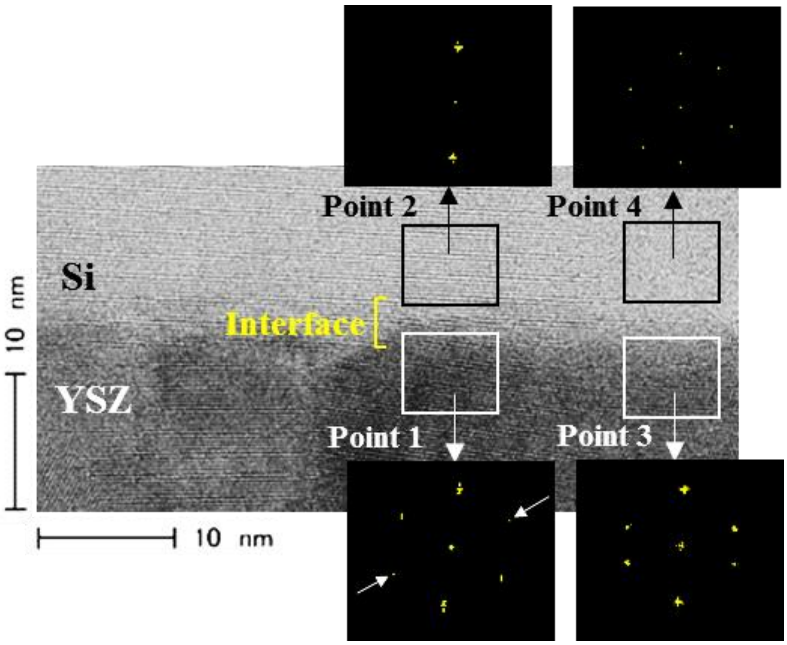

(b)

Fig. 5.18 Cross-sectional TEM images of the Si film on the YSZ/glass crystallized by the two-step method, where (a) is in low resolution and (b) is in high resolution (HR). The HR-TEM image (b) shows a close-up image around the interface in (a). The electron-diffraction patterns simulated based on the local lattice images enclosed by the white (points 1 and 3) and black (points 2 and 4) square frames for the YSZ layer and the crystallized Si film, respectively, are also shown.

compared with the direct deposited Si film at 430 °C[103] and melting crystallized Si film by excimer pulsed laser.[104] Further, incubation layer near the YSZ layer interface is hardly observed, suggesting that crystallization of the Si film grows directly from the YSZ layer without an amorphous transition region. This is confirmed by the HR-image in Fig. 5.18(b). All spots in the ED patterns of the YSZ layer (points 1 and 3) and the Si film (points 2 and 4) correspond to {111} planes, except for the two spots of YSZ {200} indicated by white arrows. From these patterns, the crystallographic orientation normal to the interface can be identified as <111>, which is the preferential orientation of the YSZ layer. From this result, it can be considered as follows: Nucleation at the YSZ interface is stimulated by the CI effect of the YSZ layer, and then crystallization of the amorphous region around the nuclei occurs and progresses up to the surface smoothly. The slight roughness at the interface is just localized and due to the surface roughness of the YSZ layer.

The impurities in the Si film were measured by SIMS. Figure 5.19 shows the concentration depth profiles of Zr and Y in the 50-nm-thick Si film, which was crystallized by the two-step method with sample moving on the YSZ/glass substrate. Since the quantitative concentrations were estimated by using a standard sample of an ion-implanted Si, only the concentrations in the Si film are valid. The concentrations near the interface

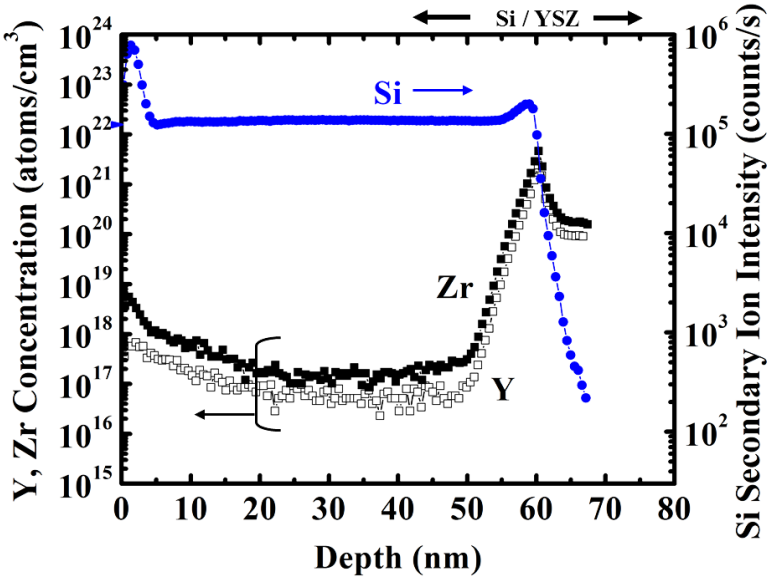

Fig. 5.19 Concentration depth profiles of Zr and Y in the crystallized Si/YSZ/glass by two-step method with sample moving. They were measured by SIMS. As a reference, the Si secondary ion intensity is shown.

and in the YSZ layer are incorrect because of the so-called matrix and charge-up effects due to the insulator of YSZ. [105] It can be seen that Zr atoms diffuse into the crystallized Si film slightly. The Zr concentration at the Si/YSZ interface is about 3×10^{17} atoms/cm^3 and slightly increases towards the surface of the Si. The Zr concentration at the Si/YSZ interface in this work is about one order smaller than that in the direct deposited Si film at 430 ^{o}C (about 5×10^{18} atoms/cm^3).[103] This shows the effectiveness of the two-step method using pulsed laser in suppression of Zr diffusion into the Si film. The Y concentration at the Si/YSZ interface is about 9×10^{16} atoms/cm^3, which is about three times lower than that of Zr, and also slightly increases towards the surface of the Si. It has been reported that, in the application of a gate insulator, Zr atoms from the ZrO_2 film hardly diffuse into Si even at 700 ^{o}C for 5min annealing.[106] The diffusion of Y from Y_2O_3 gate oxide into the Si film also does not occur at annealing temperature $\leq$ 800 ^{o}C for 2 min.[107] In our case, a certain amounts of chemically unstable Zr and Y due to HF dipping might remain on the YSZ surface before the Si film deposition. Although it is supposed that the subsequent crystallization by the pulsed laser is performed at temperature less than the melting temperature of a-Si – 1420 K or 1147 ^{o}C,[108] it maybe induce the diffusion of Zr and Y into the Si film even for a very short irradiation time. From this result, we can consider that the diffusion of Zr and Y into the crystallized Si film from the YSZ layer is small, but they should be further suppressed for device application.

5.9 Summary

From the results of the one-step method mentioned in chapter 4, we proposed the two-step method to further improve the crystallinity of the Si films, and crystallized a-Si films on YSZ CI layers by the two-step method with PLA without intentional melting. Their properties were investigated and compared with those obtained by the one-step method, using Raman spectroscopies and SEM. The obtained results are mentioned as follows: The crystallization growth from the YSZ interface is more enhanced by the two-step method than by the one-step method. The Raman analysis and SEM observation show that a high X_c, a small FWHM, and a large grain size were obtained by the two-step method compared with the one-step method at the same total pulse number N and lower total irradiation energy density E_t. Comparing the two structures of Si/YSZ/glass and Si/glass at their own optimized irradiation conditions, we obtained a higher X_c and a smaller FWHM in the

former. From these results, it can be concluded that the crystalline quality of Si films is much improved by the two-step method with the YSZ CI layer in PLA.

On the basic of the obtained optimum irradiation condition for the two-step method, we also proposed a three-step method for further improving crystalline quality of the Si film. Although crystalline fraction of the Si films obtained by the three-step method are a little higher than those of the two-step method, the film quality of the former seems to be not improved in comparison with the latter. Considering the mass production, the three-step method is not suitable. Therefore, we decided to use the two-step method for next investigations.

By applying the two-step method, the pulsed-laser crystallized a-Si films on YSZ CI layers were obtained successfully without intentionally melting under the crystallization condition for area expansion. Their film crystalline quality was investigated and compared with those of the one-step method. The results of the He-Cd Raman spectroscopy confirmed that the crystallinity of the Si films is improved by the two-step method in the case of the sample moving during the irradiation as well as the static case. Furthermore, it was found from the RHEED measurement that the (111)-preferential orientation of the YSZ was transferred into the crystallized Si film, thanks to the CI effect of the YSZ. The TEM observation showed the smooth surface of the crystallized Si film and no incubation layer at the interface. From these results, it can be expected that uniform crystalline quality of the Si film is obtained on the YSZ layer by the two-step method. SIMS results reveals that the diffusion of Zr and Y from the YSZ layer into the crystallized Si film is as small as or lower than the order of 10^{17} atoms/cm^3. However, these impurities should be further suppressed for device application.

Chapter 6:

Effect of Metal Films on Enhancing Crystalline Quality of Si Films

6.1 Sample structure for investigation

When Si films crystallized on the YSZ crystallization-induction (CI) layer by PLA method are used for TFT fabrication, it is better to use the YSZ layer as a gate insulator. To do this, a gate electrode layer must be deposited on a glass substrate, followed by a YSZ−CI layer. In this chapter, we investigate the effect of metal layer on crystalline quality of YSZ and Si films and whether our film structure is suitable for bottom-gate TFT fabrication or not. The sample structure for investigating is shown in Fig. 6.1. The fabrication process is the same with that of section 3.1 in chapter 3, except the deposition of the metal layer. A triple-layered structure of 30-nm SiN_x/30-nm W/30-nm Ti is formed on a cleaned quartz substrate prior to deposition of a 120-nm YSZ CI layer. The process sequence of the metal film deposition is shown in Fig. 6.2. Before metal films deposition, the substrate holder is heated and kept at 100 ^oC. A cleaned quartz substrate is loaded into the deposition chamber, which is evacuated to less than $2x10^{-4}$ Pa prior to depositing the films. Before each film deposition, the pre-sputtering process is conducted for 5 min in order to remove the contaminants from the previous sputtering process. Next, a Ti film is deposited by RF reactive sputtering with Ar gas, using a Ti metallic target with 2-inch-

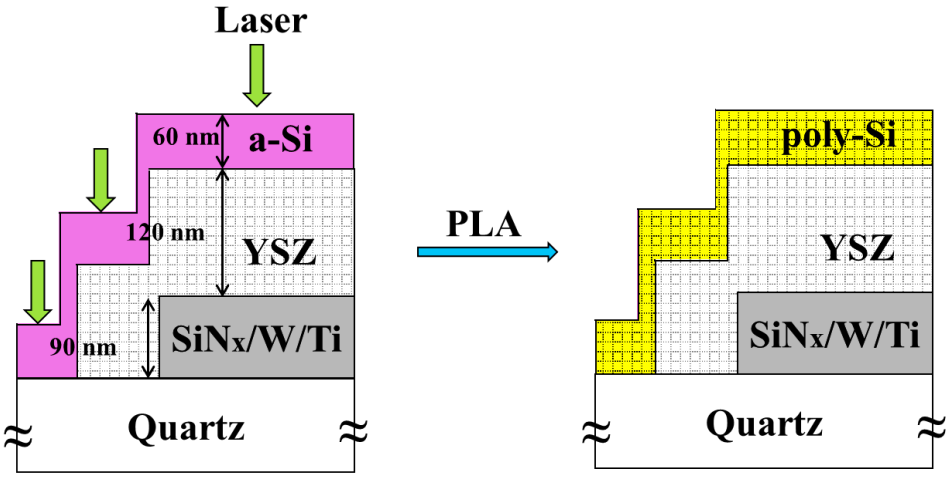

Fig. 6.1 Cross-sectional illustration of the fabricated sample structure of Si/YSZ/SiN_x/W/Ti/glass.

diameter. After the pre-sputtering, a W film is deposited on the Ti/glass substrate by RF reactive sputtering with Ar gas, using a W metallic target with 2-inch-diameter. Subsequently, a SiN_x film is deposited on the W/Ti/glass substrate by RF reactive sputtering, using a Si_3N_4 target with 2-inch-diameter in reactive N_2−Ar atmosphere. The deposition conditions of Ti, W, and SiN_x films are listed in Table 6.1.

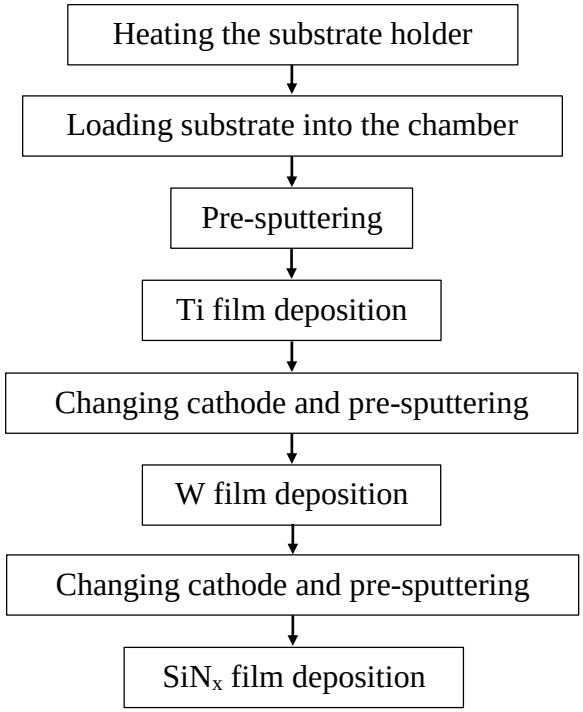

Fig. 6.2 Metal films deposition process sequence.

Table 6.1 Sputtering deposition conditions of Ti, W, and SiN_x films.

	Ti	W	SiN_x
Target	Ti metal (2 in.-ϕ)	W metal (2 in.-ϕ)	Si_3N_4 compound (2 in.-ϕ)
Target purity	99.9%	99.99%	99.99%
Substrate temperature (^oC)	100	100	100
RF power (W)	40	40	50
Gas flow (sccm)	Ar = 3.8	Ar = 3.8	Ar = 3.8, N_2 = 0.5
Gas pressure (Pa)	1.5	1.5	3.0
Thickness (nm)	30	30	30

W and its compounds are widely used as an electrode in fabrication of TFT due to its chemical stability and high conductivity.[109,110] However, the adhesion of W on glass substrate is very poor because of their different expansion coefficients. Therefore, prior to depositing a W film, it is needed to deposit a Ti layer whose role is increasing the adhesion of W on the substrate. Ti is an active metal, which is easily reacted with oxygen atoms at a surface of glass SiO_2 substrate to form titanium dioxide (TiO_2). TiO_2 is the strong and stable chemical bond, thus, it enhances the adhesion. Although deposition of the metal films are performed in clean room, there are a small amount of contaminants adsorbed on a surface of glass substrate during the transportation from cleaning space to the RF sputtering system. After metal films deposition, these contaminants are easily removed by mechanical cleaning process in ultrasonic together with W, so an insulator film of SiN_x is deposited to cover surface of the W to protect it from removal.

6.2 Pulse number *N* dependence of crystalline fraction by the one-step or conventional method

First, results obtained from the He-Ne Raman spectroscopy measurement of the one-step annealing are shown as a basic annealing information. Figures 6.3(a) and (b) show the dependences of crystalline fraction X_c and the FWHM of the c-Si peak, respectively, on the pulse number N for the **Si/YSZ/SiN_x/W/Ti/glass** structure (hereafter **Si/YSZ/metal/glass** for simplicity), where the energy density E is a parameter. The results of the Si/glass and Si/YSZ/glass, which were discussed in chapter 4, are also shown as references for comparison. It can be seen from Fig. 6.3(a) that increasing N (or annealing time) makes X_cs

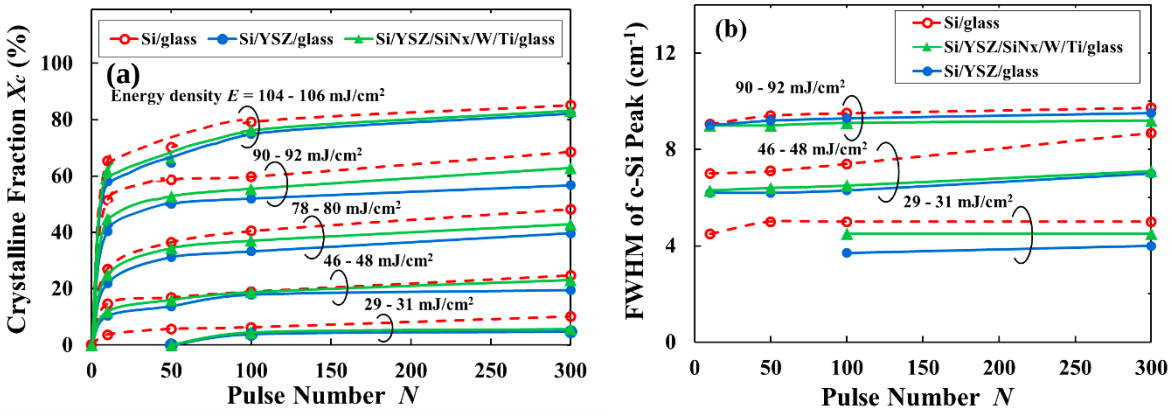

Fig. 6.3 Dependences of (a) crystalline fraction X_c and (b) c-Si peak FWHM on the pulse number N. The energy density E is the parameter.

of Si films increase for all structures. At the high energy density E, X_c increases rapidly and saturates even with the small N, which indicates bulk nucleation and growth for all structures. X_c of the Si films on the glass substrates are found to be higher, indicating faster crystallization, than those on YSZ/glass and YSZ/metal/glass at the same E and N. This is because optical absorption in Si film for the former is larger than those for the two latters as mentioned in chapter 4. The X_c of Si/YSZ/metal/glass is a little higher than that of Si/YSZ/glass. This is probably due to the metal film, which absorbs optical energy of the laser beam, so that temperature of the Si film is a little higher than that in the Si/YSZ/glass. The detailed derivation of absorptivity for the Si/YSZ/metal/glass structure is described in Appendix F.

In Fig. 6.3 (b), the behavior of FWHM for the Si/YSZ/metal/glass is the same with those of the Si/glass and Si/YSZ/glass, as mentioned at section 4.4 in chapter 4. This means, at the low E, the FWHM are small and almost the same for all the pulse numbers. However, by increasing E, the FWHM becomes larger and increases slightly with N. At the same N, the FWHMs of the Si/YSZ/metal/glass is nearly same with those of the Si/YSZ/glass and smaller than those of the Si/glass. This suggests the better crystalline quality of Si/YSZ/metal/glass than the Si/glass.

6.3 Improving crystalline quality of the Si film by the two-step method

6.3.1 Initial energy density E_i dependences of crystalline fraction and film quality

We applied the two-step method in order to further improve crystalline quality of the Si/YSZ/metal/glass. It was found that the growth energy density E_g of 108-112 mJ/cm^2 is the optimized value because it is close to but less than the critical melting energy density of the Si film on YSZ/metal/glass substrate. In the two-step method, since initial energy density E_i is a very important factor that controls the location of nucleus generation, we should optimize it by investigating the dependence of crystallization degree in the crystallized Si films on the E_i where E_g, N_i, and N_g are fixed at 108–112 mJ/cm^2, 10, and 90, respectively. Figure 6.4 shows the E_i dependences of crystalline fraction X_c and FWHM of c-Si peak for the **Si/YSZ/metal/glass**. The data of the Si/YSZ/glass at its optimized condition are also shown for comparison. It can be seen that, at E_i = 20–24 mJ/cm^2, X_c is maximum while FWHM of c-Si peak is minimum, suggesting the crystalline

quality is maximum. Comparing with the Si/YSZ/glass, the FWHM of the Si/YSZ/metal/glass is almost equal, indicating that the Si films crystallized on both the YSZ/glass and YSZ/metal/glass exhibit the same quality. However, X_c of the Si/YSZ/metal/glass is a little higher than that of the Si/YSZ/glass. This indicates the heating effect of metal layer on enhancing crystallization degree of the Si film.

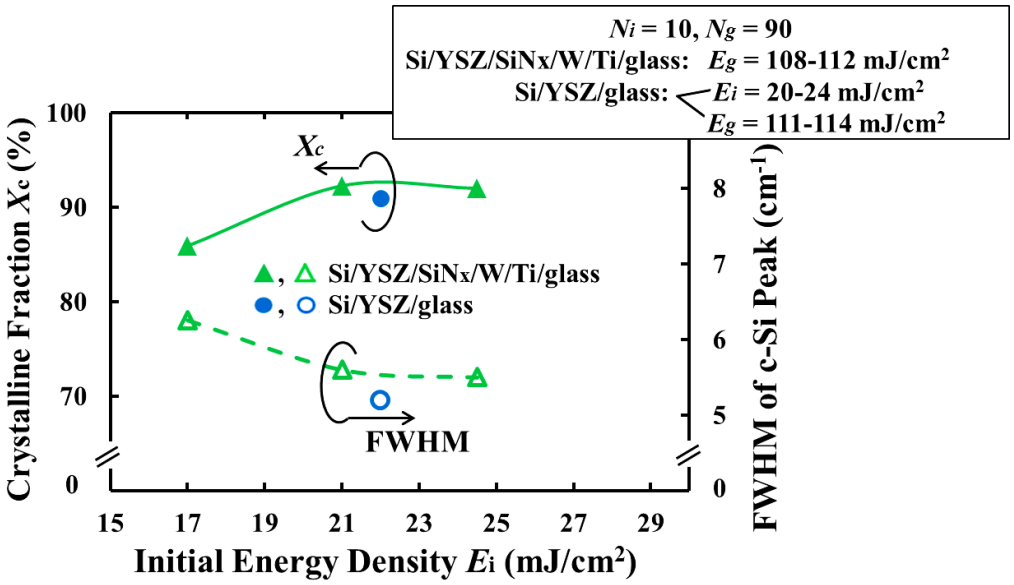

Fig. 6.4 Dependences of X_c and FWHM on E_i for the Si/YSZ/metal/glass by the two-step method. The data of Si/YSZ/glass at its optimized condition are shown for comparison.

6.3.2 Initial pulse number N_i dependences of crystalline fraction and film quality

It has been determined that the optimized energy densities for initial and growth stages of the two-step method for the Si/YSZ/metal/glass are 20-24 and 108-112 mJ/cm^2, respectively. Now, we investigate the dependences of crystalline quality on the initial pulse number N_i. Figure 6.5 shows the dependences of crystalline fraction X_c and FWHM of c-Si peak on the initial pulse number N_i for the **Si/YSZ/metal/glass** and Si/YSZ/glass in the two-step method ($N_i \neq 0$), compared with the one-step or conventional method ($N_i = 0$), where $N = N_i + N_g$. It can be seen that FWHM is reduced while X_c increases with N_i, compared with $N_i = 0$ for both the structures. This indicates that the crystalline quality of the Si film is improved significantly by using the two-step method. Moreover, at the same $N_i > 0$ (for the two-step method), X_c of **Si/YSZ/metal/glass** is a little larger while its

FWHM is slightly smaller than those of Si/YSZ/glass. This also shows that the metal film has a role in enhancing crystalline quality of the Si film on the YSZ by the two-step method.

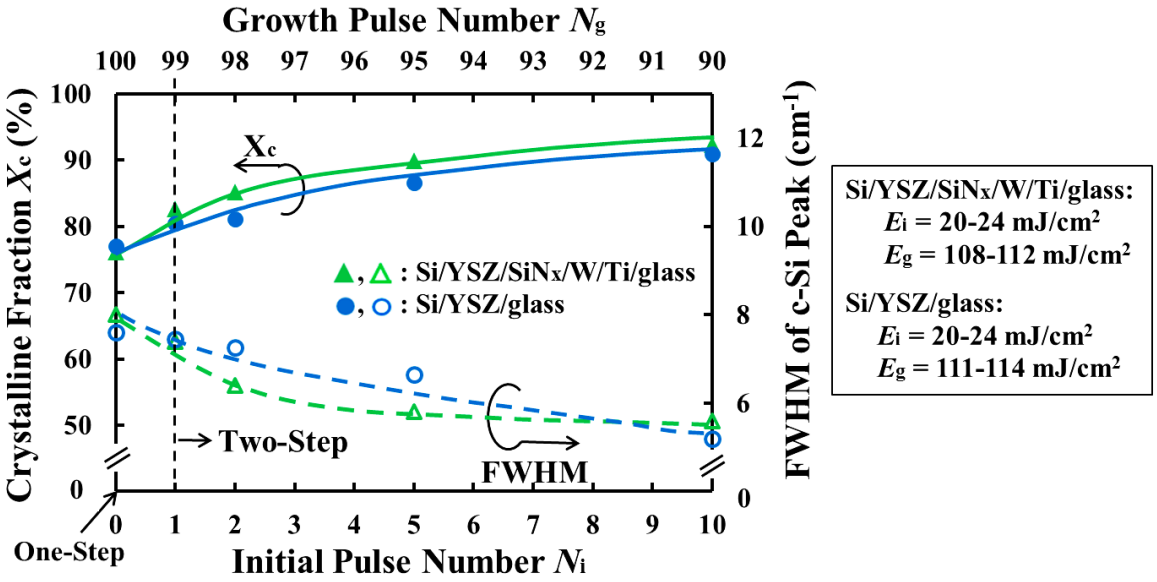

Fig. 6.5 Dependences of X_c and FWHM on N_i for the Si/YSZ/metal/glass and Si/YSZ/glass by the two-step method, where the different optimized annealing condition is used for each structure.

6.3.3 Comparison of crystalline quality of Si films among the three kinds of substrates: glass, YSZ/glass, and YSZ/metal/glass

In this section, we compare crystalline quality among the three structures of Si/glass, Si/YSZ/glass, and Si/YSZ/**metal**/glass by using He-Ne Raman spectroscopy and SEM results. Some data, which were already discussed in chapter 5, are shown again for easy comparison. Table 6.2 shows the typical X_c and FWHM values of the c-Si peak of the Si/glass, Si/YSZ/glass, and Si/YSZ/**metal**/glass in the two-step method with N_i = 10 and N_g = 90, which are obtained by He–Ne Raman spectral analysis. Three irradiation conditions were used, (A), (B), and (C). The conditions (A) and (B) are the same as Table 5.1 in chapter 5, which are E_i = 18–22 mJ/cm^2 and E_g = 106–109 mJ/cm^2 (optimized condition for the Si/glass), and E_i = 20–24 mJ/cm^2 and E_g = 111–114 mJ/cm^2 (optimized condition for the Si/YSZ/glass), respectively. The condition (C), which is the optimized condition for the Si/YSZ/**metal**/glass, is E_i = 20–24 mJ/cm^2 and E_g = 108–112 mJ/cm^2. The obtained crystallinities (crystalline fraction X_c and FWHM) of the Si/glass, Si/YSZ/glass, and

Si/YSZ/**metal**/glass by the condition (A) are labelled ①, ②, and ③, respectively, in Table 6.2. The crystallinity of the Si/YSZ/glass obtained under the condition (B) is labelled ④ and that of the Si/YSZ/**metal**/glass under the condition (C) is labelled ⑤ in Table 6.2. First, the comparison of ①, ②, and ③ shows that, although X_c of the Si/glass is highest among three structures, its FWHM is the same with those of the other structures. The difference in X_c is considered due to the difference in optical absorption in three structures. On the other hand, the FWHMs are equal for three structures and around 6, which suggests that we can improve the crystalline quality by irradiating the Si/YSZ/glass and Si/YSZ/**metal**/glass at their optimized conditions. In fact, we obtain higher X_cs and smaller FWHMs in ④ and ⑤ than in ① when using their optimized conditions. However, comparing ④ and ⑤, it is found that the crystallinities are tiny different between both the structures of Si/YSZ/glass and Si/YSZ/**metal**/glass, suggesting a small heating role of the metal layer on enhancing crystalline quality of the Si film on the YSZ.

We also observed the Secco-etched Si film crystallized on YSZ/**metal**/glass by two-step method and compare with those of the Si/glass and Si/YSZ/glass. The images are shown in Fig. 6.6 and the used irradiation conditions are the same as those in Table 6.2. The labels ①-⑤ in Fig. 6.6 correspond to the numbers or the same irradiation conditions in Table 6.2. It can be seen from Fig. 6.6 that, at the same irradiation condition (A), grain size of the Si/YSZ/glass and Si/YSZ/**metal**/glass is more uniform than that of the Si/glass. At the optimized irradiation condition for each structure, larger and uniform-sized grains are obtained for Si/YSZ/glass and Si/YSZ/**metal**/glass, compared with those of Si/glass.

Table 6.2 Crystalline fraction X_c and FWHM of c-Si peak of Si/glass, Si/YSZ/glass, and Si/YSZ/metal/glass for the two-step method.

Irradiation condition	Si/glass	Si/YSZ/glass	Si/YSZ/metal/glass
(A) E_i = 18 – 22 mJ/cm², N_i = 10, E_g = 106 – 109 mJ/cm², N_g = 90 (optimized for Si/glass)	X_c = 87% ① FWHM = 6.0	X_c = 82% ② FWHM = 6.1	X_c = 85% ③ FWHM = 6.2
(B) E_i = 20 – 24 mJ/cm², N_i = 10, E_g = 111 – 114 mJ/cm², N_g = 90 (optimized for Si/YSZ/glass)	/	X_c = 91% ④ FWHM = 5.2	/
(C) E_i = 20 – 24 mJ/cm², N_i = 10, E_g = 108 – 112 mJ/cm², N_g = 90 (optimized for Si/YSZ/metal/glass)	/	/	X_c = 93% ⑤ FWHM = 5.5

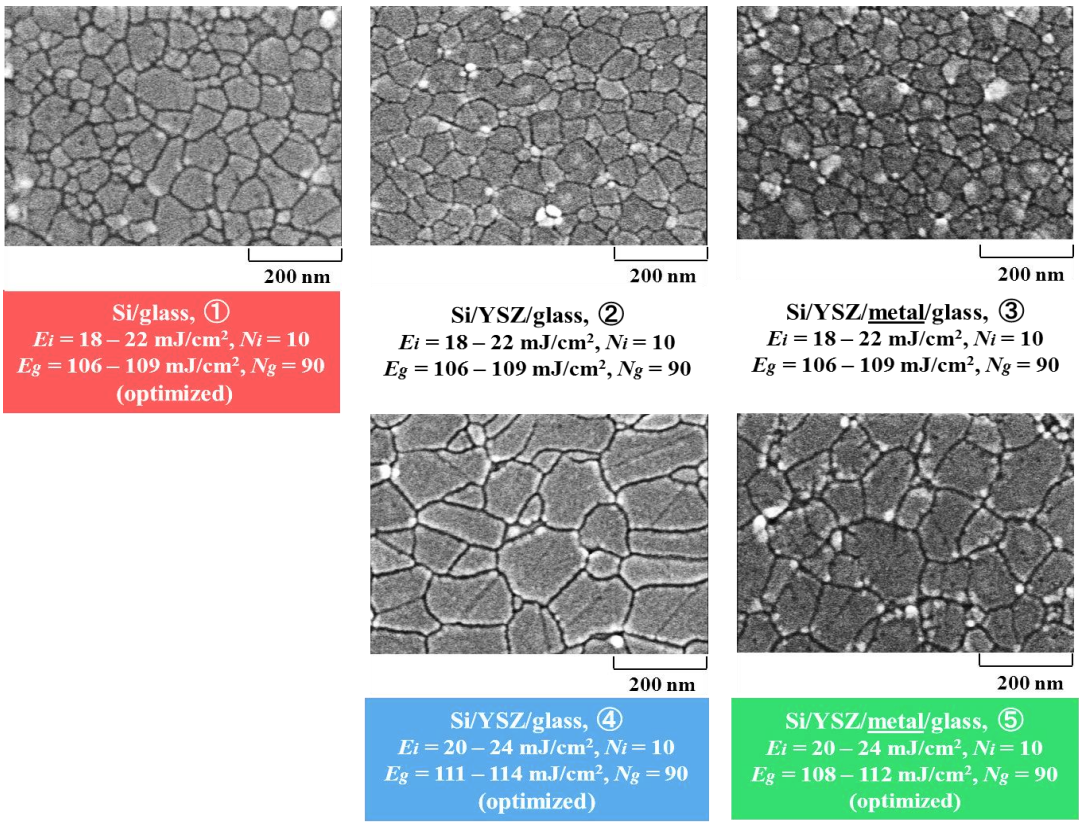

Fig. 6.6 SEM images of the Secco-etched Si films crystallized by the two-step method for the Si/glass, Si/YSZ/glass, and Si/YSZ/metal/glass. The labels ①-⑤ correspond to the numbers or the same irradiation conditions in Table 6.2.

The crystalline quality of the Si films on YSZ/metal/glass substrate has been investigated. The optimized irradiation condition in the two-step method was also obtained. However, after crystallization of the Si film on the YSZ/metal/glass substrate, we observed many bubbles or holes with the size of tens μm order appear on the surface of the Si film as shown by optical microscope image in Fig. 6.7. The forward light irradiation mode image is shown in Fig. 6.7(a), in which light irradiates the surface of the sample from the top of optical microscope. This is the normal operation mode of an optical microscope. If the light irradiates the back surface of the sample from the bottom of optical microscope, we obtain the backside light irradiation mode image [Fig. 6.7(b)]. Although the bottom of the sample is transparent glass substrate, the metal layer exist between the Si film and the glass substrate. So, the whole optical image is dark. It can be seen from Fig. 6.7(b) that bubble areas are brighter than other areas, which means that some metal regions are removed.

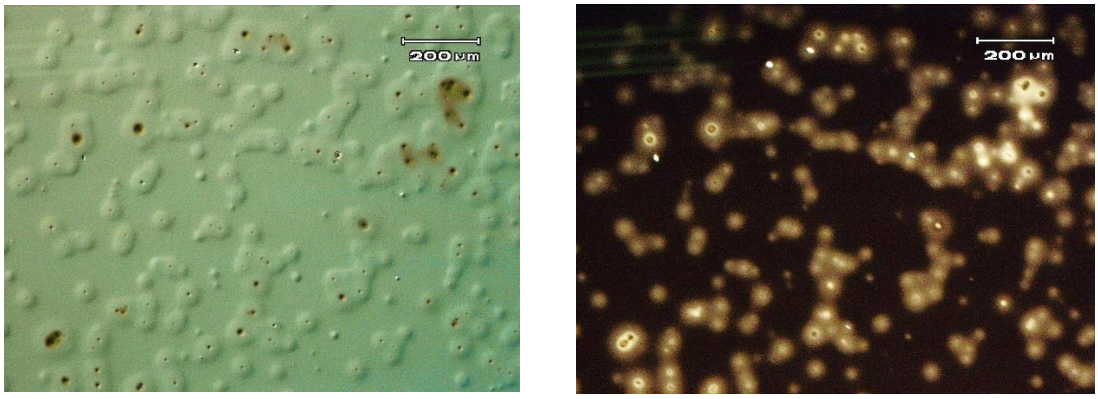

(a) **(b)**

Fig. 6.7 Optical microscope images of the Si/YSZ/SiN_x/W/Ti/glass structure from (a) forward light irradiation mode and (b) backside light irradiation mode.

Figure 6.8 shows schematic drawings of bubble formation model. The occurrence of bubbles or holes is probably due to two causes. One is the difference in thermal expansion coefficient (TEC) between W metal ($\sim 4.5\times10^{-6}$/°C at 20 °C) and quartz substrate ($\sim 0.59\times10^{-6}$/°C at 20 °C). After deposition of a YSZ layer, the substrate induces thermal compressive stress to the YSZ, SiN_x, and metal layers, which may be non-uniformly. Since the SiN_x is an amorphous and hard material compared with metals, atomic bonds in the SiN_x layers are compressed one another, and then something like small cracks are generated in the SiN_x. The second is many grain boundaries of the deposited poly-YSZ layer with grain size ~20 nm. When a sample is dipped in diluted HF solution prior to deposition of an a-Si film, the HF solution easily etched the YSZ layer through it grain boundaries and seeps through the cracks in the SiN_x film to the bottom metal layers as shown in Fig. 6.8(a). Then, the W and Ti films may be eroded or etched through their grain boundaries. Some small amount of HF penetrating to the Ti layer maybe remains on the glass substrate even after a-Si film deposition as shown in Fig. 6.8(b). When the sample is irradiated for crystallization, some remained HF reacts with the Ti film and glass substrate due to high temperature, and then some reaction gas is generated, which pushes the over layer of Si as shown in Fig. 6.8(c). As a result, the bubbles actually appear on the Si/YSZ/metal/glass as shown in Fig. 6.7. Actually, small black points can be observed around the centers of the bubbles, which seems as centers of cracks. These bubbles are considered to affect device performance if the Si/YSZ/metal/glass structure is applied for a bottom-gate TFT. Therefore, it is supposed that the Si/YSZ/glass structure is more suitable for TFT fabrication as a top-gate type.

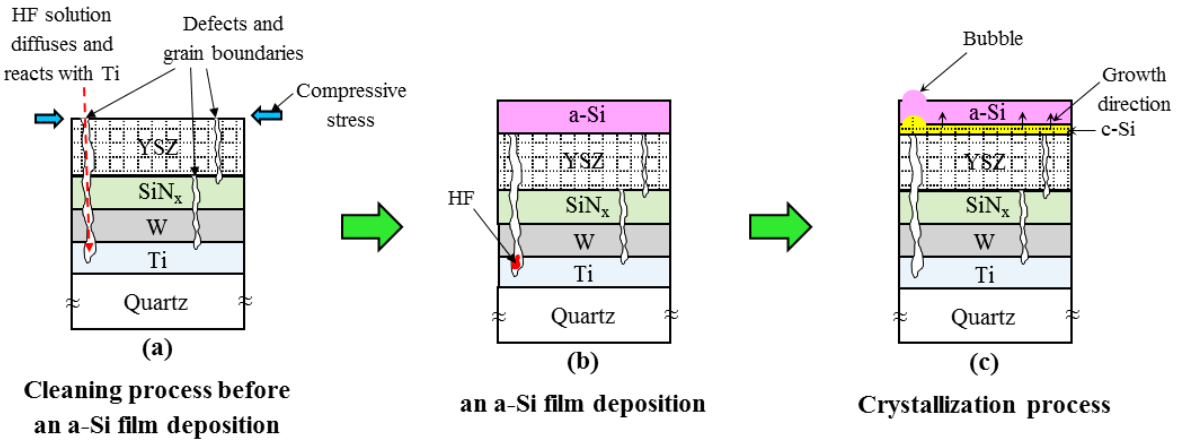

Fig. 6.8 Illustration for bubbles or holes formation on the surface of Si/YSZ/SiN_x/W/Ti/glass.

6.4 Summary

On the basis of the results obtained for the Si/glass and Si/YSZ/glass mentioned in chapters 4 and 5, we investigated crystalline quality of the **Si/YSZ/metal/glass** structure by using Raman spectroscopy and SEM. It is found that higher X_c and smaller FWHM were obtained by the two-step method compared with the one-step method at the same total pulse number N and lower total irradiation energy density. This indicates that the two-step method is effective in improving crystalline quality of Si films on **YSZ/metal/glass**. Moreover, the metal layer has a small heating effect on enhancing crystalline quality of the Si film. Irradiation condition was optimized for bottom-gate poly-Si TFTs fabrication. However, considering the occurrence of bubbles or holes on surface of the crystallized Si film, the **Si/YSZ/metal/glass** structure is not suitable for bottom-gate TFT fabrication.

Chapter 7:

Electrical Properties of Crystallized Si Films and Performance of Fabricated TFTs

7.1 Electrical properties of crystallized Si films measured by resistivity and Hall effect measurements

7.1.1 Hall effect measurement setup

In this study, electrical properties of the crystallized Si films (conductivity, carrier concentration, and Hall mobility) were measured by resistivity and alternating current (AC) Hall effect measurements using the Van der Pauw method. The most popular structure for resistivity and Hall effect measurements is probably the Van der Pauw structure because it requires fewer geometrical measurements of the sample and allows resistivity measurements to be made on any sample of uniform thickness, provided that the sample was homogeneous and there were no physical holes in it. These requirements on sample shape simplify fabrication and measurement in comparison to Hall bar techniques. The AC field Hall measurement method is effective on low mobility materials that are extremely difficult or practically impossible to measure with direct current (DC) methods. The AC field method is used for measuring Hall voltage only, not for resistivity. It is compatible with Van der Pauw sample structures at all temperature options, and with the standard and high resistance methods. In the following, we introduce more details about techniques used in our Hall effect measurements.

(a) Current reversal technique

The Hall voltage measurements using AC technique suffer from all of the unwanted signals, such as thermoelectric voltage, offset voltage, and offset current. The desired voltage is proportional to the excitation current magnitude and polarity. This linearity characteristic will be estimated for our samples in the next section. On the other hand, the unwanted signals are not proportional to the excitation current. Therefore, we used current reversal technique in order to separate the desired signals from the undesired ones. This technique is especially necessary with the AC technique because it helps eliminate uncertainty from phase calibration that is only present in the AC method. Even in a

properly calibrated system, there is some error in the lock-in amplifier phase, which can create a meaningful measurement error when the Hall voltage is small compared to the induced voltage in the leads.

(b) Geometry averaging technique

Measurement uncertainty can result if a sample is not homogeneous. For a homogeneous sample, the measured voltage $V_{ij,kl}$ is expected to equal to the voltage $V_{kl,ij}$ when the current and voltage leads are interchanged, where i, j, k, and l are indicators of contact terminals. For non-homogenous samples, the final voltage can be obtained by averaging these two voltages. This technique is called geometry averaging. It can be implemented in both Hall voltage and resistivity measurements. We used this technique to measure resistivity and Hall voltage in our samples.

(c) Temperature dependent Hall measurements technique

Temperature dependent resistivity and Hall effect measurements of a material measure the resistivity, carrier concentration, and Hall mobility as a function of temperature. The details of the temperature dependency of these material characteristics are used to understand the electronic transport properties of the material. There are many material properties that can be determined from variable temperature resistivity and Hall effect measurements. The results from temperature dependence of carrier concentration can provide information about band gap of the semiconductor, activation energy of donors or acceptors, and doping concentration values. The mobility of carriers is determined by the scattering of the carriers in the material. Each of the possible scattering mechanism will have a different temperature dependency. Careful analysis of the temperature dependent mobility will determine the major scattering mechanism in the material. In this study, we performed the temperature dependent resistivity and Hall effect measurements on the Si films with the temperature range from room temperature (RT) to 300 ^{o}C in vacuum ambient. The temperature was measured by a thermocouple in direct contact with the back of the sample. The whole setup was placed in a temperature chamber. The temperature variation during a measurement was less than ± 0.5 ^{o}C.

7.1.2 Ohmic contact check

All direct measurements of the electronic transport properties of a material require sufficient electrical contacts between the sample and the measuring instrument. Generally, low resistance ohmic contacts are desired. For Hall effect measurement performed in our work, an ohmic contact is required. Ohmic contact usually means a contact with a small linear resistance compared to the resistance of the sample being studied, and therefore having insignificant non-linear current-voltage characteristics. The most important method to characterize the contact is the ohmic check procedure. The plot of voltage versus current should be a straight line. In our Hall effect measurements, Al metal electrodes are deposited at corners of a typical square pattern as shown in Fig. 7.1 (Fig. 3.11 of chapter 3), followed by annealing in N_2 ambient at 350 ^oC for 30 min. to improve the contacts. We show Fig. 7.1 again for ease in the next investigation and discussion. Figures 7.2, 7.3, 7.4, and 7.5 show the ohmic check of four kinds of sample structures used for Hall effect measurement in our work: undoped poly-Si/YSZ/glass, undoped poly-Si/glass, P-doped Si/YSZ/glass, and P-doped Si/glass, respectively. In each figure, the ohmic check of two terminals (1−3 and 2−4) are shown together with resistances. It can be seen that contacts of all samples are ohmic, which is sufficient for Hall effect measurement.

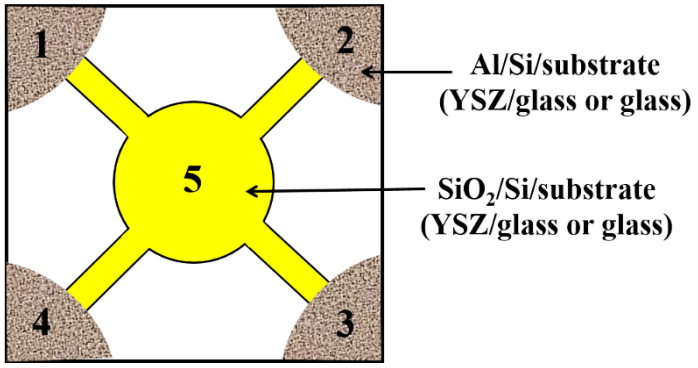

Fig. 7.1 Top-view illustration of the final Hall effect measurement pattern, which is a form of Van der Pauw pattern (the same as Fig. 3.11 of chapter 3).

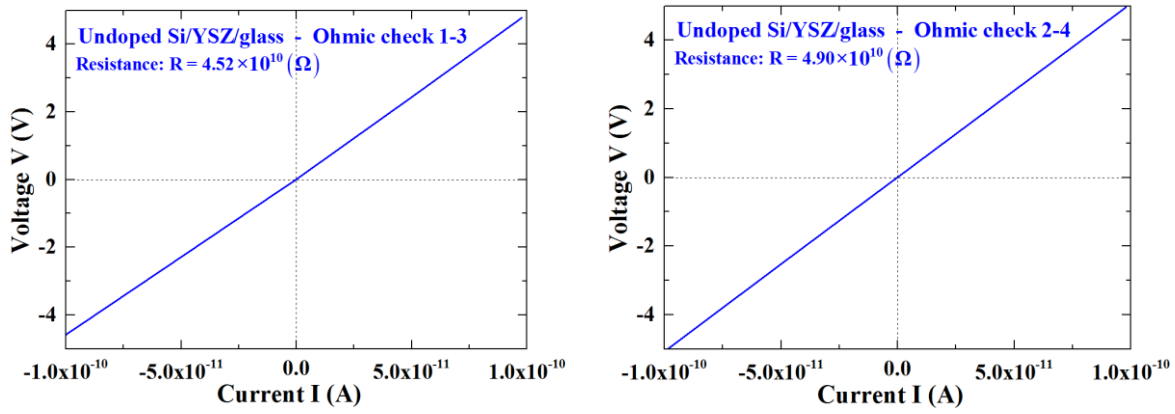

Fig. 7.2 Ohmic contact check for undoped Si/YSZ/glass structure.

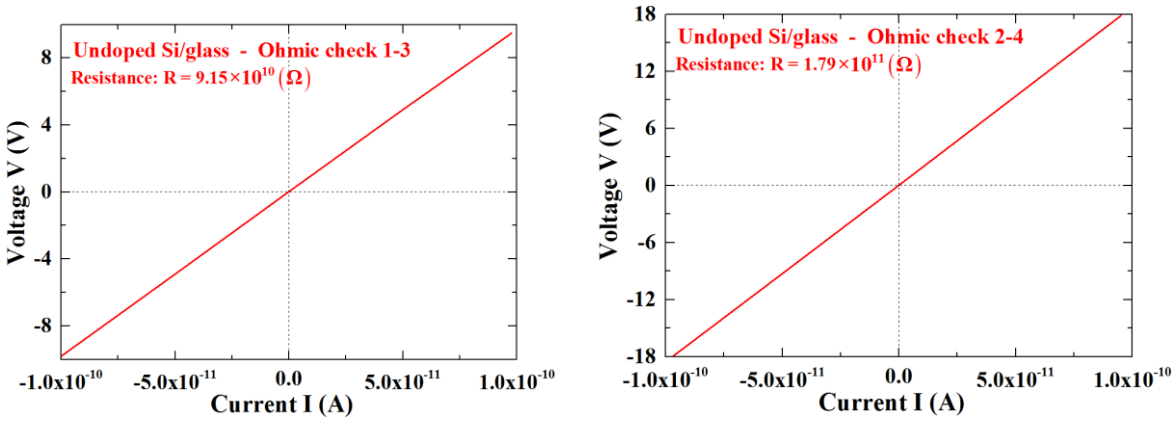

Fig. 7.3 Ohmic contact check for undoped Si/glass structure.

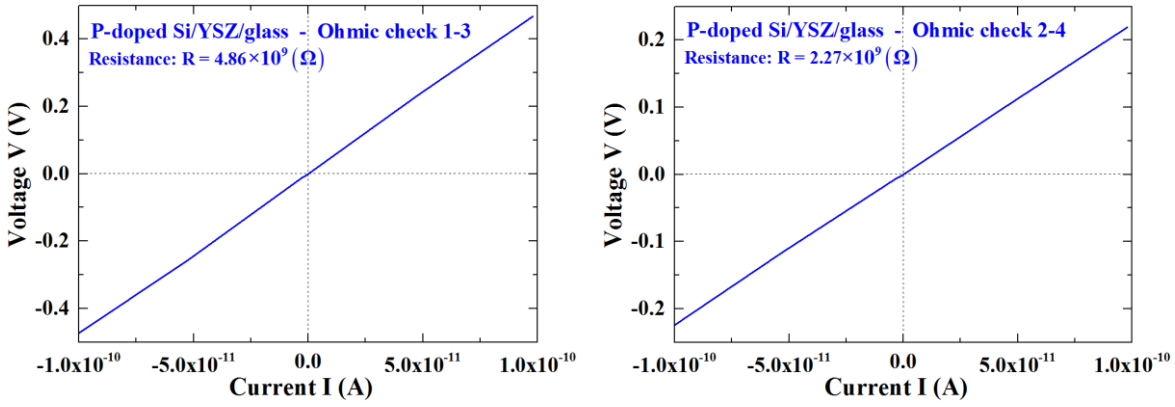

Fig. 7.4 Ohmic contact check for P-doped Si/YSZ/glass structure.

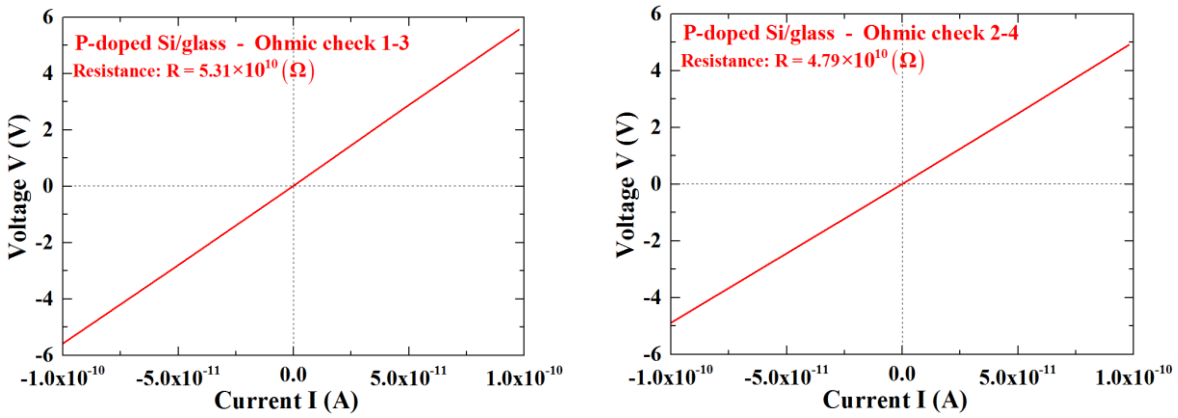

Fig. 7.5 Ohmic contact check for undoped Si/glass structure.

7.1.3 Linearity characteristics of the Hall effect measurement

The desired Hall voltage (V_H) in the Hall effect measurement is proportional to the excitation current (I) magnitude and magnetic field (B) as mentioned previously. To verify the linearity of the Hall signal, we performed measurements of V_H versus I on all undoped and doped Si films for both structures of Si/YSZ/glass and Si/glass at room temperature. In these measurements, we used two magnetic fields of 0.4 and 0.27 T. The results are shown in Figs. 7.6, 7.7. 7.8, and 7.9. In each figure, the slope ratio $\left({}^{a_1}/_{a_2}\right)$ is shown, where a_1 and a_2 are the slopes of the linearly extrapolated lines at 0.4 and 0.27 T, respectively. It can be seen that V_H increases almost linearly with increasing I, and increases with increasing B. Ideally, the $\left({}^{a_1}/_{a_2}\right)$ ratio is considered approximately equal the magnetic field ratio, i.e., 0.4/0.27 ≈ 1.48. In our films, $\left({}^{a_1}/_{a_2}\right)$ ratios are slightly deviated from the value of 1.48, which can be explained as follows.

The Hall voltage is related with carrier concentration by:

$$|V_H| = \frac{BI|R_H|}{t} = \frac{BI}{tqn_i} = a_i I\,, \tag{7.1}$$

where R_H, t, and a_i are the Hall coefficient, thickness of Si film, and proportional factor, respectively. a_i is given by:

$$a_i = \frac{B}{tqn_i}\,, \text{ where i = 1 or 2} \tag{7.2}$$

From eq. (7.2), it is considered that the proportional factor a_i depends on the carrier concentration, which is changed when changing the excitation current *I*. However, the calculated carrier concentrations for all measurement values of excitation current are almost in the same order. This suggests that the deviation of $\left({}^{a_1}/_{a_2}\right)$ ratios from the expected value of 1.48 is acceptable within an error.

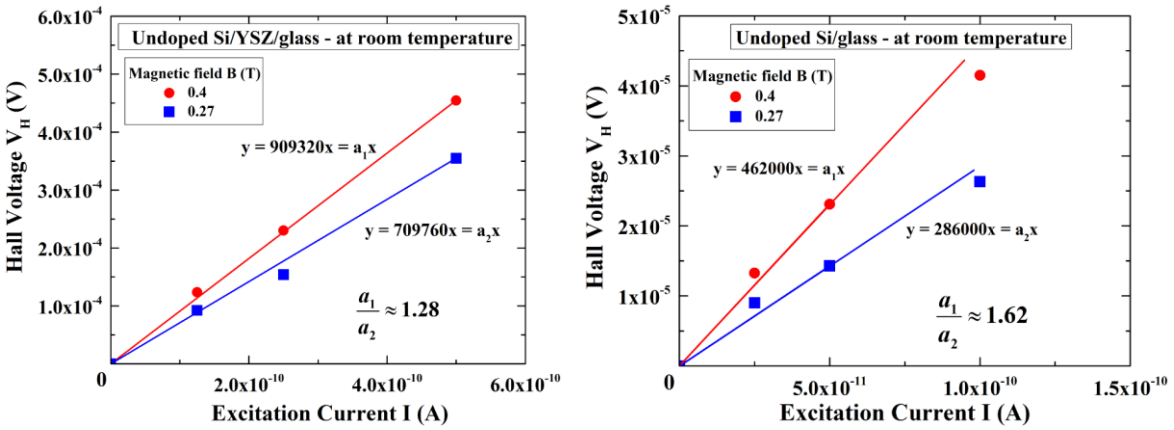

(a) **(b)**

Fig. 7.6 Dependences of Hall voltage on the excitation current and applied magnetic field for the (a) undoped Si/YSZ/glass and (b) undoped Si/glass structures.

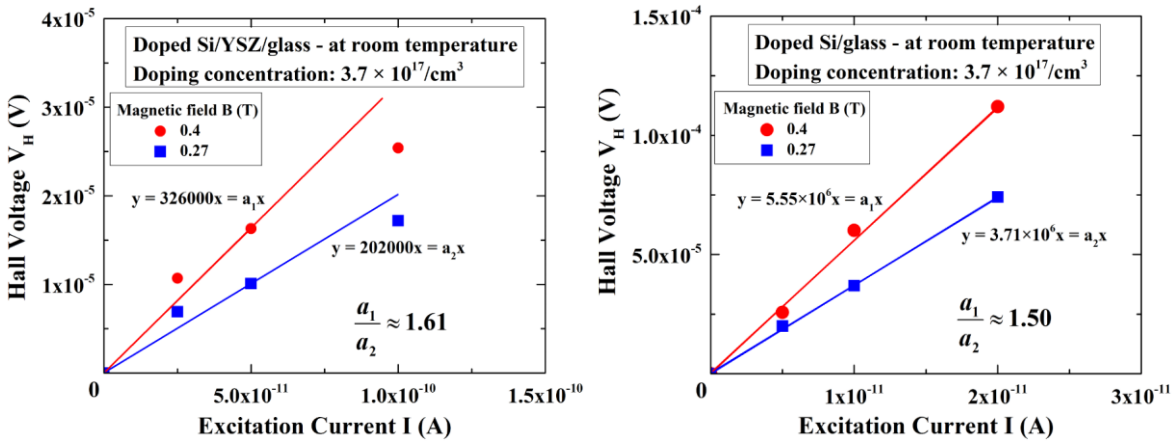

(a) **(b)**

Fig. 7.7 Dependences of Hall voltage on the excitation current and applied magnetic field for the (a) doped Si/YSZ/glass and (b) doped Si/glass structures at doping concentration of 3.7 × 10^{17}/cm^3.

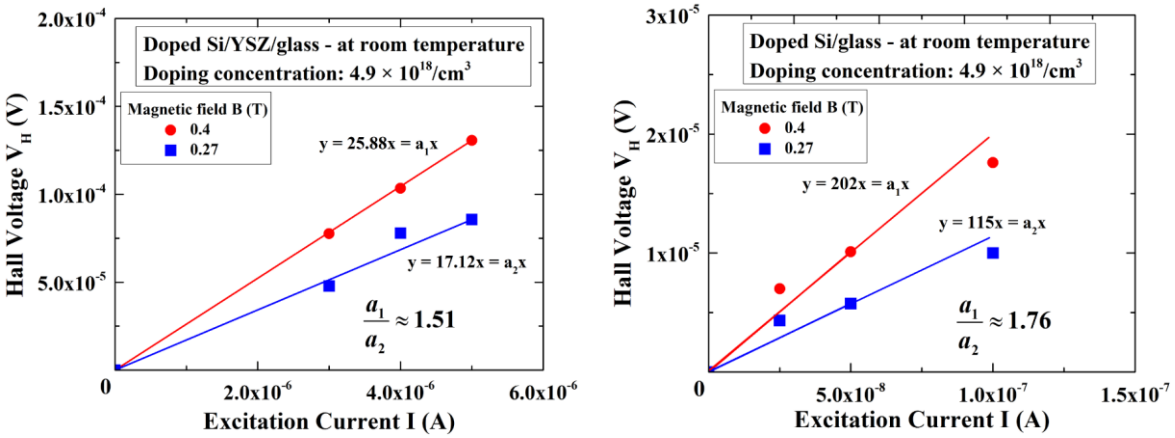

(a) **(b)**

Fig. 7.8 Dependences of Hall voltage on the excitation current and applied magnetic field for the (a) doped Si/YSZ/glass and (b) doped Si/glass structures at doping concentration of 4.9 × 10^{18}/cm^3.

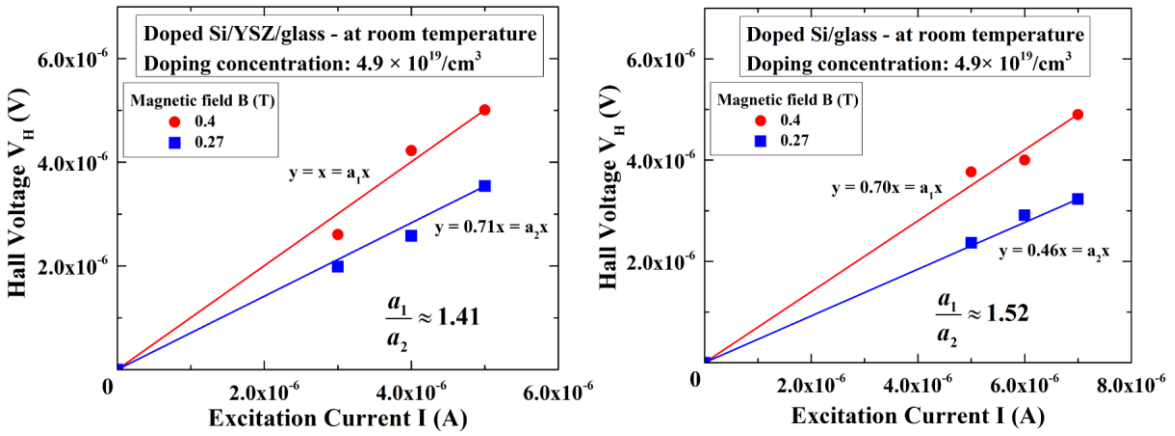

(a) **(b)**

Fig. 7.9 Dependence of Hall voltage on the excitation current and applied magnetic field for the (a) doped Si/YSZ/glass and (b) doped Si/glass structures at doping concentration of 4.9 × 10^{19}/cm^3.

7.1.4 Electrical properties of the undoped and P-doped crystallized Si/glass samples

Figures 7.10(a), (b), and (c) show the measurement temperature T dependences of carrier concentration n, Hall mobility μ_H, and conductivity σ for the undoped and P-doped Si films on the **glasses** with different average doping concentrations. The Si films were crystallized by the two-step method under area expansion condition of Fig. 5.10 in chapter 5. The activation energies E_{ni}, $E_{\mu i}$, and $E_{\sigma i}$ for n, μ_H, and σ, respectively, which are calculated by least squares method, are also shown in Fig. 7.10. The subscript "i" indicates an integer of 1 to 5. The solid black line in Fig. 7.10(a) shows the intrinsic concentration of Si for a reference. It is found that all of the Si films are n-type or the carriers are electrons. In Fig. 7.10(a), at the low doping concentration of 3.7×10^{17}cm^{-3}, the carrier concentrations are almost the same as those of the undoped film at any measurement temperature except the RT. The value at RT is probably due to a process contamination by accident. Increasing the doping concentration, the carrier concentration increases with it too, and the temperature dependence disappears or the activation energy is almost zero. In Fig. 7.10(b), the Hall mobilities for the low doped film of 3.7×10^{17}cm^{-3} are slightly higher than those of undoped film at any measurement temperature. However, at a higher doping concentration of 4.9×10^{18}cm^{-3}, mobilities abruptly decrease and the activation energy E_μ becomes higher. Further doping, Hall mobility increases again with the lower E_μ. The detailed explanation will be summarized and discussed later. In Fig. 7.10(c), on the whole, excepting at high doping concentration of 4.9×10^{19} cm^{-3}, the conductivity exhibits the behavior of an activation process for both the undoped and P-doped Si films on the **glasses**. The activation energies of the doped films are constant all over the temperature range, but that of the undoped film is changed from $E_{\sigma 1}$ = 0.12 to $E_{\sigma 2}$ =0.54 eV, a higher value, around 100 ^{o}C. The σ is proportional to a product of n and μ_H. When σ, n, and μ_H are expressed as $\sigma = \sigma_o\exp(-E_\sigma/kT)$, $n = n_o\exp(-E_n/kT)$, and $\mu_H = \mu_{Ho}\exp(-E_\mu/kT)$, respectively, σ can be shown as $\sigma = \sigma_o\exp(-E_\sigma/kT) = en_o\mu_{Ho}\exp[-(E_n+E_\mu)/kT]$. That is, $E_\sigma = E_n + E_\mu$. In these equations, σ_o, n_o, and μ_{Ho} are pre-factors, and k is the Boltzmann constant. Since E_μ is just 0.06 eV for the undoped film as shown in Fig. 7.10(b), the activation behavior of σ is mainly governed by the carrier concentration behavior. Therefore, the change of the activation energy E_σ around 100 ^{o}C for the undoped film in Fig. 7.10(c) is due to difference in E_n between low temperature region ($T \leq 100$ ^{o}C) and high temperature region ($T \geq 100$ ^{o}C). For the films at

the highest doping concentration of 4.9×10^{19} cm^{-3}, the saturation tendency of conductivity can be attributed mainly to the saturation of carrier concentration.

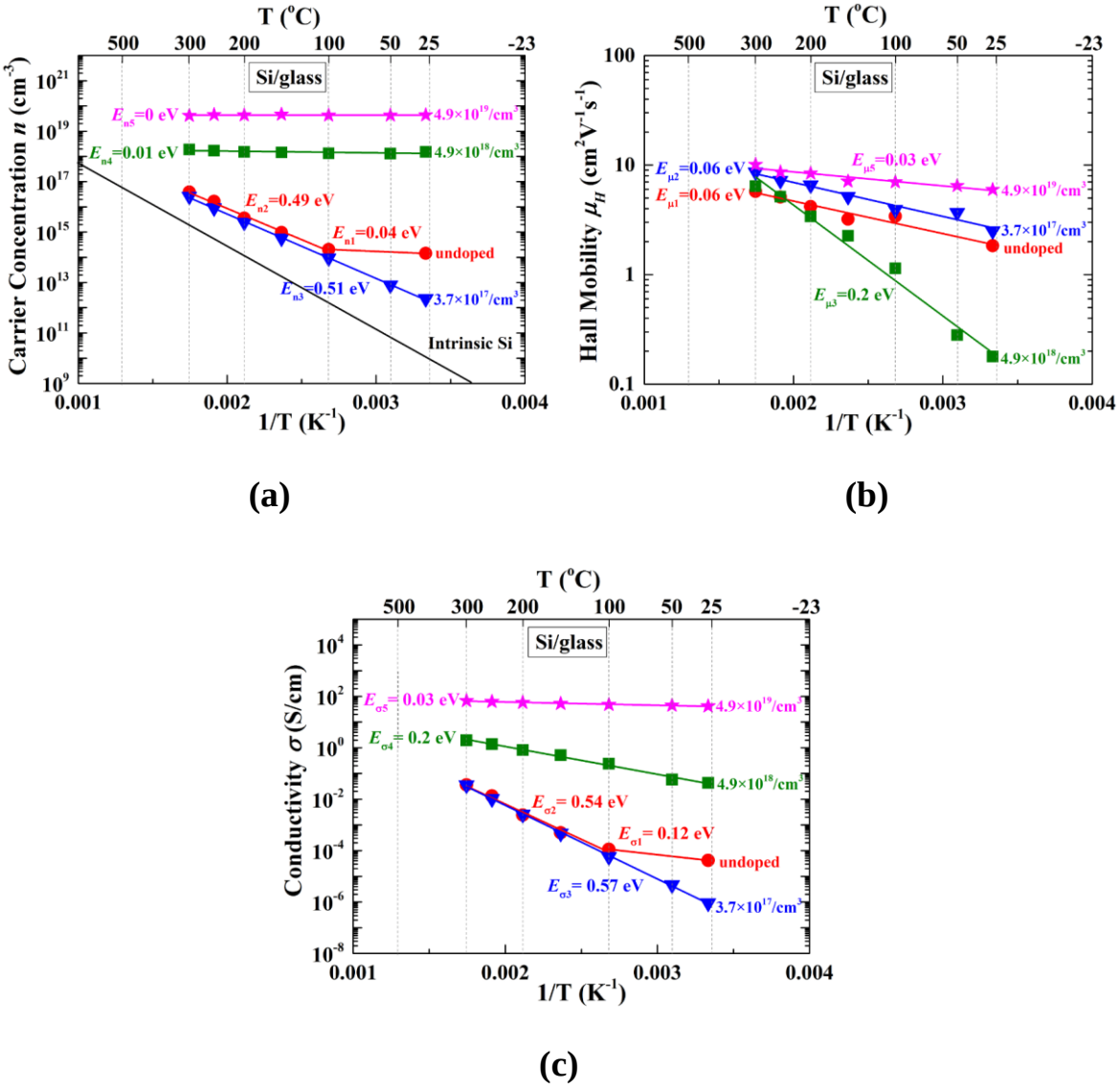

Fig. 7.10 Measurement temperature dependences of (a) carrier concentration *n*, (b) Hall mobility μ_H, and (c) conductivity σ for the undoped and P-doped Si films crystallized by the two-step method on the glasses.

7.1.5 Electrical properties of the undoped and P-doped crystallized Si/YSZ/glass samples

Figures 7.11(a), (b), and (c) show the measurement temperature *T* dependences of carrier concentration *n*, Hall mobility μ_H, and conductivity σ for the undoped and P-doped Si films on the **YSZs/glasses** under the same fabrication and measurement conditions of

Fig. 7.10. We can see from Fig. 7.11(a) that, on the whole, the carrier concentrations increase with the measurement temperature and doping concentration including the undoped film. For the undoped case, the activation energy is changed from E_{n1} = 0.23 to E_{n2} = 0.46 eV around 100 ºC. Increasing the doping concentration to 3.7×10^{17}cm^{-3}, the activation energy E_{n3} is lowered to 0.22 eV from E_{n1}. Further increasing the doping concentration to 4.9×10^{18} cm^{-3} and higher, the carrier concentrations become higher with it too, and the temperature dependence disappears as shown in Fig. 7.11(a). The Hall mobility tendency in Fig. 7.11(b) is almost the same with the carrier concentration, i.e., μ_H increases with T and doping concentration, except in the high temperature region of 4.9×10^{18} cm^{-3}. The detailed explanation will be summarized and discussed in the next section. A noticeable behavior is that, for the undoped film in Fig. 7.11(b), the activation energy of μ_H corresponding to mobility barrier height rapidly increases from $E_{\mu1}$ = 0.02 eV to $E_{\mu2}$ = 0.09 eV with increasing temperature in spite of the increase of μ_H. This seems contrary to a general concept, in which a Hall mobility decreases when a barrier height becomes higher. We discuss this behavior as shown below.

The crystallized Si film consists of lots of small grains, accompanied by formation of grain boundaries which are much defective due to dangling bonds, etc. as shown by SEM images in Fig. 5.5 of chapter 5. So, at the grain boundaries, electrical potential barriers are formed by trapped carriers of electrons, as well-known. The Hall mobility is expressed in term of activation energy E_μ as $\mu_H = \mu_{Ho} \exp(-E_\mu/kT)$. If the E_μ of the undoped Si film on the YSZ/glass is assumed to be constant and equal to 0.09 eV ($=E_{\mu2}$) of the high temperature region ($T \geq 100$ ºC), an extrapolated line of Hall mobility can be drawn like a violet-dashed line in Fig. 7.11(b). Expected Hall mobilities from the extrapolated line in the low temperature region ($T \leq 100$ ºC) are smaller than our experimental results. On the other hand, if we assume E_μ of the undoped Si film on the YSZ/glass changes from $E_{\mu2}$ = 0.09 eV to $E_{\mu1}$ = 0.02 eV at 100 ºC and a pre-factor μ_{Ho} are constant through the whole of measurement temperature range, an extrapolated line of Hall mobility can be drawn like a black-dotted line in Fig. 7.11(b). In this case, expected Hall mobilities from the extrapolated line in the low temperature region ($T \leq 100$ ºC) are higher than our experimental results. By the two general assumptions, the obtained mobility behavior in our film cannot be explained simply or the behavior of μ_H for the undoped case cannot be explained without simultaneous changes of E_μ and μ_{Ho} around T = 100 ºC.

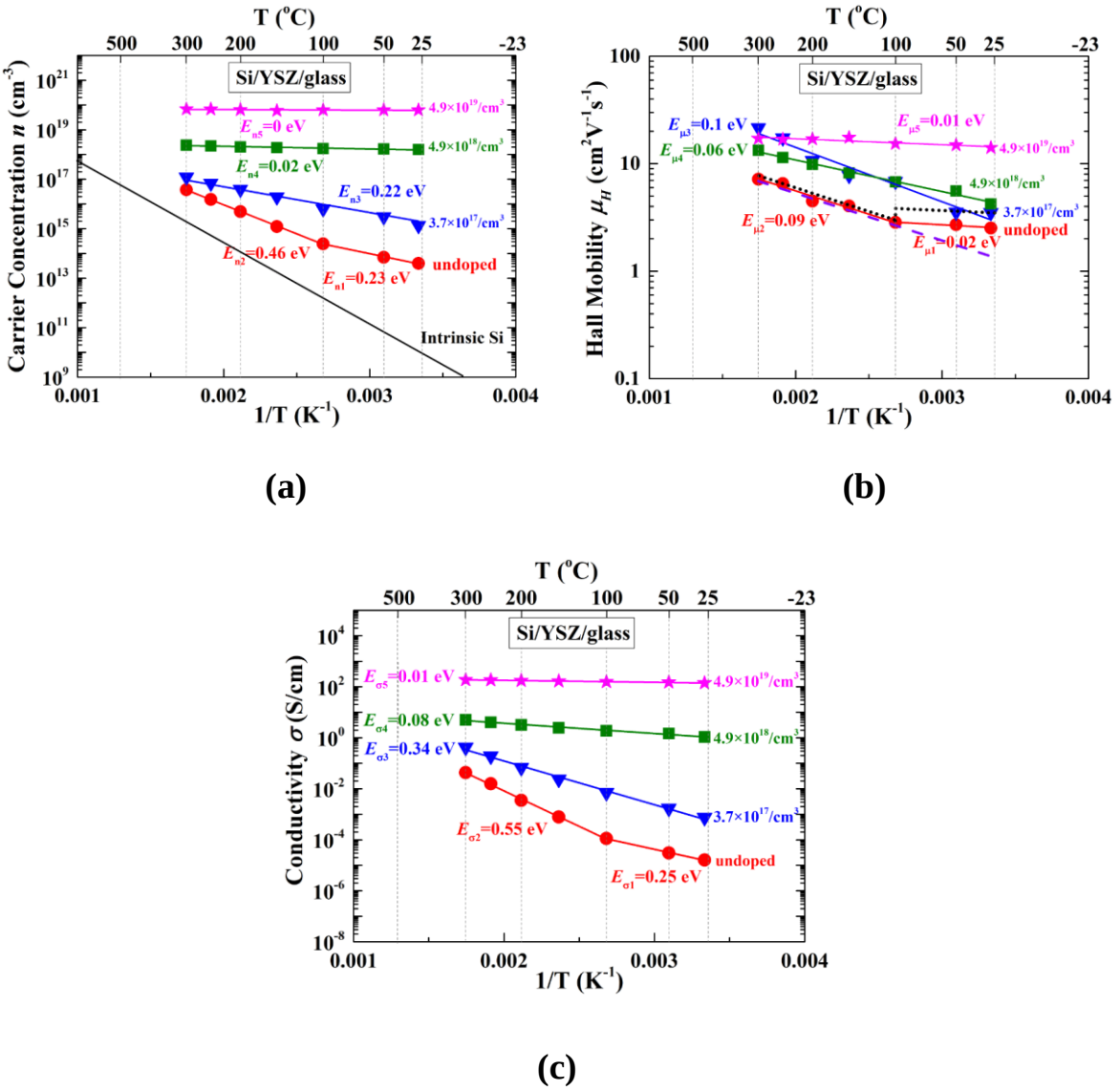

Fig. 7.11 Measurement temperature dependences of (a) carrier concentration *n*, (b) Hall mobility μ_H, and (c) conductivity σ for the undoped and doped Si films crystallized by the two-step method on the YSZs/glasses under the same fabrication and measurement conditions with Fig. 7.10.

In order to support our discussion on Hall mobility behavior of undoped film in Fig. 7.11(b), we draw energy band diagram models at the measurement temperatures of RT and 200 °C as shown in Figs. 7.12(a) and (b), respectively, based on the results of Fig. 7.11. From the carrier concentration *n*, the Fermi level E_F can be estimated by using $n = n_i \exp[(E_F - E_i)/kT]$, where n_i and E_i are the intrinsic carrier concentration and the intrinsic Fermi level, respectively. A free carrier concentration due to a donor level E_d from the conduction band edge E_c can be expressed as $n \equiv (N_d N_c)^{1/2} \exp(E_d - E_c/2kT)$, where N_d and N_c are the

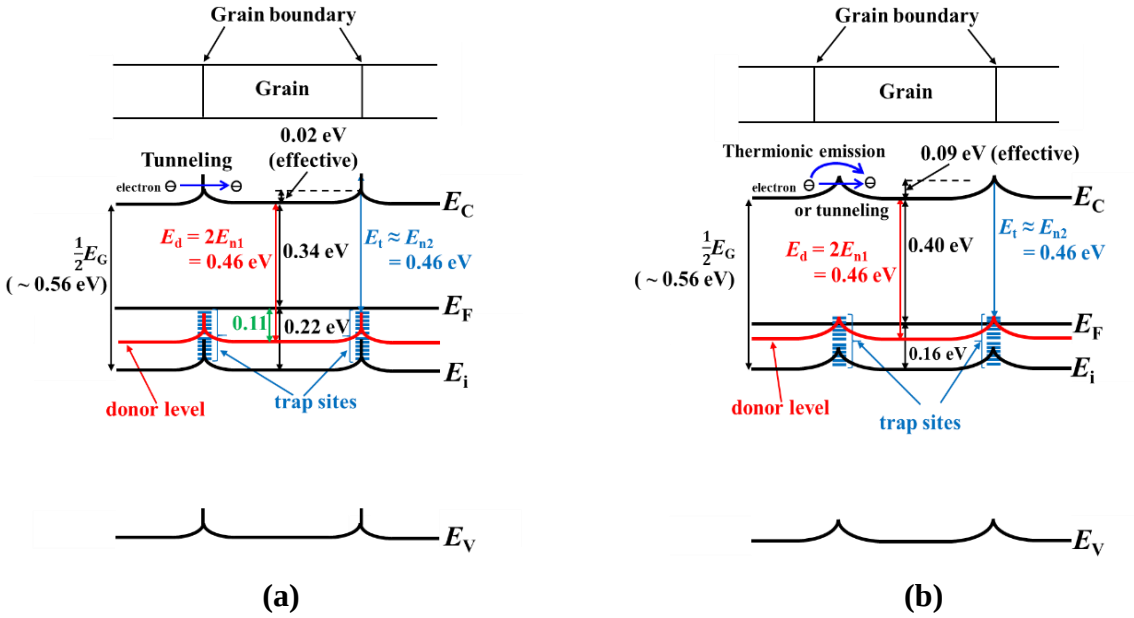

Fig. 7.12 Energy band diagrams for the undoped Si film on the YSZ/glass at the measurement temperatures of (a) RT and (b) 200 °C.

donor concentration and effective density of states of conduction band, respectively.[111] At the low temperature region ($T \leq 100$ °C), from the activation energy of E_{n1} = 0.23 eV for the undoped film [Fig. 7.11(a)], we can estimate a donor level of $E_d = 2E_{n1}$ = 0.46 eV. It is also considered that the activation energy of E_{n2} = 0.46 eV is not a donor level but a trap level E_t at the grain boundary. This is not only because the trap levels in the Si film are generally distributed near the intrinsic Fermi level E_i of ~0.56 eV, but also because $2E_{n2}$ = 0.92 eV is near the valence band, which is hardly considered as a donor level. It seems too coincidental that the E_d is almost equal to E_t, but the reason is not known well at present. At RT, since the donor level of 0.46 eV is lower than the Fermi level of 0.34 eV, most of the donor level sites are occupied by electrons so that they should be neutral. On the other hand, the trap levels which are probably located near the mid-gap of E_i at the grain boundaries (GBs) are charged much negatively by the electrons trapped fully there. For charge neutrality, the trapped electrons at the grain boundaries should be mainly terminated by holes in the valence band because ionized donors at the donor level are few at RT. When the measurement temperature increases, electrons are excited from both donor levels and trap sites at GBs to the conduction band, and the Fermi level lowers as shown in Fig. 7.12(b). As a result, the barrier height should be reduced and the mobility should increase. However, for the undoped Si film on the YSZ/glass, both the barrier

height and Hall mobility increase with the measurement temperature as shown in Fig. 7.11(b). The difference between them can be explained as follows:

At RT, as the trapped electrons are mainly terminated by holes in the valence band, it is possible that the holes gather in a very narrow region around the GBs to screen the negative charges of the trapped electrons. If so, the barrier height should be small, and the barrier width should be so thin that a tunneling effect maybe occur in the low temperature region ($T \leq 100$ °C). Figure 7.13 shows a schematic illustration of charge density distribution at a GB, where ρ_+ and ρ_- are the positive charge density of holes and ionized donor and negative charge density of electrons which shows a Dirac delta function, respectively. The total charge density ($\rho_+ + \rho_-$) is a summation of both the positive and negative charge densities. For the ρ_-, its value due to trapped electrons at the grain boundary is large and distributed in a very narrow space. ρ_- at the neutral region in grain for free electrons is constant and decreases toward near the grain boundary. This is due to the decrease of free electron concentration near the grain boundary because E_F approaches E_i. On the other hand, ρ_+ at the neutral region in grain for ionized donor is constant and equal to ρ_- at the same positions. ρ_+ increases toward near the grain boundary due to the increase of hole concentration, which is also because E_F approaches E_i. Actually, the tunneling effect on carrier transportation has been reported previously in the poly-Si film.[112,113] Taking the tunneling effect into account, the barrier height should be reduced effectively. At the high temperature region (100 °C $\leq T \leq$ 300 °C), since the carrier concentration n increases and the charge density at the GBs is reduced as mentioned above, the barrier height should be decreased, but probably still high. As the trapped electrons at

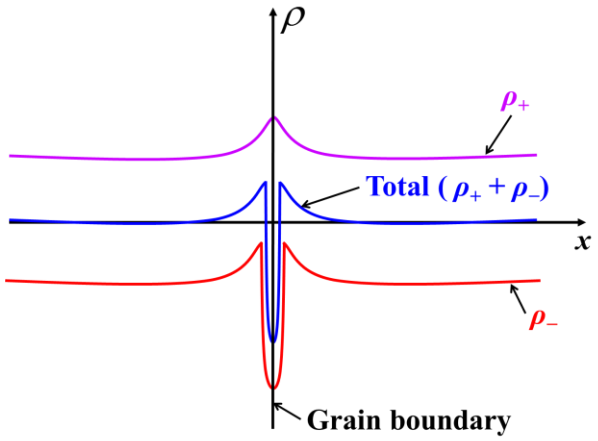

Fig. 7.13 Schematic illustration of charge density distribution at a grain boundary for energy band diagram in Fig. 7.12.

the boundaries are terminated not only by holes but also by the thermally generated donor ions, the barrier width is more extended than in the lower temperature. Because extension of the barrier width suppresses the screening of the trapped electrons and tunneling effect of electron transportation, the effective activation energy of $E_{\mu 2}$ increased to be 0.09 eV and higher than $E_{\mu 1}$ in spite of reduction of the actual barrier height.

The results of conductivity σ for the undoped and doped Si films on the **YSZs/glasses** in Fig. 7.11(c) are quite similar to those of the Si films on the **glasses** in Fig. 7.10(c). That means the conductivity exhibits the behavior of an activation process for both the undoped and P-doped films, excepting at high doping concentration of 4.9×10^{19} cm^{-3}. In Fig. 7.11(c), the activation energy of the undoped Si film on the YSZ/glass is changed from 0.25 to 0.55 eV around 100 ^{o}C. Since $E_{\sigma 2}$ is near half of energy gap $E_g/2$ or intrinsic energy level E_i, the carrier may be generated from carrier traps at grain boundaries due to thermal excitation. On the other hand, in the low temperature region ($T \leq 100$ ^{o}C), carriers are excited from the some donors with an impurity level around 0.46 eV [Fig. 7.11(b)]. Also, at the low temperature, free carriers are hardly excited from the trap levels at the GBs. For the doped Si film on the YSZ/glass cases, the activation energies are lower than $E_{\sigma 2}$ = 0.55 eV of the undoped film and decrease with increasing doping concentration. For the films at the highest doping concentration of 4.9×10^{19} cm^{-3}, the saturation tendency of conductivity can be also attributed mainly to the saturation of carrier concentration.

7.1.6 Summary of electrical properties and models for the undoped and P-doped crystallized Si films at room temperature

(a) For crystallized Si films on the glasses

In order to discuss the behaviors of electrical properties more in details, Figs. 7.14(a) and (b) show the summaries of the doping concentration dependences of carrier concentration and its activation energy, and the doping concentration dependences of Hall mobility and its activation energy, respectively, for the undoped and P-doped Si films on the **glasses** at RT. In Fig. 7.14(a), the solid black line shows the carrier concentration, equal to the doping concentration or 100 % activation line. Figures 7.14(c) and (d) show the schematic models for doped P effect on electrical property for the **Si/glass** films in the low and high doping concentrations, respectively. It can be seen from Fig. 7.14(a) that, for the undoped and low doped films, carrier concentrations n and activation energies E_ns are

almost the same. Moreover, *n* of the low doped film is much lower than the doping concentration (indicated by the solid black line). The E_ns are near the intrinsic Fermi level E_i (~0.56 eV) and considered to be the trap levels as mentioned earlier. Increasing the doping concentration up to the middle of 10^{18} cm^{-3}, the carrier concentration increases rapidly whereas its activation energy decreases abruptly to around the ionization energy of P dopants (~0.045 eV).[114,115] Further increasing doping concentration, the carrier concentration further increases and the activation energy decreases. From this result, it is considered that, for the low doped film, all of P dopants probably segregate to the GBs and passivate the crystalline defects there, such as termination of dangling bonds, as shown in

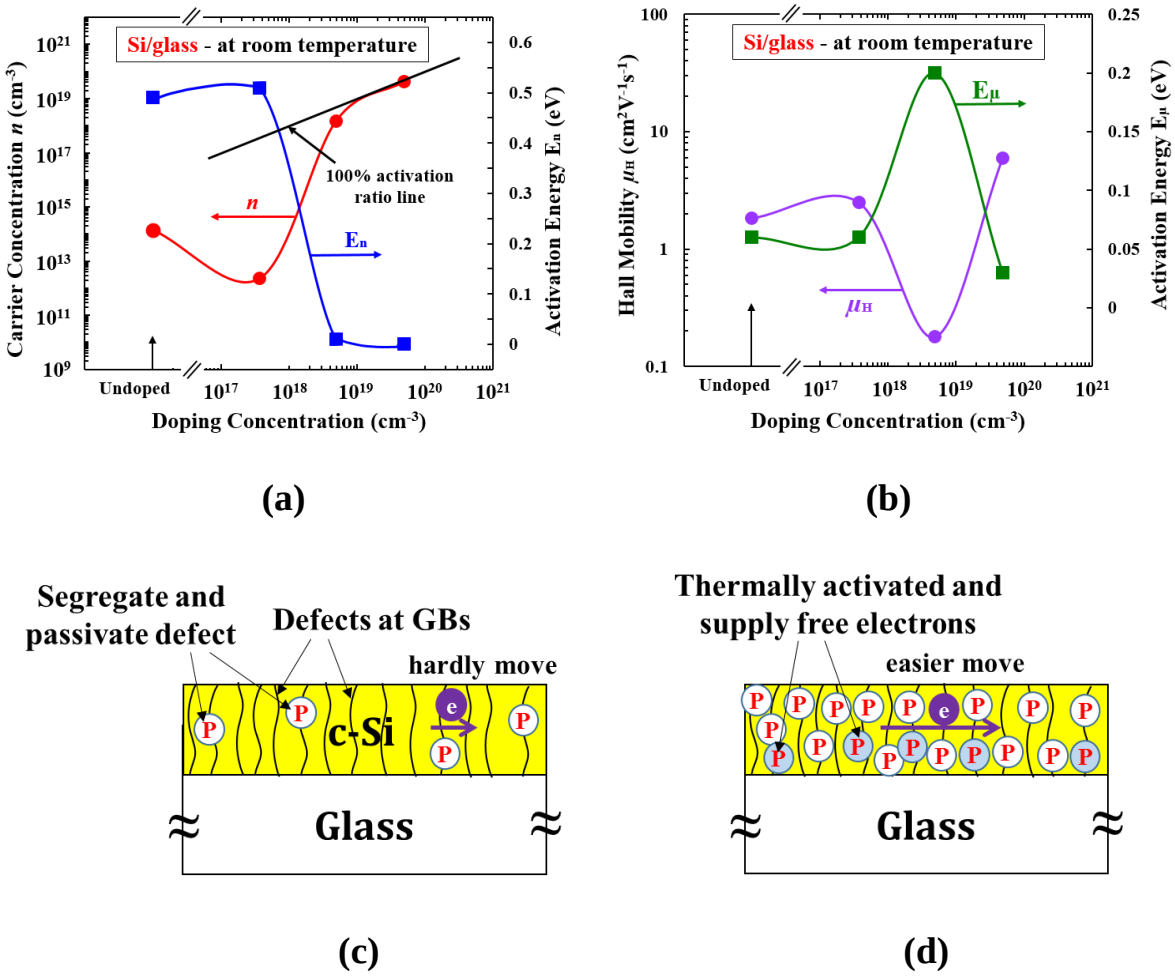

Fig. 7.14 **(a) and (b) are the summaries of the doping concentration dependences of carrier concentration and its activation energy, and the doping concentration dependences of Hall mobility and its activation energy, respectively, for the undoped and P-doped Si films on the glasses at RT. (c) and (d) are the schematic models for the doped P effect on electrical property in the low and high doping concentrations, respectively.**

Fig. 7.14(c). However, since the amount of defects is too large, the amount of P dopants are not enough to passivate most of them. On the other hand, at the high doping concentration as shown in Fig. 7.14(d), the amount of P for passivation is enough and a large number of P are thermally activated to supply the free electrons.

From Fig. 7.14(b), it is found that the Hall mobility μ_H and its activation energy E_μs for the undoped and low doped around middle of 10^{17} cm^{-3} films are almost the same. This is because the free electrons hardly move due to the large amount of crystalline defects as mentioned above. Increasing the doping concentration to around the middle of 10^{18} cm^{-3}, the μ_H decreases to a minimum whereas the E_μ or barrier height reaches a maximum. This is because the thermally activated electrons are more trapped at the GBs, which extends the depletion regions around the GBs. The doping concentration around the middle of 10^{18} cm^{-3} is considered as the critical value at which the depletion regions reach maxima or the grains are fully depleted. Further doping, the barrier height or E_μ is reduced due to the reduction of the depletion region. Free electrons can move easier and smoother. As a result, the μ_H increases again.

(b) <u>For crystallized Si films on the YSZs/glasses</u>

Figures 7.15(a) and (b) show the summaries of the doping concentration dependences of carrier concentration and its activation energy, and the doping concentration dependences of Hall mobility and its activation energy, respectively, for the undoped and P-doped Si films on the **<u>YSZs/glasses</u>** at RT. The solid black line also indicates the same in Fig. 7.14(a). Figures 7.15(c) and (d) show the schematic models for the doped P effect on electrical property for the **<u>Si/YSZ/glass</u>** films in the low and high doping concentrations, respectively. Comparing Fig. 7.15(a) with Fig. 7.14(a), the carrier concentrations of the undoped and middle 10^{17} cm^{-3} doped Si films on the **<u>YSZs/glasses</u>** are higher than those of the Si films on the **<u>glasses</u>**, indicating the larger amount of activated carriers. The activation energies E_ns of the formers are about half of those for the latters. These results suggest that the amount of crystalline defects in the Si films on the **<u>YSZs/glasses</u>** is much less than in the Si films on the **<u>glasses</u>**, or that the trap density is lower than that of the **<u>Si/glass</u>** case as shown in Fig. 7.15(c). The origin of this donor level for the Si/YSZ/glass, which is much deeper than the ionization energy of P dopant (0.045 eV) is not well-known at present, but this might be due to Zr atoms[116)] diffused from the YSZ layer into the Si film as shown in the SIMS profile of Fig. 5.19 in chapter 5. At the higher doping

concentration, behaviors of n and E_n of the Si/YSZ/glass case are similar to those of the Si/glass case in Fig. 7.14(a), but a little larger. Actually, the activation ratio of the Si/YSZ/glass is near 100 %, but that of the Si/glass is ~90 % at the doping concentration of 4.9×10^{19} cm^{-3}. The Hall mobility of the Si films on the **YSZs/glasses** in Fig. 7.15(b) increases without a minimum and the maximum of activation energy E_μ shifts toward the lower doping concentration, compared with that of the Si films on the **glasses** in Fig. 7.14(b). This result is also considered due to the smaller amount of crystalline defects in the **Si/YSZ/glass** case, compared with the **Si/glass** case, which leads to the smaller E_μ or

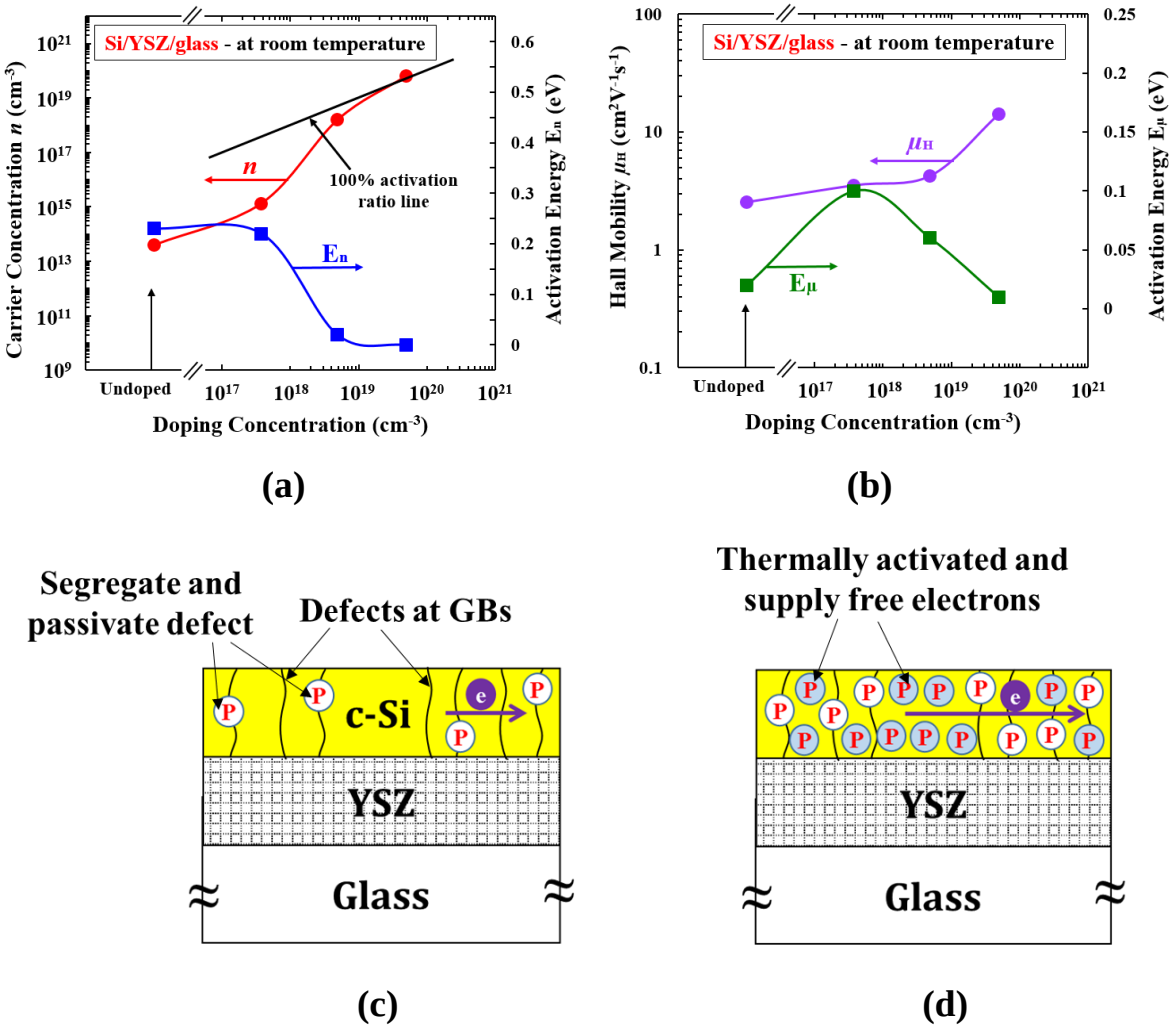

Fig. 7.15 **(a) and (b) are the summaries of the doping concentration dependences of carrier concentration and its activation energy, and the doping concentration dependences of Hall mobility and its activation energy, respectively, for the undoped and P-doped Si films on the YSZs/glasses at RT. (c) and (d) are the schematic models for the doped P effect on electrical property in the low and high doping concentrations, respectively.**

lower barrier height. As a result, free electrons can move more easily, leading to the higher Hall mobility.

7.2 Performance of fabricated TFTs

We have discussed in chapter 6 that the **Si/YSZ/metal/glass** structure is not suitable for bottom-gate TFT fabrication due to the occurrence of bubbles or holes on surface of the crystallized Si film. On the basic of crystallinity of the Si films crystallized by the two-step method using pulsed laser, we proceeded the fabrication of top-gate TFTs for the two structures of the Si/glass and Si/YSZ/glass. The fabrication procedure was already mentioned in chapter 3. It is supposed that uniform crystallization of the Si film influences the uniformity in performance of the fabricated TFTs strongly. Therefore, after fabrication, we measured and estimated the uniformity in performance of fabricated TFTs for each structure of Si/glass and Si/YSZ/glass. Figures 7.16(a) and (b) show typical transfer and output characteristics of the fabricated TFTs for the **Si/glass** structure with $W = L = 40$ μm. In Fig. 7.16(a), the transfer characteristic was measured at drain voltage $V_D = 0.1$ V. It can be seen that the TFTs can operate with relatively small off leakage current of ~10^{-12} A. The gate leakage current is also smaller than the order of 10^{-10} A (the data are not shown). The ON/OFF ratio is in the order of 10^6. Also, the highest achieved electron field-effect mobility is up to 105 $cm^2V^{-1}s^{-1}$. In Fig. 7.16(b), we can observe appropriate operation although the linear and saturation regions are not distinguished obviously. This may be ascribed to ion drift in the gate oxide film. The details will be discussed later.

Figures 7.17(a) and (b) show typical transfer and output characteristics of the fabricated TFTs for **Si/YSZ/glass** structure under the same condition as Fig. 7.16. From Fig. 7.17(a), it can be also seen that the TFTs can operate with relatively small off leakage current of ~10^{-12} A. The gate leakage current is also smaller than the order of 10^{-10} A (the data are not shown). The ON/OFF ratio is also in the order of 10^6. The highest achieved electron field effect mobility is up to 115 $cm^2V^{-1}s^{-1}$, a little higher than that for the Si/glass. From Fig. 7.17(b), we can also observe appropriate operation with higher drain currents than those of the Si/glass in Fig. 7.16(b). However, the linear and saturation regions are not also distinguished clearly like the case of Si/glass.

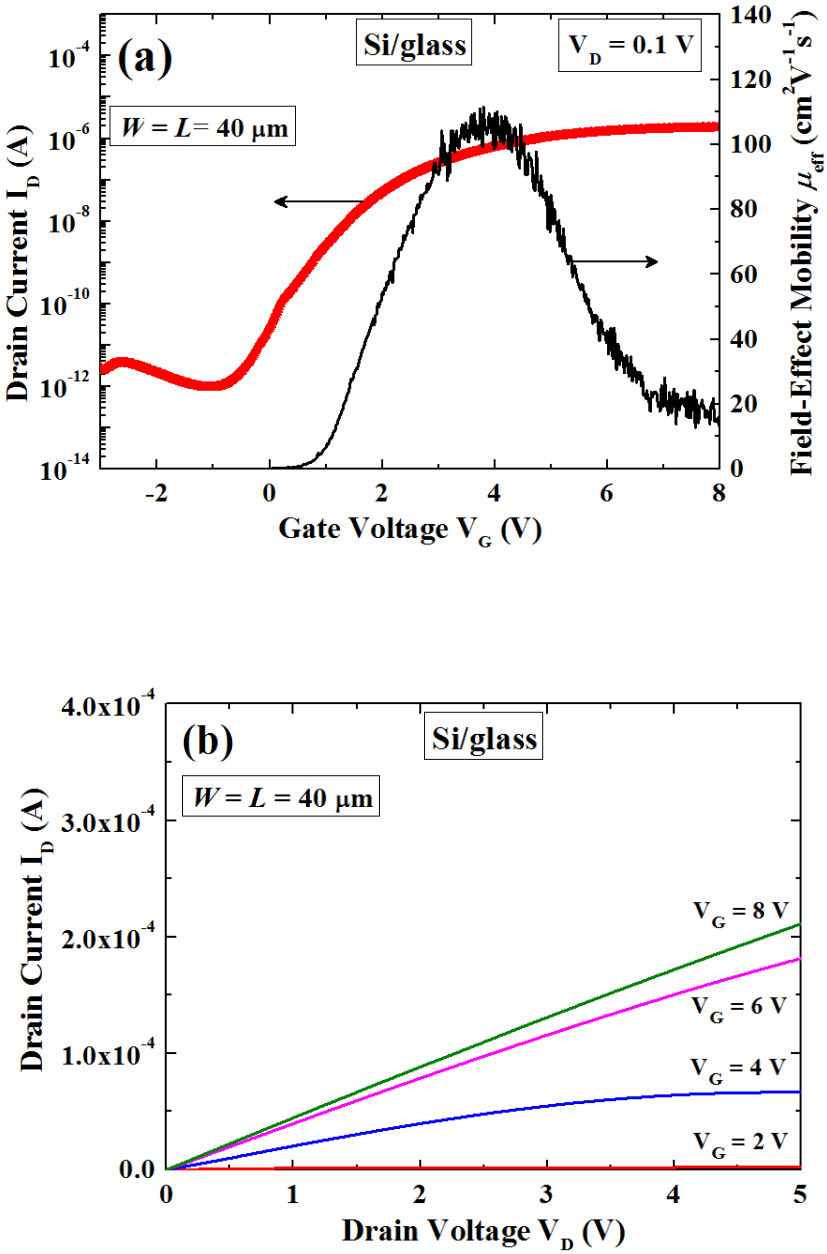

Fig. 7.16 (a) Transfer and (b) output characteristics of a fabricated poly-Si TFT for Si/glass structure with $W = L = 40$ μm.

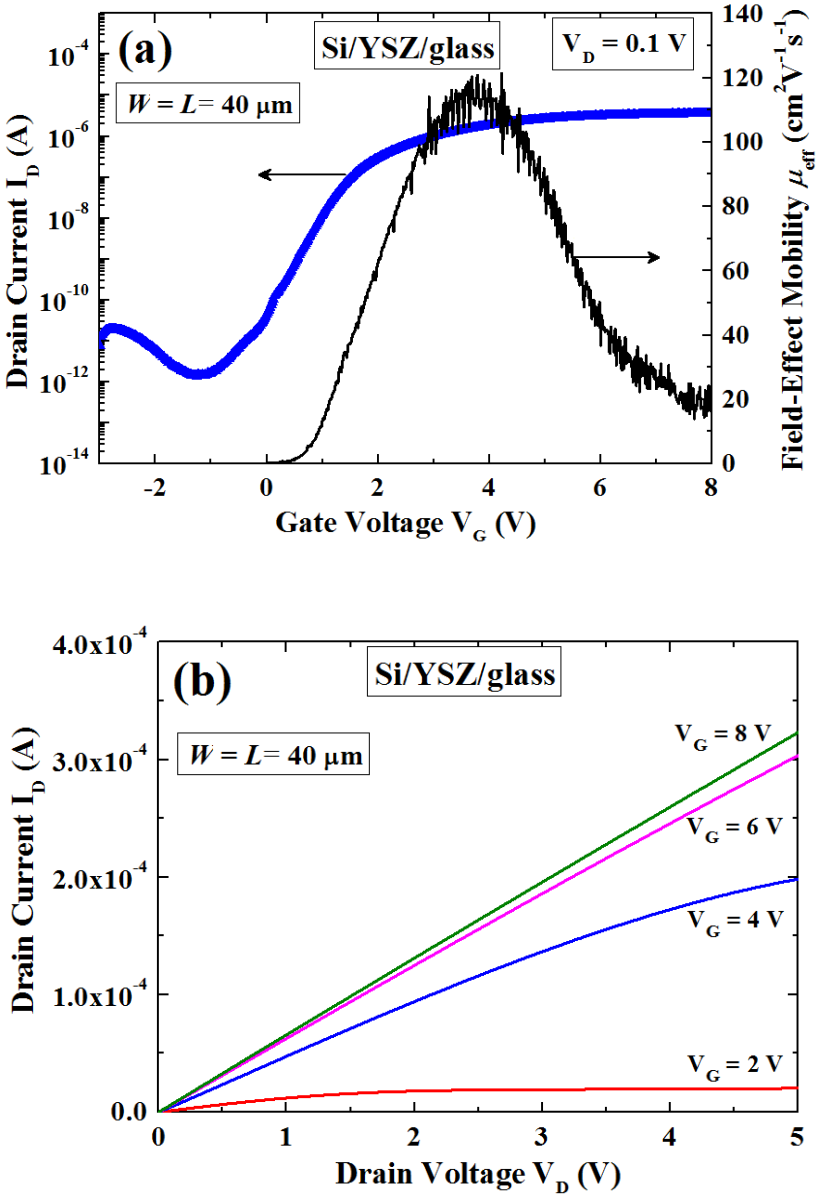

Fig. 7.17 (a) Transfer and (b) output characteristics of a fabricated poly-Si TFT for Si/YSZ/glass structure with $W = L = 40$ μm.

We estimated and summarized several important parameters of the device characteristics for the two structures of the Si/glass and Si/YSZ/glass. The field-effect mobility (μ_{eff}) and subthreshold swing (S.S) are evaluated from the linear and subthreshold regions, respectively, at V_D = 0.1 V. The ON/OFF current ratio is defined as the ratio of maximum drain current I_{Dmax} over minimum drain current I_{Dmin} within the measured range of I_D-V_G curve at V_D = 0.1 V. The threshold voltage (V_{th}) is determined by an interception of linear extrapolation of the I_D-V_G curve at V_D = 0.1 V. The detailed determination of these parameters is mentioned in Appendix K. Table 7.1 summarizes the average values of

device parameters together with their standard deviations of the TFTs with $W = L = 40$ μm for the two structures. For each structure, 15 TFTs were measured. It can be seen that the TFTs fabricated on the Si/YSZ/glass structure exhibit a relatively higher μ_{eff} with smaller deviation than those on the Si/glass. The average V_{th} and average S.S of TFTs fabricated on the Si/YSZ/glass are both smaller with smaller deviations than those on the Si/glass. On the other hand, the average ON/OFF current ratio of TFTs fabricated on the Si/YSZ/glass is a little lower than those on the Si/glass. The field-effect mobility, threshold voltage, and subthreshold swing are strongly affected by the presence of grain boundaries and defects inside the channel. Therefore, comparing to the TFTs fabricated on the Si/glass, the relatively better performance of the TFTs fabricated on the Si/YSZ/glass are considered owing to the better crystalline quality of the Si film on the YSZ/glass. This is thank to the crystallization-induction effect of the YSZ layer as discussed in the previous chapters. The superior device-to-device uniformity (expressed by smaller standard deviations) of the TFTs fabricated on the Si/YSZ/glass than on the Si/glass is considered to be due to the more uniform grain size and crystalline defects distributions in the Si films for the former than for the latter.

Table 7.1 Average values of field-effect mobility μ_{eff}, threshold voltage V_{th}, and subthreshold swing S.S together with their standard deviations, and average ON/OFF ratio of the TFTs with $W = L = 40$ μm for the two structures of the Si/glass and Si/YSZ/glass.

	Field-effect mobility μ_{eff} ($cm^2V^{-1}s^{-1}$)		**Threshold voltage V_{th} (V)**		**Subthreshold swing S.S (mV/dec.)**		**ON/OFF ratio**
	Average value	Standard deviation	Average value	Standard deviation	Average value	Standard deviation	Average value
Si/glass	40.3	28	2.83	0.78	426	99	1.74×10^6
Si/YSZ/glass	78.1	18	2	0.22	306	31	9.14×10^5

We also observed a hysteresis phenomenon in the fabricated TFTs for the both structures of the Si/glass and Si/YSZ/glass. Figure 7.18 shows transfer characteristics of the TFTs with $W = L = 40$ μm fabricated on both the Si/glass and Si/YSZ/glass structures. In the measurements, the gate voltage was swept forward from -5 to 8 V, and then backward from 8 to -5 V. It can be seen clearly that the threshold voltages of backward sweeping (BS) curve shift to lower values than those of the forward sweeping (FS). The

width of hysteresis for the Si/glass is a little larger than that for the Si/YSZ/glass. Further, the BS curve seems to show some improvement in subthreshold swing in comparison with the FS curve. At present, the reason for these hysteresises is not well known. In the C-V measurement, a hysteresis was observed in ion-drift type, which means the presence of mobile ions in the gate oxide. It is supposed that these mobile ions strongly affect the device performance of the fabricated TFTs and cause the hysteresis phenomenon. The drift ions are probably produced due to low-temperature fabrication process of the gate oxide of SiO_2. Since low-temperature process sometimes brings imperfect structure, impurities, and unreacted ions in produced films. If the post-annealing is performed at a higher temperature, e.g., 400 ^oC, the hysteresis width might be reduced. Also, these drift ions affect TFTs output characteristics like Figs. 17.6(b) and 17.7(b). Pinch-off voltage V_p is expressed by $V_p = V_G - V_{th}$. If V_{th} is a negative value due to ion drift effect, V_p should be a large positive value. For example, when V_{th} is -3 V as shown in the dashed circle A region of Fig. 7.18, V_p is 7 V for V_G = 4 V. Then, a linear region should be observed in TFT output characteristics like Figs. 7. 16(b) and 7.17 (b). But, if V_{th} is a positive value, we maybe observe a saturation region. From now on, we should further investigate to find causes for the hysteresis phenomenon clearly, including other unideal ones.

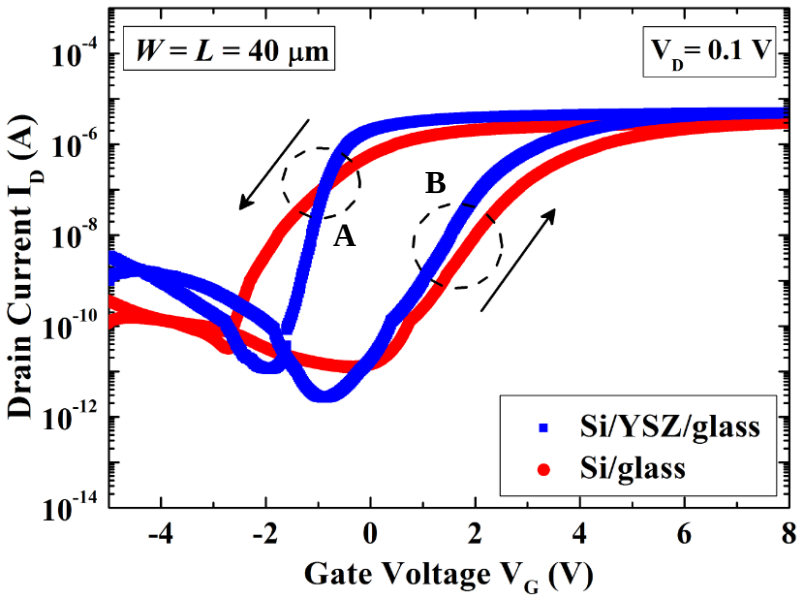

Fig. 7.18 Hysteresis phenomenon occurring in the transfer characteristics of fabricated poly-Si TFTs with *W* = *L* = 40 μm at V_D = 0.1 V for the two structures of the Si/glass and Si/YSZ/glass.

7.3 Summary

We measured the carrier concentration, Hall mobility, and conductivity of the Si films crystallized by pulsed laser in solid phase by using the two-step method and YSZ CI layer. The resistivity and AC Hall effect measurement results for both the undoped and doped Si films revealed that higher mobility and carrier concentration (therefore higher conductivities) are obtained for the Si/YSZ/glass structure, compared with those of the Si/glass. Therefore, we can conclude that Si films crystallized on the YSZ layers are more suitable for application in electronic devices. From these results, we can expect a high performance of TFTs made from an Si film crystallized on the YSZ layer by the two-step method.

Actually, we have fabricated poly-Si TFTs on the two structures of the Si/glass and Si/YSZ/glass. The device parameters of field-effect mobility μ_{eff}, threshold voltage V_{th}, subthreshold voltage S.S, and ON/OFF current ratio of the fabricated TFTs were estimated as well as their uniformity. It was found that the TFTs fabricated on the Si/YSZ/glass exhibit a relatively better performance and superior device-to-device uniformity than those on the Si/glass. This result is considered owing to the better crystalline quality of the Si film on the YSZ/glass and uniform distribution of grains as well as crystalline defects, which indicating effectiveness of the crystallization-induction effect of the YSZ layer. However, a hysteresis phenomenon was observed in the TFTs characteristics. Although the hysteresis mechanism is not well known at present, it might be related to the presence of mobile ions in the gate oxide.

Chapter 8:

General Conclusions and Future Prospects

In this study, in order to obtain a low-temperature poly-Si film with uniform grain size and crystallographic orientation, low impurities, and smooth surface, our laboratory has used a crystallization-induction (CI) layer of YSZ, which enhances the crystallization of a deposited poly-Si film due to its crystalline information. Further, to reduce the fabrication temperature to around room temperature and to reduce surface roughness as well as to avoid the diffusion of impurity from the CI-YSZ layer, we proposed to use the two-step irradiation method with pulsed laser annealing (PLA). To do this, we investigated the crystallization of a-Si films on YSZ layers by PLA. This study includes the two main parts. The first part is investigating and comparing crystalline quality of Si films crystallized on YSZ layers and on glass substrates by PLA. Thence, crystallinity information of the Si film including the CI effect of YSZ layer can be obtained. The second one is the proposal of a new irradiation method or the two-step method for further improving the crystallinity of Si films. The crystalline quality of Si films crystallized by the two-step method is investigated. In this chapter, the results and discussion of this study are summarized, followed by some suggestions for future works.

8.1 General conclusions

8.1.1 CI effect of YSZ layer on quality of crystallized Si film

Quality of the solid-phase crystallized Si films on the glass substrates with and without a YSZ-CI layer by PLA was investigated. The obtained results are as follows:

- For the Si/YSZ/glass, at a low irradiation energy density *E*, nucleation occurred faster at the YSZ interface than in the bulk of the a-Si film, which is considered thanks to the CI effect of the YSZ layer. This suggests that the nucleation sites can be controlled on the YSZ interface to make crystallization growth proceed to the film surface smoothly without random nucleation.
- It was revealed that the crystallization rate to *E* was lower for the Si/YSZ/glass than for the Si/glass. This is because the optical absorption in the Si film for the Si/YSZ/glass is lower than that for the Si/glass.

- At the same crystallization degree, crystalline quality of the Si film on the YSZ layer was better than that on the glass substrate. It can be considered that, in the Si/YSZ/glass, Si atoms are arranged more orderly during the phase transition from amorphous to crystalline and the defect density is lower than in the Si/glass. This may be due to the CI effect of the YSZ layer.
- The film tensile stress behavior was explained by the mass density change from the amorphous phase to the crystalline phase.
- The crystallization degrees of both the structures Si/glass and Si/YSZ/glass increased with the pulse number (or annealing time) and tended to saturate even at a short annealing time. This saturation behavior was found to be a self-limiting process, by which the crystallization of Si films can be performed in a relatively stable manner even if *E* fluctuates within a certain range during irradiation.

From the above results, it is expected that annealing with low *E* produces Si films with better crystallinity. However, since the crystallization rate is so low and the crystalline fraction is saturated at a short annealing time with self-limiting behavior, it should take a very long time or might be impossible to complete the crystallization. Annealing with high *E* can reduce the annealing time, but the crystallized Si film quality becomes poorer or more defective due to faster random nucleation and crystallization growth.

8.1.2 By using the two-step method, improving the Si film crystalline quality

On the basis of the aforementioned results, we proposed the two-step method to further improve the crystallinity of the Si films, and crystallized a-Si films on YSZ-CI layers by the two-step method with PLA without intentional melting. Their properties were investigated and compared with those obtained by the one-step method. We obtained the following results:

- The crystallization growth from the YSZ interface is more enhanced by the two-step method than by the one-step (or conventional) method. It was found that a higher crystallization degree, better crystalline quality, and a larger grain size were obtained by the two-step method, compared with the one-step method at the same total annealing time and lower total irradiation energy density.
- Comparing the two structures of Si/YSZ/glass and Si/glass at their own optimized irradiation conditions, we obtained a better crystalline quality in the former.

- Since the crystalline quality of Si films is much improved by the two-step method, we also proposed a three-step method for further improving crystalline quality of the Si film. Although crystalline fraction of the Si films obtained by the three-step method is a little higher than that of the two-step method, the film quality of the former seems to be inferior in comparison with the latter. Also, considering mass production, the three-step method is not suitable. Therefore, we decided to use the two-step method for next investigations.
- By applying the two-step method, we succeeded in crystallization of a-Si films on YSZ-CI layers under the crystallization condition for area expansion. Their film crystalline quality was investigated and compared with those of the one-step method. It was revealed that the crystallinity of the Si films is improved by the two-step method in the case of the sample moving during the irradiation as well as the static case. The (111)-preferential orientation of the YSZ was found to be transferred into the crystallized Si film, thanks to the CI effect of the YSZ. The smooth surface of the crystallized Si film and no incubation layer at the interface was obtained. The diffusion of Zr and Y from the YSZ layer into the crystallized Si film was found to be as small as or lower than the order of 10^{17} atoms/cm^3. However, these impurities should be further suppressed for device application.
- We also measured the carrier concentration, Hall mobility, and conductivity of the crystallized Si films by using the resistivity and AC Hall effect measurements. The results for both the undoped and doped Si films revealed that the higher mobility and carrier concentration (therefore higher conductivities) are obtained for the Si/YSZ/glass structure compared with those of the Si/glass.

8.1.3 Effect of metal films on enhancing crystalline quality of Si films

On the basis of the results obtained for the Si/glass and Si/YSZ/glass, we investigated crystalline quality of the **Si/YSZ/metal/glass** structure crystallized by both the one-step and two-step methods. It was found that higher crystallization degree and better crystalline quality were obtained by the two-step method compared with the one-step method at the same annealing time and lower total irradiation energy density. This indicates that the two-step method is also effective in improving crystalline quality of Si films on **YSZ/metal/glass**. Moreover, the metal layer has a small heating effect on enhancing crystalline quality of the Si film. Irradiation condition was optimized for bottom-gate poly-

Si TFTs fabrication. However, considering the occurrence of bubbles or holes on surface of the crystallized Si film, the **Si/YSZ/metal/glass** structure is not suitable for bottom-gate TFT fabrication.

8.1.4 Performance of the fabricated top-gate TFTs

The investigation of film crystalline quality reveals that Si films crystallized on the YSZ layers by the two-step method are more suitable for application in electronic devices. Moreover, the **Si/YSZ/metal/glass** structure is not suitable for bottom-gate TFT fabrication. Therefore, we proceeded the fabrication of top-gate TFTs on two structures of Si/glass and Si/YSZ/glass, in which Si films were crystallized by the two-step method with pulsed laser. The device parameters of field-effect mobility μ_{eff}, threshold voltage V_{th}, subthreshold voltage S.S, and ON/OFF current ratio of the fabricated TFTs were estimated as well as their uniformity. It was found that the TFTs fabricated on the Si/YSZ/glass exhibit a relatively better performance and superior device-to-device uniformity than those on the Si/glass. This result is considered owing to the better crystalline quality of the Si film on the YSZ/glass and uniform distribution of grains as well as crystalline defects, which indicating effectiveness of the crystallization-induction effect of the YSZ layer. However, a hysteresis phenomenon was observed in the TFTs characteristics. Although the hysteresis mechanism is not well known at present, it might be related to the presence of mobile ions in the gate oxide.

8.2 Future prospects

In this study, material properties of the Si thin films crystallized on the YSZ layers in solid phase by PLA method have been investigated. It is believed that Si films crystallized on the YSZ layers are more suitable for application in electronic devices than on the glass substrates. On the basis of the investigated results, we fabricated top-gate TFTs and investigated their characteristics. Although the fabricated TFTs exhibit appropriate operation with relatively high characteristics, hysteresis and other undesired phenomena occurred. Therefore, firstly, it is needed to further improve the film fabrication process as well as the crystallization process, using a CI layer of YSZ. Then, issues of TFTs should be solved and their performance should be improved. The future prospects can be concretized as follows:

8.2.1 Improving crystalline quality of Si films

a) Surface treatment of YSZ layer

Previous study pointed out that an a-Si film deposited on cleaned surface of a YSZ layer will crystallized at a lower temperature in SPC process, compared with on a glass substrate as mentioned in the chapter 1. It is considered that a cleaned surface of the YSZ layer can also enhance crystalline quality of the Si film. Therefore, in-situ cleaning of the YSZ surface in the Si film deposition chamber just before an a-Si film deposition can be considered as a method to obtain a better crystalline quality of poly-Si film. To do this, we will use a reflection high-energy electron diffraction (RHEED) beam to irradiate surface of the YSZ layer during the vacuum annealing process before an a-Si film deposition. We can expect that the electron beam irradiation has an effect on enhancement of a-Si crystallization with its better quality.

b) Reducing the diffusion of Zr and Y into the Si film

In chapter 5, we have discussed the reason of slight diffusion of Zr and Y into the Si film. This is because a certain amounts of chemically unstable Zr and Y due to HF dipping might remained on the YSZ surface before an a-Si film deposition. In order to reduce their diffusion, it is supposed that the cleaning process as well as the HF dipping before the a-Si film deposition should be optimized.

8.2.2 Improving performance of TFTs

Although the origin and mechanism of hysteresis in TFT operation have not been identified clearly at present, it is supposed that it is related to the mobile ions existing in the gate oxide. In order to reduce these mobile ions, after TFTs fabrication, we will perform a post-annealing at a higher temperature (e.g., 400 ^{o}C) than 350 ^{o}C at present, and/or longer time (e.g., 60 min) than 30 min at present. Further, in order to reduce the large subthreshold swing, the interface property between gate oxide layer and crystallized Si film should be improved by optimizing the oxide deposition and post-annealing conditions.

References

Chapter 1

1) J. E. Lilienfeld, "*Device for Controlling Electric Current*," US Pat. 1900018 (1933).

2) P. K. Weimer, Proc. IRE **50**, 1462 (1962).

3) T. P. Brody, J. A. Asars, and G. D. Dixon, IEEE Trans. Electron Dev. **ED-20**, 995 (1973).

4) Y. Kuo, The Electrochemical Society ***Interface*** • Spring, 55 (2013).

5) P. G. LeComber, W. E. Spear, and A. Ghaith, Electron. Lett. **15**, 179 (1979).

6) M. J. Powell, IEEE Trans. Electron Devices **36**, 2753 (1989).

7) M. J. Powell, Appl. Phys. Lett. **43**, 597 (1983).

8) F. R. Libsch and J. Kanicki, Appl. Phys. Lett. **62**, 1286 (1993).

9) P. F. Carcia, R. S. McLean, M. H. Reilly, and G. Nunes, Jr., Appl. Phys. Lett. **82**, 1117 (2003).

10) K. Nomura, H. Ohta, K. Ueda, T. Kamiya, M. Hirano, and H. Hosono, Science **300**, 1269 (2003).

11) K. Nomura, H. Ohta, A. Takagi, T. Kamiya, M. Hirano, and H. Hosono, Nature **432**, 488 (2004).

12) C. D. Dimitrakopoulos and P. R. L. Malenfant, Adv. Mater. **14**, 99 (2002).

13) H. Y. Choi, S. H. Kim, and J. Jang, Adv. Mater. **16**, 732 (2004).

14) P. G. le Comber, W. E. Spear, and A. Ghaith, Electron. Lett. **15**, 179 (1979).

15) T. Sameshima, S. Usui, and M. Sekiya, IEEE Electron Device Lett. **7**, 276 (1986).

16) A. Suresh and J. F. Muth, Appl. Phys. Lett. **92**, 033502 (2008).

17) J. K. Jeong, H. W. Yang, J. H. Jeong, Y.-G. Mo, and H. D. Kim, Appl. Phys. Lett. **93**, 123508 (2008).

18) K. Nomura, T. Kamiya, M. Hirano, and H. Hosono, Appl. Phys. Lett. **95**, 013502 (2009).

19) R. S. Potember, T. O. Poehler, and D. O. Cowan, Appl. Phys. Lett. **34**, 405 (1979).

20) L. Ma, S. Pyo, J. Ouyang, Q. Xu, and Y. Yang, Appl. Phys. Lett. **82**, 1419 (2003).

21) H. Matsumura, Jpn. J. Appl. Phys. **30**, L1522 (1991).

22) M. Zhu, Y. Cao, X. Guo, J. Liu, M. He, and K. Sun, Solar Energy Materials & Solar Cells **62**, 109 (2000).

23) J. K. Holt, M. Swiatek, D. G. Goodwin, R. P. Muller, W. A. Goddard III, and H. A. Atwater, Thin Solid Films **395**, 29 (2001).

24) Joo and Junghoon, J. Vac. Sci. Technol. A **18**, 2006 (2000).

25) P. Reinig, F. Fenske, W. Fuhs, A. Schopke, and B. Selle, Appl. Surf. Sci. **210**, 301 (2003).

26) D. Meakin, K. Papadopoulou, S. Friligkos, J. Stoemenos, P. Migliorato, and N. A. Economou, J. Vac. Sci. Technol. B **5**, 1547 (1987).

27) C. A. Dimitriadis, P. A. Coxon, L. Dozsa, L. Papadimitriou, and N. Economou, IEEE Trans. Electron Devices **39**, 598 (1992).

28) K. Pangal, J. C. Sturm, S. Wagner, and T. H. Buyuklimanli, J. Appl. Phys. **85**, 1900 (1999).

29) R. B. Iverson and R. Reif, J. Appl. Phys. **62**, 1675 (1987).

30) P. Kwizera and R. Reif, Appl. Phys. Lett. **41**, 379 (1982).

31) R.B. Iverson and R. Reif, Materials Letters **5**, 460 (1987).

32) T. Ohshima, T. Noguchi, and H. Hayashi, Jpn. J. Appl. Phys. **25**, L291 (1986).

33) N. Yamauchi, J-J. J. Hajja, and R. Reif, IEEE Trans. Electron Dev. **38**, 55 (1991).

34) R Kakkad, J. Smith, W. S. Lau, S. J. Fonash, and R Kerns, J. Appl. Phys. **65**, 2069 (1989).

35) G. Liu and S. J. Fonash, Appl. Phys. Lett. **55**, 660 (1989).

36) D. M. Moffatt, MRS Proc. **377**, 871 (1995).

37) J. N. Lee, Y. W. Choi, B. J. Lee, and B. T. Ahn, J. Appl. Phys. **82**, 2918 (1997).

38) F. Oki, Y. Ogawa, and Y. Fujiki, Jpn. J. Appl. Phys. **8**, 1056 (1969).

39) J. R. Bosnell and U. C. Voisey, Thin Solid Films **6**, 161 (1970).

40) S. R. Herd, P. Chaudhari, and M. H. Brodsky, J. of Non-Cryst. Solids **7**, 309 (1972).

41) R. C. Cammarata, C. V. Thompson, C. Hayzelden and K. N. Tu, J. Mater. Res. **5**, 2133 (1990).

42) S. Y. Yoon, K. H. Kim, C. O. Kim, J. Y. Oh, and J. Jang, J. Appl. Phys. **82**, 5865 (1997).

43) G. Radnoczi, A. Robertsson, H. T. G. Hentzell, S. F. Gong, and M.-A. Hasan, J. Appl. Phys. **69**, 6394 (1991).

44) S. W. Lee, Y. C. Jeon, and S. K. Joo, Appl. Phys. Lett. **66**, 1671 (1995).

45) S. W. Lee and S. K. Joo, IEEE Electron Device Lett. **17**, 160 (1996).

46) Z. H. Jin, G. A. Bhat, M. Yeung, H. S. Kwok, and M. Wong, J. Appl. Phys. **84**, 194 (1998).

47) F. Priolo and E. Rimini, Materials Science Reports **5**, 319 (1990).

48) L. A. Marques, M.-J. Caturla, T. D. d. l. Rubia, and G. H. Gilmer, J. Appl. Phys. **80**, 6160 (1996).

49) J. S. Im and H. A. Atwater, Appl. Phys. Lett. **59**, 2314 (1991).

50) C. Spinella, A. Battaglia, F. Priolo, and S. U. Campisano, Europhys. Lett. **16**, 313 (1991).

51) A. Yin and S. J. Fonash, IEDM Technical Digest., 397 (1993).

52) A. Yin and S. J. Fonash, J. Vac. Sci. Technol. **12**, 1237 (1994).

53) A. Yin, S. J. Fonash, D. M. Reber, Y. M. Li, and M. Bennett, MRS **345**, 81 (1994).

54) K. Pangal, J. C. Sturm, and S. Wagner, IEDM Technical Digest., 371 (1998).

55) Norbert H. Nickel, *Laser crystallization of silicon*, vol. **75** (Elsevier, 2003) chap. 1.

56) R. A. Lemons, M. A. Bosch, A. H. Dayem, J. K. Grogan, and P. M. Mankiewich, Appl. Phys. Lett. **40**, 469 (1982).

57) T. E. Dyer, J. M. Marshall, W. Pickin, A. R. Hepburn and J. F. Davies, J. Non-Cryst. Solids **164-166**, 1001 (1993).

58) T. Sameshima, M. Hara, and S. Usui, Jpn. J. Appl. Phys. **28**, L2131 (1989).

59) J. C. C. Fan and H. J. Zeiger, Appl. Phys. Lett. **27**, 224 (1975).

60) S. Hana, Dr. Thesis, School of Materials Science, Japan Advanced Institute of Science and Technology (JAIST), Japan (2009).

61) C. W. Han, J. H. Park, S. M. Han, M. K. Han, K. Y. Kim, I. J. Chung, S. J. Yun, and J. W. Lim, Jpn. J. Appl. Phys. **45**, 4365 (2006).

62) D. Y. Kim, B. J. Ahn, S. I. Moon, C. Y. Won, and J. Yi, Sol. Energy Mater. Sol. Cells **70**, 415 (2002).

63) J. K. Ko, D. Y. Kim, J. H. Park, S. W. Choi, S. H. Park, and J. Yi, Thin Solid Films **427,** 259 (2003).

64) S. C. Hwang, H. G. Lee, and H. S. Shin, Korean J. Chem. Eng., **15**(3), 243 (1998).

65) http://www.doitpoms.ac.uk/tlplib/fuel-cells/sofc_electrolyte.php.

66) I. Golecki, H. M. Manasevit, L. A. Moudy, J. J. Yang, and J. E. Mee, Appl. Phys. Lett. **42**, 501 (1983).

67) S. Horita, M. Muranaka, and T. Fujiyama, Jpn. J. Appl. Phys. **34**, 1942 (1995).

68) V. R. PaiVerneker, A. N. Petelin, F. J. Crowne, and D. C. Nagle, Phys. Rev. B **40**, 8555 (1989).

69) S. J. Wang, C. K. Ong, S. Y. Xu, P. Chen, W. C. Tjiu, A. C. H. Huan, W. J. Yoo, J. S. Lim, W. Feng, and W. K. Choi, Semicond. Sci. Technol.**16**, L13 (2001).

70) S. Horita and H. Sukreen, Appl. Phys. Express **2**, 041201 (2009).

71) S. Hana, T. Akahori, and S. Horita, Proc. 16th Int. Display Workshops (IDW'09), 2009, p. 271.

72) S. Horita and S. Hana, Jpn. J. Appl. Phys. **49**, 105801 (2010).

Chapter 2

73) G. L. Olson and J. A. Roth, Mater. Sci. Rep. **3**, 1 (1988), and references therein.

74) K. Pangal, J. C. Sturm, S. Wagner, and T. H. Buyuklimanli, J. Appl. Phys. **85**, 1900 (1999).

75) R. B. Iverson and R. Reif, J. Appl. Phys. **62**, 1675 (1987).

76) L. Csepregi, J. W. Mayer, and T. W. Sigmon, Phys. Lett. A **54**, 157 (1975).

77) K. N. Tu, J. W. Mayer, and L. C. Feldman, in *Electronic Thin Film Science for Electrical Engineers and materials Scientists*, ed. D. Johnstone (Macmillan, USA, 1992) pp. 256-263.

78) K. N. Tu, D. A. Smith, and B. Z. Weiss, Phys. Rev. B **36**, 8948 (1987).

79) D. Turnbull, Mater. Res. Soc. Symp. Proc. **51**, 71 (1985).

80) F. Spaepen and D. Turnbull, in *Laser Annealing of Semiconductors*, eds. J. M. Poate and J.W. Mayer (Academic Press, New York, 1982) pp. 15-42.

81) E. P. Donovan, F. Spaepen, D. Turnbull, J. M. Poate and D. C. Jacobson, Appl. Phys. Lett. **42**, 698 (1983).

82) E.P. Donovan, F. Spaepen, D. Turnbull, J. M. Poate and D. C. Jacobson, J. Appl. Phys. **57**, 1795 (1985).

Chapter 3

83) S. Ray, S. Mukhopadhyay, T. Jana, and R. Carius, J. Non-Cryst. Solids **299–302**, 761 (2002).

84) R. Tsu, J. Gonzalez-Hernandez, S. S. Chao, S. C. Lee, and K. Tanaka, Appl. Phys. Lett. **40**, 534 (1982).

85) T. Okada, T. Iwaki, H. Karasawa, and K. Yamamoto, Jpn. J. Appl. Phys. **24**, 161 (1985).

Chapter 4

86) S. Hana, K. Nishioka, and S. Horita, Thin Solid Films **517**, 5830 (2009).

87) S. Horita and S. Hana, Jpn. J. Appl. Phys. **49**, 105801 (2010).

88) S. Horita, K. Kanazawa, K. Nishioka, K. Higashimine, and M. Koyano, MRS Proc. **910**, 577 (2006).

89) L. Haji, P. Joubert, M. Guendouz, N. Duhamel, and B. Loisel, MRS Proc. **230**, 177 (1992).

90) J. N. Lee, B. J. Lee, D. G. Moon, and B. T. Ahn, Jpn. J. Appl. Phys. **36**, 6862 (1997).

91) D. Edwards, in *Handbook of Optical Constants of Solids*, ed. E. Palik (Academic Press, New York, 1985) pp. 564, 578.

92) S. Heiroth, R. Ghisleni, T. Lippert, J. Michler, and A. Wokaun, Acta Mater. **59**, 2330 (2011).

93) S. Horita, H. Kaki, and K. Nishioka, Jpn. J. Appl. Phys. **46**, 3527 (2007).

94) K. Kitahara, K. Suga, A. Hara, and K. Nakajima, Jpn. J. Appl. Phys. **35**, L1473 (1996).

95) K. Kitahara, Y. Ohashi, Y. Katoh, A. Hara, and N. Sasaki, J. Appl. Phys. **95**, 7850 (2004).

96) S. M. Sze, in *Physics of Semiconductor Devices* (Wiley, New York, 1969) 2nd ed., p. 851.

97) S.-G. Ryu, I. Gruber, C. P. Grigoropoulos, D. Poulikakos, and S.-J. Moon, Thin Solid Films **520**, 6724 (2012).

98) P. Lengsfeld, N. H. Nickel, C. Genzel, and W. Fuhs, J. Appl. Phys. **91**, 9128 (2002).

99) S.-C. Hwang, H.-G. Lee, and H.-S. Shin, Korean J. Chem. Eng. **15**, 243 (1998).

100) H. Kumomi and T. Yonehara, J. Appl. Phys. **75**, 2884 (1994).

101) A. K. Kalkan and S. J. Fonash, MRS Proc. **558**, 225 (1999).

Chapter 5

102) Y. Komem and Z. A. Weinberg, J. Appl. Phys. **56**, 2213 (1984).

103) S. Horita and S. Hana, Jpn. J. Appl. Phys. **49**, 105801 (2010).

104) A. Hara, K. Kitahara, K. Nakajima, and M. Okabe, Jpn. J. Appl. Phys. **38**, 6624 (1999).

105) R. G. Wilson, F. A. Stevie, and C. W. Magee, in *Secondary Ion Mass Spectroscopy* (Wiley, New York, 1989), Chap. 2.3.

106) W.-J. Qi, R. Nieh, B. H. Lee, L. Kang, Y. Jeon, K. Onishi, T. Ngai, S. Banerjee, and J. C. Lee: IEDM Tech. Dig., 1999, p. 145.

107) B. W. Busch, J. Kwo, M. Hong, J. P. Mannaerts, B. J. Sapjeta, W. H. Schulte, E. Garfunkel, and T. Gustafsson, Appl. Phys. Lett. **79**, 2447 (2001).

108) E. P. Donovan, F. Spaepen, D. Turnbull, J. M. Poate, and D. C. Jacobson, Appl. Phys. Lett. **42**, 698 (1983).

Chapter 6

109) David R. Lide, in "*Handbook of Chemistry and Physics*", 80th edition (CRC Press LLC, USA, 1999), p. 4-31.

110) H. Sato, H. Nakamura, Y. Masuda, T. Nakazono, M. Kobayashi, K. Mori, and N. Harada, IEEE Transactions on Consumer Electronics **41**, 1181(1995).

Chapter 7

111) Charles Kittel, in *Introduction to Solid State Physics* (8th edition), (John Willey & Sons, Inc., 2005), pp. 213-214.

112) J. Y. W. Seto, J. Appl. Phys. **46**, 5247 (1975).

113) M. M. Mandurah, K. C. Saraswat, and T. I. Kamins, IEEE Trans. Electron Devices **ED-28**, 1163 (1981).

114) S. M. Sze and Kwok K. Ng, in *Physics of Semiconductor Devices* (3rd edition), (John Willey & Sons, Inc., 2007), p. 22.

115) R. S. Muller, T. I. Kamins, and M. Chan, in *Device Electronics for Integrated Circuits* (3rd edition), (John Willey & Sons, Inc., 2003), p. 54.

116) H. Lemke, phys. stat. sol. (a) **122**, 617 (1990).

Appendixes:

117) K. Wasa, in *Handbook of Sputter Deposition Technology* (Elsevier Inc., 2012) 2nd ed., pp. 322-323.

118) S. Hana, Dr. Thesis, School of Materials Science, Japan Advanced Institute of Science and Technology (JAIST), Japan (2010).

119) S. Horita, K. Toriyabe, and K. Nishioka, Jpn. J. Appl. Phys. **48**, 035502 (2009).

120) Charles Kittel, in *Introduction to Solid State Physics* (8th edition), (John Willey & Sons, Inc., 2005), p. 25.

121) Gardiner, in *Practical Raman spectroscopy*, (Springer – Verlag, 1989), p. 84.

122) Mark Fox, in *Optical properties of solids*, (Oxford University Press Inc., 2001), pp. 218-222.

123) D. R. Lide, in *Handbook of Chemistry and Physics*, 80th edition (CRC Press LLC, USA, 1999), p. 12-146.

124) A. Ichimiya and P. I. Cohen, in *Reflection High Energy Electron Diffraction*, (Cambridge University Press, 2004), pp. 1-10.

125) D. McMullan, Scanning **17**, 175 (1995).

126) Nuts & Bolts, NH Materials Laboratory **8** (1998).

127) L. Reimer and H. Kohl, in *Transmission Electron Microscopy: Physics of Image Formation* (5th edition), (Springer, 2008), pp. 1-5.

128) R. G. Wilson, F. A. Stevie, and C. W. Magee, in *Secondary Ion Mass Spectrometry*: *A Practical Handbook for Depth Profiling and Bulk Impurity Analysis*, (John Wiley & Sons, 1989), p. 8.

129) R. S. Muller and T. I. Kamins, in *Device Electronics for Integrated Circuits*, (3rd edition), (John Wiley & Sons, 2003), pp. 39-41.

130) User's Manual of Model 8403 AC/DC Hall Effect Measurement System, ToYo Corporation.

Research Achievements

I. Journal publications

1. **Mai Thi Kieu Lien** and Susumu Horita: "*Raman Spectra Analysis of Si Films Solid-Phase-Crystallized on Glass Substrates by Pulse Laser with Crystallization-Induction Layers of Yttria-Stabilized Zirconia*", Jpn. J. Appl. Phys. **53**, 03CB01 (2014). (Chapter 4 is referred from this paper.)

2. **Mai Thi Kieu Lien** and Susumu Horita: "*Improving Crystalline Quality of Poly-Si Thin Films Crystallized on Yttria-Stabilized Zirconia Crystallization-Induction Layers by the Two-step Irradiation Method of Pulse Laser Annealing",* Jpn. J. Appl. Phys. **54**, 03CA01(2015). (Chapter 5 is referred from this paper.)

3. **Mai Thi Kieu Lien** and Susumu Horita: "*Material Properties of Pulsed-Laser Crystallized Si Thin Films Grown on YSZ Crystallization-Induction Layers by Two-Step Irradiation Method*" (submitted).

II. International conferences

1. **Mai Thi Kieu Lien**[o] and Susumu Horita: "*Effect of a Stimulation Layer on Solid-Phase Crystallization of an Amorphous Si Film by Pulse Laser Irradiation*", The 20th Active Matrix & Flat Panel Display (AM-FPD'13), Kyoto, Japan (July, 2013), P–L5, pp.175–176. (poster, underwent a peer review)

2. **Mai Thi Kieu Lien**[o] and Susumu Horita: "*Improving Crystalline Quality of Si Thin Films Solid-Phase Crystallized on Yttria-Stablized Zirconia Layers by Pulse Laser*", The 20th International Display Workshop (IDW'13), Sapporo, Japan (December, 2013), FMCp–29L, pp. 655–656. (poster, underwent a peer review)

3. **Mai Thi Kieu Lien**[o] and Susumu Horita: "*Improvement of Crystalline Quality of Poly-Si Thin Films Crystallized on YSZ Layers by New Two-Step Irradiation Method with PLA*", The 21st Active Matrix & Flat Panel Display (AM-FPD'14), Kyoto, Japan (July, 2014), P–31, pp. 185–188. (poster, underwent a peer review)

4. **Mai Thi Kieu Lien**[o], Masayuki Yamano, Tatsuaki Hirata, Shin-Ichiro Kuroki, and Susumu Horita: "*Area Expansion of Crystallized Si Films on YSZ Layers by Two-*

step Method in PLA", The 21st International Display Workshop (IDW'14), Sapporo, Japan (December, 2014), AMD8–2L, pp. 259–260. (oral, underwent a peer review)

5. **Mai Thi Kieu Lien[o]** and Susumu Horita: "*Temperature Dependences of Conductivity in Undoped and Doped Poly-Si Thin Films Grown on YSZ Crystallization-Induction Layers by Two-Step Irradiation Method with Pulsed Laser*", The 22nd Active Matrix & Flat Panel Display (AM-FPD'15), Kyoto, Japan (July, 2015), L-2, pp. 225–226. (oral, underwent a peer review)

III. Domestic conferences

1. **Mai Thi Kieu Lien[o]**, Kazuhide Mochizuki, and Susumu Horita: *"Improvement of Solid Phase Crystallization of an Si Film on a YSZ Gate Insulator with a Bottom Gate Electrode"*, The Japan Society of Applied Physics (JSAP), 73rd Autumn Meeting, Matsuyama, Ehime, Japan (September, 2012). (poster, non-underwent a peer review)
2. **Mai Thi Kieu Lien[o]**, Kazuhide Mochizuki, and Susumu Horita: *"Properties of the Low-Temperature Polycrystalline Silicon Film on Bottom Gate Electrode by Using Yttria-Stabilized Zirconia Stimulation Layer and Solid Phase Crystallization Methods"*, The 9th Thin Film Materials & Devices Meeting (TFMD 9th), Nara, Japan (November, 2012). (poster, underwent a peer review)
3. Kazuhide Mochizuki[o], **Mai Thi Kieu Lien**, and Susumu Horita: *"Solid Phase Crystallization of an Amorphous Si Film on a High Y Ratio Stimulation Layer and Si Crystalline Seed Layer"*, The 9th Thin Film Materials & Devices Meeting (TFMD 9th), Nara, Japan (November, 2012). (poster, underwent a peer review)
4. Kazuhide Mochizuki[o], **Mai Thi Kieu Lien**, and Susumu Horita: *"Solid Phase Crystallization of an Amorphous Si Film on a Crystallization-Induction Layer by Pulse Laser Irradiation"*, The Japan Society of Applied Physics (JSAP), 60th Spring Meeting, Kanagawa, Japan (March, 2013). (oral, non-underwent a peer review)
5. **Mai Thi Kieu Lien[o]** and Susumu Horita: *"Comparison of Crystalline Quality of SPC Si Films Grown on YSZ Layers with That on Glass Substrates in Pulse Laser Annealing"*, The Japan Society of Applied Physics (JSAP), 74th Autumn Meeting, Kyoto, Japan (September, 2013). (oral, non-underwent a peer review)
6. **Mai Thi Kieu Lien[o]** and Susumu Horita: *"Irradiation Time Dependence of*

Crystallinity of Solid-Phase Crystallized Silicon Thin Films on Crystallization-Induction Layers of Yttria-Stabilized Zirconia by Using Pulse Laser", The 10th Thin Film Materials & Devices Meeting (TFMD 10th), Kyoto, Japan (November, 2013). (oral, underwent a peer review)

7. **Mai Thi Kieu Lien[o]** and Susumu Horita: *"Improving Crystalline Quality of Pulsed-Laser-Microcrystallized Si Thin Films by the Two-Step Irradiation Method"*, The Japan Society of Applied Physics (JSAP), 61st Spring Meeting, Kanagawa, Japan (March, 2014). (oral, non-underwent a peer review)

8. **Mai Thi Kieu Lien[o]** and Susumu Horita: *"Pulsed-Laser-Microcrystallization of Si Thin Films on Metal Film with Crystallization-Induction Layers of YSZ by the Two-Step Irradiation Method"*, The Japan Society of Applied Physics (JSAP), 75th Autumn Meeting, Hokkaido, Japan (September, 2014). (poster, non-underwent a peer review)

9. **Mai Thi Kieu Lien[o]** and Susumu Horita: *"Application of Two-Step Irradiation Method to a Large Area for Pulsed-Laser Crystallized Poly-Si Thin Films on YSZ"*, The 11th Thin Film Materials & Devices Meeting (TFMD 11th), Kyoto, Japan (November, 2014). (oral, underwent a peer review)

10. **Mai Thi Kieu Lien[o]** and Susumu Horita: *"First Trial Fabrication of Poly-Si TFTs using Crystallization-Induction Layers of Yttria-Stabilized Zirconia and Pulsed Laser Annealing Crystallization Methods"*, The Japan Society of Applied Physics (JSAP), 62nd Spring Meeting, Tokyo, Japan (March, 2015). (poster, non-underwent a peer review)

11. **Mai Thi Kieu Lien[o]** and Susumu Horita: *"Electrical Properties of Pulsed-Laser Crystallized Poly-Si Thin Films Grown on YSZ Crystallization-Induction Layers by Two-Step Irradiation Method"*, The Japan Society of Applied Physics (JSAP), 76th Autumn Meeting, Nagoya, Japan (September, 2015). (poster, non-underwent a peer review)

12. **Mai Thi Kieu Lien[o]** and Susumu Horita: *"Electrical Properties of Pulsed-Laser Crystallized Si Thin Films Grown on YSZ Crystallization-Induction Layers by Two-Step Irradiation Method"*, The 12th Thin Film Materials & Devices Meeting (TFMD 12th), Kyoto, Japan (November, 2015). (submitted)

IV. Awards

1. The 20th International Display Workshop (IDW'13) Outstanding Poster Paper Award (December 2013).
2. The Electrical Science and Engineering Promotion Student Paper Award (2013). (The former name is OHM Technology Award)
3. Marubun Research Promotion Foundation Grant (2014). (This Grant supported 1,500,000 Japanese yen for research activities from Apr. 2014 to Mar. 2015)

Appendix A:

Films Cleaning Processes

A.1 Substrate cleaning before a YSZ layer deposition

Figure A.1 shows a substrate cleaning process before the deposition of YSZ layer. First, the substrate is cleaned with Semico Clean 56 glass cleaner for 5 min in ultrasonic to remove adsorbed contaminants from the atmosphere. Then, it is rinsed twice with deionized water (DIW) in ultrasonic to remove Semico Clean 56 solution. Next, the substrate is rinsed with ethanol in ultrasonic to further cleaning the surface. After that, it is dipped in boiled ethanol for ten minutes. Finally, it is dried with nitrogen gun.

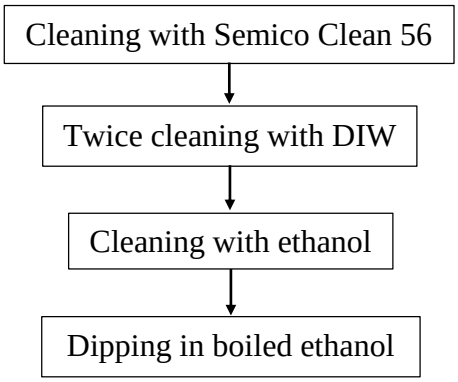

Fig. A.1 Substrate cleaning process sequence before YSZ film deposition.

A.2 Cleaning and setting processes of a YSZ/glass film before deposition of an a-Si film

A chemical cleaning process of a YSZ/glass film before an a-Si film deposition is shown in Fig. A.2. The cleaning process can be divided into three main parts of pre-cleaning, HF-dipping, and rinsing. The pre-cleaning consists of three steps, starting from cleaning with DIW to cleaning with ethanol, followed by rinsing with DIW. It is known that the as-deposited YSZ layer surface is dirty because of the exposure to the atmosphere when the sample is stored and transported in the

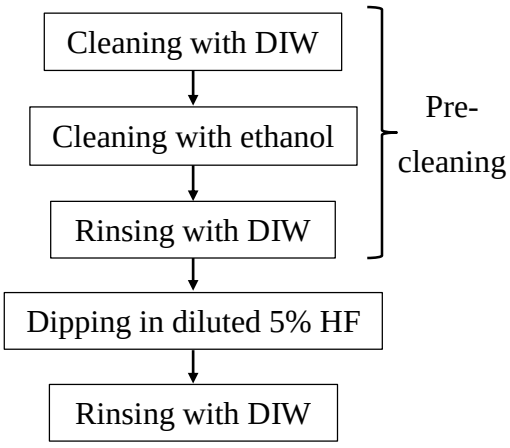

Fig. A.2 YSZ/glass film cleaning process sequence before a-Si film deposition.

laboratory environment. These contaminants will be removed roughly by the pre-cleaning process. After that, the heavily contaminated and damaged surface of the as-deposited YSZ layer is removed more effectively by dipping in diluted 5 % HF for 3 min. The sample is then rinsed in DIW to remove HF and fluorine (F) from the YSZ layer surface. Finally, it is dried with nitrogen gun. The pre-cleaning and rinsing processes are carried out in ultrasonic for 3 min.

The cleaned YSZ/glass sample is then put on a molybdenum sample holder with indium (In) as a binder in order to increase the thermal contact between the holder and the substrate, which increases the heating uniformity for the sample. First, the sample holder is heated up to 250 ^{o}C by using hot plate. Then, a small amount of pure In is put on the sample holder. Under the condition of 250 ^{o}C, In is quickly melted because it has a low melting point of 156.60 ^{o}C. After that, the melting In is spread out an area which equals in size to the sample. Next, the sample is put on the sample holder carefully.

A.3 Cleaning process of an as-deposited a-Si film before crystallization

The as-deposited a-Si film is cleaned with Radio Corporation of America (RCA) method before the crystallization. RCA cleaning method involves three main steps: removal of the organic contaminants, removal of thin oxide layer, and removal of ionic contamination. The Si wafer or glass substrate is prepared by soaking them in DI water. The first step is performed with a 1:1:4 solution of NH_4OH (ammonium hydroxide) + H_2O_2 (hydrogen peroxide) + H_2O (water) at 75 or 80 °C typically for 10 minutes. This treatment results in the formation of a thin silicon dioxide layer (about 0.1 nm) on the Si surface or glass substrate, along with a certain degree of metallic contamination (notably Iron) that will be removed in subsequent steps. This is followed by transferring the wafer or glass substrate into a DI water bath. The second step is a short immersion in a 1:50 solution of HF + H_2O at 25 °C, in order to remove the thin oxide layer and some fraction of ionic contaminants. The third and last step is performed with a 1:1:6 solution of HCl + H_2O_2 + H_2O at 75 or 80 °C. This treatment effectively removes the remaining traces of metallic (ionic) contaminants.

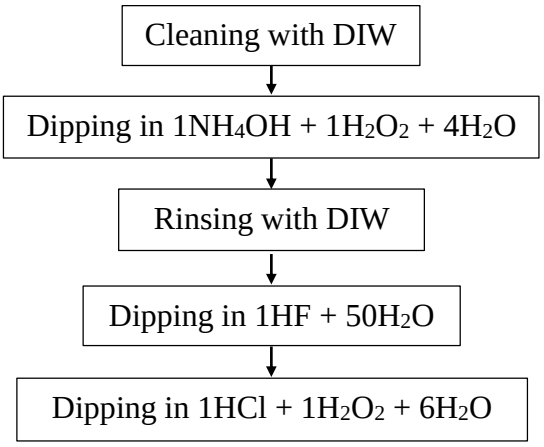

Fig. A.3 RCA cleaning method.

Appendix B:

Deposition Modes for YSZ Layers

Generally, the changes in condition of the metallic target surface are affected by the reactive gas flow. In the deposition of YSZ film, sputtering target consist of (Zr + Y) metallic cathode target. Sputtering deposition is conducted at (Ar + O_2) mixed gases. The oxygen is the reactive gas element, which will oxidize the metallic target surface at a certain flow rate or partial pressure. An increase in reactive-gas injection causes an increase in the density of reactive species on the cathode surface and/or growing surface of thin films. The reactive gas elements are incorporated in the deposited thin films. Depending on the flow of reactive gas, operating can be divided into two distinct regions, which are a metallic mode and a compound (or in our case, oxide) mode. The former occurs at a low flow rate of oxygen gas whereas the latter occurs at a high flow rate of oxygen gas. Figures B.1(a) and (b) show the schematic illustrations of the metallic and oxide modes, respectively. In the metallic mode, the target surface is free from reaction products and pure metal particles are sputtered. The reactive gas is absorbed by or reacted with the sputtered metal atoms at the substrate surface, so that an oxide film is deposited. For the oxide mode, the target surface is completely covered with a thin oxide layer. Oxide particles are sputtered from this layer. The sputtering yield of the oxide particles in most cases is lower, resulting in a lower deposition rate, than that in the metallic mode. The

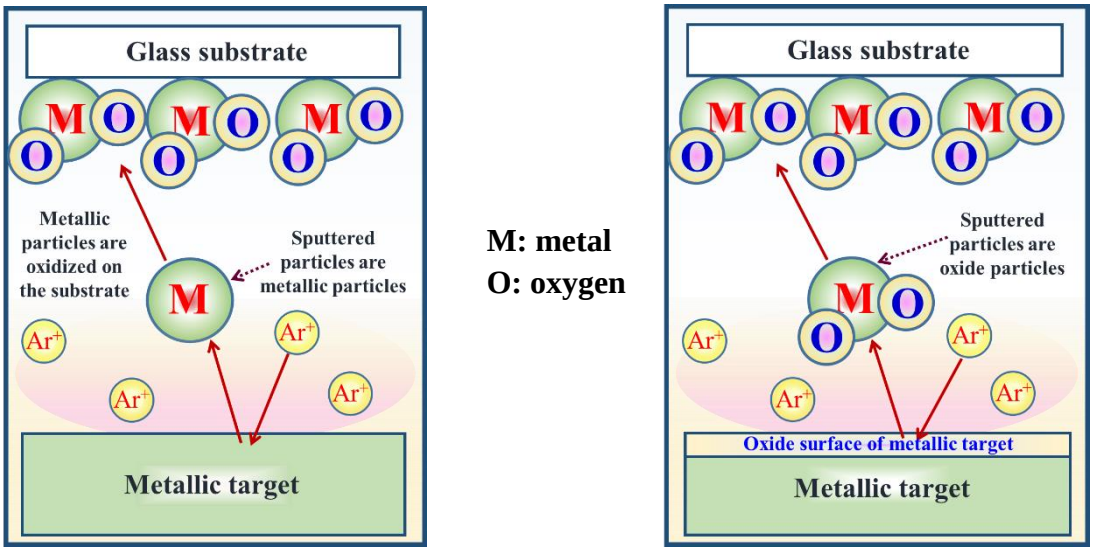

(a) Metallic mode **(b) Oxide mode**

Fig. B.1 Schematic illustration of deposition modes for YSZ layers.

transition between both modes is normally abrupt and exhibits a hysteresis behavior, for example in the discharge, as shown in Fig. B.2.

Figure B.2 (a) shows the relationship between discharge voltage and O_2 flow rate with a total pressure of 1 mTorr from the literature,[117] and a similar characteristic is observed in our work as shown in Fig. B.2(b).[118] The closed and open circles represent the increasing stage from 0% to 11% of O_2 flow rate and decreasing stage from 11% to 0%, respectively. In Fig. B.2(a), the drop in discharge voltage from 530 to 390 V at point B in the increasing stage is attributed to the formation of oxides on the target surface. This oxide is removed when the O_2 flow rate reduced to 4% in the decreasing stage where the oxygen flow can no longer maintain the oxide layer during the continuous sputtering. The target surface now becomes metallic again. It is supposed that emission of the secondary electrons from the

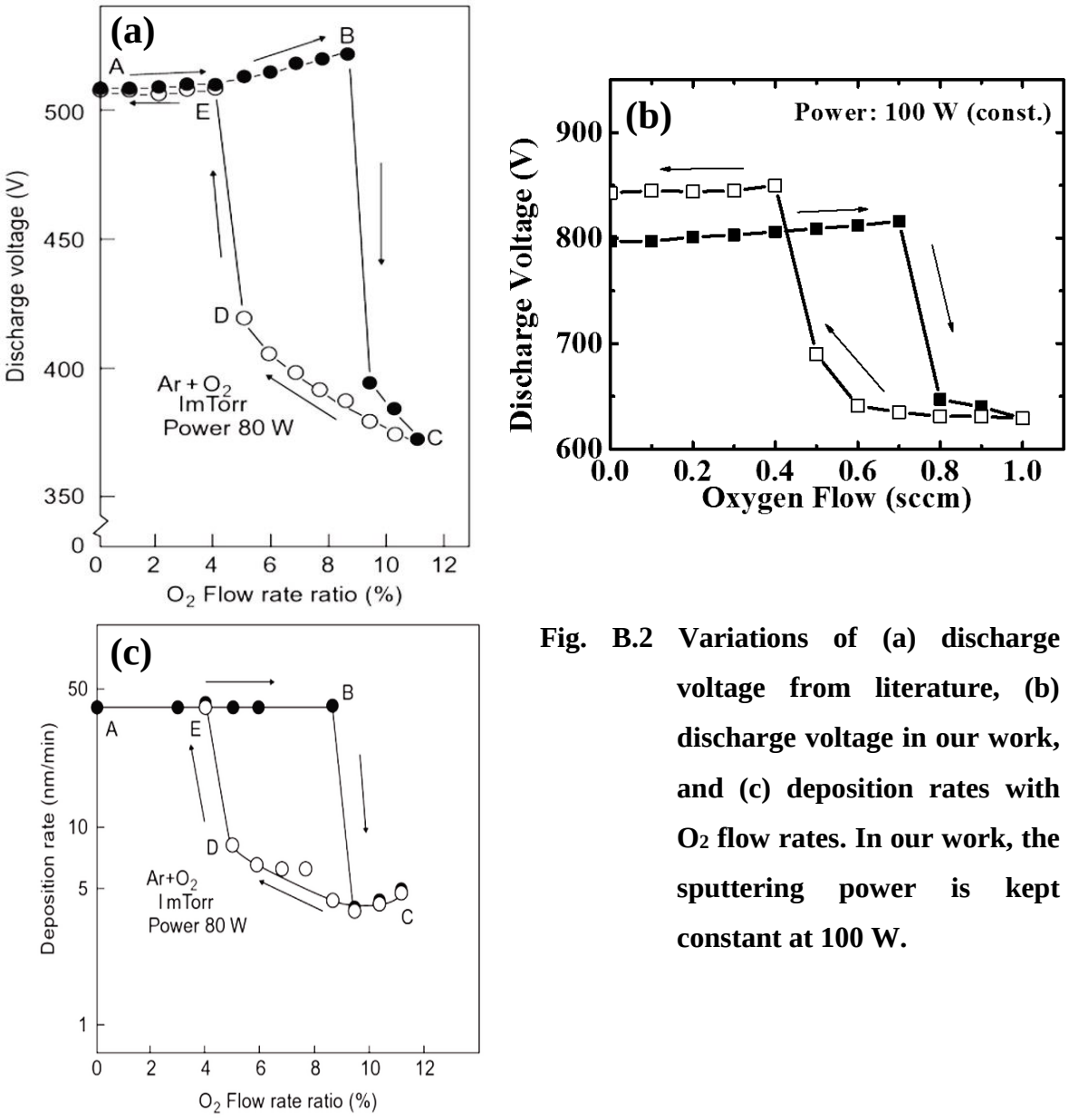

Fig. B.2 Variations of (a) discharge voltage from literature, (b) discharge voltage in our work, and (c) deposition rates with O_2 flow rates. In our work, the sputtering power is kept constant at 100 W.

target surface is one of the causes for the changes in discharge voltage. Normally, the emission coefficient of the secondary electrons from an oxide surface is larger than that from metal surface. This means that more secondary electrons are emitted from the oxide surface than from the metallic surface, resulting in a higher discharge current. If the sputtering system power is kept constant, the increase in discharge current leads to the decrease in discharge voltage, and vice versa. In our work [Fig. B.2(b)], the final discharge voltage after decreasing oxygen flow to 0 sccm is higher than the voltage at the initial stage of the experiment. The reason can be considered that our target surface is partially oxidized before the experiment.

Since the sudden decrease of the discharge voltage is drastic, the deposition rate will also be affected and change with the O_2 flow rate. Figure B.2(c) is a plot of deposition rate versus oxygen flow rate. It also shows a hysteresis loop similar to Fig. B.2(a), the deposition rate is almost constant at 40 nm/min from A to B for increasing O_2 flow rate from zero, and the films obtained are metallic. At O_2 flow rates greater than 10%, the target is completely covered with an oxide layer which causes a smaller sputtering yield so that the deposition rate decreases drastically to 4 nm/min and the film becomes a transparent oxide material. Upon reducing the O_2 flow rate from C to A, the deposition rate returns to the original metallic mode at point E.

Appendix C:

Capping and Passivation Layers Deposition by APCVD, and Ion Implantation

C.1 Deposition of silicon oxide (SiO_2) capping and passivation layers

C.1.1 Atmosphere pressure chemical vapor deposition (APCVD) system

Figure C.1 shows the schematic illustration of APCVD system used to deposit SiO_2 films in this work. The system consists of a deposition chamber, which is connected with a silicone oil (SO) flask and an ozonizer. The SO ($[SiO(CH_3)_2]_nO[Si(CH_3)_3]_2$) vapor (GE Toshiba Silicones TSF451-10, kinematic viscosity of 10 mm^2/s) is vaporized directly by bubbling with N_2 gas.[119] The ozone (1–5%) is generated by the ozonizer from 99.9995% O_2 gas. Since ozone (O_3) is very harmful to the atmosphere and human health, the remaining O_3 is destroyed by the reaction with atomic oxygen (O) to form O_2 gas in the electric furnace before being exhausted to the atmosphere.

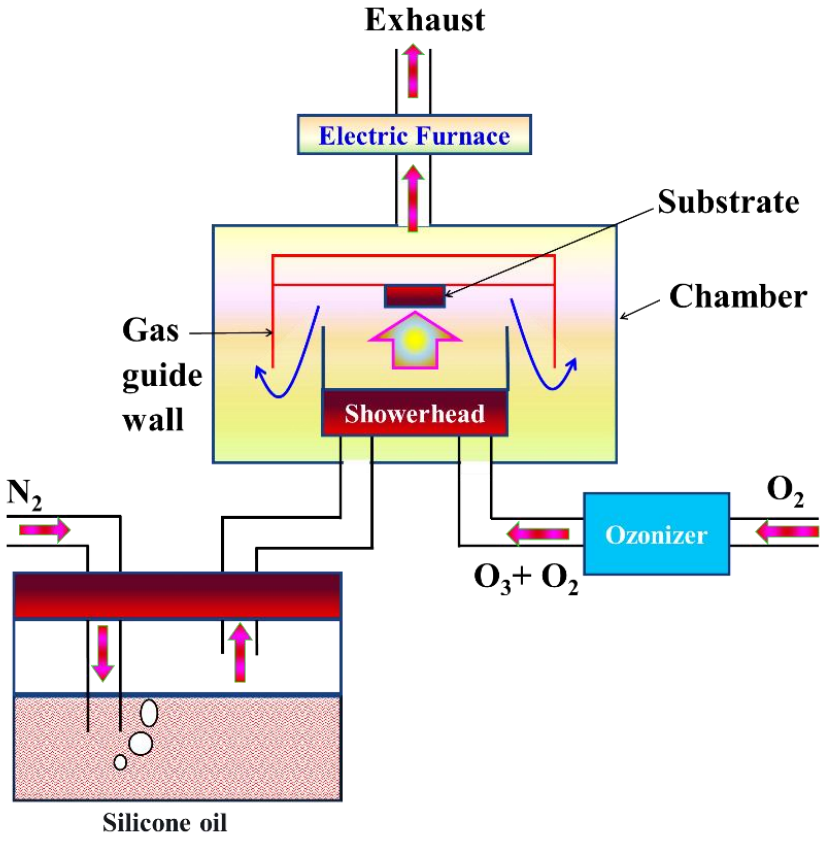

Fig. C.1 Schematic illustration of the APCVD system used for the deposition of SiO_2 films using SO vapor and O_2 + O_3 gas.

C.1.2 Deposition procedure

The chemically cleaned samples with as-deposited a-Si films by RCA method (see Appendix A.3) are put on the substrate holder, which then is loaded in the deposition chamber. Next, the showerhead, substrate holder, and the SO are heated at temperatures of 50 ^{o}C, 200 ^{o}C, and 50 ^{o}C, respectively. Subsequently, the SO is vaporized directly by bubbling with N_2 gas at a flow rate of 0.35 slm through a Teflon tube heated to about 50 ^{o}C to avoid condensation of SO vapor. The generated ozone by ozonizer at O_2 gas flow rate of 0.1 slm is introduced into the deposition chamber together with the SO vapor. The deposition of SiO_2 is carried out with a deposition rate of ~12 nm/min.

C.2 Phosphorus (P) ion implantation

After the deposition of SiO_2 capping layer, the samples are post-annealed in N_2 ambient at 350 ^{o}C for 30 min to improve quality of the SiO_2. Then, they are rinsed with ethanol prior to setting into the sample holder of ion implantation system. The used implantation system is NH-20SR produced by Nisshin electric company. Table C.1 lists some important features of the NH-20SR. Phosphorus atoms are implanted into the a-Si films at an acceleration voltage and ion dose of 40 kV and 4.44×10^{12} cm^{-2}, respectively.

Table C.1 Some important features of NH-20SR ion implanter.

Acceleration energy	10 keV to 200 keV
Implantation area	within a diameter of 90 mm
Ion species	a lot of materials can be used
Sample temperature	−195.79 °C (liq. N_2 temperature) to 400 °C
Dose amount	10^{10} to 10^{16} (or 10^{17}) atoms/cm^2

Appendix D:

X-ray Diffraction (XRD)

X-ray diffraction (XRD) is one of the non-destructive analytical techniques, which reveals information about crystal structure of materials and thin films. This technique is based on diffraction phenomenon of X-ray. The measurement system observes the scattered intensity of an X-ray beam hitting a sample as a function of incident and scattered angles. XRD is used in this study to evaluate crystallinity of YSZ layers.

In XRD, characteristics X-rays from materials such as copper (Cu), cobalt (Co), and molybdenum (Mo) are generally used. The used system has a Cu target for the X-ray beam. The diffraction of X-rays depends on the crystal structure and on the wavelength. At a wavelength of the radiation which is comparable with or smaller than the lattice constant, we may find diffracted beam directions quite different from the incident direction.[120)] W. L. Bragg presented a simple explanation of the diffracted beams from a crystal. It is supposed that the incident waves are reflected from parallel planes of atoms in the crystal, with each plane reflecting like a mirror, but only a very small fraction of the radiation. In mirror-like reflection, the angle of incidence is equal to the angle of reflection. The diffracted beams are found when the reflections from parallel planes of atoms interfere constructively, as shown in Fig. D.1(a). Considering parallel lattice planes spaced *d* apart, the path difference for rays reflected from adjacent planes is $2d\sin\theta$, where θ is measured from the plane [Fig. D.1(b)]. Constructive interference of the radiation from successive planes occurs when the path difference is an integral number *n* of wavelengths λ, so that

$$2d\sin\theta = n\lambda \tag{D.1}$$

This is the Bragg's law, which can only be satisfied when $\lambda \leq 2d$.

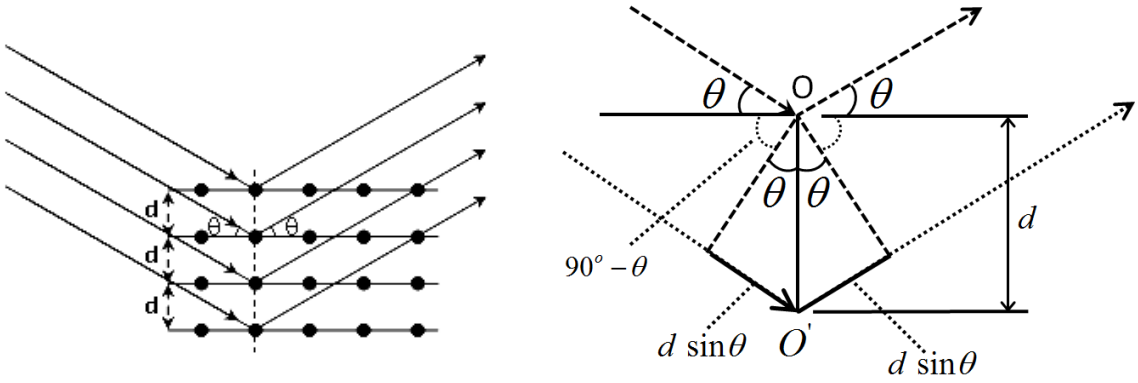

(a) **(b)**

Fig. D.1 Schematic illustration for XRD in a crystal.

XRD can be applied to:

- measure the average spacing *d* between layers or row of atoms,
- identify crystalline phases and orientation,
- determine structural properties: lattice parameters, strain, grain size, epitaxy, phase composition, preferred orientation, order-disorder transformation, thermal expansion,
- measure thickness of thin films and multi-layers, and
- determine atomic arrangement.

Appendix E:

Raman Spectroscopy

Raman spectroscopy is a spectroscopic technique used to study vibrational, rotational, and other low-frequency modes in a system.[121] It relies on Raman scattering of monochromatic light, which is discovered by C. V. Raman in 1928. It can detect both organic and inorganic species, and measure crystallinity of solids. Raman spectroscopy is used in this study to evaluate crystallinity of Si films.

Raman scattering is inelastic scattering of light with a momentum energy transfer between photons and scattering materials. Raman effect itself is based on three single processes happening within the time limited by the Heisenberg uncertainty (Fig. E.1). First, an incoming photon with a wave vector $\vec{k}_1$ and frequency ω_1 is absorbed, and the absorbing material is excited from its initial state *i* to an intermediate virtual state *v*. Then, an elementary excitation (phonon) with a wave vector $\vec{q}$ and frequency ω is created (Stokes process) or annihilated (anti-Stokes process). Finally, the material undergoes a transition from the intermediate state *v* to the final state *f*. This process is accompanied with the emission of a scattered photon with a wave vector $\vec{k}_S$ and frequency ω_S.

In most cases, the energy transfer is small compared to the energy of the incoming photon. The maximum value of *q* for standard Raman experiments in typical solids is of 10^7 m^{-1} order. This value, which occurs when the outgoing photon is emitted in the direction back towards the source, is very small compared to the size of the Brillouin zone in a typical crystal (~ 10^{10} m^{-1}). Thus, Raman scattering can only probe the phonon modes with $q \approx 0$ which gives little information about the dispersion of optical phonons, and its main use is to determine the frequencies of the longitudinal optic (LO) and transverse optic (TO) phonon modes near the Brillouin zone center.[122]

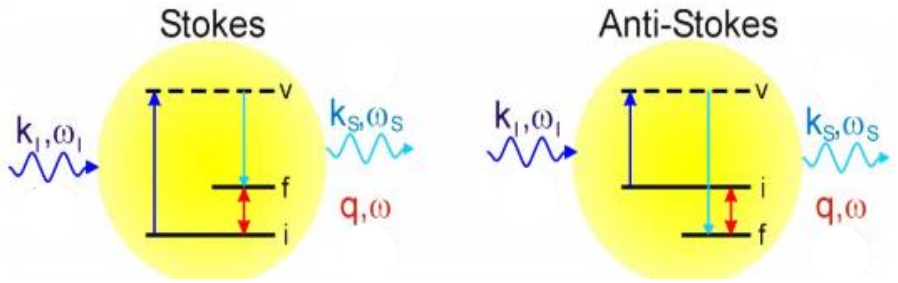

Fig. E.1 Raman scattering, Stokes (left) and anti-Stokes (right).

Figure E.2 shows a basic experimental arrangement that can be used to measure Raman spectra. The sample is excited with a suitable laser, and the scattered light is collected and focused onto the entrance slit of a scanning spectrometer. The number of photons emitted at a particular wavelength is registered using a photon-counting detector [usually made with charge coupled devices (CCD arrays)]. Then, the results are stored on a computer for analysis. By orientating the sample appropriately, the reflected laser light can be arranged to miss the collection optics. In order to reduce the saturation of detector due to elastically scattered laser photons, a high resolution spectrometer with good stray light rejection characteristics is used.

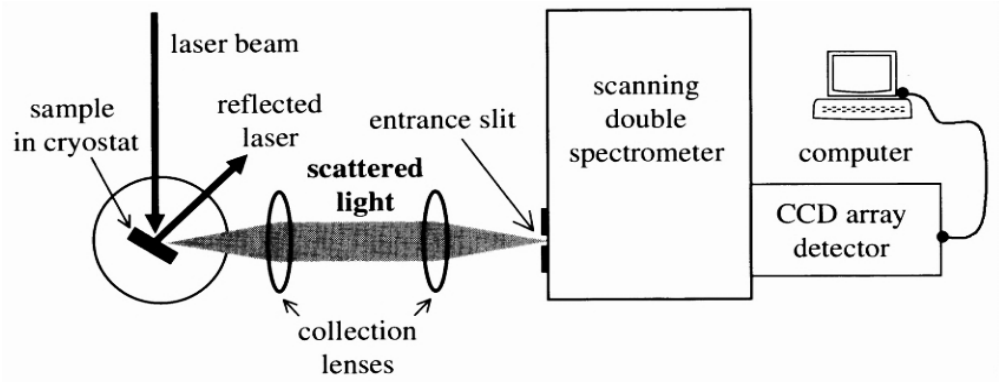

Fig. E.2 Experimental apparatus used to record Raman spectra.

Appendix F:

Calculation of The Power Reflectivity $\mathcal{R}$, Power Transmissivity $\mathcal{T}$, and Total Absorptivity A for Si Films

In this section, we present the detailed calculation of the power reflectivity $\mathcal{R}$, power pransmissivity $\mathcal{T}$, and total absorptivity A for Si films, which are mentioned in chapter 3, Fig. 4.5 of chapter 4, and chapter 7. Figure F.1 shows the schematic calculation model of the sample structure in accordance with the actual experimental conditions. In this model, we consider multireflection in a Si film, a YSZ layer, and metal layers in a normal incidence case. We also assume that the reflected beam from the bottom of the glass substrate is neglected. This is because the reflected power from the bottom of the substrate is very small (less than 5% for an incident angle ≤ 20°) and the thickness of glass is ~0.5 mm, which is more than 900 times the wavelength λ = 532 nm. The reflection coefficient r_j and transmission coefficient t_j at the (j-1/ j) interface from layer j-1 to layer j and from

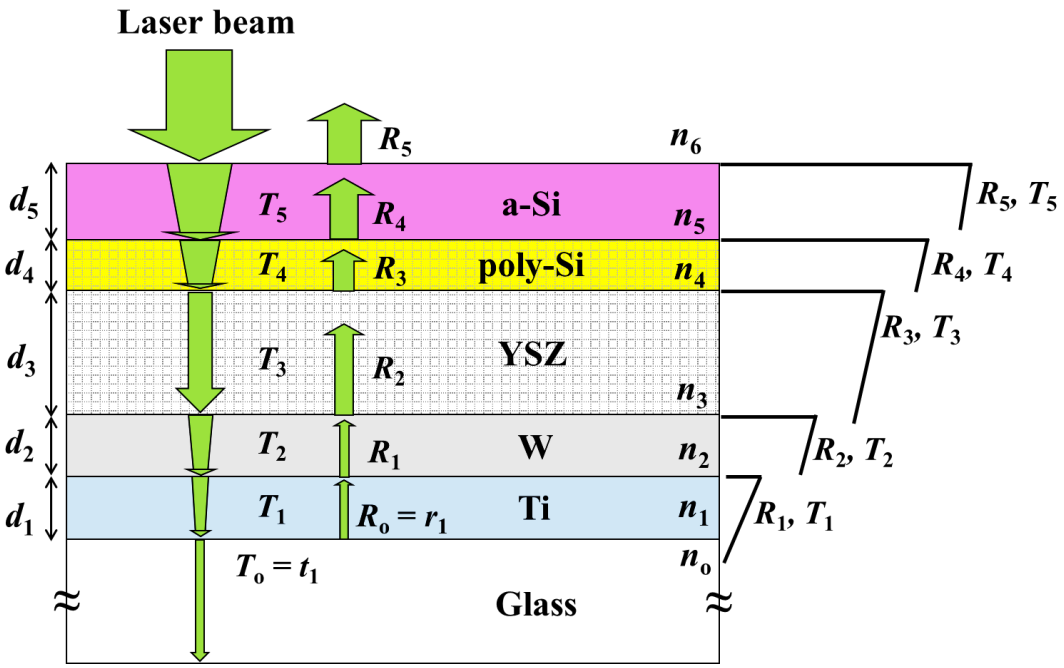

Fig. F.1 Schematic model of the sample structure for the calculations of Si film power reflectivity, power transmissivity, and total absorptivity.

layer j to layer j-1, respectively, in the case of normal incidence are given by

$$r_j = \frac{n_j - n_{j-1}}{n_j + n_{j-1}} \quad \text{and} \quad t_j = \frac{2n_j}{n_j + n_{j-1}}, \qquad j = 1 \div 5 \tag{F.1}$$

where n_j and n_{j-1} are the refractive indices of layers j and j-1, respectively. The reflection and transmission coefficients R_j and T_j, respectively, at each interface in the sample structure of Fig. (F.1), taking into account the multireflection in the underlayers, are calculated as

$$R_j = \frac{r_{j+1} + R_{j-1} exp\left(-2i\phi_j\right)}{1 + r_{j+1} R_{j-1} exp\left(-2i\phi_j\right)} \quad \text{and} \quad T_j = \frac{t_{j+1} + T_{j-1} exp\left(-i\phi_j\right)}{1 + r_{j+1} R_{j-1} exp\left(-2i\phi_j\right)}, \quad j = 1 \div 5 \tag{F.2}$$

where $R_o = r_1$, $T_o = t_1$, and $\phi_j = 2\pi \times n_j \times d_j/\lambda$, in which d_j is the thickness of layer j. It is noted that if layer j is absorbent, its refractive index contains real and imaginary parts. This means that n becomes $\tilde{n} = n - ik$. The power reflectivity $\mathcal{R}$ and power transmissivity $\mathcal{T}$, taking into account all multireflections, are given by

$$\mathcal{R} = |R_5|^2 = R_5 \times R_5{}^* \quad \text{and} \quad \mathcal{T} = \frac{n_o}{n_6}|T_5|^2 = \frac{n_o}{n_6} \times T_5 \times T_5{}^*, \tag{F.3}$$

where $R_5{}^*$ and $T_5{}^*$ are the conjugates of R_5 and T_5, respectively. The total Si film absorptivity A, which is defined as the fraction of dissipated power of the laser beam when it goes through the Si film, is determined by

$$A = 1 - \mathcal{R} - \mathcal{T}. \tag{F.4}$$

On the basis of the aforementioned derivation, we calculate the $\mathcal{R}$, $\mathcal{T}$, and A of Si films at three different incident laser wavelengths of 441.6, 532, and 632.8 nm for three structures of Si/glass, Si/YSZ/glass, and Si/YSZ/W/Ti/glass. Table F.1 lists the real and imaginary parts of refractive indexes for a-Si, poly-Si, YSZ, W, Ti, and glass (SiO_2) at wavelengths of 441.6, 532, and 632.8 nm.[91,123)] Figures F.2, F.3, and F.4 show the $\mathcal{R}$, $\mathcal{T}$, and A as functions of the poly-Si thickness d_4 from the glass substrate interface for the **Si/glass** structure (shown in Fig. F.1) at three normal incident laser wavelengths of 441.6, 532, and 632.8 nm, respectively. Thicknesses of the total Si film (d_4 + d_5) are fixed to be 60 nm. It is noted that the thicknesses of YSZ, W, and Ti layers are zero, or we remove these layers in calculation for the Si/glass structure.

Table F.1 Real and imaginary parts of refractive indexes for a-Si, poly-Si, YSZ, W, Ti, and glass (SiO_2) at wavelengths of 441.2, 532, and 632.8 nm.

Wavelength (nm)	Material	*n*	*k*
441.6	a-Si	4.69	1.6474
	poly-Si	4.76	0.1654
	YSZ	2.18	−
	W	3.3	2.488
	Ti	1.68	2.248
	SiO_2	1.46	−
532	a-Si	4.53	0.897
	poly-Si	4.15	0.0428
	YSZ	2.18	−
	W	3.49	2.719
	Ti	1.84	2.532
	SiO_2	1.46	−
632.8	a-Si	4.21	0.4178
	poly-Si	3.88	0.0196
	YSZ	2.18	−
	W	3.64	2.915
	Ti	2.15	2.92
	SiO_2	1.46	−

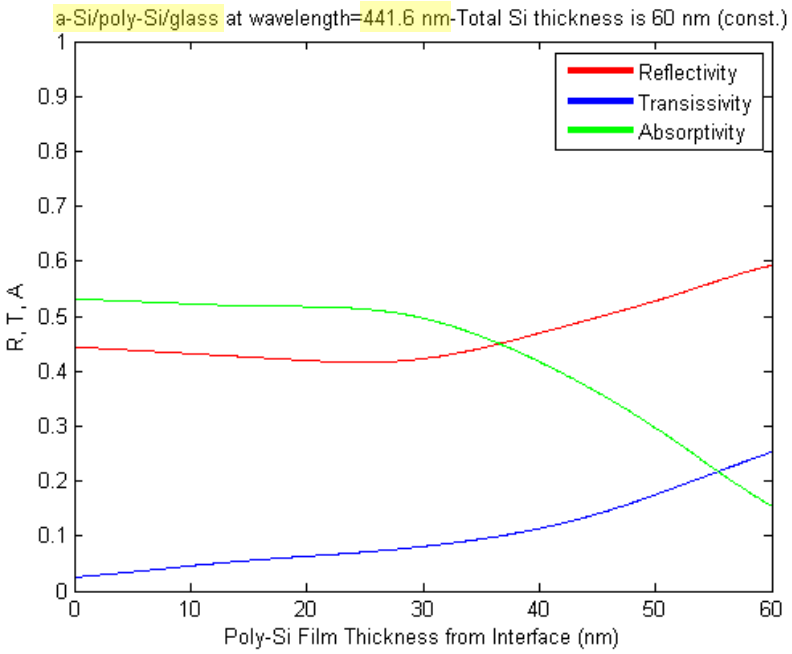

Fig. F.2 The calculated $\mathcal{R}$, $\mathcal{T}$, and A as functions of the poly-Si thickness d_4 from the glass substrate interface for Si/glass structure at normal incident laser wavelengths of 441.6 nm.

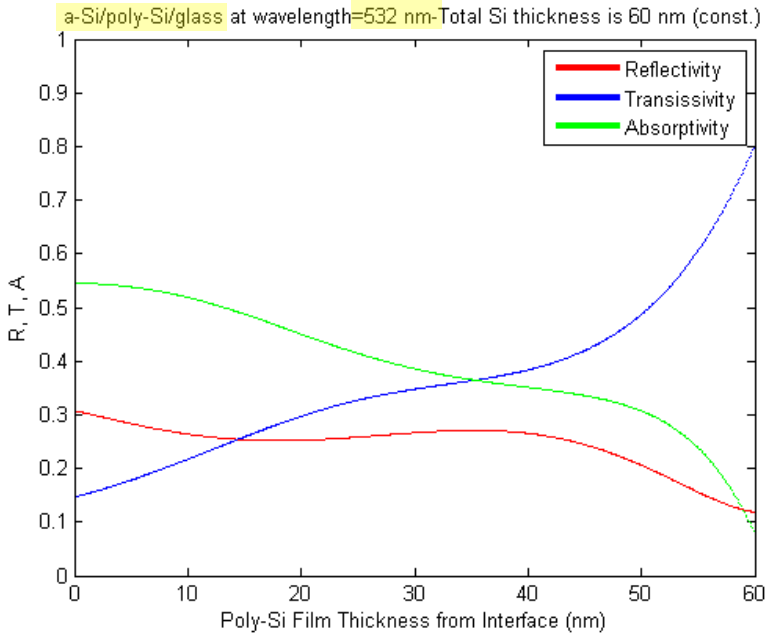

Fig. F.3 The calculated $\mathcal{R}$, $\mathcal{T}$, and A as functions of the poly-Si thickness d_4 from the glass substrate interface for Si/glass structure at normal incident laser wavelengths of 532 nm.

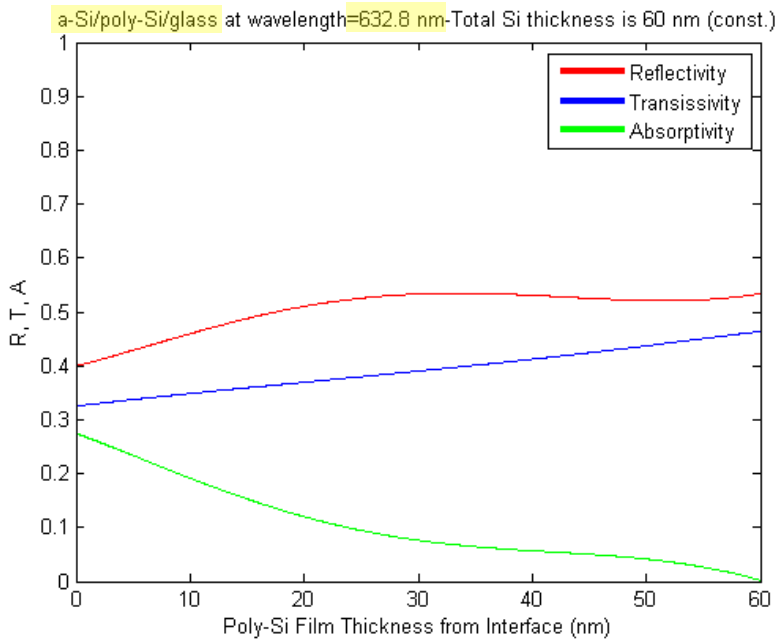

Fig. F.4 The calculated $\mathcal{R}$, $\mathcal{T}$, and A as functions of the poly-Si thickness d_4 from the glass substrate interface for Si/glass structure at normal incident laser wavelengths of 632.8 nm.

Figures F.5, F.6, and F.7 show the $\mathcal{R}$, $\mathcal{T}$, and A as functions of the poly-Si thickness d_4 from the YSZ interface for the **Si/YSZ/glass** structure (shown in Fig. F.1) at three normal incident laser wavelengths of 441.6, 532, and 632.8 nm, respectively. Thicknesses of the YSZ film (d_3) and the total Si film (d_4 + d_5) are fixed to be 60 nm. It is noted that the thicknesses of W and Ti layers are zero, or we remove these layers in calculation for the Si/YSZ/glass structure.

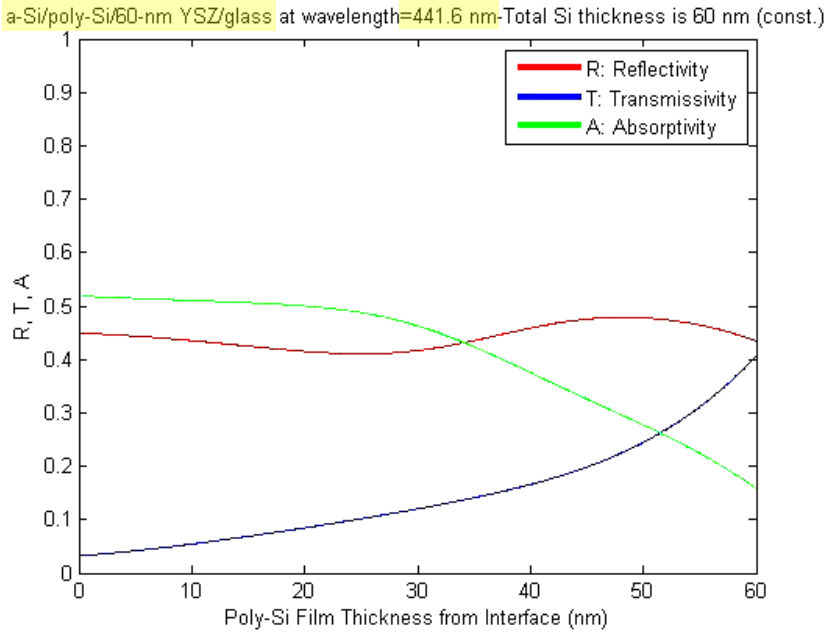

Fig. F.5 The calculated $\mathcal{R}$, $\mathcal{T}$, and A as functions of the poly-Si thickness d_4 from the YSZ interface for Si/YSZ/glass structure at normal incident laser wavelengths of 441.6 nm.

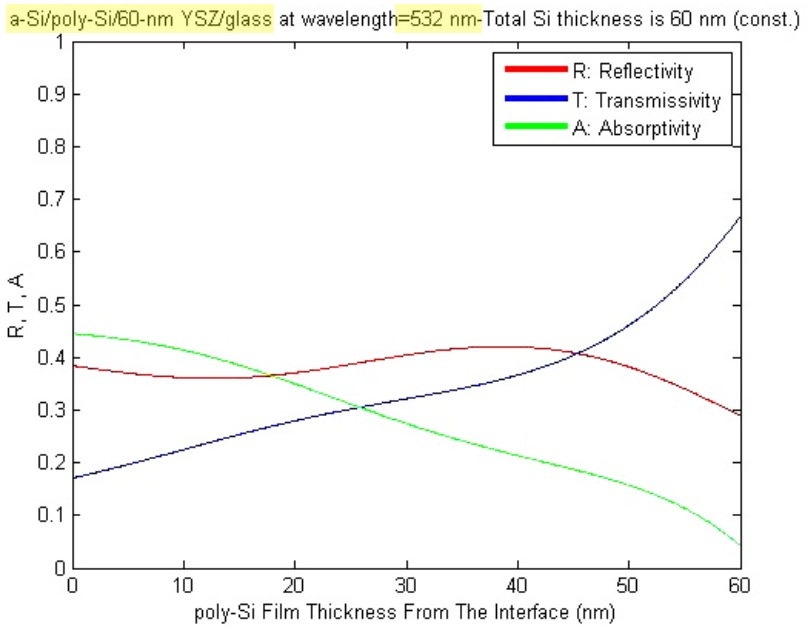

Fig. F.6 The calculated $\mathcal{R}$, $\mathcal{T}$, and A as functions of the poly-Si thickness d_4 from the YSZ interface for Si/YSZ/glass structure at normal incident laser wavelengths of 532 nm.

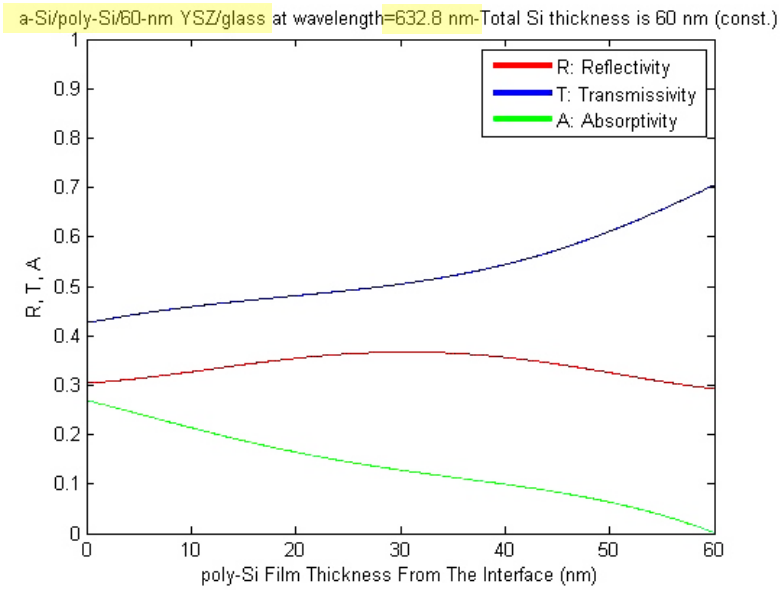

Fig. F.7 The calculated $\mathcal{R}$, $\mathcal{T}$, and A as functions of the poly-Si thickness d_4 from the YSZ interface for Si/YSZ/glass structure at normal incident laser wavelengths of 632.8 nm.

Figures F.8, F.9, and F.10 show the $\mathcal{R}$, $\mathcal{T}$, and A as functions of the poly-Si thickness d_4 from the YSZ interface for the **Si/YSZ/W/Ti/glass** structure (shown in Fig. F.1) at three normal incident laser wavelengths of 441.6, 532, and 632.8 nm, respectively. Thickness d_3 of the YSZ film is 60 nm. The total Si film (d_4 + d_5) are fixed at 60 nm. Thicknesses of the Ti (d_1) and W (d_2) layers are 30 nm.

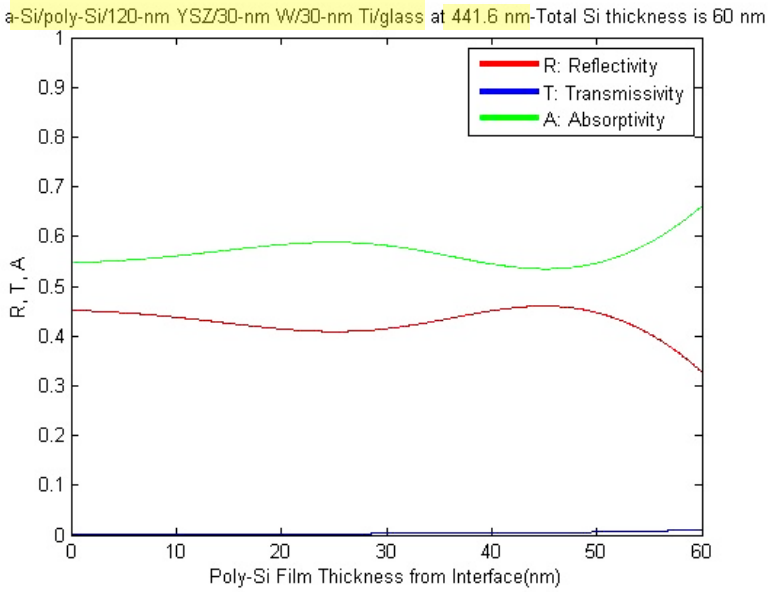

Fig. F.8 The calculated $\mathcal{R}$, $\mathcal{T}$, and A as functions of the poly-Si thickness d_4 from the YSZ interface for Si/YSZ/W/Ti/glass structure at normal incident laser wavelengths of 441.6 nm.

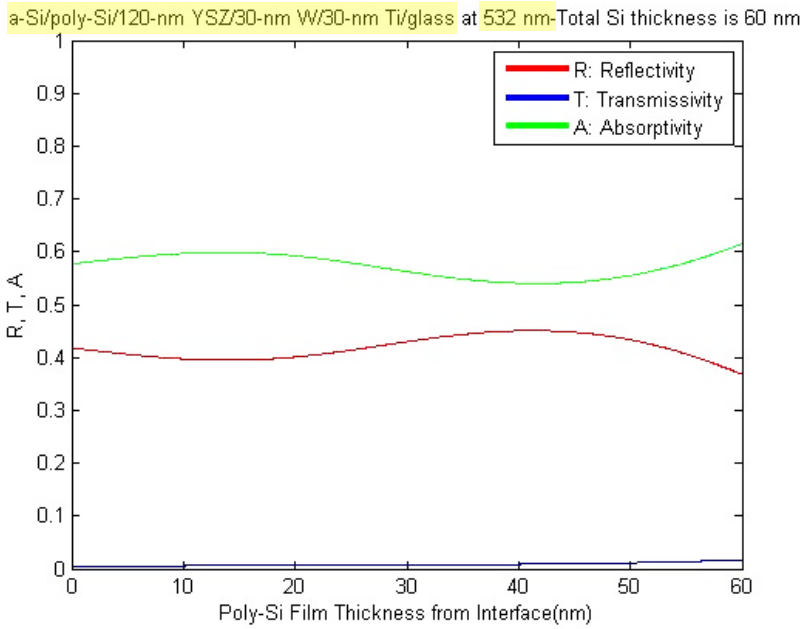

Fig. F.9 The calculated $\mathcal{R}$, $\mathcal{T}$, and A as functions of the poly-Si thickness d_4 from the YSZ interface for Si/YSZ/W/Ti/glass structure at normal incident laser wavelengths of 532 nm.

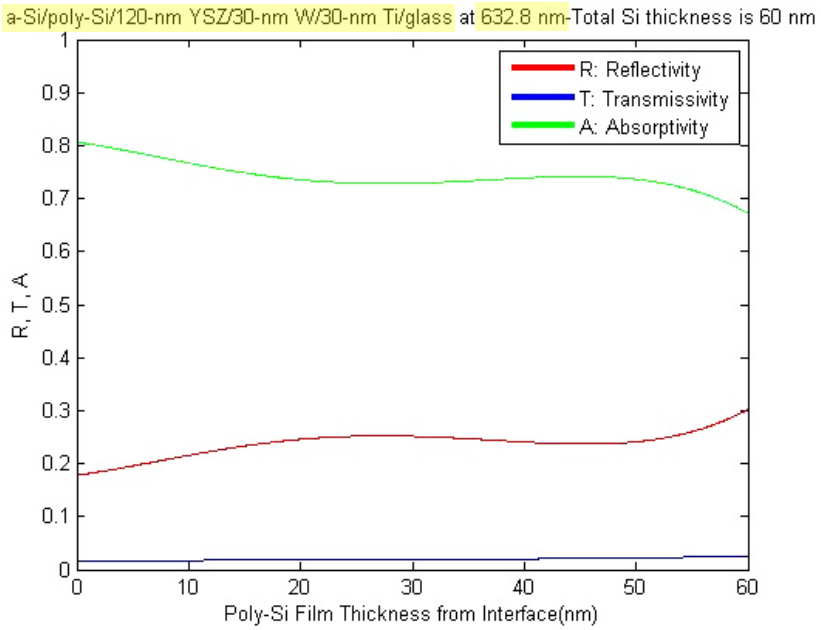

Fig. F.10 The calculated $\mathcal{R}$, $\mathcal{T}$, and A as functions of the poly-Si thickness d_4 from the YSZ interface for Si/YSZ/W/Ti/glass structure at normal incident laser wavelengths of 632.8 nm.

From the results of total absorptivity A at the wavelength of 532 nm (pulsed laser beam), we estimate the component absorptivities of a-Si (A_a) and poly-Si (A_p) for the Si/glass and Si/YSZ/glass structures, and of a-Si (A_a), poly-Si (A_p), and metals (A_m) for the Si/YSZ/W/Ti/glass structure at that wavelength.

According to the energy conservation law at layer j:

Absorbed energy in layer j (P_{Aj}) = Incident energy (P_I) – Reflected energy from layer j (P_{Rj}) – Transmitted energy through layer j (P_{Tj}).

Therefore, the absorptivity A_j in layer j is given by

$$A_j = \frac{P_{Aj}}{P_I} \tag{F.5}$$

If we call E_i the incident electric field from the air at the a-Si surface, incident energy into the a-Si is:

$$P_I = \sqrt{\frac{\varepsilon_o}{\mu_o}} n_6 \left|E_i\right|^2 \tag{F.6}$$

where ε_o, μ_o, and n_6 are permittivity of free space, permeability of free space, and refractive index of the air, respectively.

The electric field E_{ap} at the interface between the a-Si and poly-Si (in Fig. F.1) is determined by:

$$E_{ap} = \frac{\left(1+R_4\right) E_i t_5 \, exp\left(-i\phi_5\right)}{1+R_4 r_5 \, exp\left(-2i\phi_5\right)} \tag{F.7}$$

The magnetic field H_{ap} at the interface between the a-Si and poly-Si is given by:

$$H_{ap} = \frac{\sqrt{\frac{\varepsilon_o}{\mu_o}} n_5 \left(1-R_4\right) E_i t_5 \, exp\left(-i\phi_5\right)}{1+R_4 r_5 \, exp\left(-2i\phi_5\right)} \tag{F.8}$$

Intensity of the Poynting vector $\overrightarrow{S_{ap}}$ or the electromagnetic power per area at the interface between the a-Si and poly-Si is the vector product of $\overrightarrow{E_{ap}}$ and $\overrightarrow{H^*_{ap}}$ (conjugate of $\overrightarrow{H_{ap}}$). The real part of $\overrightarrow{S_{ap}}$ is the transmitted energy P_{Ta} through the a-Si and also the incident energy into the poly-Si. It is noted that, in the calculation of $\overrightarrow{S_{ap}}$, we take into account the multireflection in the underlayers. In the case of normal incidence, we have:

$$\overrightarrow{S_{ap}} = \overrightarrow{E_{ap}} \times \overrightarrow{H^*_{ap}} = \frac{\sqrt{\frac{\varepsilon_o}{\mu_o}} n_5^* \left(1-R_4^*\right)\left(1+R_4\right)\left|E_i\right|^2 \left|t_5\right|^2 exp\left[\left(-i\phi_5\right)\cdot\left(-i\phi_5\right)^*\right]}{\left|1+R_4 r_5 \, exp\left(-2i\phi_5\right)\right|^2} \tag{F.9}$$

The absorptivity A_a in the a-Si is determined by:

$$\begin{aligned} A_a = \frac{P_{Aa}}{P_I} = \frac{P_I - P_{Ra} - P_{Ta}}{P_I} &= \frac{\sqrt{\frac{\varepsilon_o}{\mu_o}} n_6 \left|E_i\right|^2 - \mathcal{R}\sqrt{\frac{\varepsilon_o}{\mu_o}} n_6 \left|E_i\right|^2 - \text{Real}\left(\overrightarrow{S_{ap}}\right)}{\sqrt{\frac{\varepsilon_o}{\mu_o}} n_6 \left|E_i\right|^2} \\ &= 1 - \mathcal{R} - \text{Real}\left(\frac{n_5^*\left(1-R_4^*\right)\left(1+R_4\right)\left|t_5\right|^2 exp\left[\left(-i\phi_5\right)\cdot\left(-i\phi_5\right)^*\right]}{n_o\left|1+R_4 r_5 \, exp\left(-2i\phi_5\right)\right|^2}\right) \end{aligned} \tag{F.10}$$

To estimate absorptivity A_p in the poly-Si, now we consider the interface between poly-Si and YSZ. The electric field E_{py} at the interface between the poly-Si and YSZ (in Fig. F.1) is determined by:

$$E_{py} = \frac{(1+R_3)E_i t_4 t_5 \exp\left[-i(\phi_4+\phi_5)\right]}{\left[1+R_3 r_4 \exp(-2i\phi_4)\right]\left[1+R_4 r_5 \exp(-2i\phi_5)\right]} \tag{F.11}$$

The magnetic field H_{py} at the interface between the poly-Si and YSZ is given by:

$$H_{py} = \frac{\sqrt{\frac{\varepsilon_o}{\mu_o}} n_4 (1-R_3) E_i t_4 t_5 \exp\left[-i(\phi_4+\phi_5)\right]}{\left[1+R_3 r_4 \exp(-2i\phi_4)\right]\left[1+R_4 r_5 \exp(-2i\phi_5)\right]} \tag{F.12}$$

Intensity of the Poynting vector $\overrightarrow{S_{py}}$ at the interface between the poly-Si and YSZ in the case of normal incidence is:

$$\overrightarrow{S_{py}} = \overrightarrow{E_{py}} \times \overrightarrow{H_{py}^*} = \frac{\sqrt{\frac{\varepsilon_o}{\mu_o}} n_4^* (1-R_3^*)(1+R_3)|E_i|^2 |t_4|^2 |t_5|^2 \exp\left\{\left[-i(\phi_4+\phi_5)\right]\cdot\left[-i(\phi_4+\phi_5)\right]^*\right\}}{\left|\left[1+R_3 r_4 \exp(-2i\phi_4)\right]\right|^2 \left|1+R_4 r_5 \exp(-2i\phi_5)\right|^2} \tag{F.13}$$

Since we have taken into account the multireflection in the underlayers when we calculated the $\overrightarrow{S_{ap}}$, the absorbed energy P_{Ap} in the poly-Si is the subtract amount of the incident energy P_{Ip} into the poly-Si [$=\text{Real}\left(\overrightarrow{S_{ap}}\right)$] and the transmitted energy P_{Tp} through the poly-Si[$=\text{Real}\left(\overrightarrow{S_{py}}\right)$]. Therefore, the absorptivity A_p in the poly-Si is determined by:

$$\begin{aligned} A_p &= \frac{P_{Ap}}{P_I} = \frac{P_{Ip}-P_{Tp}}{P_I} = \frac{\text{Real}\left(\overrightarrow{S_{ap}}\right)-\text{Real}\left(\overrightarrow{S_{py}}\right)}{\sqrt{\frac{\varepsilon_o}{\mu_o}} n_6 |E_i|^2} \\ &= \text{Real}\left(\frac{n_5^*(1-R_4^*)(1+R_4)|t_5|^2 \exp\left[(-i\phi_5)\cdot(-i\phi_5)^*\right]}{n_o \left|1+R_4 r_5 \exp(-2i\phi_5)\right|^2}\right) \\ &\quad - \text{Real}\left(\frac{n_4^*(1-R_3^*)(1+R_3)|t_4|^2 |t_5|^2 \exp\left\{\left[-i(\phi_4+\phi_5)\right]\cdot\left[-i(\phi_4+\phi_5)\right]^*\right\}}{n_o \left|\left[1+R_3 r_4 \exp(-2i\phi_4)\right]\right|^2 \left|1+R_4 r_5 \exp(-2i\phi_5)\right|^2}\right) \end{aligned} \tag{F.14}$$

The absorptivity A_m in the metal layers can be calculated as the same procedure as of A_a and A_p, or it is simply determined by:

$$A_m = A - A_a - A_p\,, \tag{F.15}$$

where absorptivities of the YSZ layer and glass substrate are assumed to be zero. The calculated component absorptivities for the Si/glass, Si/YSZ/glass, and Si/YSZ/W/Ti/glass at an incident wavelength of 532 nm are shown in Figs. F.11, F.12, and F.13, respectively.

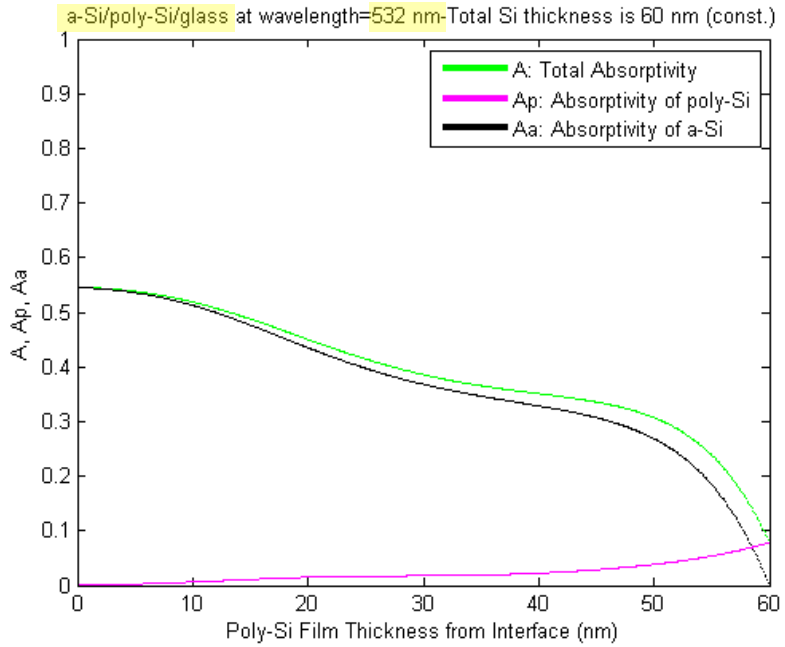

Fig. F.11 The calculated A, A_p, and A_a as functions of the poly-Si thickness d_4 from the glass substrate interface for Si/glass structure at normal incident laser wavelengths of 532 nm.

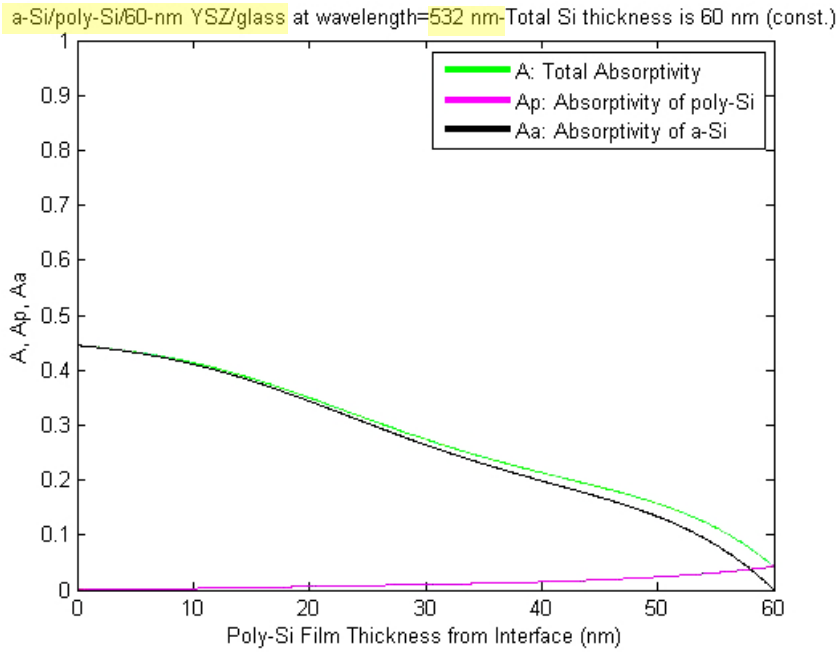

Fig. F.12 The calculated A, A_p, and A_a as functions of the poly-Si thickness d_4 from the YSZ interface for Si/YSZ/glass structure at normal incident laser wavelengths of 532 nm.

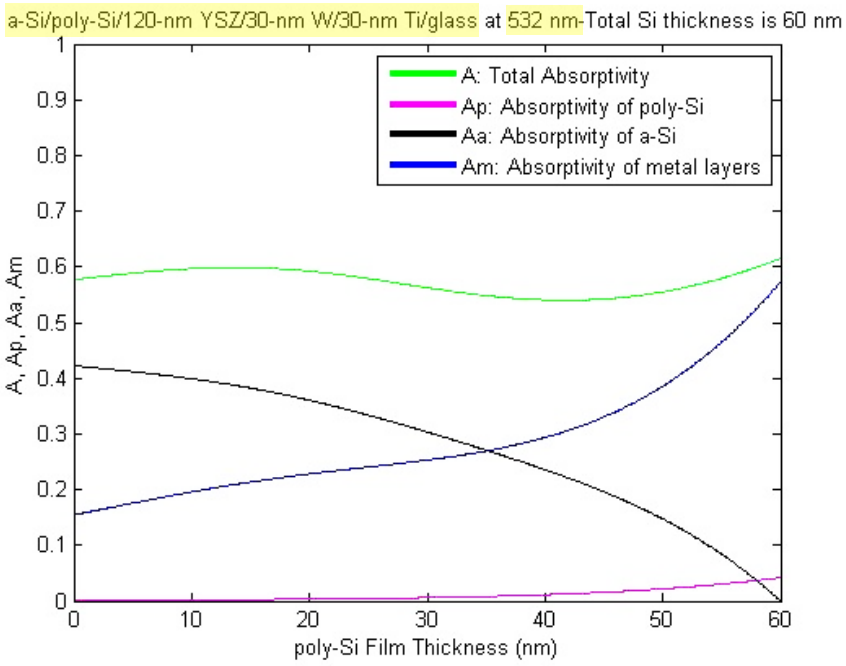

Fig. F.13 The calculated A, A_p, A_a, and A_m as functions of the poly-Si thickness d_4 from the YSZ interface for Si/YSZ/W/Ti/glass structure at normal incident laser wavelengths of 532 nm.

Appendix G:

Reflection High-Energy Electron Diffraction (RHEED)

Reflection high-energy electron diffraction (RHEED or R-HEED) is a technique for surface structural analysis that is remarkably simple to implement, requiring at the minimum only an electron gun, a phosphor screen, and a clean surface. The first RHEED experiment was conducted by Nishikawa and Kikuchi in 1928 at nearly the same time as the discovery of electron diffraction by Davison and Germer (1927). However, until 1969, the RHEED measurement was incorporated into an apparatus for the molecular beam

epitaxy (MBE) by Arthur and LePore. RHEED has become an important technique because of its compatibility with the methods of vapor deposition used for the epitaxial growth of thin films. Since its penetration depth is small, owing to the interaction between incident electrons and atoms, RHEED is primarily sensitive to the atomic structure of the first few planes of a crystal lattice.[124)]

The principle behind RHEED is a high-energy electron beam (5-100 keV) that is directed to a sample at a grazing angle and subsequently picked up by detectors as it bounces off the sample. The atomic structure of the material being investigated disrupts the path of the high-speed electrons, which produces differing patterns of electron streaks on a phosphor screen detector. These patterns of streaks are then interpreted to yield the atomic structure of the material being investigated. The schematic illustration of RHEED measurement principle is shown in Fig. G.1.

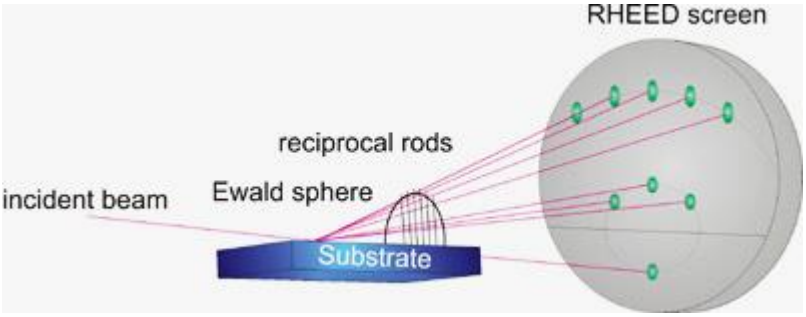

Fig. G.1 Schematic illustration of RHEED measurement principle.

Appendix H:

Scanning Electron Microscopy (SEM)

Scanning electron microscopy (SEM), which was first developed with a submicron probe by von Ardenne (1938),[125)] is a type of electron microscopy that produces images of a sample by scanning it with a focused beam of electrons. The electrons interact with atoms in the sample, producing various signals that can be detected and that contain information about the sample's surface topography and composition. The electron beam is generally scanned in a raster scan pattern, and the beam's position is combined with the detected signal to produce an image. SEM can achieve a resolution better than 1 nm. Specimens can be observed in high vacuum, in low vacuum, in dry conditions, and at a

wide range of cryogenic or elevated temperatures. Figure H.1 shows a schematic illustration of a SEM.

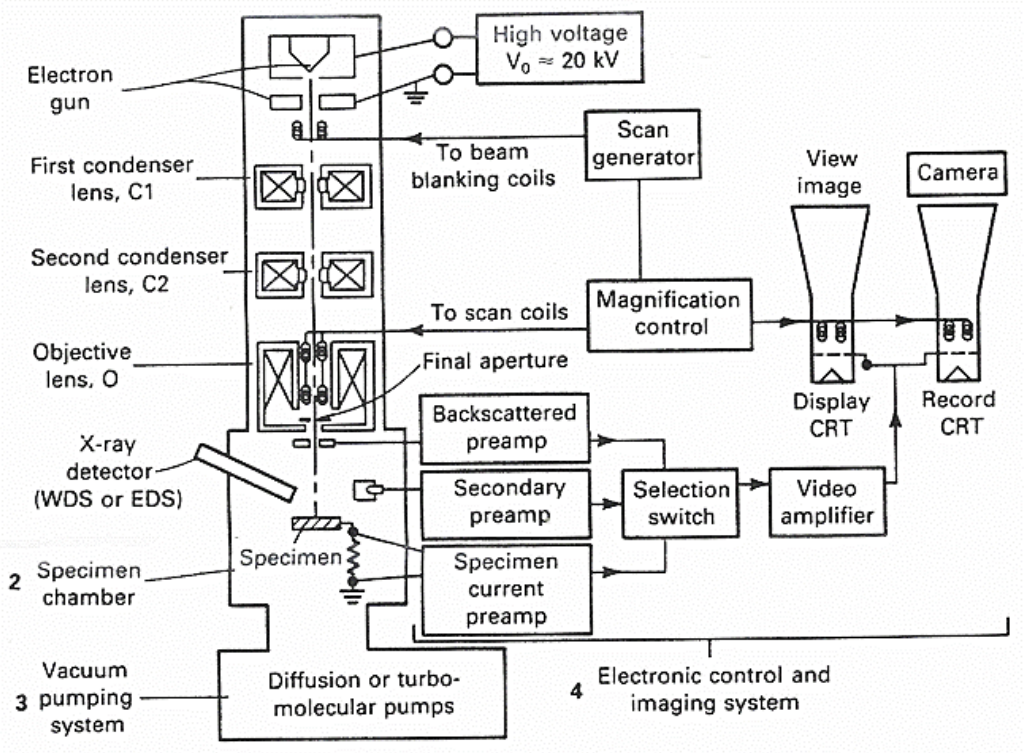

Fig. H.1 Basic components of SEM. The various components of the microscope can be categorized as (1) electron column, (2) specimen chamber, (3) vacuum pumping system and (4) electron control and imaging system.[126] (WDS: wavelength dispersive spectrometer; EDS: energy dispersive spectrometer; CRT: cathode ray tube)

The electron gun at the top of the column produces an electron beam that is focused into a fine spot as small as 1 nm in diameter on the specimen surface. This beam is scanned in a rectangular raster over the specimen and the intensities of various signals created by interactions between the beam electrons and the specimen are measured and stored in computer memory. The stored values are then mapped as variations in brightness on the image display. The secondary electron (SE) signal is the most frequently used signal. It varies with the topography of the sample surface. The ratio of the size of the displayed image to the size of the area scanned on the specimen gives the magnification.

Appendix I:

Transmission Electron Microscopy (TEM)

Transmission electron microscopy (TEM) is a microscopy technique in which a beam of electrons is transmitted through an ultra-thin specimen, interacting with the specimen as it passes through. Figure I.1 shows an optical components layout of a conventional TEM system. A thin specimen is irradiated with an electron beam of uniform current density. Depending on the type of the system, the acceleration voltage is in the range from 100 kV (for routine instruments) to 3 MV (for high voltage electron microscopy). Electron beam emitted from the electron gun is condensed before being irradiated on the specimen. A three- or four-stage condenser-lens system permits variation of the illumination aperture

and the area of the illuminated specimen. The electron-intensity distribution behind the specimen is imaged with a lens system, composed of three to eight lenses. The image is magnified and focused onto an imaging device, or to be detected by a sensor such as CCD camera.

Electrons interact strongly with atoms by elastic and inelastic scatterings. The specimen must be very thin, typically of the order of 5 – 100 nm for 100 keV electrons, depending on the density and elemental composition of the object and the desired resolution. Special sample preparation techniques are needed for this. There are three primary imaging modes of TEM: bright field, dark field, and high resolution. Images formed with only transmitted electrons are bright field images and those formed with specific diffracted beam are dark field images. High resolution TEM (HR-TEM) gives structural information of the sample in an atomic scale, or also known as lattice imaging. HR-TEM has become a very important tool for interface analysis.

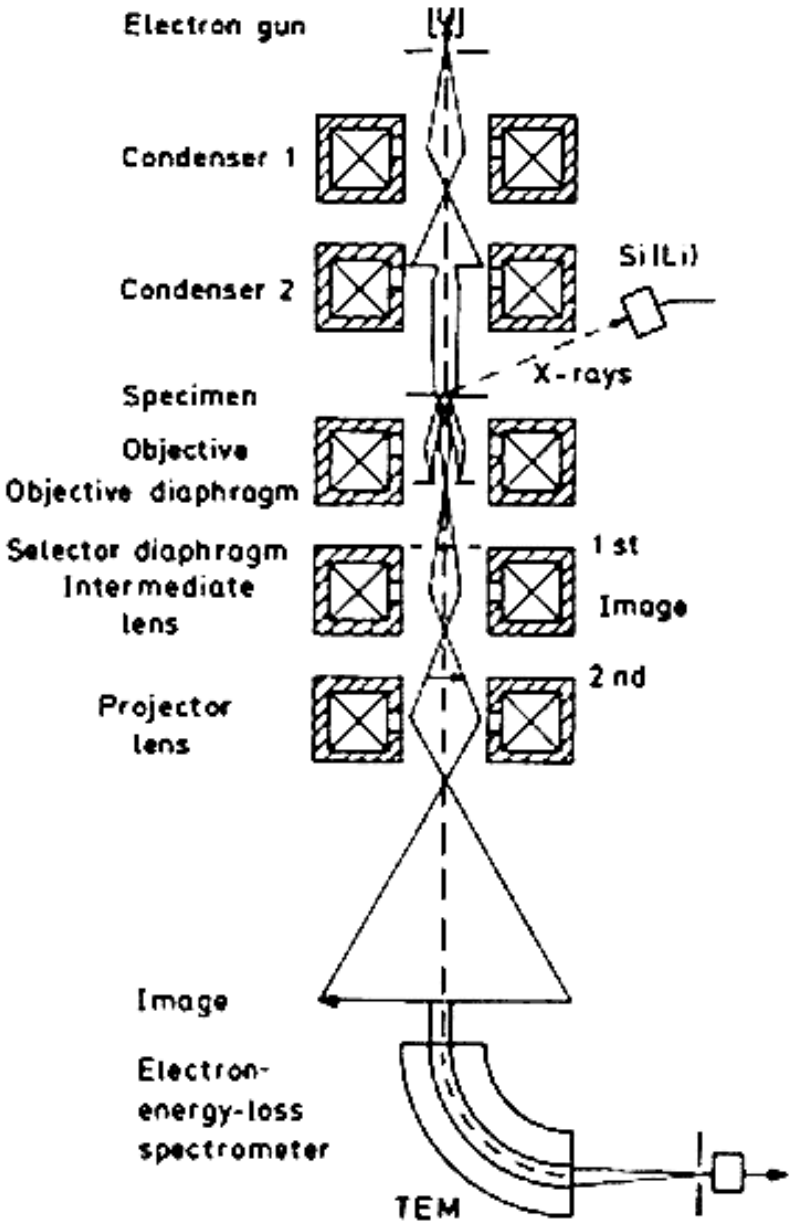

Fig. I.1 Schematic ray path for a TEM equipped with additional x-ray and electron energy-loss spectroscopy.[127)]

Appendix J:

X-ray Photoelectron Spectroscopy (XPS)

X-ray photoelectron spectroscopy (XPS), also known as electron spectroscopy for chemical analysis (ESCA) is now a widely-used analytical technique for investigating the chemical composition of solid surfaces, allowing all elements except hydrogen and helium to be detected. The principle of XPS is illustrated in Fig. J.1.

Using a characteristic X-ray line from an X-ray tube to illuminate the sample, photoelectrons are emitted from the sample surface. An electron energy analyzer determines the binding energy of the photoelectrons. Usually, MgKα (1253.6 eV) or AlKα (1486.6 eV) is used. The used system in this study has the X-ray source of AlKα (1486.6 eV). The photoelectrons have kinetic energies given by:

$$E_k = h\upsilon - E_b - \phi_s , \qquad \text{(J.1)}$$

where $h\upsilon$ is the energy of the photons, E_b is the binding energy of the atomic orbitals from which the electrons originate, and ϕ_s is the spectrometer work function. Knowing $h\upsilon$, the spectrometer measures E_k of the emitted electrons from the sample and E_b can be calculated. In XPS spectrum, intensity of photoelectrons is shown as a function of their binding energy.

XPS can provide the information about:

- Surface analysis: XPS can analyze surface layers or thin film structures which is used in many applications such as polymer surface modification, catalysis, corrosion, adhesion, semiconductor and dielectric materials, electronics packaging, magnetic media, and thin film coatings.

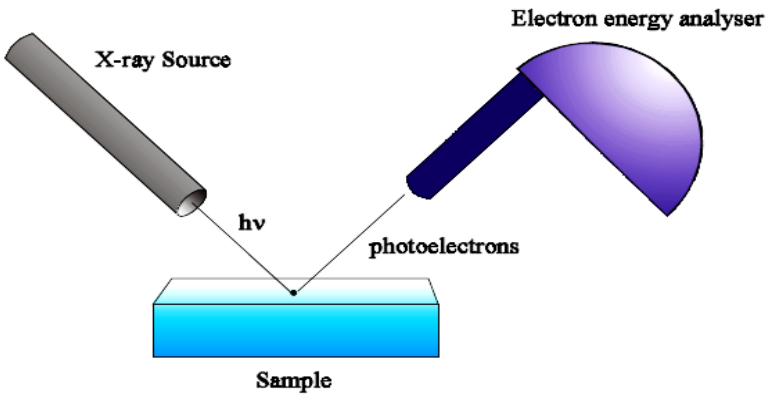

Fig. J.1 Schematic illustration of XPS measurement principle.

- Qualitative analysis: Qualitative analysis of a specimen consists in identifying elements that are present.
- Quantitative analysis: XPS can determine surface composition of a specimen.
- Chemical analysis: XPS allows to obtain information on chemical state of elements of a sample.

Appendix K:

Secondary Ion Mass Spectroscopy (SIMS)

Secondary ion mass spectroscopy (SIMS) is a technique for surface and thin-film analysis developed from the early 1960s. SIMS technique is capable of detecting all elements as well as isotopes and molecular species. It is the most sensitive of all the beam techniques, with the detection limits for some elements in the 10^{14} to $10^{15}/cm^3$ range. The basic components of a SIMS system is shown in Fig. K.1.

A destructive SIMS technique is basically a removal of material from the sample by sputtering and the ejected material is analyzed by a mass analyzer. During the SIMS analysis, the sample surface is slowly sputtered away. Continuous analysis while sputtering produces information as a function of depth, called a depth profile. During the bombardment of the sample surface by an ion beam, sputtering takes place when atoms near the surface receive sufficient energy from the incident ion to be ejected from the sample. The ejected particles are mostly neutral atoms, thus cannot be detected by the conventional SIMS. However, there are also positively or negatively charged ions and these ions are analyzed, with respect to their mass and energy. The escape depth of the sputtered atoms is generally a few monolayers for primary energies of 10 to 20 keV. The primary ions lose their energy in the process and come to rest tens of nm below the sample surface. This means that ion bombardment leads not only to sputtering, but also to ion implantation and lattice damage.

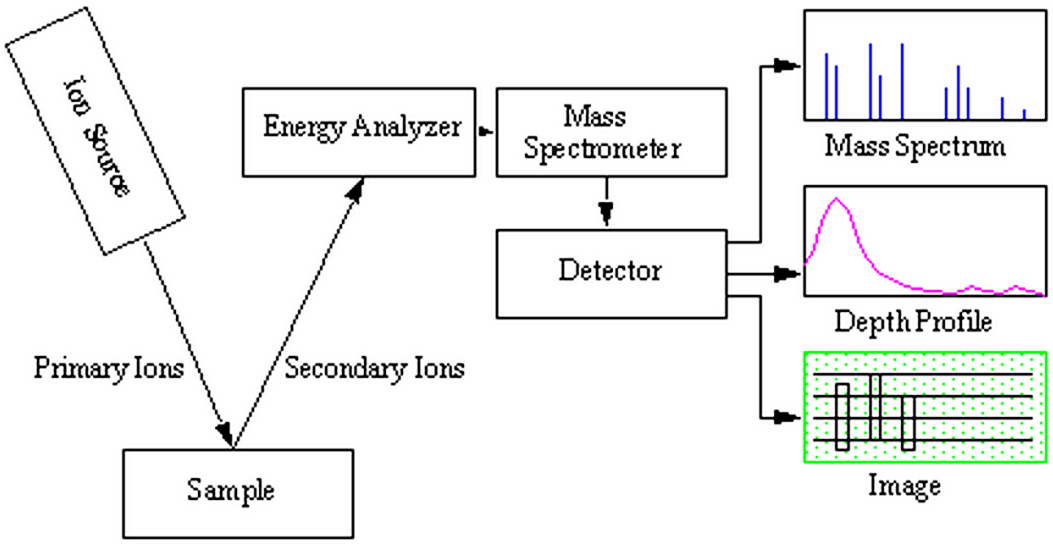

Fig. K.1 SIMS technique block diagram.[128)]

Appendix L:

Hall Effect Measurement

Hall effect measurement technique has found wide application in the characterization of semiconductor materials. It is used to evaluate the transport properties (carrier concentration, mobility, and resistivity) in semiconductors. The Hall effect is usually used with an extrinsic semiconductor so that one carrier dominates and the other has a negligible density. However, in this Appendix, we show the Hall effect for both electrons and holes.

The Hall effect is illustrated schematically in Fig. L.1. Considering a current-carrying conductor placed in a magnetic field $\vec{B}$, the current carriers (electrons or holes) in a conductor experience a force in a direction perpendicular to both the magnetic field and the carrier velocity. When an electric current flows in positive *x* direction through a conductor in a magnetic field $\vec{B}$ (in positive *z* direction), the generated force (in minus *y* direction) pushes the moving charges toward one side of the conductor producing a charge separation. As a result, a measurable voltage in the direction perpendicular to both the magnetic field and the current is produced. This is known as the Hall effect, and the measureable voltage is known as the Hall voltage, V_H. The force $\vec{F}$ on the moving charge *q* in a magnetic field $\vec{B}$ with velocity $\vec{v}$ is written given by

$$\vec{F} = q\left(\vec{E} + \vec{v} \times \vec{B}\right) \tag{L.1}$$

In the steady state, this force is balanced by an induced electric field that results from a

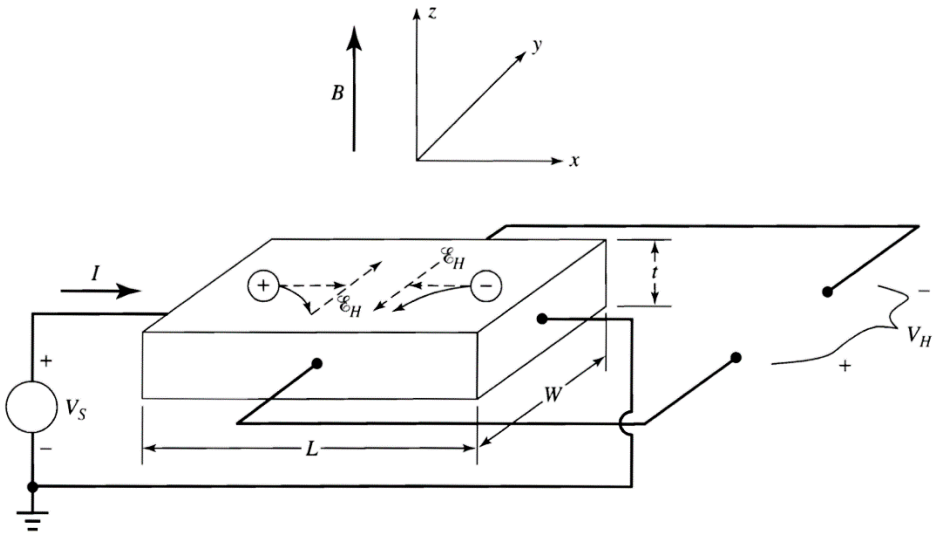

Fig. L.1 Schematic illustration of the Hall effect.[129)]

slight charge redistribution. These forces must be balance because there can be no net steady-state motion of the carriers in the transverse direction.[129)] The induced electric field is called the Hall field E_H and along the y direction. The current flow in x direction for electrons is

$$I = J_x A = qnv_x A = qnv_x wt \tag{L.2}$$

and for holes $$I = J_x A = qpv_x A = qpv_x wt \tag{L.3}$$

where n and p are in turn the carrier concentrations of electrons and holes, v_x is the current drift velocity, and w and t are the width and thickness of the sample, respectively. In y direction, there is no net force, thus

$$qE_H = qv_x B \tag{L.4}$$

where $v_x = -J_x/qn$ for electrons and $v_x = J_x/qp$, which gives

$$E_H = -\frac{J_x B}{qn} = R_H J_x B \qquad \text{for electrons} \tag{L.5}$$

and $$E_H = \frac{J_x B}{qp} = R_H J_x B \qquad \text{for holes} \tag{L.6}$$

Here, R_H is called the Hall coefficient, which is defined simply as

$$R_H = \frac{E_H}{J_x B} = -\frac{1}{qn} \qquad \text{for electrons} \tag{L.7}$$

and $$R_H = \frac{E_H}{J_x B} = \frac{1}{qp} \qquad \text{for holes} \tag{L.8}$$

R_H carries a (−) sign in the case where the current carriers are electrons and (+) sign for holes. The Hall voltage V_H produced by the Hall field E_H is

$$V_H = -\int_w^0 E_H dy = \int_w^0 \frac{J_x B}{qn} = \int_w^0 \frac{IB}{wtqn} = -\frac{IB}{tqn} \qquad \text{for electrons} \tag{L.9}$$

$$V_H = -\int_w^0 E_H dy = -\int_w^0 \frac{J_x B}{qp} = -\int_w^0 \frac{IB}{wtqp} = \frac{IB}{tqp} \qquad \text{for holes} \tag{L.10}$$

R_H can also be written as

$$R_H = \frac{tV_H}{BI} \tag{L.11}$$

The voltage along the x direction V_s is

$$V_s = IR = \frac{I\rho L}{wt} \tag{L.12}$$

Therefore, the resistivity ρ is

$$\rho = \frac{wtV_s}{IL} \tag{L.13}$$

The Hall mobility μ_H is defined by

$$\mu_H = \frac{|R_H|}{\rho} \tag{L.14}$$

In this work, we performed the AC Hall effect measurement using the Van der Pauw method. Generally, it is very difficult to measure low conductive or low carrier concentration thin films by DC Hall effect measurement because of its large noise. This time, by using the AC measurement, it was possible to estimate low conductive films. In the ideal case, AC and DC field Hall effect measurements are very similar. In practice, the system configuration is different. The primary difference is the presence of a lock-in amplifier in the AC field option. Modern, digital lock-in amplifiers are the perfect tool for extracting the small Hall voltage from its background. A model of this extraction is shown in Fig. L.2.

The DC current source provides the measurement current through the current leads of the sample. The lock-in amplifier's oscillator output drives the power supply for the magnet that generates a sinusoidal, AC magnetic field at the desired frequency. The changing field generates an AC voltage across the samples voltage leads which is filtered

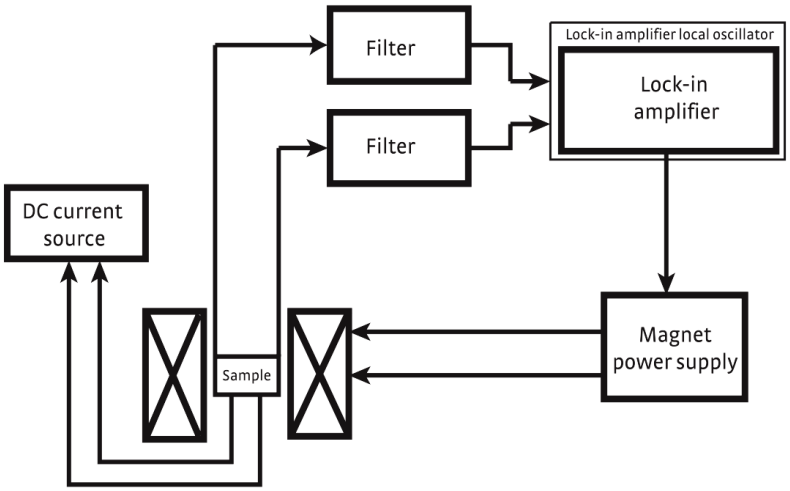

Fig. L.2 Hall voltage extraction process for the lock-in amplifier in AC Hall effect measurement.[130)]

and directed back to the lock-in amplifier. The lock-in amplifier then measures the amplitude and phase of the filtered AC voltage. Synchronous detection in the lock-in amplifier allows it to discriminate the desired Hall voltage, which is at the same frequency as the lock-in amplifier's oscillator output frequency and has a known phase.

Appendix M:

Estimation of Thin-Film Transistor Parameters

Precision semiconductor parameter analyzer 4156A is used to measure several important parameters of the fabricated TFTs, which are the peak field-effect mobility (μ_{eff}), subthreshold swing (S.S), ON/OFF current ratio, and threshold voltage (V_{th}).

M.1 Peak field-effect mobility (μ_{eff})

For $V_D < V_{Dsat}$, the μ_{eff} ($cm^2V^{-1}s^{-1}$) is determined by:

$$\mu_{eff} = \frac{Lg_m}{WC_{ox}V_D}, \quad \text{(M. 1)}$$

where L, W, g_m, C_{ox}, V_D, and V_{Dsat} are channel length, channel width, transconductance, gate dielectric capacitance per unit area, drain voltage, and saturation drain voltage, respectively. The transconductance g_m relates the output and input of the transistor and is defined by:

$$g_m \equiv \frac{\partial I_D}{\partial V_G} \quad \text{(M. 2)}$$

At a fixed V_D, μ_{eff} is maximum when g_m is maximum under condition that L, W, and C_{ox} are constant. The peak μ_{eff} is determined ad the maximum value of μ_{eff}.

M.2 Subthreshold swing (S.S)

The measurement of subthreshold current can be used to obtain a value of the slope by the parameter S.S called the subthreshold slope or subthreshold swing. S.S is usually specified in units of mV of applied gate voltage V_G per decade of subthreshold current change. An equation for S.S is:

$$S.S = ln(10)\frac{\partial V_G}{\partial[ln(I_D)]}, \quad \text{(M. 3)}$$

In our study, S.S is determined as the smallest value when $\partial[\ln(I_D)]$ is maximum at ∂V_G = constant.

M.3 ON/OFF current ratio

The ON/OFF current ratio is defined as the ratio of maximum drain current I_{Dmax} over minimum drain current I_{Dmin} within the measured range of I_D-V_G curve at V_D = 0.1 V.

M.4 Threshold voltage (V_{th})

The V_{th} in our study is determined by an interception of linear extrapolation of the I_D-V_G curve at V_D = 0.1 V.